



Università degli Studi di Napoli “Federico II”

DOTTORATO DI RICERCA IN
FISICA

Ciclo XXXIII

Coordinatore: prof. Salvatore Capozziello

Plasmonic nanostructures for optical biosensing

Settore Scientifico Disciplinare FIS/07

Dottorando
Antonio MINOPOLI

Tutor
Prof. Raffaele VELOTTA

Anni 2018/2020

Contents

List of abbreviations	7
Introduction.....	12
Chapter 1. Theory of plasmonics	16
1.1 Maxwell's equations.....	16
1.2 Plasma model	19
1.3 Volume plasmons	22
1.4 Surface plasmon polaritons	23
1.4.1 Propagating surface electromagnetic waves	23
1.4.2 Single dielectric/metal interface.....	25
1.4.3 Configurations sustaining surface plasmon polaritons	29
1.5 Localized surface plasmon	31
1.5.1 Electrodynamic approach.....	32
1.5.2 Quasi-static approximation	35
1.5.3 Gans theory	41
1.6 Numerical simulations.....	43
1.6.1 Discrete dipole approximation	43
1.6.2 Boundary element method	45
1.6.3 Finite element method.....	48
1.6.4 Finite-difference time-domain	51
1.6.5 Lumerical: high-performance photonic simulation software.....	54
Chapter 2. Optical biosensing	56

2.1	Nanoparticle-based sensors	56
2.1.1	Effect of particle size, shape, and material.	58
2.1.2	Surface biofunctionalization	60
2.1.3	Gold nanoparticle aggregation-based colorimetric biosensors	62
2.2	Realization of AuNP-based colorimetric immunosensors	64
2.2.1	Synthesis of gold nanoparticles.....	64
2.2.2	Optical and morphological characterization of bare and functionalized AuNPs.....	65
2.3	Detection of 17 β -estradiol in tap water	68
2.3.1	Dose-response curve	70
2.3.2	Morphological characterization of AuNP aggregates	73
2.3.3	Optical response of AuNP aggregates (FDTD simulations).....	74
2.3.4	Dynamics of aggregation	79
2.3.5	Repeatability, stability, recovery, and specificity assay	80
2.3.6	Discussion	82
2.4	Detection of SARS-CoV-2 in nasal and throat swabs.....	83
2.4.1	Optical response of SARS-CoV-2@f-AuNPs (measurements and FDTD simulations) 85	
2.4.2	SARS-CoV-2 testing of hospital patients	87
2.4.3	Dose-response curve	89
2.4.4	Discussion	90
Chapter 3.	Collective surface plasmon	92
3.1	Two-dimensional array of AuNPs.....	92
3.1.1	Coupled-dipole system.....	92
3.1.2	Quasi-static limit	94
3.1.3	Dynamic response	96
3.1.4	Plasmonic surface lattice resonance.....	97
3.2	Fabrication of nanostructured substrates	98

3.2.1	Electrostatic self-assembly of gold nanoparticles	99
3.2.2	Block copolymer micelle nanolithography	100
3.3	Morphological and optical characterization (measurements and numerical simulations)	101
3.3.1	Array of randomly positioned AuNPs	101
3.3.2	Array of ordered AuNPs	103
3.3.3	Branched array of AuNPs	108
Chapter 4. Plasmon-enhanced fluorescence		111
4.1	Beyond the classical interpretation of the fluorescence	111
4.1.1	Fluorescence spectral modification	111
4.1.2	Mechanisms of plasmon-fluorescence interaction	113
4.2	Calculation of the fluorescence amplification	115
4.2.1	Enhancement of the fluorophore excitation rate	116
4.2.2	Enhancement of the fluorophore quantum yield	118
4.2.3	Modification of the luminescence collection efficiency	121
4.3	Applications to biosensing	122
4.4	A comparative study on device performance	124
4.4.1	Plasmon-fluorophore spectral overlap	125
4.4.2	Surface biofunctionalization through PIT	126
4.4.3	Binding kinetic study	127
4.4.4	Dose-response curve	128
4.4.5	Fluorescence enhancement factor	132
4.4.6	Specificity	134
4.4.7	Discussion	135
Conclusions		138
Appendix A. Nanoparticle synthesis		141
A.1	Turkevich's method	141
A.2	Pollitt's method	141

A.3	Gold growth.....	142
Appendix B. Fabrication of 2D AuNP array.....		143
B.1	Fabrication of randomly positioned AuNPs.....	143
B.2	Honeycomb lattice of AuNPs.....	143
B.3	Branched arrays of AuNPs.....	144
Appendix C. Morphological characterization.....		145
C.1	Analysis of SEM images.....	145
C.2	Coding of the simulation model.....	146
Appendix D. Biofunctionalization, blocking and detection.....		148
D.1	UV-lamp.....	148
D.2	Colloidal solution.....	148
D.2.1	Colorimetric immunosensor for detecting 17 β -estradiol in tap water	149
D.2.2	Colorimetric immunosensor for detecting SARS-CoV-2 in naso-oropharyngeal swabs 150	
D.3	Solid substrate	151
D.3.1	Ab-analyte-Apt* sandwich scheme realization.....	151
D.3.2	Processing and analysis of the fluorescence images.....	152
Appendix E. Supplementary Data.....		154
References.....		162

List of abbreviations

2D	Two-dimensional
5-FAM	5-carboxyfluorescein
Ab	Antibody
Abs*	Fluorescently labelled antibody
AgNP	Silver nanoparticle
Anti-PLDH	Pan malaria antibody
Apt	Aptamer
Apt*	Fluorescently labelled aptamer
APTEC	Aptamer-tethered enzyme capture
APTES	(3-Aminopropyl)triethoxysilane
AuNP	Gold nanoparticle
BC	Boundary condition
BCMn	Block copolymer micelle nanolithography
BEM	Boundary element method
BSA	Bovine serum albumin

C_t	Cycle threshold
CTAB	hexadecyltrimethylammonium bromide
Cy5	Cyanine 5
DDA	Discrete dipole approximation
DLA	Diffusion-limited aggregation
DLS	Dynamic light scattering
DR	Dynamic range
DTSSP	3,3'-dithiobis(sulfosuccinimidyl propionate)
E2	17 β -estradiol
E-field	Electric field
ELISA	Enzyme-linked immunosorbent assay
EM	Electromagnetic
Fab	Fragment antigen-binding
f-AuNP	Functionalized-gold nanoparticle
FDTD	Finite-difference time-domain
FE	Fluorescence enhancement
FEM	Finite element method
FESEM	Field emission scanning electron microscope
FOM	Figure of merit

FRET	Förster resonance energy transfer
FWHM	Full width at half maximum
HPLC	High-performance liquid chromatography
IC	Internal control
LC-MS	Liquid chromatography-mass spectrometry
LDOS	Local density optical states
LFA	Lateral flow assay
LOD	Limit of detection
LSP	Localized surface plasmon
LSPR	Localized surface plasmon resonance
MDL	Molecular detection limit
MUA	11-mercaptoundecanoic acid
NA	Numerical aperture
OD	Optical density
P2VP	Poly(2-vinylpyridine)
pAb	Polyclonal antibody
PCR	Polymerase chain reaction
PD	Photodetector
PEF	Plasmon-enhanced fluorescence

PEG-SH	Thiolated polyethylene glycol
<i>Pf</i> LDH	<i>Plasmodium falciparum</i> lactate dehydrogenase
PIT	Photochemical immobilization technique
<i>PL</i> DH	<i>Plasmodium</i> lactate dehydrogenase
POC	Point of care
PS	Polystyrene
<i>Pv</i> LDH	<i>Plasmodium vivax</i> lactate dehydrogenase
QY	Quantum yield
ROC	Receiver operating characteristic
ROI	Region of interest
RT-PCR	Reverse transcriptase-polymerase chain reaction
SAM	Self-assembled monolayer
SD	Standard deviation
SEM	Scanning electron microscopy
SERS	Surface-enhanced Raman scattering
SLR	Surface lattice resonance
SPP	Surface plasmon polariton
SPR	Surface plasmon resonance
STEM	Scanning transmission electron microscopy

TEM	Transmission electron microscopy
UTM	Universal transport medium
WHO	World Health Organization

Introduction

In the last few decades, an increasing interest for nanotechnologies is spanning more and more fields of application thanks to the unique properties exhibited by metal nanomaterials if stimulated by external electromagnetic radiations. Indeed, a new research field called *plasmonics* is emerging and fast growing as a result of the recent technological progress and a deeper understanding of such phenomena.

First plasmon-related effects can be traced back to the turn of the 20th century with the works of A. Sommerfeld and J. Zenneck on the propagation of electromagnetic waves along the surface of a conductor.^{1,2} Concurrently, R. H. Wood reported the observation of anomalous intensity drops in the spectrum of visible light diffracted by a metal grating.³ Several efforts were made in order to provide a theoretical interpretation of these effects albeit with limited success.^{4,5} Only half century later, a clear comprehension of such effects took place giving rise to the concept of *surface plasmon polaritons* – i.e., electromagnetic surface waves coupled to collective excitations of the conduction electrons, propagating along the interface between a dielectric and a conductor – and their excitation through both fast electrons^{6,7} and prisms coupling.^{8,9} When such a coupled excitation occurs in non-extended metal nanostructures, the collective excitation of the conduction electrons gives rise to a non-propagating plasmon polariton called *localized surface plasmon*.^{10,11} Two remarkable features of these plasmon modes are the subwavelength confinement of the fields at the metal/dielectric interface and their enhancement of several orders of magnitude thereby opening up the possibility for manipulating light at nanometric scale, well below the diffraction limit.¹⁰

The high potential of the surface plasmons has been further emphasised at the beginning of the 21st century by H. A. Atwater outlining the promises that plasmonics surely would hold in the near future.¹² The realization of some of them has been represented a breakthrough in many application fields such as cancer treatment,¹³ ultrasensitive molecule detection,¹⁴ integrated circuitry,¹⁵ quantum optics,¹⁶ optoelectronics,¹⁷ photovoltaics.¹⁸

Recently, several types of plasmonic nanostructures are being conceived aiming at improving the performance of plasmon-based devices. For instance, sharp nanostructures exhibit higher field enhancement than smooth surfaces thereby representing a remarkable advantage in applications relying on signal amplification such as surface-enhanced Raman spectroscopy (SERS)¹⁹ and plasmon-enhanced fluorescence (PEF).²⁰ In addition, when nanostructures are ordered in periodic arrays, collective modes can arise as a result of the field coupling among the surface plasmons so as to promote the occurrence of impressive effects such as lattice resonances.^{21,22} Therefore, the possibility to tune the optical response of a nanostructure by tailoring the nanomaterial shape and size, as well as the structure arrangement, is spurring the researchers to explore new approaches, in terms of both nanofabrication and nano applications, in order to go beyond the current limits of many techniques.

The aim of the work in this thesis is to provide an understanding of this growing field of research and to convey the main features in biosensing applications. To date, several biosensor-based approaches including colorimetric, electrochemical, and fluorescence analysis have been explored to effectively work alongside – or even replace – the gold standard methods in a wide variety of applications including environmental pollution monitoring²³ and medical diagnostics.²⁴ Although the conventional laboratory techniques such as high-performance liquid chromatography (HPLC), liquid chromatography-mass spectrometry (LC-MS), reverse transcriptase-polymerase chain reaction (RT-PCR), and microscope observation exhibit remarkable performance in terms of sensitivity, selectivity, and reliability, the need for well-equipped laboratories and skilled personnel, the use of significant amounts of toxic solvents, and their expensiveness and time consumption strongly limit their adoption for mass screening, and routinely contaminant monitoring.

In this regard, biosensors offer a rapid, affordable, and practical approach in many fields of applications paving the way for point of care (POC) tests and high-throughput analysis, albeit most of them still suffering from difficulties in surface biofunctionalization, complex fabrication, limited sensitivities, and unpractical industrial implementation.^{25,26} Thus, effective strategies are highly desirable to improve the feasibility of the biosensor-based methods. A partial alternative is provided by immuno-techniques such as the well-established enzyme-linked immunosorbent assay (ELISA), currently the main colorimetric technique for routine detection of analytes of interest in complex samples as wastewater, urine, or blood. Most of the available ELISA assays provide a large detection range and very low limits of detection, but the technique is limited by the long assay time (up to some hours), the relatively high cost of the kits, and the need for a trained personnel.^{27,28} A promising alternative to reduce the costs of the antibody-based assays relying on the adoption of nucleic acid

aptamers as capture bioreceptors. Aptamer-tethered enzyme capture (APTEC) methods boast remarkable performance – comparable with those exhibited by ELISA – while drastically reducing the assay costs.^{29,30} Nevertheless, the need for complex microfluidic system as well as the lack of simple strategies for the immobilization and low awareness of the Apts strongly limit their routinely adoption.

Fluorescence-based techniques are of growing interest since their potential high-throughput analysis, POC applications, and improvable sensitivity through PEF effect. However, some sample pretreatments may be necessary to reduce the turbidity of the non-transparent media.^{31,32} On the other hand, when quickness, practicality, and easiness of use are preferred rather than extremely high sensitivity and accuracy, colorimetric biosensors relying on metal nanoparticles are the ideal candidates since their capability to produce a qualitative response in a few minutes visible by naked eye (a portable and handheld spectrophotometer can be employed if a quantitative measurement is required).^{33,34}

The thesis has been organised to gradually introduce the readers into the world of plasmonics and throughout the conducted experiments. Particularly, Chapter 1 opens with the basis of the plasmonics by introducing the Drude model to investigate the response of metals when stimulated by external electromagnetic radiations. In addition, the concept of volume plasmons is explained before getting into the thick of a deeper description of plasmonics. Then, a mathematical description of propagating surface plasmon polaritons is formulated as a starting point sustaining the core of this thesis. Afterwards, the optical response of metal nanoparticles is investigated through both the electrodynamic approach of the Mie theory and within a quasi-static framework. Eventually, several numerical techniques are introduced, which are apt to simulate the scattering of the electromagnetic radiation from metal nanostructures. The finite-difference time-domain method has been used to simulate the optical response of all the nanostructures described throughout the work.

Chapter 2 offers an overview on colorimetric biosensors relying on metal nanoparticles, in particular focusing on colloidal solutions of antibody-functionalized gold nanoparticles capable of detecting the presence of analytes of interest by changing their optical properties. The performance of such colorimetric biosensors have been tested for detecting small molecules, such as 17 β -estradiol in tap water, and SARS-CoV-2 virions in naso-oropharyngeal swabs.

Chapter 3 conveys an investigation of collective modes arising when metal nanoparticles are ordered in two-dimensional periodic arrays. In this view, the optical response of the substrate is addressed within a point-dipole description by considering an effective polarizability accounting for the

collective response of a system composed of coupled emitting dipoles. The chapter ends with the morphological and optical characterization of the two-dimensional nanostructured substrates fabricated through electrostatic self-assembly of gold nanoparticles and block copolymer micelle nanolithography.

In Chapter 4, one of the most fascinating – and not yet fully understood – plasmon-related effects is introduced, the so-called plasmon-enhanced fluorescence. Although the first experimental observation can be ascribed to K. H. Drexhage in 1974,³⁵ only in the last two decades such a phenomenon can rely on a more rigorous theoretical interpretation thanks to the pioneering works of J. R. Lakowicz and C. D. Geddes.^{36,37} Nevertheless, a certain gap between theoretical predictions and measured fluorescence amplification factors is still present thereby highlighting the need to examine the emitter-nanostructure interaction mechanisms even deeper. Throughout this chapter, effects occurring when a fluorophore is located in close proximity to a metal nanoparticle are described and, eventually, some promising results are shown on the possibility to detect proteins in whole blood down to femtomolar level by combining honeycomb arrays of gold nanoparticle and an appropriate fluorescent dye.

After a brief conclusion, the last part of this work contains supplementary material such as a list of chemical and reagents, fabrication procedures, analysis details, supplementary data, and a cross-reference index. Specifically, the protocols adopted to synthesise colloidal solutions of gold nanoparticles are described in Appendix A; details about the fabrication of two-dimensional substrates – consisting of randomly positioned, honeycomb lattice, and branched arrays of gold nanoparticles – are provided in Appendix B; technical details about the analysis of the scanning electron micrographs and the coding of the simulation model are contained in Appendix C; detailed information on biosensor realization and transduction are included in Appendix D; all the supplementary data cited throughout the work are collected in Appendix E.

Chapter 1. Theory of plasmonics

1.1 Maxwell's equations

Metals exhibit different optical behaviour depending on the frequency ω of the interacting electromagnetic (EM) field. Particularly, (i) in the low-frequency regime – up to far-infrared region –, metals show a high reflectance and hence only a negligible fraction of the incident radiation penetrates the bulk. In these conditions, metals can be approximated as perfect conductors.^{11,38} (ii) At higher frequencies – near infrared and visible range –, the EM field component propagating through the metal becomes significant giving rise to an increase of dissipation effects.^{11,38} (iii) At ultraviolet frequencies, EM perturbation can propagate into the metals with degrees of attenuation that depend on the electronic band structure. For instance, alkali metals show an ultraviolet transparency thus their response can be retrieved by considering a free-electron-like model, whereas the occurrence of interband transitions in noble metals leads to a strong absorption of the incident radiation.^{11,38}

Aiming at phenomenologically describing the interaction between EM waves and metals – thereby ignoring the fundamental interactions among charged particles – macroscopic Maxwell's Equations (1.1) can be considered within a classical framework as long as the frequency of interacting radiation is far from the range of interband transitions.^{11,38}

$$\nabla \cdot \mathbf{D} = \rho_{\text{ext}} \quad (1.1a) \qquad \nabla \cdot \mathbf{B} = 0 \quad (1.1b)$$

$$\nabla \times \mathbf{E} = -\partial_t \mathbf{B} \quad (1.1c) \qquad \nabla \times \mathbf{H} = \mathbf{J}_{\text{ext}} + \partial_t \mathbf{D} \quad (1.1d)$$

Here, the macroscopic fields \mathbf{E} (electric field), \mathbf{D} (dielectric displacement), \mathbf{B} (magnetic induction) and \mathbf{H} (magnetic field) are driven by the external charge density ρ_{ext} and current density \mathbf{J}_{ext} . Moreover, the macroscopic fields are linked with the polarization \mathbf{P} and the magnetization \mathbf{M} fields through the following constitutive relations

$$\mathbf{D} = \varepsilon_0 \mathbf{E} + \mathbf{P} \quad (1.2a)$$

$$\mathbf{H} = \frac{1}{\mu_0} \mathbf{B} - \mathbf{M} \quad (1.2b)$$

where ε_0 and μ_0 are the electric permittivity and magnetic permeability of vacuum, respectively. The future considerations will be restricted to nonmagnetic media because the fundamental role for understanding the optical behaviour of metals is played by the electric polarization effects. The external electric field induces the alignment of the microscopic dipoles inside the medium, which leads to a macroscopic polarization field described as electric dipole moment per unit volume. By considering the charge conservation $\nabla \cdot \mathbf{J} = -\partial_t \rho$, the polarization is related to the charge density ρ_P and current density \mathbf{J}_P by

$$\nabla \cdot \mathbf{P} = -\rho_P \quad (1.3a)$$

$$\mathbf{J}_P = \partial_t \mathbf{P} \quad (1.3b)$$

For linear, isotropic, and nonmagnetic ($\mu = 1$) media, the constitutive Equations (1.2) become

$$\mathbf{D} = \varepsilon_0 \varepsilon \mathbf{E} \quad (1.4a)$$

$$\mathbf{B} = \mu_0 \mathbf{H} \quad (1.4b)$$

where ε is the relative permittivity of the medium. By inserting Equation (1.4a) into (1.2a), the polarization field is linearly related with the electric field through the dielectric susceptibility χ .

$$\mathbf{P} = \varepsilon_0 \chi \mathbf{E} \quad (1.5)$$

In the case of ohmic and isotropic metals, the current density is proportional to the electric field by the conductivity σ .

$$\mathbf{J}_P = \sigma \mathbf{E} \quad (1.6)$$

Equations (1.4a) and (1.6) are strictly valid for linear and non-dispersive media.

Since the optical response of metals strongly depends on the frequency of the impinging EM wave, the non-locality in time and space has to be recovered, thus it results^{11,38}

$$\mathbf{D}(\mathbf{r}, t) = \varepsilon_0 \int dt' d\mathbf{r}' \varepsilon(\mathbf{r} - \mathbf{r}', t - t') \mathbf{E}(\mathbf{r}', t') \quad (1.7a)$$

$$\mathbf{J}(\mathbf{r}, t) = \int dt' d\mathbf{r}' \sigma(\mathbf{r} - \mathbf{r}', t - t') \mathbf{E}(\mathbf{r}', t') \quad (1.7b)$$

In frequency domain, the convolutions (1.7) can be simplify by decomposing the fields into individual plane wave components of wavevector \mathbf{k} and frequency ω .

$$\tilde{\mathbf{D}}(\mathbf{k}, \omega) = \varepsilon_0 \tilde{\mathbf{E}}(\mathbf{k}, \omega) \quad (1.8a)$$

$$\tilde{\mathbf{J}}(\mathbf{k}, \omega) = \tilde{\sigma}(\mathbf{k}, \omega) \tilde{\mathbf{E}}(\mathbf{k}, \omega) \quad (1.8b)$$

Therefore, by considering the Fourier transform of (1.2a) and (1.3b), Equations (1.8) lead to the fundamental relationship between optical dispersion – described by the dielectric function ε – and the electric conductivity σ (in order to simplify the notation, the symbol \sim indicating the Fourier transform will be omitted).

$$\varepsilon(\mathbf{k}, \omega) = 1 + \frac{i\sigma(\mathbf{k}, \omega)}{\varepsilon_0 \omega} \quad (1.9)$$

At frequencies up to ultraviolet regime, the wavelength λ of the incident radiation is significantly longer than both the lattice spacing of metal and the mean free path of the electrons. In such a condition, the response of the metal can be evaluated locally in the space by assuming $\varepsilon(\mathbf{k} = 0, \omega) \equiv \varepsilon(\omega)$.^{11,38} Generally, the permittivity is a complex function of the frequency $\varepsilon(\omega) = \varepsilon'(\omega) + i\varepsilon''(\omega)$ and it is related to the complex refractive index of the material $\underline{n}(\omega) = n(\omega) + i\kappa(\omega)$ through^{11,38}

$$\underline{n}(\omega) = \sqrt{\varepsilon(\omega)} \quad (1.10)$$

The extinction coefficient κ describes the attenuation experienced by EM waves propagating through the material while the real part n of the refractive index quantifies the decrease of the phase velocity due to the polarization of the medium.^{11,38} The statement (1.10) entails the relations

$$\varepsilon' = n^2 - \kappa^2 \quad (1.11a) \quad \varepsilon'' = 2n\kappa \quad (1.11b)$$

$$n^2 = \frac{\varepsilon'}{2} + \frac{1}{2}\sqrt{\varepsilon'^2 + \varepsilon''^2} \quad (1.11c) \quad \kappa = \frac{\varepsilon''}{2n} \quad (1.11d)$$

For $|\varepsilon'| \gg |\varepsilon''|$, the real part of the refractive index mainly depends on the real part of the permittivity and hence contributes to the polarization of the material, whereas the imaginary part of the dielectric function affects the absorption of the propagating radiation.

In absence of external source $\rho_{\text{ext}} = 0$ and $\mathbf{J}_{\text{ext}} = 0$, Maxwell's Equations (1.1c) and (1.1d) can be combined to obtain the wave equation describing the propagation of EM field inside the medium

$$\nabla \times \nabla \times \mathbf{E} = -\mu_0 \frac{\partial^2 \mathbf{D}}{\partial t^2} \quad (1.12a)$$

$$\mathbf{k}(\mathbf{k} \cdot \mathbf{E}) - k^2 \mathbf{E} = -\varepsilon(\mathbf{k}, \omega) \frac{\omega^2}{c^2} \mathbf{E} \quad (1.12b)$$

in the time and frequency domains, respectively. In Equation (1.12b), the constant $c = 1/\sqrt{\varepsilon_0 \mu_0}$ is the speed of light in vacuum. For transverse waves ($\mathbf{k} \cdot \mathbf{E} = 0$), the Equation (1.12b) yields the dispersion relation (1.13a), whereas for longitudinal waves, the condition (1.13b) defines the frequencies that allow the occurrence of longitudinal collective oscillation.^{11,38}

$$k^2 = \varepsilon(\mathbf{k}, \omega) \frac{\omega^2}{c^2} \quad (1.13a) \quad \varepsilon(\mathbf{k}, \omega) = 0 \quad (1.13b)$$

1.2 Plasma model

At frequencies far from the interband transitions, the optical properties of metals can be adequately described by considering a free electron-like system, in which electron-electron interactions and lattice potential are not taken into account.^{11,38,39} In such a system, the oscillations of electrons are driven by the impinging EM waves while damped by collisions inside the plasma with a characteristic frequency $\gamma = 1/\tau$, where τ is the relaxation time of the free electron gas. The equation of motion in time domain for a single electron is

$$m\ddot{\mathbf{x}} + m\gamma\dot{\mathbf{x}} = -e\mathbf{E} \quad (1.14)$$

where m and e are the effective optical mass and the charge of the conduction electron, respectively. By assuming a harmonic time dependence of the external stimulus, Equation (1.14) in the frequency domain become

$$\mathbf{x}(\omega) = \frac{e}{m(\omega^2 + i\gamma\omega)} \mathbf{E}(\omega) \quad (1.15)$$

The displacement of the electrons gives rise to a macroscopic polarization that reads

$$\mathbf{P}(\omega) = -\frac{ne^2}{m(\omega^2 + i\gamma\omega)} \mathbf{E}(\omega) \quad (1.16)$$

where n is the number density of free electrons. By replacing the Equation (1.16) into the Fourier transform of the constitutive relation (1.2a), the dielectric displacement results

$$\mathbf{D}(\omega) = \varepsilon_0 \left(1 - \frac{\omega_p^2}{\omega^2 + i\gamma\omega} \right) \mathbf{E}(\omega) \quad (1.17a)$$

$$\omega_p^2 \equiv \frac{ne^2}{\varepsilon_0 m} \quad (1.17b)$$

where ω_p is defined as the plasma frequency of the free electron gas. Therefore, the comparison between Equations (1.4a) and (1.17a) provides the dispersion relation for a metal in the plasma model approximation.

$$\varepsilon(\omega) = 1 - \frac{\omega_p^2}{\omega^2 + i\gamma\omega} \quad (1.18a)$$

$$\varepsilon'(\omega) = 1 - \frac{\omega_p^2}{\gamma^2 + \omega^2} \quad (1.18b)$$

$$\varepsilon''(\omega) = \frac{\omega_p^2 \gamma}{\omega(\gamma^2 + \omega^2)} \quad (1.18c)$$

From this perspective, the plasma frequency can be assumed as a threshold to understand the optical behaviour of metals. In the low-frequency regime $\omega < \omega_p$, metals retain their metallic character exhibiting high reflectivity and conductivity. Particularly, at very low frequencies ($\omega \ll \gamma$), the imaginary part of the dielectric function dominates over its real part yielding comparable magnitude for real (1.11c) and imaginary (1.11d) part of the refractive index. In this regime, the incident EM radiation is strongly absorbed in close proximity of the metal interface preventing wave propagation through the metal (skin effect).^{11,38,39} At higher frequencies ($\gamma \ll \omega < \omega_p$), the dielectric function becomes predominantly real, thus Equation (1.19) can be considered as the dielectric function of an undamped free electron plasma.^{11,38,39}

$$\varepsilon(\omega) = 1 - \frac{\omega_p^2}{\omega^2} \quad (1.19)$$

On the contrary, at frequencies higher than the plasma frequency ($\omega > \omega_p$), EM waves are able to penetrate the metals with a degree of attenuation that decreases as ω increases. In fact, at $\omega \gg \omega_p$, it results $\varepsilon \rightarrow 1$ while $\kappa \rightarrow 0$ thereby allowing the undamped propagation of EM waves through the metal.^{11,38,39} In such a transparency regime, the dispersion relation of a traveling wave is obtained by replacing Equation (1.19) into (1.13a).

$$\omega^2 = \omega_p^2 + k^2 c^2 \quad (1.20)$$

Thus, the plasma supports the propagation of transverse waves with a group velocity v_g for $\omega > \omega_p$ while forbids it for lower frequencies (Figure 1.1).

$$v_g = \frac{d\omega}{dk} = \frac{c^2 k}{\omega} < c \quad (1.21)$$

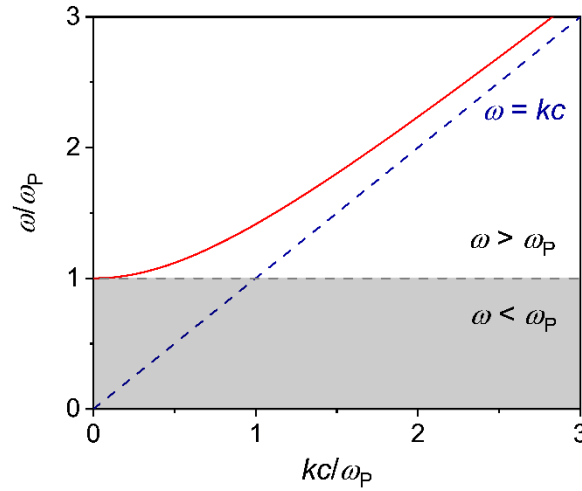


Figure 1.1. Dispersion relation of the free electron gas (red solid line). The propagation of EM waves is only allowed for frequencies higher than the plasma frequency while prohibiting at lower frequencies (grey shaded area). The dashed blue line represents the light line of air.

The residual polarization due to the presence of the positive lattice composed of metal ions provides an additional contribution $\mathbf{P}_\infty = \varepsilon_0(\varepsilon_\infty - 1)\mathbf{E}$ into the (1.2a).^{11,39} Therefore, the generic dispersive relation for metals reads

$$\varepsilon(\omega) = \varepsilon_\infty - \frac{\omega_p^2}{\omega^2 + i\gamma\omega} \quad (1.22)$$

Since the filled d-band close to the Fermi surface produces a highly polarized environment, such an extension of the plasma model is necessary when noble metals exhibiting interband transition at frequencies lying in the visible range are to be considered.^{11,39} Figure 1.2 shows the real and imaginary part of the dielectric function calculated for gold by using Equations (1.18).⁴⁰ The plasma model adequately describes the optical behaviour of noble metals up to frequencies lying in the visible range due to the occurrence of interband transitions that lead to an increase of ε'' and, hence, a strong absorption of the travelling wave.

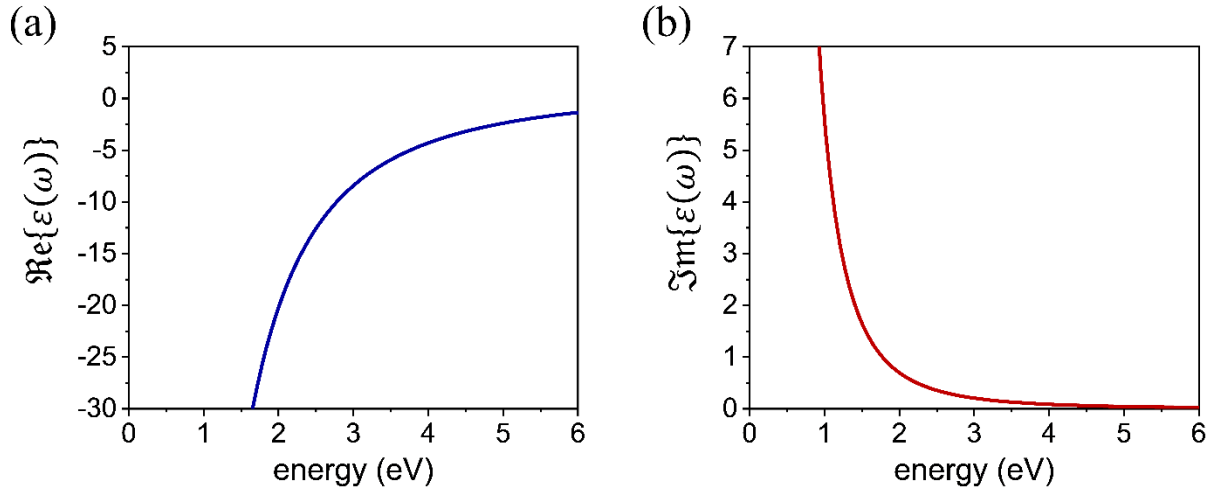


Figure 1.2. (a) Real and (b) imaginary part of dielectric function calculated for gold by using Equations (1.18).

1.3 Volume plasmons

As it concerns the longitudinal mode, the condition (1.13b) is realized at frequencies close to the plasma frequency (small damping limit) for which Equation (1.19) delivers $\epsilon(\omega_P) = 0$ and hence from (1.4a) and (1.2a) it results $\mathbf{D} = 0 = \epsilon_0 \mathbf{E} + \mathbf{P}$ revealing an electric field purely depolarizing with $\mathbf{E} = -\mathbf{P}/\epsilon_0$. The excitation occurring at the plasma frequency yields a collective longitudinal oscillation of the conduction electron cloud against the positive metal lattice.^{11,39,41} Aiming at understanding such longitudinal oscillations, the metal can be assumed as a plasma slab while the external electric perturbation leads to a displacement of the conduction electron cloud by a distance u that gives rise to a surface charge density $\sigma = \pm neu$ at the slab boundaries (Figure 1.3).

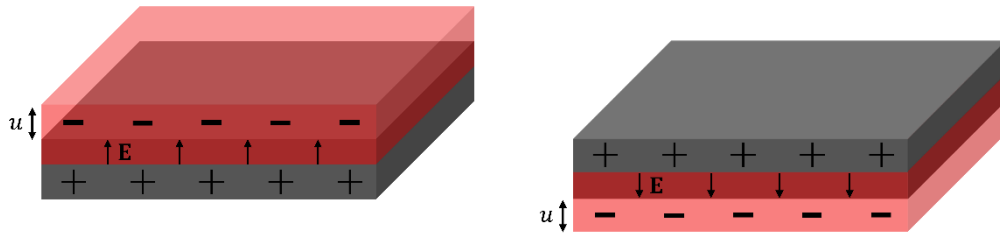


Figure 1.3. Displacement of the conduction electron cloud from the positive ion core of the plasma slab.

Such a system is analogous to a parallel-plate capacitor with homogeneous internal electric field.

$$\mathbf{E} = \frac{ne\mathbf{u}}{\varepsilon_0} \quad (1.23)$$

The electron cloud experiences a restoring force (1.24a) that entails collective harmonic oscillation of frequency ω_p (1.24b).

$$nm\ddot{\mathbf{u}} = -ne\mathbf{E} \quad (1.24a) \quad \ddot{\mathbf{u}} + \omega_p^2\mathbf{u} = 0 \quad (1.24b)$$

In this approach, the plasma frequency turns out to be the natural frequency of free collective oscillations of the conduction electrons. The quantization of these collective oscillations yields the so-called volume plasmons whose energy results

$$\mathcal{E}_p = \hbar\omega_p = \hbar \sqrt{\frac{ne^2}{m\varepsilon_0}} \quad (1.25)$$

It is worth to highlight that previous considerations rely on coherent oscillation of the conduction electrons, a condition fulfilled in the long-wavelength regime ($\mathbf{k} = 0$). Given their longitudinal nature, volume plasmons do not couple to transverse electromagnetic perturbations and hence only impacting particles can excite such an oscillating mode.^{11,39,41}

1.4 Surface plasmon polaritons

1.4.1 Propagating surface electromagnetic waves

In addition to bulk phenomena arising when metals interact with external perturbations, the coupling between EM field and conduction electrons can lead to the excitation of propagating surface waves called surface plasmon polaritons (SPPs).^{11,39,41,42} SPPs are EM waves – produced by the oscillation of conduction electrons – traveling at the conductor/dielectric interface, evanescently confined in the normal direction. The SPP features can be investigated by considering the Maxwell's Equations (1.1) in the case of a flat metal/dielectric interface.

In absence of external stimuli ($\rho_{\text{ext}} = 0$ and $\mathbf{J}_{\text{ext}} = 0$) and by using the vector identities $\nabla \times \nabla \times \mathbf{E} \equiv \nabla(\nabla \cdot \mathbf{E}) - \Delta\mathbf{E}$ and $\nabla \cdot (\varepsilon\mathbf{E}) \equiv \mathbf{E} \cdot \nabla\varepsilon + \varepsilon\nabla \cdot \mathbf{E}$, the electric wave equation (1.12a) turns into

$$\nabla \left(-\frac{1}{\varepsilon} \mathbf{E} \cdot \nabla \varepsilon \right) - \Delta \mathbf{E} = -\mu_0 \varepsilon_0 \varepsilon \frac{\partial^2 \mathbf{E}}{\partial t^2} \quad (1.26a)$$

$$\Delta \mathbf{E} - \frac{\varepsilon}{c^2} \frac{\partial^2 \mathbf{E}}{\partial t^2} = 0 \quad (1.26b)$$

where Equation (1.26b) is retrieved by assuming a negligible variation of the dielectric function over distances comparable with the optical wavelength ($\nabla \varepsilon = 0$). In the case of harmonic time dependence of the electric field $\mathbf{E}(\mathbf{r}, t) = \mathbf{E}(\mathbf{r})e^{-i\omega t}$, Equation (1.26b) becomes the Helmholtz equation^{11,38}

$$\Delta \mathbf{E} + k_0^2 \varepsilon \mathbf{E} = 0 \quad (1.27)$$

where $k_0 = \omega/c$ is the wavevector of the propagating wave in vacuum.

In an effort to simplify the study without worsening the generality of the results, a one-dimensional problem as shown in Figure 1.4 is considered. The waves exhibit no spatial variation along y -direction while traveling along x -direction (plane $z = 0$). In such a geometry, the dielectric function depends only on the z coordinate and the propagating waves can be described as $\mathbf{E}(x, y, z) = \mathbf{E}(z)e^{i\beta x}$ where $\beta = k_x$ is the propagation constant corresponding to the wavevector component along the propagation direction.

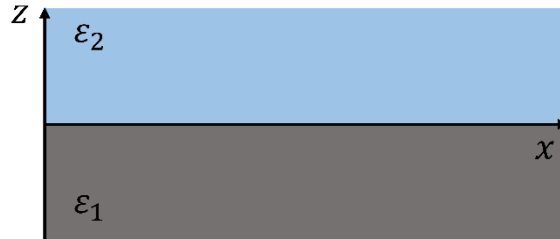


Figure 1.4. Geometry for SPP propagation at a single interface between a metal ($z < 0$) and a dielectric ($z > 0$).

Thus, Equation (1.27) turns into wave equation (1.28) that describes the propagation of EM waves at a flat metal/dielectric interface.

$$\frac{\partial^2 \mathbf{E}(z)}{\partial z^2} + (k_0^2 \varepsilon - \beta^2) \mathbf{E} = 0 \quad (1.28)$$

As it concerns the spatial field profile and dispersion relation of SPPs, the problem can be addressed by considering the explicit components of Equations (1.1c) and (1.1d) within the simplest framework sustaining SPPs that consists of a single flat interface between a dielectric non-absorbing medium

with positive dielectric constant ε_2 and a conductor characterized by the dielectric function $\varepsilon_1(\omega)$, as shown in Figure 1.4.

$$\frac{\partial E_y}{\partial z} = -i\omega\mu_0 H_x \quad (1.29a)$$

$$\frac{\partial H_y}{\partial z} = i\omega\mu_0 E_x \quad (1.29d)$$

$$\frac{\partial E_x}{\partial z} - i\beta E_z = i\omega\mu_0 H_y \quad (1.29b)$$

$$\frac{\partial H_x}{\partial z} - i\beta H_z = -i\omega\varepsilon_0\varepsilon E_y \quad (1.29e)$$

$$i\beta E_y = i\omega\mu_0 H_z \quad (1.29c)$$

$$i\beta H_y = -i\omega\varepsilon_0\varepsilon E_z \quad (1.29f)$$

The system of Equations (1.29) provides two sets of self-consistent solutions with different wave polarization.^{11,38} For transverse magnetic waves (TM mode), only the components E_x , E_z and H_y are nonzero thereby yielding Equations (1.30). On the contrary, for transverse electric waves (TE mode), Equations (1.28) and (1.29) lead to Equations (1.31).

$$E_x = -i \frac{1}{\omega\varepsilon_0\varepsilon} \frac{\partial H_y}{\partial z} \quad (1.30a)$$

$$H_x = i \frac{1}{\omega\mu_0} \frac{\partial E_y}{\partial z} \quad (1.31a)$$

$$E_z = -\frac{\beta}{\omega\varepsilon_0\varepsilon} H_y \quad (1.30b)$$

$$H_z = \frac{\beta}{\omega\mu_0} E_y \quad (1.31b)$$

$$\frac{\partial^2 H_y}{\partial z^2} + (k_0^2\varepsilon - \beta^2)H_y = 0 \quad (1.30c)$$

$$\frac{\partial^2 E_y}{\partial z^2} + (k_0^2\varepsilon - \beta^2)E_y = 0 \quad (1.31c)$$

1.4.2 Single dielectric/metal interface

In the case of TM mode, a particular solution of H_y that fulfils the geometry constraints is

$$H_y(z) = A_j e^{i\beta x} e^{-k_j|z|} \quad (1.32)$$

where k_j is the component of the wavevector normal to the interface while $j = \{1, 2\}$ refers to the metal ($z < 0$) and dielectric ($z > 0$) half-spaces, respectively. Note that reciprocal value of k_j defines the evanescent decay length of the fields along the normal direction (typically 0.1-10 μm in the infrared-visible region).^{11,42} Thus, by inserting (1.32) into the Equations (1.30a) and (1.30b), the nonzero components of the electric field are

$$E_x(z) = \text{sgn}(z) i A_j \frac{1}{\omega \varepsilon_0 \varepsilon_j} k_j e^{i\beta x} e^{-k_j |z|} \quad (1.33a)$$

$$E_z(z) = -A_j \frac{\beta}{\omega \varepsilon_0 \varepsilon_j} e^{i\beta x} e^{-k_j |z|} \quad (1.33b)$$

The continuity of the tangential components E_x and H_y at the interface ($z = 0$) as well as of the normal component $D_z = \varepsilon_j E_z$ leads to the conditions (1.34a) and (1.34b), respectively.

$$A_1 = A_2 \quad (1.34a) \quad \frac{k_2}{k_1} = -\frac{\varepsilon_2}{\varepsilon_1} \quad (1.34b)$$

Particularly, Equation (1.34b) entails that SPPs – evanescently confined along the z -direction – are sustained only at interfaces between medium with opposite signs of the real part of their dielectric functions, namely in presence of a conductor $\Re\{\varepsilon_1\} < 0$ and an insulator $\varepsilon_2 > 0$. It is worth to notice that the condition $\Re\{\varepsilon_1\} < 0$ is fulfilled only at frequencies lower than ω_p for which conductors retain their metallic features.^{11,38} The combination of (1.34b) and (1.35a) – retrieved by replacing the particular solution of H_y for TM mode (1.32) into the wave Equation (1.30c) – gives the dispersion relation (1.35b) of SPPs traveling at metal/dielectric interface. In the case of an interface between metal described by a dielectric function (1.19) and air ($\varepsilon_2 = 1$), the real part of the dispersion relation (1.35b) can be expressed as Equation (1.35b).

$$k_j^2 = \beta^2 - k_0^2 \varepsilon_j \quad (1.35a) \quad \beta = k_0 \sqrt{\frac{\varepsilon_1 \varepsilon_2}{\varepsilon_1 + \varepsilon_2}} \quad (1.35b)$$

$$\frac{\omega}{\omega_p} = \sqrt{\left(\frac{\beta c}{\omega_p}\right)^2 + \frac{1}{2} - \sqrt{\left(\frac{\beta c}{\omega_p}\right)^4 + \frac{1}{4}}} \quad (1.35c)$$

A similar approach can be followed to investigate the possibility of TE surface modes.

$$E_y(z) = A_j e^{i\beta x} e^{-k_j |z|} \quad (1.36a)$$

$$H_x(z) = -\text{sgn}(z) i A_j \frac{1}{\omega \mu_0} k_j e^{i\beta x} e^{-k_j |z|} \quad (1.36b)$$

$$H_z(z) = A_j \frac{\beta}{\omega \mu_0} e^{i\beta x} e^{-k_j |z|} \quad (1.36c)$$

The continuity of E_y and H_x at the interface yields

$$A_1 = A_2 \quad (1.37a)$$

$$A_1 k_1 + A_2 k_2 = 0 \quad (1.37b)$$

Since the confinement to the interface requires $\Re\{k_j\} > 0$, the conditions (1.37) lead to $A_j = 0$ and hence no surface modes exist for TE polarization.

Figure 1.5 shows the SPP dispersion relation (1.35b) (solid red line) traveling at the interface between a metal with negligible damping ($\Im\{\varepsilon_1\} \sim 0$) and air.

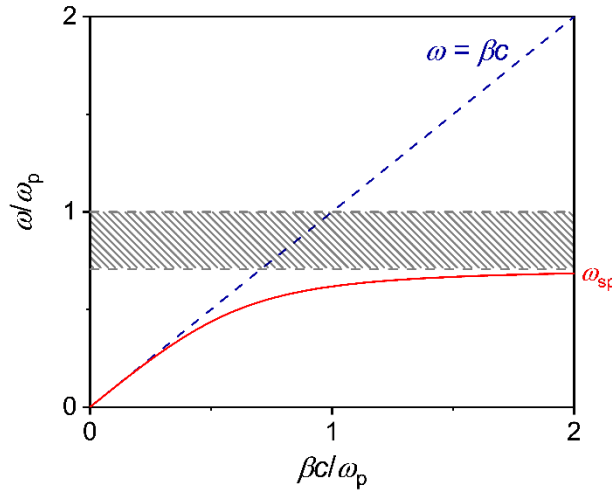


Figure 1.5. Dispersion relation of SPPs at the interface between a non-absorbing metal and air (solid red line). Between the regime of the bound and radiative modes, a frequency gap region with purely imaginary β prohibiting propagation exists (pattern grey region). The dashed blue line represents the light line of air.

Given the bound nature of these propagating surface modes, SPP excitations only occur for frequencies corresponding to the part of the dispersion curve that lies to the right of the light line of air (dashed blue line).^{11,39,42} For small wavevectors corresponding to microwave and mid-infrared regime, the SPP propagation constant is close to k_0 at the light line allowing the extension of SPP wave over many wavelengths into the dielectric half-space. In this case, SPPs propagate as grazing-incident light field (Sommerfeld-Zenneck waves).⁴³ On the contrary, for large wavevectors, the SPP frequency (1.35b) approaches the characteristic surface plasmon frequency ω_{sp} (1.38) while the group velocity tends to zero ($v_g = \partial\omega/\partial k \rightarrow 0$).

$$\omega_{sp} = \frac{\omega_p}{\sqrt{1 + \epsilon_2}} \quad (1.38)$$

In this regime ($\beta \rightarrow \infty$), the surface mode shows an electrostatic behaviour called surface plasmon.^{11,39,42} Thus, at $\omega = \omega_{sp}$, the traveling character of the SPPs is replaced by a resonant oscillation of the conduction electrons at the interface, so-called surface plasmon resonance (SPR). The region embedded between bound ($\omega < \omega_{sp}$) and radiative mode ($\omega > \omega_p$) is characterized by purely imaginary β thereby prohibiting wave propagation.

In the case of real metals, the excitation of the conduction electrons takes place together with free-electron and interband damping and hence $\epsilon_1(\omega)$ and, consequently, β are complex.^{11,39,42} The traveling SPPs are damped with a propagation length (1.39), usually taking values in the range 10-100 μm at frequencies lying in the visible region.^{11,42}

$$L_{SPP} = \frac{1}{2 \Im\{\beta\}} \sim \frac{c}{\omega} \left(\frac{\epsilon_2 + \epsilon'_1}{\epsilon_2 \epsilon'_1} \right)^{3/2} \frac{(\epsilon'_1)^2}{\epsilon''_1} \quad (1.39)$$

Figure 1.6a shows the SPP dispersion relations obtained at silver/air (solid blue line) and silver/silicon (solid red line) interfaces while Figure 1.6b the corresponding propagation lengths.^{11,42}

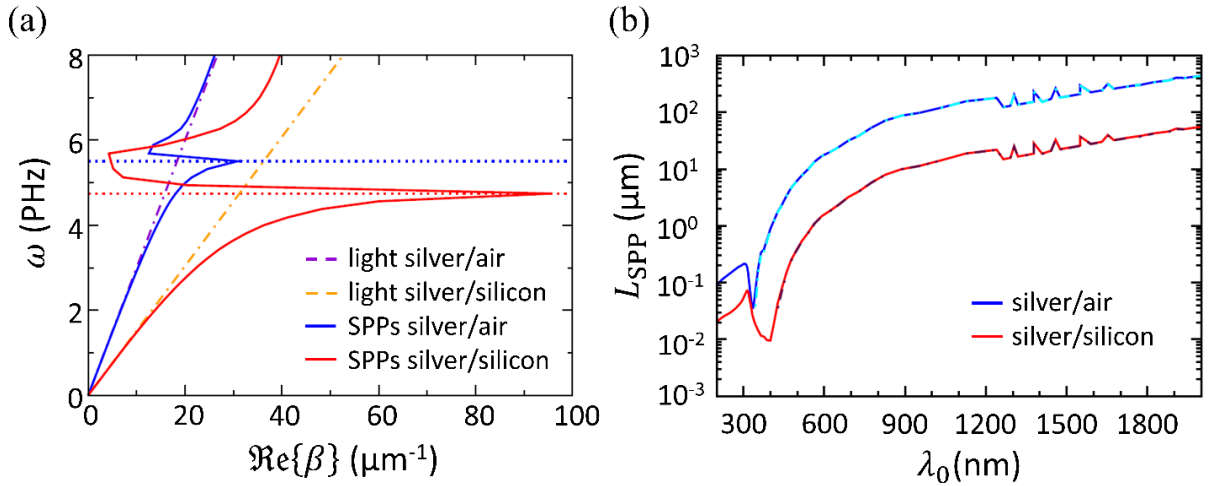


Figure 1.6. (a) Dispersion relation of SPPs at silver/air (solid blue line) and silver/silicon (solid red line) interfaces. Due to damping, the wavevector of the bounded SPP modes is limited to a maximum value (dotted lines). (b) Propagation lengths of SPPs at metal/dielectric interfaces (from Ref. ⁴²).

Due to the damping, the wavevector of the bound SPPs approaches a finite maximum value at the surface plasmon frequency corresponding to a finite wavelength (1.40) (dotted lines in Figure 1.6).

$$\lambda_{\text{sp}} = \frac{2\pi}{\Re\{\beta\}} \quad (1.40)$$

The field confinement experienced by the traveling SPPs can be quantifying in both half-spaces by introducing the penetration depth $\zeta_j = 1/\Re\{k_j\}$ yielding

$$\zeta_1 \sim \frac{c}{\omega} \sqrt{\frac{|\varepsilon'_1| - \varepsilon_2}{(\varepsilon'_1)^2}} \quad (1.41a)$$

$$\zeta_2 \sim \frac{c}{\omega} \sqrt{\frac{|\varepsilon'_1| - \varepsilon_2}{\varepsilon_2^2}} \quad (1.41b)$$

Figure 1.7 shows the behaviour of the penetration depth as a function of the EM field wavelength in vacuum. In metals, the penetration depth is roughly constant at frequencies lower than ω_{sp} (solid purple line) while grows into the dielectric half-space as the wavelength (frequency) increases (decreases) (solid blue line).^{11,42}

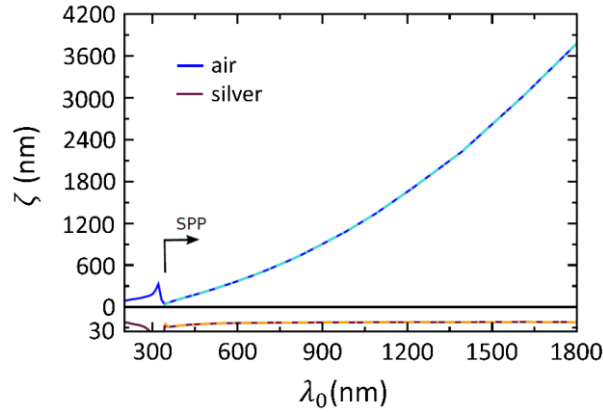


Figure 1.7. Penetration depths of the electromagnetic fields due to SPPs into air (solid blue line) and silver (solid purple line). The dot-dashed lines correspond to the approximate values obtained by using Equations (1.41) (from Ref. ⁴²).

1.4.3 Configurations sustaining surface plasmon polaritons

SPPs on a flat metal/dielectric interface cannot be excited directly by light beams since β_{SPP} is always larger than the wavevector of light k on the dielectric side of the interface (Figure 1.5). In fact, the projection along the interface of the wavevector $k_x = k \sin \theta$ of the impinging photons is smaller than the SPP propagation constant β , even at grazing incidence ($\theta = \pi/2$), preventing the occurrence of the phase-matching. However, the phase-matching to SPPs can be effectively achieved through a three-layer system consisting of a thin metal film embedded in two different dielectric media.^{11,44} In fact, a beam reflected at the interface between the medium of higher dielectric constant and metal has

an in-plane momentum $k_x = k\sqrt{\epsilon} \sin \theta$ larger enough to excite SPPs at the interface between the metal and the lower-index dielectric (Figure 1.8). Note that the phase-matching to SPPs at the metal/prism interface cannot be achieved since the respective SPP dispersion lies outside the prism light cone.

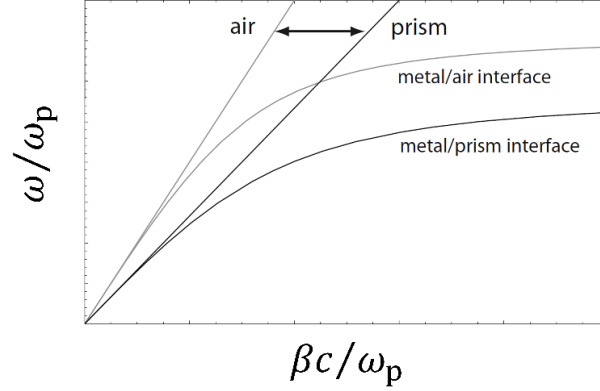


Figure 1.8. Dispersion relations of SPPs at metal/air (grey curve) and metal/prism (black curve) interfaces. Only propagation constants within the light lines of air and prism are accessible to excite SPPs, resulting in additional SPP damping due to leakage radiation into the prism. The excited SPPs have propagation constants inside the prism light cone (from Ref. 11).

Two different geometries for the prism coupling are possible: Otto and Kretschmann configurations (Figure 1.9a and b, respectively).⁴⁴ In the Otto configuration, the prism is separated from the metal film by a thin air gap. Total internal reflection takes place at the prism/air interface exciting SPPs through tunnelling of the field to the metal/air interface. On the contrary, in Kretschmann configuration, a thin metal film is evaporated onto the prism. Photons impinging at an angle larger than the critical angle of total internal reflection tunnel through the metal film exciting SPPs at the metal/air interface.

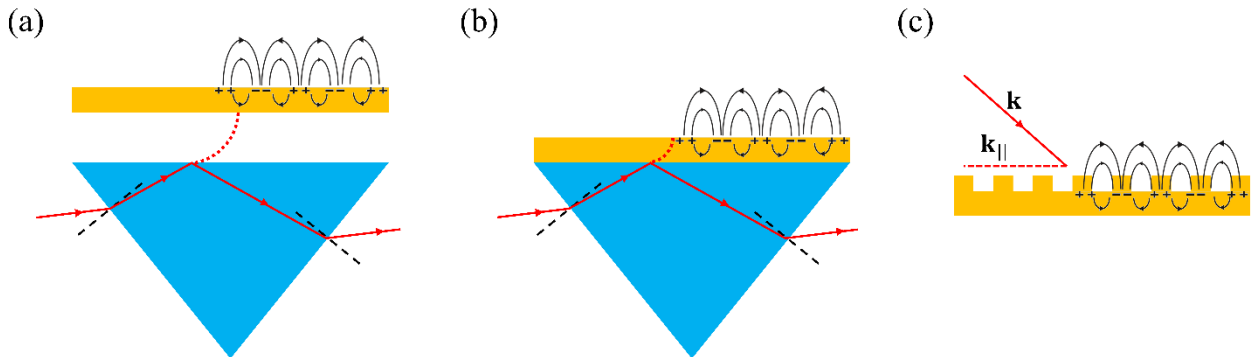


Figure 1.9. Examples of configurations sustaining SPPs. (a) Otto configuration. (b) Kretschmann configuration. (c) Grating configuration.

Note that SPPs excited by phase-matching $\beta = k\sqrt{\epsilon} \sin \theta$ are inherently leaky waves since they lose energy not only due to the inherent absorption inside the metal, but also due to the leakage of the radiation inside the prism.^{11,44} The minimum in the intensity of the reflected beam is due to destructive interference between such a leakage radiation and the reflected part of the excitation beam. For an optimal metal film thickness, the destructive interference leads to a zero-intensity in the reflected beam preventing the detection of the leakage radiation.⁴⁴

Such a phase-matching can be analogously realized by patterning the metal surface with a shallow grating of grooves or holes (Figure 1.9c).⁴⁴ By considering a one-dimensional groove grating, the phase-matching required¹¹

$$\beta = k \sin \theta \pm v \frac{2\pi}{d} \quad (1.42)$$

where d is the lattice constant and v a positive integers.

1.5 Localized surface plasmon

The interaction of EM waves with non-extended metal nanoparticles gives rise to non-propagating oscillations of the conduction electrons against the positive core of the nanostructure. Such a non-propagating surface mode, called localized surface plasmon (LSP), results from the scattering problem of a conductive nanoparticle – whose dimensions are comparable or lower than the wavelength of the incident radiation – in an oscillating EM field.^{11,41,45,46} In particular, while the external electric field induces the oscillation of the conduction electrons, the surface curvature of the nanoparticle exerts a restoring force on the displaced electrons yielding a localized surface plasmon resonance (LSPR) that enhances the field both inside and in the near region outside the particle. A formal solution of the scattering problem is only possible for restricted geometries of nanoparticles and within an electrostatic framework.^{11,41,47} In fact, spherical and spheroidal particle shapes interacting with time-harmonic electric field provide analytical solutions as long as their size is much smaller than the wavelength of the external radiation thereby considering constant the phase of the field over the whole particle volume.

1.5.1 Electrodynamic approach

Generally, when particle dimensions are comparable with the wavelength of the incident radiation, the quasi-static approximation is not valid because of the significant variation of the phase of the EM field experienced by the particle over its whole volume. Thus, the effects entailed by the retarded potentials have to be considered for adequately investigating the scattering fields produced by a plane wave incident on a conducting sphere embedded in a linear, isotropic, and homogeneous medium.^{41,45,46,48} Given the spherical symmetry of the system, the scattering problem can be conveniently addressed by introducing the vector spherical harmonics \mathbf{M} and \mathbf{N} – generated by a scalar function $\psi(r, \theta, \varphi)$ – that satisfy the wave equation (1.27).^{45,46,48}

$$\mathbf{M}_{lm} = \nabla \times (r\psi_{lm}) \quad (1.43a) \quad \mathbf{N}_{lm} = \frac{1}{nk} (\nabla \times \mathbf{M}_{lm}) \quad (1.43b)$$

By following this approach, the problem of finding solutions for EM field reduces to the comparatively simpler problem of finding solutions to the scalar wave equation (1.44) expressed in spherical coordinates.

$$\Delta\psi + k^2\psi = 0 \quad (1.44)$$

Equation (1.44) can be solved by using the product ansatz $\psi(r, \theta, \varphi) = R(r)S(\theta)T(\varphi)$ that allows to separate the wave equation for the three spherical components. The general solution is given by a linear combination of even and odd generating function.⁴⁸

$$\psi_{lm}^{\text{even}} = \cos(m\varphi) P_l^m(\cos \theta) z_l(kr) \quad (1.45a)$$

$$\psi_{lm}^{\text{odd}} = \sin(m\varphi) P_l^m(\cos \theta) z_l(kr) \quad (1.45b)$$

Here, $P_l^m(\cos \theta)$ are the associated Legendre functions of the first kind of degree l and order m , whereas the symbol z_l is representative of the four spherical Bessel functions j_l , y_l , $h_l^{(1)}$, $h_l^{(2)}$. Equations (1.46) represent two possible solutions of (1.44).⁴⁸

$$u = e^{-i\omega t} \cos(\varphi) \sum_{l=1}^{\infty} (-i)^l \frac{2l+1}{l(l+1)} P_l^1(\cos \theta) j_l(kr) \quad (1.46a)$$

$$v = e^{-i\omega t} \sin(\varphi) \sum_{l=1}^{\infty} (-i)^l \frac{2l+1}{l(l+1)} P_l^1(\cos \theta) j_l(kr) \quad (1.46b)$$

The EM fields satisfying the Maxwell's equations (1.1) can be expressed as functions of the particular vector spherical harmonics arisen from the generating functions (1.46).^{45,46,48}

$$\mathbf{E} = \mathbf{M}_v + i\mathbf{N}_u \quad (1.47a) \quad \mathbf{H} = n(-\mathbf{M}_u + i\mathbf{N}_v) \quad (1.47b)$$

The Mie solution inside and outside the sphere can be found by imposing the boundary conditions onto the surface of the sphere and at infinite. Particularly, the field inside the sphere is generated by

$$u = e^{-i\omega t} \cos(\varphi) \sum_{l=1}^{\infty} n c_l (-i)^l \frac{2l+1}{l(l+1)} P_l^1(\cos \theta) j_l(nkr) \quad (1.48a)$$

$$v = e^{-i\omega t} \sin(\varphi) \sum_{l=1}^{\infty} n d_l (-i)^l \frac{2l+1}{l(l+1)} P_l^1(\cos \theta) j_l(nkr) \quad (1.48b)$$

while the field outside the sphere results from the superposition of the incident plane wave and the scattered wave

$$u = e^{-i\omega t} \cos(\varphi) \sum_{l=1}^{\infty} a_l (i)^l \frac{2l+1}{l(l+1)} P_l^1(\cos \theta) h_l^{(2)}(kr) \quad (1.49a)$$

$$v = e^{-i\omega t} \sin(\varphi) \sum_{l=1}^{\infty} b_l (i)^l \frac{2l+1}{l(l+1)} P_l^1(\cos \theta) h_l^{(2)}(kr) \quad (1.49b)$$

Note that the different spherical Bessel functions j_l and $h_l^{(2)}$ appearing in Equations (1.48) and (1.49) is due to the asymptotic behaviour of the finite field at the origin and the scattered wave at infinite, respectively. In an effort to lighten the notation, the Mie coefficients a_l , b_l , c_l , and d_l can be expressed by introducing the Riccati-Bessel functions (1.50).

$$\psi_l(\rho) = \rho j_l(\rho) \quad (1.50a) \quad \xi_l(\rho) = \rho h_l^{(1)}(\rho) \quad (1.50b)$$

Thus, the Mie coefficients in case of nonmagnetic conductive sphere ($\mu = 1$) embedded in a linear, isotropic, and homogeneous medium result^{45,46,48}

$$a_l = \frac{m\psi_l(mx)\psi_l'(x) - \psi_l(x)\psi_l'(mx)}{m\psi_l(mx)\xi_l'(x) - \xi_l(x)\psi_l'(mx)} \quad (1.51a)$$

$$b_l = \frac{\psi_l(mx)\psi'_l(x) - m\psi_l(x)\psi'_l(mx)}{\psi_l(mx)\xi'_l(x) - m\xi_l(x)\psi'_l(mx)} \quad (1.51b)$$

$$c_l = \frac{m\psi_l(x)\xi'_l(x) - m\xi_l(x)\psi'_l(x)}{\psi_l(mx)\xi'_l(x) - m\xi_l(x)\psi'_l(mx)} \quad (1.51c)$$

$$d_l = \frac{m\psi_l(x)\xi'_l(x) - m\xi_l(x)\psi'_l(x)}{m\psi_l(mx)\xi'_l(x) - \xi_l(x)\psi'_l(mx)} \quad (1.51d)$$

where the parameters m and x are defined as $m \equiv \underline{n}_1/n_2$, in which \underline{n}_1 is the complex refractive index of the metal (1.10) and n_2 is the real refractive index of the surrounding medium, and $x = k_2 a$, in which $k_2 = 2\pi/\lambda_2$ is the wavenumber in the surrounding medium and a the radius of the particle. Therefore, by considering Equations (1.47) and the particular solutions (1.48) and (1.49), the incident (i), internal (t), and scattered (s) fields expressed in spherical harmonics formally reads^{45,46,48}

$$\mathbf{E}_i = \sum_{n=1}^{\infty} i^n \frac{2n+1}{n(n+1)} \mathbf{E}_0 [\mathbf{M}_{01n}^{(1)} - i\mathbf{N}_{e1n}^{(1)}] \quad (1.52a)$$

$$\mathbf{H}_i = -\frac{k}{\omega\mu} \sum_{n=1}^{\infty} i^n \frac{2n+1}{n(n+1)} \mathbf{E}_0 [\mathbf{M}_{e1n}^{(1)} + i\mathbf{N}_{01n}^{(1)}] \quad (1.52b)$$

$$\mathbf{E}_t = \sum_{n=1}^{\infty} i^n \frac{2n+1}{n(n+1)} \mathbf{E}_0 [c_n \mathbf{M}_{01n}^{(1)} - i d_n \mathbf{N}_{e1n}^{(1)}] \quad (1.52c)$$

$$\mathbf{H}_t = -\frac{k_t}{\omega\mu_t} \sum_{n=1}^{\infty} i^n \frac{2n+1}{n(n+1)} \mathbf{E}_0 [d_n \mathbf{M}_{e1n}^{(1)} + i c_n \mathbf{N}_{01n}^{(1)}] \quad (1.52d)$$

$$\mathbf{E}_s = \sum_{n=1}^{\infty} i^n \frac{2n+1}{n(n+1)} \mathbf{E}_0 [i a_n \mathbf{N}_{e1n}^{(3)} - b_n \mathbf{M}_{01n}^{(3)}] \quad (1.52e)$$

$$\mathbf{H}_s = -\frac{k}{\omega\mu} \sum_{n=1}^{\infty} i^n \frac{2n+1}{n(n+1)} \mathbf{E}_0 [i b_n \mathbf{N}_{01n}^{(3)} + a_n \mathbf{M}_{e1n}^{(3)}] \quad (1.52f)$$

The corresponding scattering, extinction, and absorption cross sections result from the optical theorem yielding⁴⁸

$$\sigma_{\text{sca}} = \frac{2\pi}{|k|^2} \sum_{l=1}^{\infty} (2l+1)(|a_l|^2 + |b_l|^2) \quad (1.53a)$$

$$\sigma_{\text{ext}} = \frac{2\pi}{|k|^2} \sum_{l=1}^{\infty} (2l+1) \Re\{a_l + b_l\} \quad (1.53b)$$

$$\sigma_{\text{abs}} = \sigma_{\text{ext}} - \sigma_{\text{sca}} \quad (1.53c)$$

where l represents the multipole order of the scattering. Figure 1.10 shows the extinction, absorption, and scattering cross sections calculated for gold and silver sphere of 150 nm diameter.^{40,48}

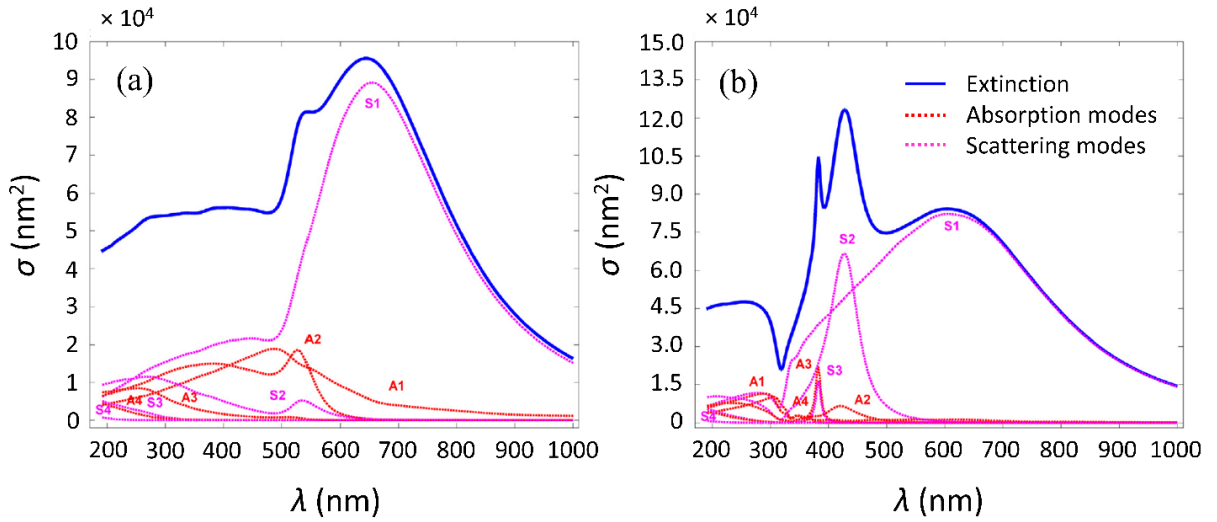


Figure 1.10. Extinction (solid blue line), absorption (solid red line), and scattering (solid pink line) cross sections calculated for (a) gold and (b) silver sphere of 150 nm diameter. The spectra are decomposed into contributions from absorption and scattering modes for dipole (A₁ and S₁), quadrupole (A₂ and S₂), hexapole (A₃ and S₃), and octupole (A₄ and S₄) mode, respectively (from Ref. ⁴⁹).

1.5.2 Quasi-static approximation

In the case of nanostructures whose dimensions are much smaller than the wavelength of the external EM field, the Mie problem can be addressed by adopting the quasi-static approximation. Since the phase of the oscillating external field is approximately constant over the particle volume, the system acts as a conductive particle in an electrostatic field. Although the quasi-static approximation is strictly valid only for vanishingly small particles, in practice it provides reliable results for nanoparticles whose dimensions are lower than 100 nm.^{11,41} For larger particles, the phase of the electric field varies over the particle volume, hence an electrodynamic approach is required.

An analytical solution to the scattering problem is obtained by considering a metal nanosphere of radius $a \ll \lambda$ – embedded in a linear, isotropic, and homogeneous medium – interacting with an external time-harmonic EM field. Firstly, the spatial field distribution is conveniently investigated by considering an electrostatic configuration as shown in Figure 1.11.

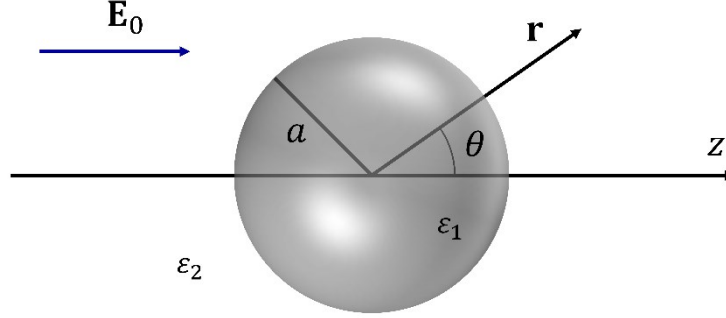


Figure 1.11. Homogeneous and isotropic metal nanosphere placed into an electrostatic field.

Given the azimuthal symmetry of the system, the general solution of the electrical potential provided by the Laplace equation $\Delta\Phi = 0$ is^{11,41}

$$\Phi(r, \theta) = \sum_{l=0}^{\infty} [A_l r^l + B_l r^{-(l+1)}] P_l(\cos \theta) \quad (1.54)$$

where $P_l(\cos \theta)$ are the Legendre polynomials of order l and θ the angle between \mathbf{r} and the z -axis. The expression (1.54) can be written by separating the contribution of the potential inside and outside the sphere.

$$\Phi_{\text{in}}(r, \theta) = \sum_{l=0}^{\infty} A_l r^l P_l(\cos \theta) \quad (1.55a)$$

$$\Phi_{\text{out}}(r, \theta) = \sum_{l=0}^{\infty} [B_l r^l + C_l r^{-(l+1)}] P_l(\cos \theta) \quad (1.55b)$$

Note that the coefficient relative to $r^{-(l+1)}$ in the (1.55a) has to be zero to keep finite the potential solution in the center of the sphere. The determination of the coefficients A_l , B_l and C_l is provided by imposing the boundary conditions at infinite and onto the surface of the sphere. Particularly, at $r \rightarrow \infty$ the potential results $\Phi_{\text{out}} \rightarrow -E_0 z = -E_0 r \cos \theta$ following $B_1 = -E_0$ and $B_l = 0$ for $l \neq 1$, whereas at $r = a$ the continuity of the tangential component of the electric field and of the normal components of the displacement field demands

$$-\frac{1}{a} \frac{\partial \Phi_{\text{in}}}{\partial \theta} \Big|_{r=a} = -\frac{1}{a} \frac{\partial \Phi_{\text{out}}}{\partial \theta} \Big|_{r=a} \quad (1.56a)$$

$$-\varepsilon_0 \varepsilon_1 \frac{\partial \Phi_{\text{in}}}{\partial r} \Big|_{r=a} = -\varepsilon_0 \varepsilon_2 \frac{\partial \Phi_{\text{out}}}{\partial r} \Big|_{r=a} \quad (1.56b)$$

By inserting the expressions of the potential (1.55) into the conditions (1.56), the remaining nonzero coefficients are

$$A_1 = -\frac{3\varepsilon_2}{\varepsilon_1 + 2\varepsilon_2} E_0 \quad (1.57a) \quad C_1 = \frac{\varepsilon_1 - \varepsilon_2}{\varepsilon_1 + 2\varepsilon_2} a^3 E_0 \quad (1.57b)$$

Therefore, the solutions for potential inside and outside the sphere are

$$\Phi_{\text{in}}(r, \theta) = -\frac{3\varepsilon_2}{\varepsilon_1 + 2\varepsilon_2} E_0 r \cos \theta \quad (1.58a)$$

$$\Phi_{\text{out}}(r, \theta) = -E_0 r \cos \theta + \frac{\varepsilon_1 - \varepsilon_2}{\varepsilon_1 + 2\varepsilon_2} E_0 a^3 \frac{\cos \theta}{r^2} \quad (1.58b)$$

The solution (1.58b) describes the superposition of the electrostatic field and that produced by an electric dipole located in the center of the sphere. Thus, the potential outside the sphere can be written in terms of the dipole moment \mathbf{p} .

$$\Phi_{\text{out}} = -E_0 r \cos \theta + \frac{\mathbf{p} \cdot \mathbf{r}}{4\pi\varepsilon_0\varepsilon_2 r^3} \quad (1.59a)$$

$$\mathbf{p} = 4\pi\varepsilon_0\varepsilon_2 a^3 \frac{\varepsilon_1 - \varepsilon_2}{\varepsilon_1 + 2\varepsilon_2} \mathbf{E}_0 \quad (1.59b)$$

Such a dipole moment corresponds to that induced inside the metal sphere by the external field \mathbf{E}_0 yielding $\mathbf{p} = \varepsilon_0\varepsilon_2\alpha\mathbf{E}_0$ of magnitude proportional to polarizability α .

$$\alpha = 4\pi a^3 \frac{\varepsilon_1 - \varepsilon_2}{\varepsilon_1 + 2\varepsilon_2} \quad (1.60)$$

The polarizability (1.60) experiences a resonant enhancement at the minimum of $|\varepsilon_1 + 2\varepsilon_2|$. In the case of slow-varying $\Im\{\varepsilon_1(\omega)\} \equiv \varepsilon_1''$ around the resonance, the minimum is provided by the Fröhlich condition (1.61) and the associated mode is called dipole surface plasmon.^{11,41}

$$\Re\{\varepsilon_1(\omega)\} \equiv \varepsilon'_1 = -2\varepsilon_2 \quad (1.61)$$

It is worth to notice that in real cases the magnitude of the polarizability α in Equation (1.60) is limited by $\varepsilon'_1 \neq 0$ in the denominator.^{11,41}

The spatial distribution of the electric field inside and outside the sphere can be retrieved by calculating the gradient of the potentials (1.58) yielding

$$\mathbf{E}_{\text{in}} = \frac{3\varepsilon_2}{\varepsilon_1 + 2\varepsilon_2} \mathbf{E}_0 \quad (1.62a)$$

$$\mathbf{E}_{\text{out}} = \mathbf{E}_0 + \frac{3\mathbf{n}(\mathbf{n} \cdot \mathbf{p}) - \mathbf{p}}{4\pi\varepsilon_0\varepsilon_2} \frac{1}{r^3} \quad (1.62b)$$

Note that a resonance in polarizability entails an enhancement of both the internal and dipolar fields. The harmonic time dependence of the electric field $\mathbf{E}(\mathbf{r}, t) = \mathbf{E}_0 e^{-i\omega t}$ can be recovered in the framework of the quasi-static approximation since the spatial retardation effects are negligible over the whole particle volume for subwavelength nanospheres. Thus, the oscillating electric field induces a coherent dipole moment $\mathbf{p} = \varepsilon_0\varepsilon_2\alpha\mathbf{E}_0 e^{-i\omega t}$ as shown in Figure 1.12.

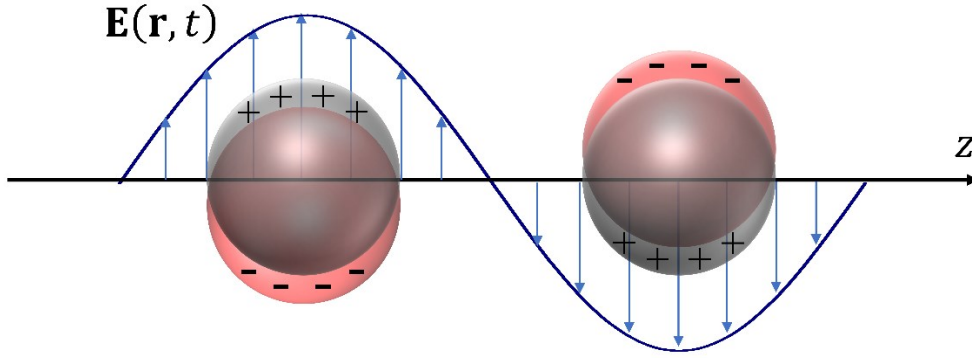


Figure 1.12. Excitation of LSPs realized by illuminating the metal nanoparticles with an oscillating electric field. The displacement of the conduction electrons with respect to the positive ion core gives rise to a coherent oscillating dipole moment in the nanoparticles.

In turn, the oscillating dipoles produce an EM field that leads to the scattering of the external radiation. The electric and magnetic fields emitted by an oscillating dipole are^{11,38}

$$\mathbf{H} = \frac{ck^2}{4\pi} (\mathbf{n} \times \mathbf{p}) \frac{e^{ikr}}{r} \left(1 - \frac{1}{ikr}\right) \quad (1.63a)$$

$$\mathbf{E} = \frac{1}{4\pi\epsilon_0\epsilon_2} \left\{ k^2 (\mathbf{n} \times \mathbf{p}) \times \mathbf{n} \frac{e^{ikr}}{r} + [3\mathbf{n}(\mathbf{n} \cdot \mathbf{p}) - \mathbf{p}] \left(\frac{1}{r^3} - \frac{ik}{r^2} \right) e^{ikr} \right\} \quad (1.63b)$$

where \mathbf{n} is the unit vector in the direction of the point of interest. In the near region ($kr \ll 1$), Equations (1.63) become

$$\mathbf{H} = \frac{i\omega}{4\pi} (\mathbf{n} \times \mathbf{p}) \frac{1}{r^2} \quad (1.64a)$$

$$\mathbf{E} = \frac{3\mathbf{n}(\mathbf{n} \cdot \mathbf{p}) - \mathbf{p}}{4\pi\epsilon_0\epsilon_2} \frac{1}{r^3} \quad (1.64b)$$

In this zone, the electric field dominates over the magnetic field. Particularly, for static field ($ka \rightarrow 0$), the magnetic field are vanishingly small.^{11,38} In the radiative zone ($kr \gg 1$), the fields propagate through spherical-waves of form reading^{11,38}

$$\mathbf{H} = \frac{ck^2}{4\pi} (\mathbf{n} \times \mathbf{p}) \frac{e^{ikr}}{r} \quad (1.65a)$$

$$\mathbf{E} = \sqrt{\frac{\mu_0}{\epsilon_0\epsilon_2}} \mathbf{H} \times \mathbf{n} \quad (1.65b)$$

At the resonance frequency both absorption and scattering of the impinging EM radiation occur. In the quasi-static approximation, the scattering and absorption cross sections results^{11,41}

$$\sigma_{\text{sca}} = \frac{k^4}{6\pi} |\alpha|^2 = \frac{8\pi}{3} k^4 a^6 \left| \frac{\epsilon_1 - \epsilon_2}{\epsilon_1 + 2\epsilon_2} \right|^2 \quad (1.66a)$$

$$\sigma_{\text{abs}} = k \Im[\alpha] = 4\pi k a^3 \Im \left[\frac{\epsilon_1 - \epsilon_2}{\epsilon_1 + 2\epsilon_2} \right] \quad (1.66b)$$

For subwavelength particles ($a \ll \lambda$), the absorption efficiency – proportional to a^3 – dominates over the scattering, which scales with a^6 . For a sphere of volume V in the quasi-static approximation, the extinction cross section $\sigma_{\text{ext}} = \sigma_{\text{abs}} + \sigma_{\text{sca}}$ is^{11,41}

$$\sigma_{\text{ext}} = 9V \frac{\omega}{c} \frac{\epsilon_1'' \epsilon_2^{3/2}}{[\epsilon_1' + 2\epsilon_2]^2 + \epsilon_1''^2} \quad (1.67)$$

Note that the expressions (1.66) and (1.67) are valid for both metals and dielectric media. In the case of metal nanoparticles, both absorption and scattering – and thus extinction – are resonantly enhanced at the plasmon resonance entailed by condition (1.61). Figure 1.13 shows the extinction cross section of a silver nanosphere surrounded by air (black points) and silica (grey points) in the quasi-static approximation calculated by using Equation (1.67).^{11,40}

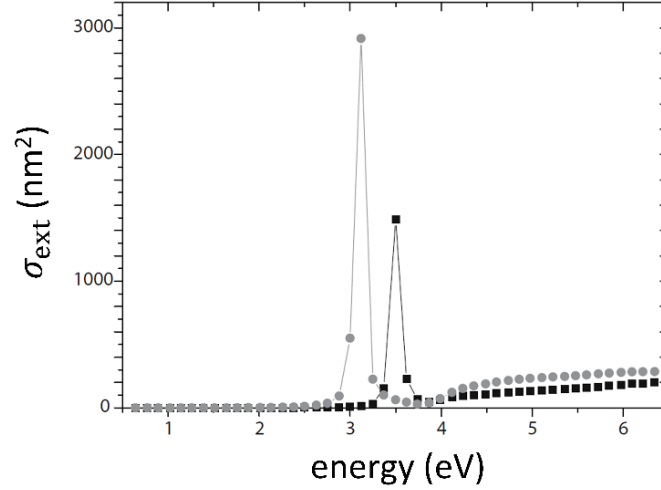


Figure 1.13. Extinction cross section calculated for a silver nanosphere of 10 nm diameter surrounded by air (black points) and silica (grey points) (from Ref. 11).

For a metal nanosphere characterized by a dielectric function (1.18a), the Fröhlich condition (1.61) is fulfilled at

$$\omega_{\text{LSPR}} = \frac{\omega_p}{\sqrt{2\varepsilon_2 + 1}} \quad (1.68a)$$

$$\lambda_{\text{LSPR}} = \lambda_p \sqrt{2n_2^2 + 1} \quad (1.68b)$$

where $n_2 = \sqrt{\varepsilon_2}$ is the refractive index of the surrounding medium and $\lambda_p = 2\pi c/\omega_p$ is the wavelength corresponding to the plasma frequency of the bulk metal. Equations (1.68) clearly shows that the plasmon resonance strongly depends on the dielectric environment, in particular the LSPR peak red-shifts as the dielectric constant of the medium increases.^{11,50} Such a dependence turns out to be approximately linear only over small ranges of the refractive index (at optical frequencies).⁵⁰

Due to the higher field confinement exerted by subwavelength nanostructures, the characteristic decay length l_d of the LSP near-field is much shorter (approximately 5-10 nm)^{51,52} as compared to that obtained in the case of SPPs by Equations (1.41) (typically, in the range of 0.1-1 μm).⁵³ Such a feature is also evident by considering the exponential dependence of the coupling strength $\Delta\lambda/\lambda_0$ on the gap distance s in a nanoparticle dimer configuration⁵⁴

$$\frac{\Delta\lambda}{\lambda_0} = ke^{-s/l_d} \quad (1.69)$$

where λ_0 is the LSPR wavelength of the individual nanoparticle forming the dimer while $\Delta\lambda$ is the difference between dimer and single nanoparticle resonance. An empirical measurement of the decay length has been conducted on metal nanoparticle pairs lithographically fabricated with systematically varying the interparticle separations turning out that the decay length is always approximately 0.2 times the nanoparticle diameter ($l_d \approx 2a/5$),⁵⁵ even though the pre-exponential factor k , which represents the maximum plasmon shift for the nanoparticle pair, does change depending on the system conditions.⁵⁴ The size-scaling trend represented by Equation (1.69) is quite universal regardless of the type of the metal, the shape of the particle, or the surrounding medium.^{54,55} The origin of such an universal size-scaling of the plasmon coupling can be understood based on a simple dipolar coupling model. The fractional plasmon shift $\Delta\lambda/\lambda_0$ reflects the strength of the interparticle near-field coupling, which is determined by the combination of the polarizability of the nanoparticle (1.60), which is proportional to a^3 , and the decay of EM near-field (1.64b) with distance r away from the nanoparticle surface as $1/r^3$. As a result, the coupling strength (and hence $\Delta\lambda/\lambda_0$) is a function of $(a/r)^{-3}$ that can be well-approximated by an exponential decay irrespective of the other parameters of the system.⁵⁴

1.5.3 Gans theory

The assumption of spherical shape can be relaxed to retrieve Equations (1.66) in the case of elongated particles. Gans theory provides an analytical solution within a quasi-static framework in the case of ellipsoids (Figure 1.14) – with semiaxes a_1 , a_2 and a_3 much smaller than the excitation wavelength – by decomposing the plasmon excitation along the three symmetry axes.^{41,47}

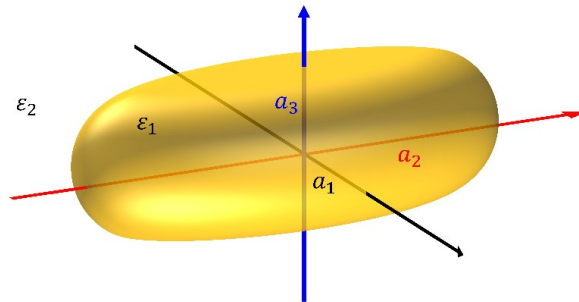


Figure 1.14. Geometry of an ellipsoidal metal particle used in Gans theory.

In this case, the absorption and scattering cross sections are^{41,47}

$$\sigma_{\text{sca},i} = \frac{k^4}{6\pi} |\alpha_i|^4 \quad (1.70a)$$

$$\sigma_{\text{abs},i} = k \Im\{\alpha_i\} \quad (1.70b)$$

where the subscript $i = \{1, 2, 3\}$ refers to the direction of the principal axes of the ellipsoid. The polarizabilities α_i appearing in Equations (1.70) is provided by solving the Laplace equation in ellipsoidal coordinates.^{41,47}

$$\alpha_i = 4\pi a_1 a_2 a_3 \frac{\varepsilon_1 - \varepsilon_2}{3\varepsilon_2 + 3L_i(\varepsilon_1 - \varepsilon_2)} \quad (1.71a)$$

$$L_i = \frac{a_1 a_2 a_3}{2} \int_0^\infty \frac{dq}{(a_i^2 + q)f(q)} \quad (1.71b)$$

$$f(q) = \sqrt{(q + a_1^2)(q + a_2^2)(q + a_3^2)} \quad (1.71c)$$

Since the scattering cross section (1.70a) scales with the fourth power of the nanoparticle volume while the absorption cross section (1.70b) exhibits a linear dependence, the spheroid size introduces a nonlinearity in the extinction cross section $\sigma_{\text{ext},i} = \sigma_{\text{sca},i} + \sigma_{\text{abs},i}$. The geometrical factor L_i has to fulfil the relation $\sum_i L_i = 1$. Generally, the polarizability of elongated particles is expressed in terms of the depolarization factors \tilde{L}_i linked to the geometrical factor L_i through^{41,47}

$$\tilde{L}_i = \frac{\varepsilon_1 - \varepsilon_2}{\varepsilon_1 - 1} \frac{L_i}{\varepsilon_0 \varepsilon_2} \quad (1.72)$$

Such a depolarization factor is defined as $E_{1i} = E_{0i} - \tilde{L}_i P_{1i}$, where E_{1i} and P_{1i} are the electric field and polarization, respectively, induced inside the particle by the impinging field E_{0i} along the principal axis i . Thus, the plasmon resonance wavelengths λ_i along the principal axes result^{41,47}

$$\lambda_i = \lambda_p \sqrt{\varepsilon_\infty + \left(\frac{1}{\tilde{L}_i} - 1\right) \varepsilon_2} \quad (1.73a)$$

$$\lambda_p = \sqrt{\frac{2\pi^2 c^2 m \varepsilon_\infty}{n e^2}} \quad (1.73b)$$

where ε_∞ is the high-frequency dielectric constant of the metal, m the effective mass of the conduction electron and n the conduction electron density.

In the case of oblate ($a_1 = a_2$) or prolate ($a_2 = a_3$) spheroidal metal nanoparticles, two different plasmon resonance modes – corresponding to the oscillations of the conduction electrons along major

and minor axis – arise from the scattering problem with an external oscillating field. Such resonances exhibit different behaviour as compared to the plasmon resonance delivered by a nanosphere. Particularly, the resonance mode along the major (minor) axis delivers a red-shift of the plasmon resonance wavelength significantly higher (lower) than that arisen from a metal nanosphere with equal volume.^{47,50}

Moreover, in the case of spheroidal nanoparticles, the scattering problem has to be investigated as well by holding the external field polarization in order to decompose the plasmon resonance into longitudinal and transverse LSPR mode. From Gans theory, it results that the shape and size of spheroidal nanoparticles strongly affects Equations (1.70), in particular the extinction cross section of both longitudinal and transverse plasmon modes is enlarged as the aspect ratio of the spheroid increases.^{47,50} In addition, the plasmon resonance wavelength of longitudinal (transverse) mode significantly red-shifts (vanishingly blue-shifts) as the aspect ratio is enlarged due to the higher (lower) polarizability of the spheroid at the longitudinal (transverse) plasmon resonance.^{47,50}

As it concerns the electric field distribution in the case of elongated nanoparticles, regions with low radii of curvatures, for instance at the ends of the spheroid along the major axis, can concentrate the conduction electrons at higher volume densities thereby leading to a larger electric field enhancement.⁴⁷ Moreover, in the case of noble metals, the significantly higher red-shift experienced by the longitudinal plasmon wavelength – as compared to the case of metal nanosphere with equal volume – entails a monotonic growth of the electric field enhancement with the aspect ratio of the spheroid due to the occurrence of longitudinal plasmon resonance far from the region characterized by interband transitions.⁴⁷

1.6 Numerical simulations

1.6.1 Discrete dipole approximation

The discrete dipole approximation (DDA) is a numerical technique for computing EM scattering and absorption experienced by nanostructures of arbitrary shape relying on approximating the continuum target by a finite point array.^{56–58} In response to the local electric field each point acquires a dipole moment allowing the resolution of the scattering problem in a self-consistent way. For a finite array of point dipoles – separated by a interdipole distance much smaller as compared to any structural lengths in the target and to the wavelength of the external field – the scattering problem may be solved

exactly.^{56–58} This method circumvents the imposition of difficult boundary conditions in the light scattering calculations by dividing the particle into elements and allowing the elements to interact only through dipole-dipole interactions (Figure 1.15).^{56,57}

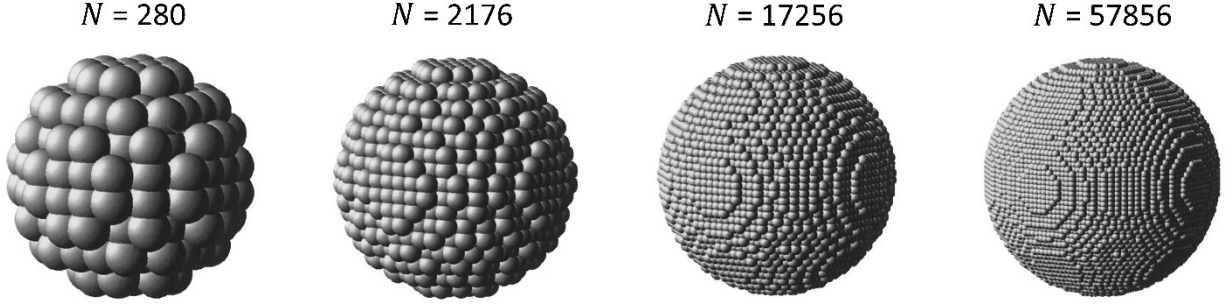


Figure 1.15. Schematic representation of the models used for the DDA calculations. The spheres are discretized into N elements interacting each other through dipole-dipole interactions (from Ref. ⁵⁷).

In the DDA approach, the particle is represented by a cubic array of N point dipoles with polarizabilities α_i and located at position \mathbf{r}_i . The interaction of each dipole with a local electric field $\mathbf{E}_{\text{local}}(\mathbf{r}_i)$ – given by the superposition of the incident field $\mathbf{E}_{\text{ext}}(\mathbf{r}_i)$ and the retarded dipole field $\mathbf{E}_{\text{dipole}}(\mathbf{r}_i)$ arising from all other $N - 1$ dipoles in the particle – induces a polarization (1.74a).^{56,57}

$$\mathbf{P}_i = \alpha_i \mathbf{E}_{\text{local}}(\mathbf{r}_i) \quad (1.74a)$$

$$\mathbf{E}_{\text{local}}(\mathbf{r}_i) \equiv \mathbf{E}_{\text{local},i} = \mathbf{E}_{\text{ext},i} + \mathbf{E}_{\text{dipole},i} = \mathbf{E}_0 e^{ik\mathbf{r}_i} - \sum_{j \neq i} \mathbf{A}_{ij} \cdot \mathbf{P}_j \quad (1.74b)$$

$$\mathbf{A}_{ij} \cdot \mathbf{P}_j = \frac{e^{ik\mathbf{r}_{ij}}}{r_{ij}^3} \left[k^2 \mathbf{r}_{ij} \times (\mathbf{r}_{ij} \times \mathbf{P}_j) + \frac{1 - ik\mathbf{r}_{ij}}{r_{ij}^2} \times \{ (r_{ij}^2 \mathbf{P}_j) - 3\mathbf{r}_{ij}(\mathbf{r}_{ij} \cdot \mathbf{P}_j) \} \right] \quad (1.74c)$$

The term $-\mathbf{A}_{ij} \cdot \mathbf{P}_j$ appearing in Equations (1.74), in which the $3N \times 3N$ interaction matrix \mathbf{A} is defined for $i \neq j$, accounts for the contribution to the electric field at position i due to the dipole at position j whereby the reciprocal distance \mathbf{r}_{ij} is defined as $\mathbf{r}_i - \mathbf{r}_j$. The diagonal elements of the matrix \mathbf{A} is defined as $\mathbf{A}_{ii} \equiv \alpha_i^{-1}$. Therefore, the scattering problem can be formulated as a set of N inhomogeneous linear complex vector equations.^{56,57}

$$\sum_{j=1}^N \mathbf{A}_{ij} \cdot \mathbf{P}_j = \mathbf{E}_{\text{dipole},i} \quad (1.75)$$

Note that the interaction matrix \mathbf{A} is symmetric. By introducing the $3N$ -dimensional vectors $\tilde{\mathbf{P}} = (P_1, P_2, \dots, P_N)$ and $\tilde{\mathbf{E}}_{\text{dipole}} = (E_{\text{dipole},1}, E_{\text{dipole},2}, \dots, E_{\text{dipole},N})$ and the $3N \times 3N$ symmetric matrix $\tilde{\mathbf{A}}$, the problem is reduced to the following single matrix equation^{56,57}

$$\tilde{\mathbf{A}} \tilde{\mathbf{P}} = \tilde{\mathbf{E}}_{\text{dipole}} \quad (1.76)$$

Since the number of dipoles is of the order of 10^4 - 10^5 for a typical nanoparticle,⁵⁶⁻⁵⁸ the direct inversion of $\tilde{\mathbf{A}}$ to solve Equation (1.76) is impractical. Generally, the determination of the unknown vector $\tilde{\mathbf{P}}$ is achieved by an iterative method that improves the estimate for $\tilde{\mathbf{P}}$ until the user-defined error criterion is satisfied (usually the error tolerance may be smaller than 10^{-5}).⁵⁶⁻⁵⁸

Once the polarizations \mathbf{P}_i are determined, the extinction cross sections for the nanoparticle is computed from the forward-scattering amplitude by using the optical theorem, the absorption cross section is obtained by summing over the rate of energy dissipation by each of the dipoles, and the scattering cross section by calculating the power radiated by the array of oscillating dipoles.^{57,58}

$$\sigma_{\text{ext}} = \frac{4\pi k}{|\mathbf{E}_{\text{dipole}}|^2} \sum_{i=1}^N \Im\{\mathbf{E}_{\text{dipole},i}^* \cdot \mathbf{P}_i\} \quad (1.77a)$$

$$\sigma_{\text{abs}} = \frac{4\pi k}{|\mathbf{E}_{\text{dipole}}|^2} \sum_{i=1}^N \left[\Im\{\mathbf{P}_i \cdot (\alpha_i^{-1})^* \mathbf{P}_i^*\} - \frac{2}{3} k^3 \mathbf{P}_i \cdot \mathbf{P}_i^* \right] \quad (1.77b)$$

$$\sigma_{\text{sca}} = \frac{k^4}{|\mathbf{E}_{\text{dipole}}|^2} \int d\Omega \left| \sum_{i=1}^N [\mathbf{P}_i - \mathbf{n}(\mathbf{n} \cdot \mathbf{P}_i)] e^{-ik\mathbf{n} \cdot \mathbf{r}_i} \right|^2 \quad (1.77c)$$

In Equation (1.77c), \mathbf{n} is the unit vector in the direction of the scattering and $d\Omega$ is the element of the solid angle.

1.6.2 Boundary element method

The boundary element method (BEM) is a computational technique for solving linear partial differential equations by reducing them to boundary integral equations.^{59,60} Particularly, the exact solution of Maxwell's equations (1.1) in the presence of arbitrarily shaped dielectric interfaces can be expressed in terms of surface integral equations involving interface charges and current that act as sources of the induced electromagnetic field.⁶⁰ By following this approach, the continuous surface

charge can be approximated as a discrete number of points located at the centroids of small surface elements and connected through the Green's function (Figure 1.16).

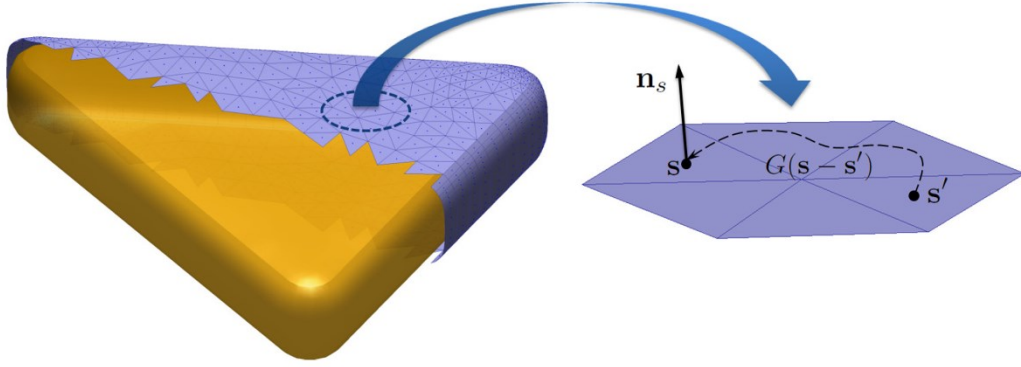


Figure 1.16. After discretizing the particle surface, the corresponding continuous surface charge and currents are approximated as points in the centroids of the small surface elements. The Green's function connects these different points with each other (from Ref. ⁴⁹).

Firstly, it is convenient to introduce the potentials \mathbf{A} and Φ whereby the fields are defined as³⁸

$$\mathbf{H} = \frac{1}{\mu} \nabla \times \mathbf{A} \quad (1.78a)$$

$$\mathbf{E} = -\nabla\Phi + ik\mathbf{A} \quad (1.78b)$$

Given the gauge invariance of the potentials, \mathbf{A} and Φ can be chosen in such a way as to fulfil the Lorenz condition³⁸

$$\nabla \cdot \mathbf{A} - ik\epsilon\mu\Phi = 0 \quad (1.79)$$

This condition yields two decoupled wave equations for the potentials that are completely equivalent to the coupled Maxwell's equations (1.1).^{38,59}

$$\Delta\Phi + k^2\epsilon\mu\Phi = -4\pi\left(\frac{\rho}{\epsilon} + \sigma_s\right) \quad (1.80a)$$

$$\Delta\mathbf{A} + k^2\epsilon\mu\mathbf{A} = -\frac{4\pi}{c}(\mu\mathbf{J} + \mathbf{m}) \quad (1.80b)$$

where σ_s and \mathbf{m} account for the additional polarization charges and currents on the dielectric boundary originating in the discontinuity of ϵ and μ .^{38,59}

$$\sigma_s = \frac{1}{4\pi} \mathbf{D} \cdot \nabla \left(\frac{1}{\epsilon} \right) \quad (1.81a)$$

$$\mathbf{m} = -\frac{1}{4\pi} [i\omega\Phi\nabla(\varepsilon\mu) + c\mathbf{H} \times \nabla\mu] \quad (1.81b)$$

In nonmagnetic material, \mathbf{m} is normal to the interface and, hence, it does not represent a physical current. Outside the interface, it results $\sigma_s = 0$ and $\mathbf{m} = 0$.

The differential Helmholtz equations for the potentials (1.80) can be turned into two integral equations by introducing the retarded Green's function (1.82a) obeying the Equation (1.82c).^{38,59,60}

$$G_j(\mathbf{r} - \mathbf{r}') = \frac{e^{ik_j|\mathbf{r}-\mathbf{r}'|}}{|\mathbf{r} - \mathbf{r}'|} \quad (1.82a) \quad k_j = \frac{\omega}{c} \sqrt{\varepsilon_j\mu_j} \quad (1.82b)$$

$$[\Delta + k_j^2]G_j(\mathbf{r} - \mathbf{r}') = -4\pi\delta(\mathbf{r} - \mathbf{r}') \quad (1.82c)$$

Note that the square root in Equation (1.82b) is understood to yield positive imaginary parts warranting that the potentials Φ and \mathbf{A} vanish at infinite. Thus, the integral equations for the potentials inside each medium j result^{38,59,60}

$$\Phi(\mathbf{r}) = \frac{1}{\varepsilon_j} \int_{\Omega_j} G_j(|\mathbf{r} - \mathbf{r}'|) \rho(\mathbf{r}') d\mathbf{r}' + \int_{\partial\Omega_j} G_j(|\mathbf{r} - \mathbf{s}|) \sigma_j(\mathbf{s}) d\mathbf{s} \quad (1.83a)$$

$$\mathbf{A}(\mathbf{r}) = \frac{\mu_j}{c} \int_{\Omega_j} G_j(|\mathbf{r} - \mathbf{r}'|) \mathbf{J}(\mathbf{r}') d\mathbf{r}' + \int_{\partial\Omega_j} G_j(|\mathbf{r} - \mathbf{s}|) \mathbf{h}_j(\mathbf{s}) d\mathbf{s} \quad (1.83b)$$

where $\partial\Omega_j$ refers to the boundary of the medium $j = \{1, 2\}$, whereas σ_j and \mathbf{h}_j are the boundary charges and currents, respectively. Thus, integral equations of potentials (1.83) – valid inside and outside the domain as well as on its boundary – deliver EM fields through Equations (1.78).

The scattering, absorption, and extinction cross sections are derived from the Poynting vector by using the optical theorem.^{38,58}

$$\sigma_{\text{sca}} = n_2 \oint_{\partial\Omega} \Re\{\mathbf{n} \cdot (\mathbf{E} \times \mathbf{B}^*)\} dS \quad (1.84a)$$

$$\sigma_{\text{ext}} = \frac{1}{n_2} \oint_{\partial\Omega} \Re\{\mathbf{n} \cdot (\mathbf{E} \times \mathbf{B}_{\text{ext}}^* + \mathbf{E}_{\text{ext}}^* \times \mathbf{B})\} dS \quad (1.84b)$$

$$\sigma_{\text{abs}} = \sigma_{\text{ext}} - \sigma_{\text{sca}} \quad (1.84c)$$

where n_2 is the refractive index of the surrounding medium and \mathbf{n} the unit vector pointing in the scattering direction. Figure 1.17a shows the scattering cross section computed for a gold nanotriangle of $55 \times 50 \times 8 \text{ nm}^3$ size surrounded by water while Figure 1.17b and c the electric field distribution calculated at the resonance wavelength of 792 nm at the nanotriangle surface and on the outside, respectively.⁶¹

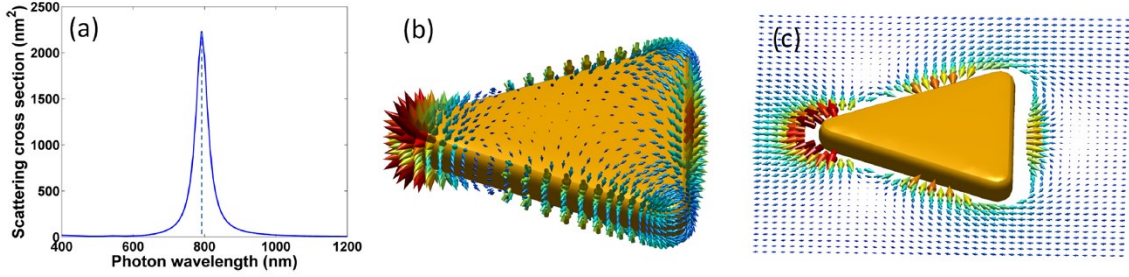


Figure 1.17. (a) Scattering cross section of a gold nanotriangle ($55 \times 50 \times 8 \text{ nm}^3$, $n_2 = 1.34$). Electric field at the resonance wavelength (792 nm) worked out (b) at the particle surface and (c) on the outside (from Ref. ⁴⁹).

1.6.3 Finite element method

The finite element method (FEM) is a numerical technique used to solve partial differential equations by transforming them into a matrix equation.⁶² To this aim, the FEM divides a large system into smaller cells, called finite elements, by discretizing the volume over a flexible non-uniform mesh. Thus, the numerical domain for the solution has a finite number of points. The simple equations that model these finite elements are then assembled into a larger matrix of equations modelling the entire problem. For this reason, the FEM is particularly suitable to describe the optical response of systems characterized by complex-shaped objects.

Aiming at introducing the FEM, the Laplace equation is a natural choice because of its simplicity.⁶² Then, the outcomes can be easily extended to more complex partial differential equations, such as Helmholtz equations (1.27) arising in many EM problems, in which the radiation condition has to be included in the whole consideration.

Consider the Laplace equation in two-dimensional space $\Delta u(x, y) = 0$ where $u(x, y)$ represents the potential distribution and introduce the differential operator $L = \Delta$. A functional F is constructed so that it achieves its minimum at a function being the solution of the Laplace equation.⁶²

$$F(u) = \int_{\Omega} |\nabla u|^2 d\Omega \quad (1.85)$$

Here, Ω is the domain where the potential is to be determined and it covers not only the radiating and scattering objects, but also the empty space surrounding them. Note that the functional (1.85) is linearly proportional to the stored energy in the system and the minimum energy state is exactly the solution to the differential Laplace equation.

Once the variational form of the problem is fully constructed, the domain of the problem has to be discretized into finite elements connected in a non-overlapping way thereby completely covering the entire space of the problem. Triangular-shaped finite elements are widely used since they can easily conform to structures with irregular boundaries (Figure 1.18).

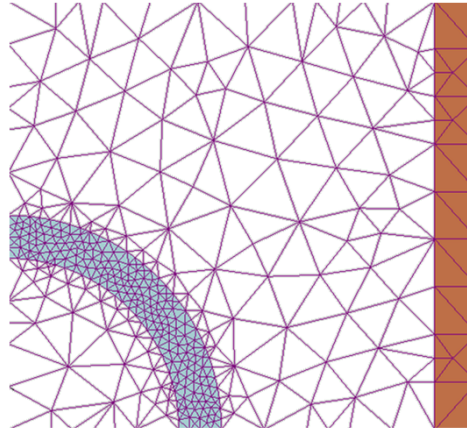


Figure 1.18. Example of non-uniform mesh made of non-overlapping finite elements using to discretize smooth-boundary surfaces (from Creative Commons CC BY-SA 3.0, author I. Zureks, 2007).

Then, the unknown function is determined over each finite elements through a combination of linear two-dimensional basis functions. In case of a triangular mesh, a linear two-dimensional function is fully characterized by its values at the three vertices of the triangle. Thus, the potential over a single triangular finite element reads⁶²

$$u = \sum_{i=1}^3 u_i \psi_i(x, y) \quad (1.86a)$$

$$\psi_i = \frac{1}{2A} (x_j y_k - x_k y_j) + (y_j - y_k)x + (x_k - x_j)y \quad (1.86b)$$

where u_i are the potential values at the three vertices, ψ_i are the basis functions defined over a single triangular element of area A , and $\{i, j, k\}$ constitutes a right-handed index triplet. Note that first-order elements involve only three potential values at the vertices of the triangle. Higher-order triangular elements can be constructed by expanding the field using piecewise-polynomial functions that involve a higher number of nodes and, hence, it requires the interpolation of polynomials of higher powers of x and y .

The description of the potential (1.86a) in terms of piecewise-planar functions allows the functional (1.85) to be calculated by adding the contributions from each elements.

$$F^{(e)}(u) = \sum_{i=1}^3 \sum_{j=1}^3 u_i u_j S_{ij}^{(e)} \quad (1.87a) \quad S_{ij}^{(e)} \equiv \int_{\Omega^{(e)}} |\nabla \psi_i \cdot \nabla \psi_j| d\Omega \quad (1.87b)$$

Equation (1.87a) can be expressed through the following matrix notation

$$F^{(e)} = U^T S^{(e)} U \quad (1.88a)$$

$$U = \begin{bmatrix} u_1 \\ u_2 \\ u_3 \end{bmatrix} \quad (1.88b) \quad U^T = [u_1 \quad u_2 \quad u_3] \quad (1.88b)$$

To retrieve the global solution, boundary nodal values have to be imposed to connect the functionals each other. A domain made of two triangular finite elements can be considered to convey the matrix assembly procedure. The sum of the corresponding two functionals is given by

$$F^{(e1)} + F^{(e2)} = U^{(e1+e2)T} S^{(e1+e2)} U^{(e1+e2)} \quad (1.89a)$$

$$U^{(e1+e2)} = \begin{bmatrix} u_1^{(e1)} \\ u_2^{(e1)} \\ u_3^{(e1)} \\ u_1^{(e2)} \\ u_2^{(e2)} \\ u_3^{(e2)} \end{bmatrix} \quad (1.89b) \quad S^{(e1+e2)} = \begin{bmatrix} S^{(e1)} & 0 \\ 0 & S^{(e2)} \end{bmatrix} \quad (1.89c)$$

When the elements are assembled, the local numbering scheme that references the nodes of separated elements will no longer be useful and it has to be replaced by a global numbering scheme that appropriately enumerates all the shared nodes (Figure 1.19).

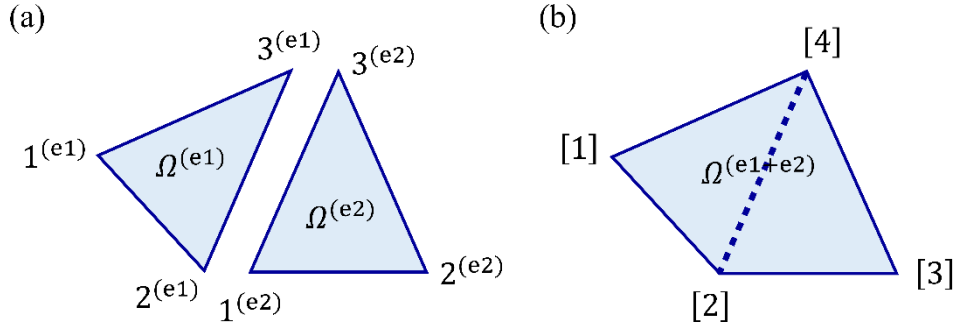


Figure 1.19. Example of (a) local and (b) global numbering of nodes.

Thus, the vector matrix (1.89b) turns into (1.90) by introducing the connectivity matrix C .

$$U_{\text{local}} = C U_{\text{global}} \quad (1.90)$$

By applying the matrix transformation (1.90) to Equation (1.89a), it results

$$F = F^{(e1)} + F^{(e2)} = U_{\text{global}}^T C^T S^{(e1+e2)} C U_{\text{global}} \quad (1.91)$$

Thus, Equation (1.91) is the functional describing the discrete system obtained by using two triangular finite elements. Eventually, the global solution of the potential can be found by minimizing Equation (1.91).

$$\frac{\partial F}{\partial u_i} = 0 \quad (1.92)$$

1.6.4 Finite-difference time-domain

The finite-difference time-domain (FDTD) method is a volume-based solution to Maxwell's differential equations (1.1) which are numerically solved in the time domain by evaluating the evolution of the EM field in unit volumes whose physical parameters are well-defined.^{62,63} Since the FDTD is a time-domain technique, the solution worked out by a single simulation is represented as a time-domain waveform. Thus, it can be decomposed into its spectral components using the Fourier transform allowing the system to be simultaneously investigated over a wide range of frequencies.

In FDTD approach, the entire workspace is divided into a uniform mesh whose lattice parameter has to be much smaller as compared to the shortest wavelength of interest. Over each cell, the \mathbf{E} and \mathbf{H} field components are defined and the general solution is obtained through the leapfrog method in

time.⁶² Firstly, such a problem can be conveniently addressed within a two-dimensional framework making easier the generalization to the three-dimensional case.

By assuming a field invariance in the z -direction, Maxwell's equations (1.1) reduce to one of two possible sets of equations: Equations (1.29) for TM polarization and Equations (1.94) for TE polarization.⁶²

$$\mu \frac{\partial H_x}{\partial t} = -\frac{\partial E_z}{\partial y} \quad (1.93a)$$

$$\varepsilon \frac{\partial E_x}{\partial t} + \sigma E_x = \frac{\partial H_z}{\partial y} \quad (1.94a)$$

$$\mu \frac{\partial H_y}{\partial t} = \frac{\partial E_z}{\partial x} \quad (1.29b)$$

$$\varepsilon \frac{\partial E_y}{\partial t} + \sigma E_y = -\frac{\partial H_z}{\partial x} \quad (1.94b)$$

$$\varepsilon \frac{\partial E_z}{\partial t} + \sigma E_z = \frac{\partial H_y}{\partial x} - \frac{\partial H_x}{\partial y} \quad (1.29c)$$

$$\mu \frac{\partial H_z}{\partial t} = \frac{\partial E_x}{\partial y} - \frac{\partial E_y}{\partial x} \quad (1.94c)$$

Once the space is discretized over a mesh, \mathbf{E} and \mathbf{H} field components are staggered in the grid (Figure 1.20). Since the mesh is uniform in the x - and y -directions, the location of the fields can be identified by the indices (i, j) .

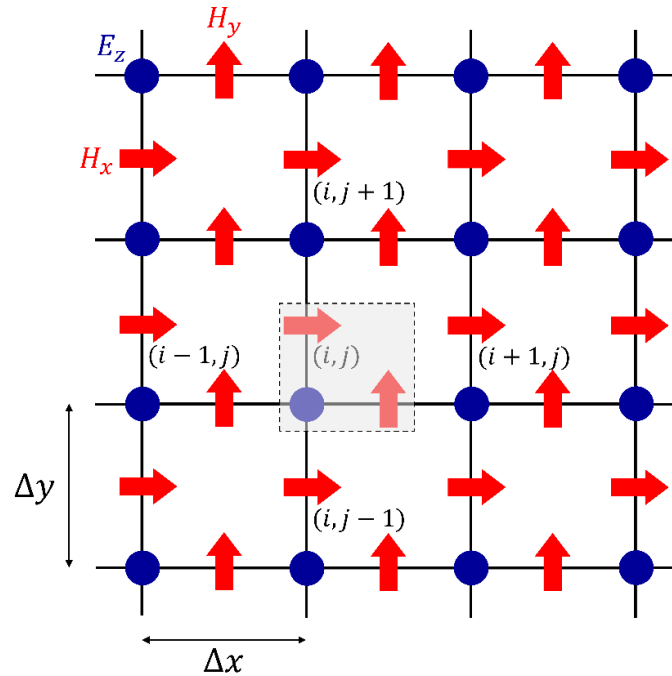


Figure 1.20. Two-dimensional FDTD mesh for the TM polarization case showing the staggering of the \mathbf{E} and \mathbf{H} fields. The roles of the \mathbf{E} and \mathbf{H} field components are reversed for the TE case. The indices (i, j) refer to the field components lying on the bottom and left sides of the unit cell (shaded grey square).

Similarly, the time scale is discretized into uniform time steps spaced by a time interval Δt . The field at the spatial location $(i\Delta x, j\Delta y)$ and time step $n\Delta t$ is denoted by

$$\mathbf{E}(i\Delta x, j\Delta y, n\Delta t) \equiv \mathbf{E}^n(i, j) \quad (1.95)$$

Thus, the spatial and temporal derivatives in Equations (1.29) and (1.94) have to be approximated by using the central difference approximation at second-order of accuracy.

$$\left. \frac{\partial E_z}{\partial y} \right|_{y=(j+\frac{1}{2})\Delta y} \rightarrow \frac{E_z(i, j+1) - E_z(i, j)}{\Delta y} \quad (1.96a)$$

$$\left. \frac{\partial E_z}{\partial x} \right|_{x=(i+\frac{1}{2})\Delta x} \rightarrow \frac{E_z(i+1, j) - E_z(i, j)}{\Delta x} \quad (1.96b)$$

$$\left. \frac{\partial H_x}{\partial t} \right|_{t=n\Delta t} \rightarrow \frac{H_x^{n+\frac{1}{2}} - H_x^{n-\frac{1}{2}}}{\Delta t} \quad (1.96c)$$

$$\left. \frac{\partial H_y}{\partial t} \right|_{t=n\Delta t} \rightarrow \frac{H_y^{n+\frac{1}{2}} - H_y^{n-\frac{1}{2}}}{\Delta t} \quad (1.96d)$$

$$\left. \frac{\partial E_z}{\partial t} \right|_{t=n\Delta t} \rightarrow \frac{E_z^{n+1} - E_z^n}{\Delta t} \quad (1.96e)$$

similarly, for the remaining derivatives in TE mode. Note that in FDTD method, the \mathbf{E} and \mathbf{H} fields are evaluated at two points in time separated by one half-time step. The staggering of the field components one half-cell apart in space, and at time instances that are on half-step apart in time, allows to evaluate the time-domain evolution of the field components from the start to the end of the simulation. Figure 1.21 shows a schematic representation of the leapfrog method for evaluating the \mathbf{E} and \mathbf{H} field components by staggering them in time.

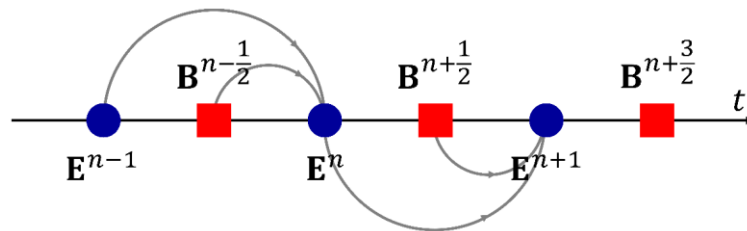


Figure 1.21. Leapfrog scheme used in the FDTD method.

By replacing the approximations (1.96) into the TM mode equations (1.29) (similarly, for the TE polarization case), it results⁶²

$$H_x^{n+\frac{1}{2}}(i,j) = H_x^{n-\frac{1}{2}}(i,j) - \frac{\Delta t}{\mu_{ij}\Delta y} [E_z^n(i,j+1) - E_z^n(i,j)] \quad (1.97a)$$

$$H_y^{n+\frac{1}{2}}(i,j) = H_y^{n-\frac{1}{2}}(i,j) - \frac{\Delta t}{\mu_{ij}\Delta x} [E_z^n(i+1,j) - E_z^n(i,j)] \quad (1.97b)$$

$$\begin{aligned} E_z^{n+1}(i,j) = E_z^n(i,j) &+ \frac{\Delta t}{\varepsilon_{ij}\Delta x} \left[H_y^{n+\frac{1}{2}}(i+1,j) - H_y^{n+\frac{1}{2}}(i,j) \right] + \\ &- \frac{\Delta t}{\varepsilon_{ij}\Delta y} \left[H_x^{n+\frac{1}{2}}(i,j+1) - H_x^{n+\frac{1}{2}}(i,j) \right] - \frac{\sigma_{ij}\Delta t}{\varepsilon_{ij}} E_z^{n+\frac{1}{2}}(i,j) \end{aligned} \quad (1.97c)$$

where ε_{ij} , μ_{ij} and σ_{ij} correspond to the permittivity, permeability, and conductivity of each cell in the mesh.

Because the FDTD method is a time-domain technique, the time iteration has to conform to causality principles implying that the progression from one lattice node to the next, in any direction, does not exceed the speed of light. This constraint depends on the cell size, reading

$$\Delta t < \frac{1}{v\sqrt{(1/\Delta x)^2 + (1/\Delta y)^2}} \quad (1.98)$$

where v is the speed of light in the medium.

1.6.5 Lumerical: high-performance photonic simulation software

The optical response of the nanostructures used throughout the experiments – later described in this work – was simulated by the “FDTD solutions” tool implemented in Lumerical software that solves the Maxwell’s equations (1.1) via the FDTD method within a Mie problem-like framework. To this aim, a linearly polarized EM radiation traveling along the z direction was used to investigate the system. Photodetectors (PDs) conveniently positioned in the workspace could measure the intensity of the EM field over time. A PD – located on the opposite side of the workspace respect to the light source – was dedicated to measure the transmission spectrum of the nanostructure. A schematic representation of the simulation workspace is shown in Figure 1.22.

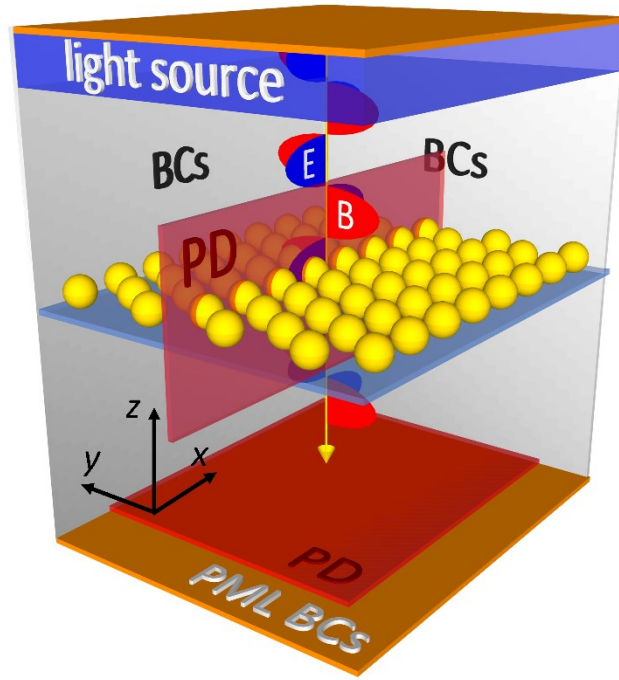


Figure 1.22. Schematic representation of the simulation workspace consisting of light source, plasmonic nanostructure, dielectric substrate, surrounding medium (not depicted in the sketch), photodetectors, and appropriate boundary conditions (BCs).

As it concerns the boundary conditions (BCs), symmetric (anti-symmetric) BCs – acting as mirrors for the electric (magnetic) field and anti-mirrors for the magnetic (electric) field – were set along x and y direction for geometries exhibiting one or more symmetry planes to extend the plasmonic response over an infinite x - y plane while reducing the simulation time by a factor 8 without worsening the accuracy of the results. Bloch BCs were used only for polarization studies in order to compensate the phase shift arising when an EM disturbance with a non-zero angle should be re-injected at the opposite side of the workspace. Perfect matched layer BCs set along z direction assured perfect absorption of the EM waves backscattered through the plane containing the light source and incident upon the opposite side of the workspace.⁶⁴ Eventually, the workspace was discretized over a spatial mesh dense enough to warrant high accuracy of the results while keeping reasonable the simulation time.

Chapter 2. Optical biosensing

2.1 Nanoparticle-based sensors

Colorimetric detection based on metal nanoparticles takes advantage of the colour change occurring in a colloidal suspension as a result of both changes in the refractive index of the surrounding environment and plasmon coupling among the nanoparticles.^{50,65–67}

Since the LSPR wavelength is approximately linear with changes in refractive index of the surrounding medium over small ranges of n (at optical frequencies),⁵⁰ the refractive index sensitivity S of a particular nanoparticle type is usually reported in nanometers of peak shift per refractive index unit (nm/RIU).

$$S = \frac{d\lambda_{\text{LSPR}}}{dn} \quad (2.1)$$

Moreover, the refractive index sensitivity can be expressed in terms of resonance wavelength by introducing the resonance condition, which determines the real part of the dielectric function at resonance $\varepsilon'(\lambda_{\text{LSPR}})$ for a given particle structure and refractive index n , and the wavelength dependence on the dielectric function, which determines λ_{LSPR} given $\varepsilon'(\lambda_{\text{LSPR}})$.⁶⁶

$$S = \frac{d\varepsilon'(\lambda_{\text{LSPR}})}{dn} / \left(\frac{d\varepsilon'(\lambda)}{d\lambda} \right)_{\lambda_{\text{LSPR}}} \quad (2.2)$$

Using a Drude-like model, the real part of the dielectric function (1.18b) varies nearly linearly with wavelength and can be approximated as follows⁶⁶

$$\varepsilon' = m\lambda + \varepsilon_0 \quad (2.3)$$

where $m \equiv d\varepsilon'(\lambda)/d\lambda$ is the slope. By inserting the linear parametrization (2.3) into Equation (2.2), it results

$$\frac{d\lambda_{\text{LSPR}}}{dn} = \frac{1}{m} \frac{d\varepsilon'(\lambda_{\text{LSPR}})}{dn} \quad (2.4)$$

For spheroidal particles much smaller than the wavelength of the light, the polarizability can be approximated by the quasistatic polarizability (1.71a). At wavelengths whereby the imaginary part of the dielectric function (1.18c) is slowly varying, the resonance occurs at poles of (1.71a), yielding

$$\varepsilon'(\lambda_{\text{LSPR}}) = -2\chi n^2 \quad (2.5a)$$

$$\chi = \frac{1}{2} \left(\frac{1-L}{L} \right) \quad (2.5b)$$

where χ is a shape-dependent parameter related to the depolarization factor L ($\chi = 1$ for a sphere and $\chi > 1$ for non-spherical shapes). Therefore, the resonance condition influences the sensitivity of the peak wavelength to the refractive index of the surrounding medium through its derivative with respect to n . Replacing Equation (2.5a) into (2.4), and considering the linear parametrization (2.3), the refractive index sensitivity of the plasmon peak wavelength results⁶⁶

$$\frac{d\lambda_{\text{LSPR}}}{dn} = \frac{2}{n} \left(\lambda_{\text{LSPR}} + \frac{\varepsilon_0}{m} \right) \quad (2.6)$$

Larger nanoparticles tend to have higher sensitivities, but their peaks are broadened by multipolar excitations and radiative damping.⁵⁰ In order to characterize the nanoparticle sensing capabilities, the figure of merit (FOM) is introduced

$$\text{FOM} = \frac{S}{\Delta\lambda} \quad (2.7)$$

where $\Delta\lambda$ is the resonance line width. Because it is difficult to define a consistent LSPR line width for more complex plasmonic nanostructures, a more general figure of merit FOM^* can be defined in terms of relative intensity change dI/I that occurs at a given wavelength λ_0 upon a small change dn to the local refractive index and does not include the line width.⁵⁰ Thus, sensors based on changes in intensity and those based on peak shifts can be directly compared through

$$\text{FOM}^* = \frac{dI/dn}{I} \Big|_{\text{max}} = \frac{S}{I} \frac{dI}{d\lambda} \Big|_{\text{max}} \quad (2.8)$$

The LSPR shift occurring as a consequence of the environmental changes allows nanoparticles to be used for both bulk refractive index sensing and molecular sensing. In the latter case, the change to

the particle dielectric environment is confined to a nanoscale volume around the nanoparticle due to the rapidly decay of LSPR with the distance from the surface.^{68–70} In case of molecular sensing, the figure of merit FOM_{mol} is defined as the maximum number of bound molecules on the nanoparticles (or dynamic range, DR) divided by the minimum number of detectable molecules (or molecular detection limit, MDL). The MDL is calculated as⁵⁰

$$MDL = \frac{V_S \sqrt{U_{system}^2 + U_{fit}^2}}{V_A \Delta RI e^{-2r/l_d} 3S_0} \quad (2.9)$$

where V_S is the sensing volume, V_A is the analyte volume, ΔRI is the refractive index difference between the analyte and the surrounding medium, U_{system} is the uncertainty in the physical detection of the LSPR peak, U_{fit} is the uncertainty in the fitting of the LSPR peak, S_0 is the bulk refractive index sensitivity, r is the distance of the analyte from the nanoparticle surface, and l_d is the decay length of the electric field from the particle surface. Figure 2.1 shows an illustration of the geometric parameters.

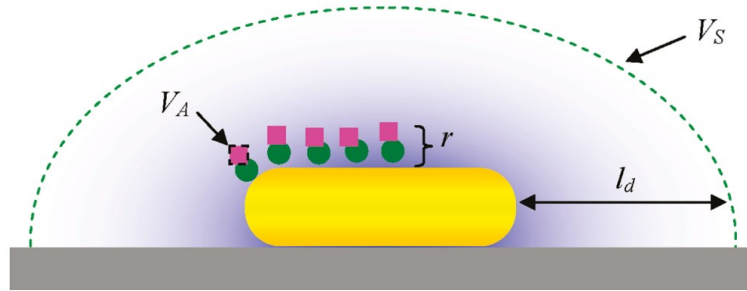


Figure 2.1. Schematic representation of the geometrical parameters in molecular sensing (from Ref. ⁵⁰).

2.1.1 Effect of particle size, shape, and material.

For metal nanoparticles of a given shape and material composition, the LSPR properties strongly depend on the particle size. According to Mie theory, for the smallest particles, LSPR extinction is dominated by absorption, and as particle size increases, scattering takes over. For gold nanospheres, the LSPR wavelength can be tuned over 60 nm by varying the particle size in the range 10-100 nm,⁷¹ exhibiting transition in their optical behaviour at ~80 nm in diameter.⁷² The plasmon resonance line width also varies with particle size due to the occurrence of interband transitions and higher-order plasmon modes, which contribute to increased line width for small and larger particles, respectively.⁷¹ In case of spheroidal nanoparticles, longitudinal and transverse modes take place giving rise to

different LSPR resonances. Generally, elongated nanoparticles exhibit higher sensitivity as the aspect ratio increases. For example, the sensitivity of gold nanorods with radius of 10 nm increases from 157 to 497 nm/RIU for aspect ratio increasing from 1.0 to 3.4,⁶⁷ while for gold bipyramids the sensitivity increases from 150 to 540 nm/RIU for aspect ratio increasing from 1.5 to 4.7.⁷³

As it concerns the dependence of LSPR sensitivity on the nanoparticle shape, an analytical description cannot be retrieved for non-spheroidal particles, but it has been demonstrated experimentally and in electrodynamic simulations⁶⁶ that particles with sharp tips or cavities produce much higher refractive index sensitivities than that predicted by considering only their aspect ratio.⁷⁴ In fact, silver nanotriangles show a higher sensitivity (350 nm/RIU) than spheres (160 nm/RIU),⁷⁵ whereas gold nanoshells have a much higher sensitivity (409 nm/RIU) as compared to the sphere (60 nm/RIU).⁷⁶

It is worth to distinguish whether the varying refractive index sensitivities are due to the varying plasmon resonance wavelength of the particles, or if there are intrinsic effects of the particle shape. As seen in Figure 2.2, theoretical predictions of refractive index sensitivity for hollow nanoshells, nanodisks, and cylinders lie on the same line thereby implying that the intrinsic shape effects are much smaller than the plasmon resonance effect.⁶⁶ However, for nanoshells with dielectric core the slope decreases and the linearity is worsening as the particle size increases as compared to that of solid metal nanoparticles due to the plasmon damping effect of the dielectric material.⁶⁶

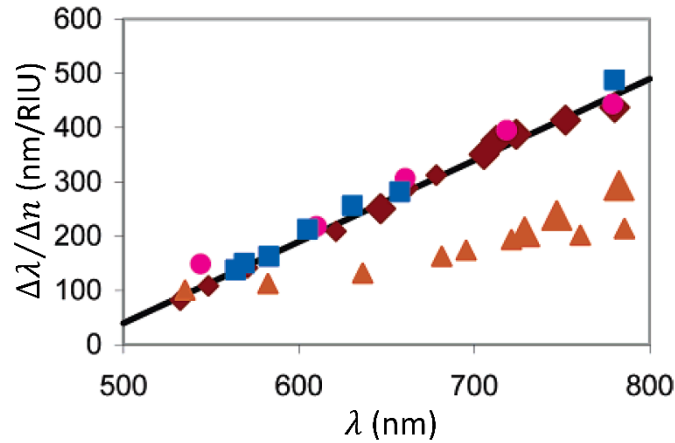


Figure 2.2. Theoretical predictions of the refractive index sensitivity for hollow nanoshells (brown diamonds, larger diamonds showing larger hollow nanoshells), dielectric-core nanoshells (orange triangles, larger triangles showing larger particles, the refractive index of the core is 2.332), nanodisks (blue squares), and nanocylinders (pink circles) of varying plasmon resonance wavelength. The solid black line shows the analytical fit of Equation (2.6) for gold (from Ref. ⁶⁶).

Furthermore, the LSPR sensitivity also exhibits a strong dependence on the particle material. In fact, by considering spheres of 50-60 nm in diameter, the refractive index sensitivity is 60 nm/RIU at $\lambda_{\text{LSPR}} = 530$ nm for gold⁷⁶ and 160 nm/RIU at $\lambda_{\text{LSPR}} = 435$ nm for silver.⁷⁵ Analogously, for nanocubes 30-

50 nm in size, the refractive index sensitivity is 83 nm/RIU at $\lambda_{\text{LSPR}} = 538$ nm for gold⁷³ and 146 nm/RIU at $\lambda_{\text{LSPR}} = 510$ nm for silver.⁷⁷ Although silver has sharper resonances and higher refractive index sensitivity, gold is generally preferred to other metals to design nanoparticle for biosensing applications due to its surface chemistry, resistance to oxidation and biocompatibility.⁷⁸

2.1.2 Surface biofunctionalization

A key issue to address when metal nanoparticles are used in biosensing is the biofunctionalization of the active surface since it deeply affects both the sensitivity and specificity.²⁵ Antibodies (Abs) are the prime candidates as bioreceptors thanks to their inherent specificity, versatility, and reliability. However, due to their moderate long-time stability and the need to immobilize them both with the right orientation and high surface density, the accomplishment of a robust and effective Abs surface functionalization is still an open issue.⁷⁹ Several methods have been explored to promote the attachment of Abs onto the gold nanoparticle (AuNP) surface in upright orientation including nanoparticle coating with thiolated polyethylene glycol (PEG-SH) that allows the Abs to covalently interact with the carboxyl terminated PEG, and self-assembled monolayer (SAM) of 11-mercaptoundecanoic acid (MUA) or 3,3'-dithiobis(sulfosuccinimidyl propionate) (DTSSP) as mediators to create thiol-gold link for protein A/G as antibody anchors.²⁵

In this respect, the well-established photochemical immobilization technique (PIT) is a simple, fast and effective strategy to tether Abs directly onto gold surfaces with one fragment antigen-binding (Fab) exposed to the surrounding environment.^{80–82} Such a technique consists of UV irradiation of Abs that produces the selective photoreduction of the disulfide bridge in specific cysteine-cysteine/tryptophan (Cys-Cys/Trp) triads,⁸³ which are a typical structural feature of the immunoglobulin G (IgG).⁸⁴ The UV excitation of the Trp residue leads to the generation of solvated electrons that are captured by the nearby disulphide bridge resulting in its destabilization and subsequent breakage of the Cys-Cys bond. The breakage of such Cys-Cys bonds in both Ab Fab fragments produces four free thiol groups (Figure 2.3a), two of which are able to interact with the proximal gold surface giving rise to a covalent Ab tether. Functionalization by PIT assures both close-packing and control over the orientation of the immobilized Abs, with one of their binding sites exposed to the surrounding environment (Figure 2.3b).^{82,85}

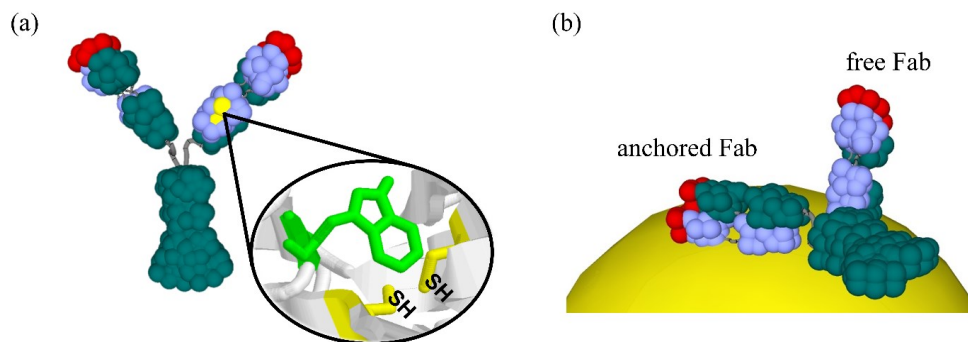


Figure 2.3. (a) UV irradiation of Abs leads to the selective production of four thiol groups (two of them are not visible in the figure). (b) The opposite position of the thiols with respect to the plane containing the Fabs allows the Abs to be immobilized with one of their binding sites exposed to the surrounding environment.

This strategy has been demonstrated to enhance the antigen detection efficiency of immunosensors based on quartz-crystal microbalances⁸⁶ as well as on screen-printed electrodes for electrochemical sensing.⁸⁷ Moreover, PIT was also successfully applied to functionalize AuNPs in colloidal solutions to provide either a ballasting tool for mechanical platforms⁸⁸ or colorimetric transducers.^{89,90} In the latter case, since citrate-stabilized AuNPs might undergo irreversible aggregation during functionalization process with thiolate ligands, several strategies have been investigated to conquer this problem,⁹¹ including surfactant as capping agent⁹² or thioctic acid as an intermediate via a two-step functionalization.⁹³ However, the requirement for high dilution makes large scale production challenging.⁹¹ A simple approach to prevent the citrate-induced aggregation during the functionalization relies on the removal of citrate capping via some washing and centrifuge steps. Once the citrate concentration is reduced (lower than 10%),⁹⁰ the functionalization can take place without inducing significant AuNP aggregation.

A promising alternative class of bioreceptors is represented by aptamers (Apts) consisting of short nucleic acid sequences – synthesized *in vitro* through molecular evolution approaches – capable to bind targets with extremely high specificity.⁹⁴ One particular advantage of Apts is their consistent negative charge in the phosphoribose backbone which likely enables a more homogeneous upright orientation surface relative to Abs. Despite several research efforts showing great results in terms of reliability and specificity,^{95,96} aptamers have not yet been routinely adopted. Reasons for this may include a lack of simple methods for immobilization and low awareness of Apts relative to Abs in the biosensing field.

2.1.3 Gold nanoparticle aggregation-based colorimetric biosensors

A colloidal solution of subwavelength AuNPs exhibits a wine-red colour with an LSPR wavelength lying in the range 520-530 nm.⁹⁷ The aggregation of AuNPs results in a large red-shift of the LSPR peak that leads to a colour change from red to blue.⁶⁵ Such an unique feature has been exploited to develop aggregation-based colorimetric assays for detecting proteins,⁹⁰ small molecules,⁸⁹ inorganic ions,⁹⁸ oligonucleotides,⁹⁹ and viruses.¹⁰⁰

Generally, colorimetric assays rely upon two different detection methods: labelled and label-free. The labelled method directly attaches ligands – usually bioreceptors such as Abs and Apts – onto AuNPs through chemical bonds. Ligand-modified AuNPs exhibit higher steric hindrance, stronger interparticle repulsion, and are more stable at high ionic strength conditions than bare AuNPs.³⁴

The analyte detection in label-based colorimetric approaches can be achieved by cross-linking, non-cross-linking, or destabilization-induced aggregation. In cross-linking method, AuNP aggregation is induced by the controlled assembly of ligand-functionalized AuNPs through intermolecular bonds between ligands and analytes, which overpower the interparticle electrostatic repulsion (Figure 2.4). In such a case, the analytes can act as both linkers among ligand-functionalized AuNPs inducing their aggregation (Figure 2.4b) and anchoring sites wherein the LSPR shift arises from the close-packing of ligand-functionalized AuNPs around the analyte (Figure 2.4c).

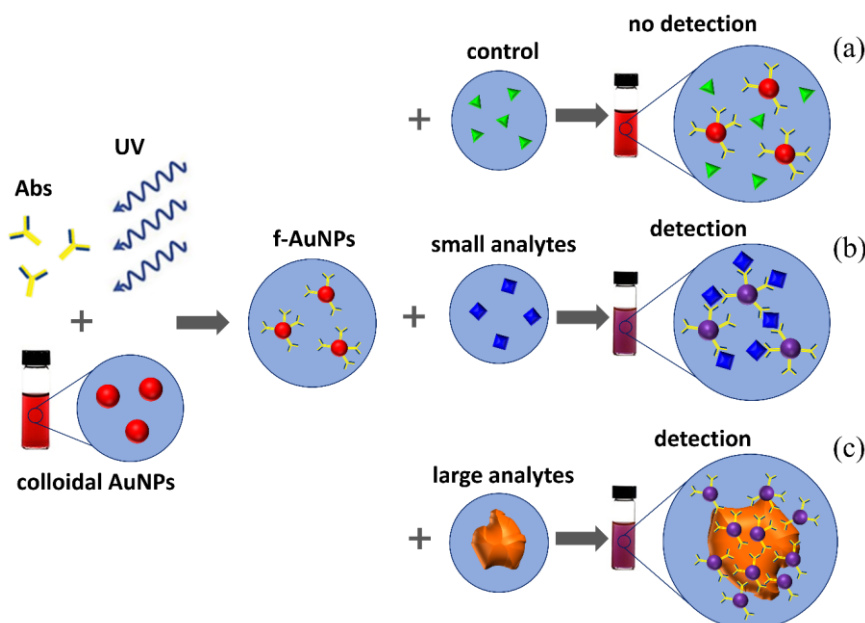


Figure 2.4. Detection scheme of a colorimetric immunosensor based on a colloidal solution of PIT-functionalized AuNPs with Abs (f-AuNPs). (a) No optical change is measured if the analytes are not recognised by f-AuNPs. (b) Small analytes act as linkers due to multiple binding sites allowing the f-AuNPs to aggregate. (c) Large analytes are surrounded by f-AuNPs promoting their plasmon coupling.

Although cross-linking aggregation method offers a convenient colorimetric assay, its sensitivity is usually limited to the nanomolar levels due to the lack of feasible amplification steps while its dynamic range spans only few decades of the analyte concentration due to the occurrence of the hook effect – i.e. the saturation of ligand binding sites that prevents the AuNP aggregation at higher analyte concentrations.^{34,50}

In non-cross-linking method, the aggregation of ligand-functionalized AuNPs is induced by increasing the ionic strength of the aqueous solution. It has been demonstrated that only specific ligands allow nanoparticles to aggregate in a medium of high ionic strength because the interparticle electrostatic and steric repulsion between ligand-modified AuNPs can hinder their aggregation (Figure 2.5).^{101,102}

Structure of DNA on Surface				
	Single-stranded	Fully Matched	Mismatched	Overhang
AuNP	Dispersion	Aggregation	Dispersion	Dispersion

Figure 2.5. Different colloidal behaviours of DNA-functionalized AuNPs in a medium of high ionic strength. Double-pointed arrows for terminal mismatch and overhang (shown in red) denote the fraying motion of unpaired mononucleotides (from Ref. ¹⁰²)

The destabilization-induced aggregation method relies on reducing the electrosteric repulsion between functionalized AuNPs by cleaving a part of the ligand (Figure 2.6). Such a method is widely used to monitoring the enzymatic activity.¹⁰³

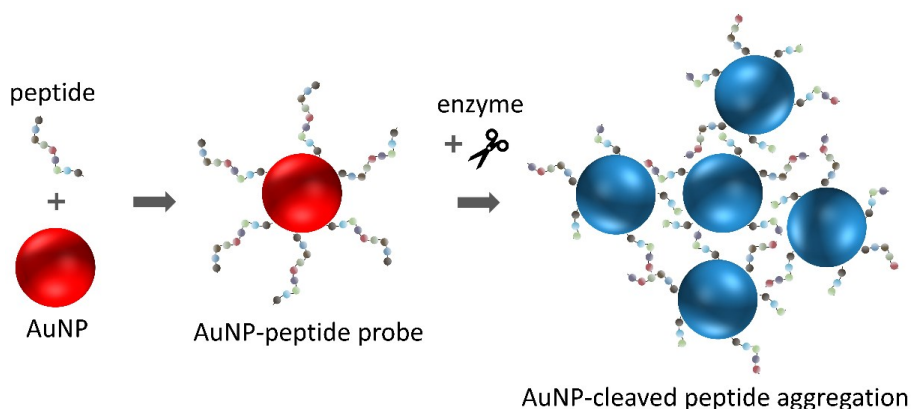


Figure 2.6. Schematic representation of destabilization-induced aggregation method for measuring enzymatic activity. The aggregation of peptide-capped AuNPs is induced by cleaving the capping peptides thereby reducing the electrosteric stabilization.

Unlike the label-based detection methods, the label-free colorimetric approaches are mostly regulated by electrostatic stabilization. The analyte-triggered aggregation for chemical and biological sensing applications relies on the affinity of analytes – such as electrostatic or hydrogen-bonding interaction – toward unmodified AuNPs. In this case, a repulsive electric layer can be generated from the surface charges of AuNPs to stabilize the colloids. Thus, the neutralization of the surface charges results in the formation of unstable AuNPs promoting their aggregation.¹⁰⁴

Aptamers are widely used in label-free colorimetric assays since the adsorption of negatively charged Apts onto the AuNP surface leads to well-dispersed negatively charged Apt-capped AuNPs in media of moderately high ionic strength. The presence of analyte promotes the detachment of the Apts from the AuNP surface entailing salt-induced aggregation (Figure 2.7).¹⁰⁵

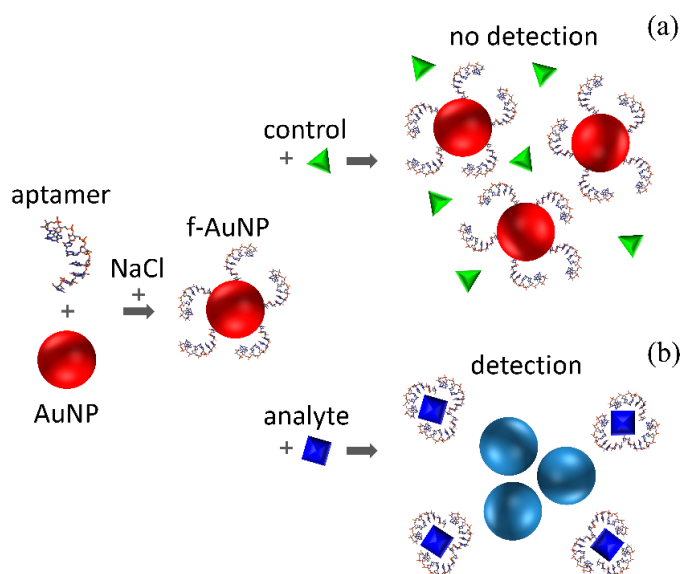


Figure 2.7. Schematic representation of analyte detection through a label-free colorimetric aptasensors. The functionalization of AuNPs with aptamers is realized in a medium of high ionic strength. (a) Aptamer capping prevents AuNP salt-induced aggregation if the analytes are not recognised by f-AuNPs. (b) The presence of analytes of interest causes the detachment of aptamers from the nanoparticle surface leading to the salt-induced aggregation of bare AuNPs.

2.2 Realization of AuNP-based colorimetric immunosensors

2.2.1 Synthesis of gold nanoparticles

A large variety of methods have been developed in the last few decades for synthesizing AuNPs by controlling size^{106,107} and shape.¹⁰⁸ A method widely employed to prepare dilute solutions of stable spherical AuNPs with diameter of 10-20 nm relying on the chemical reduction of tetrachloroauric

acid (HAuCl₄) through citric acid in boiling water, in which the citrate acts as both reducing and stabilizing agent.^{109,110} In fact, the dissolution of HAuCl₄ in water gives rise to ions Au³⁺ that reduce to gold atoms Au⁰ in presence of reducing agents. In case of sodium citrate as reducing agent, the reaction equation in aqueous solution results¹¹¹



Gold atoms – continuously produced until the depletion of ions Au³⁺ – bind the preexisting gold seeds to form gold nuclei. During the particle nucleation, the negatively charged ion citrate are adsorbed onto the gold surface preventing nanoparticle aggregation through electrostatic repulsion. In case of supersaturated solution, the excess of gold atoms precipitates yielding the formation of sub-nanometric particles.¹¹¹ Figure 2.8 shows a schematic representation of the AuNP synthesis through chemical reduction of HAuCl₄.

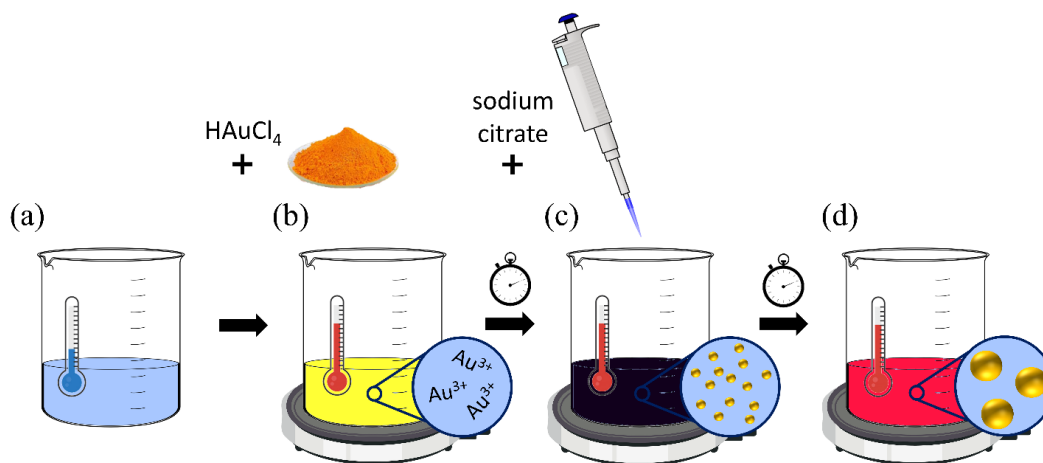


Figure 2.8. Schematic representation of AuNP synthesis through chemical reduction of HAuCl₄. (a) Ultrapure water as solvent prevents salt-induced aggregation during the AuNP synthesis. (b) Dissolution of the gold precursor and heating of the solution under vigorous stirring. (c) Addition of sodium citrate during boiling induces the formation of gold seeds. The colour of the solution appears blackish. (d) The colour of the solution moves to pink-red due to the particle nucleation.

2.2.2 Optical and morphological characterization of bare and functionalized AuNPs

Herein, two different synthesis methods were followed to produce colloidal solutions of AuNPs with different size for tailoring their optical and morphological features to the optimization of the analyte detection. Gold nanoparticles of 20 nm diameter were synthesized by chemical reduction of HAuCl₄ as described in Appendix A.1.¹⁰⁹ Figure 2.9a shows the extinction spectrum of bare AuNPs, in which the LSPR peak at 523 nm is clearly visible as expected for gold nanospheres of 20 nm diameter in water.⁹⁷ Size and shape of AuNPs were also characterized by transmission electron microscopy

(TEM) and dynamic light scattering (DLS) measurements, which highlighted the presence of quite regular spherical monodisperse nanoparticles with a diameter of approximately 20 nm (Figure 2.9b and c, respectively). Figure 2.9d shows the ζ -potential distribution peaked at (-30 ± 1) mV conveying the high stability delivered by the negatively charged capping around the citrate-stabilized AuNPs corroborating the mono-dispersion of the synthesized colloidal solution.

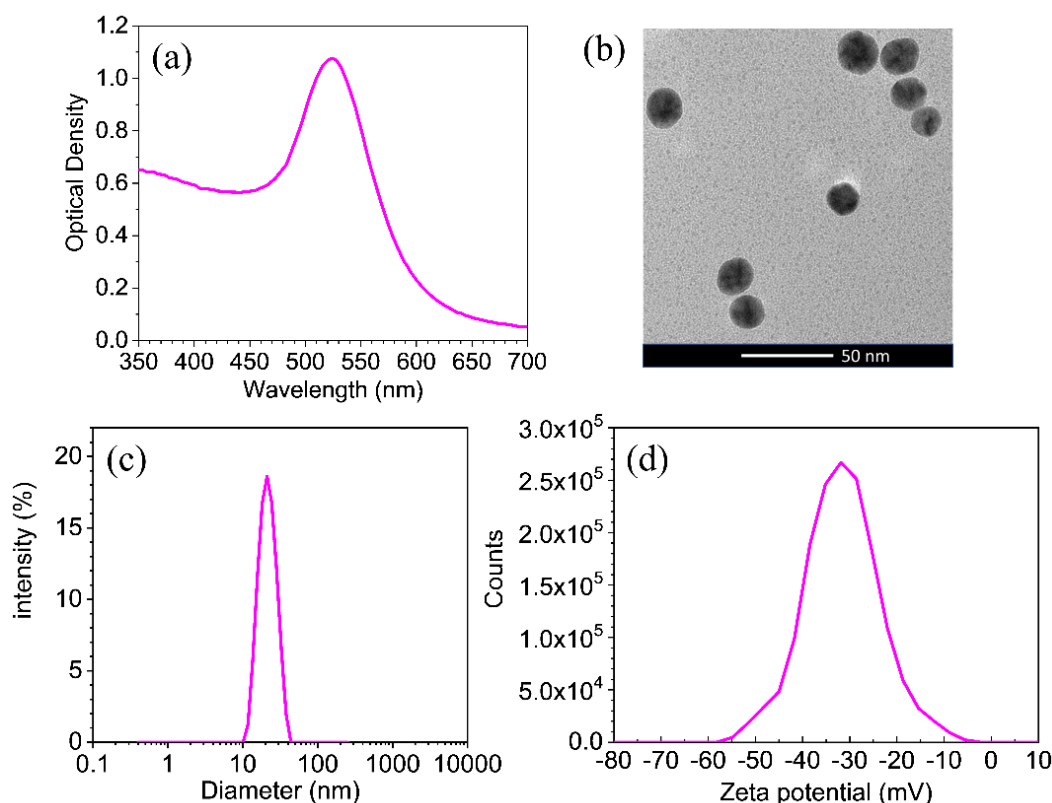


Figure 2.9. (a) Extinction spectrum of naked AuNP colloidal solution (b) TEM image of naked AuNPs. (c) Intensity-size distribution of naked AuNPs. (d) Zeta potential distribution of naked AuNPs.

The functionalization of the AuNPs was achieved by PIT (see Appendix D.2) that entails a red-shift of the LSPR peak of 3.8 nm due to the change of the refractive index surrounding the nanoparticles (Figure 2.10a). The lack of any optical change in the extinction spectrum after the centrifugation and blocking steps (dashed blue line in Figure 2.10a) corroborates the close-packing arrangement of Abs onto the AuNP surface as a consequence of functionalization through PIT. Figure 2.10b shows the kinetic study aimed at finding out the optimal Ab concentration to functionalize the AuNPs. The LSPR peak red-shifted as the Ab concentration increased up to 10 μ g/mL corresponding to a maximum red-shift of 3.8 nm. For larger amounts of Abs, AuNP surface was fully covered and no change in LSPR wavelength was detectable.

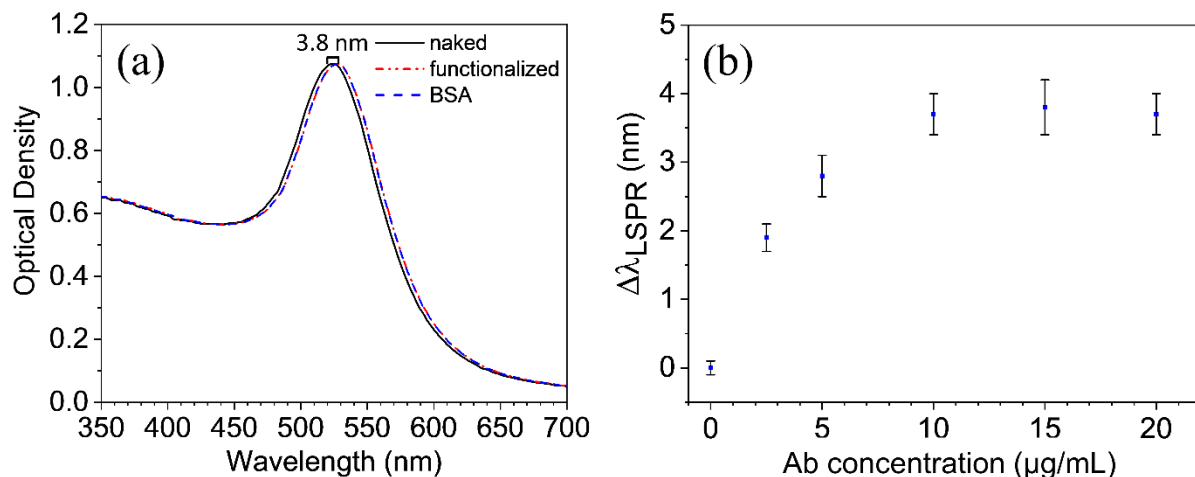


Figure 2.10. (a) Extinction spectra of naked (black continuous line), functionalized (dashed-dotted red line) and blocked (dashed blue line) AuNPs. (b) Shift of the LSPR peak as a function of Ab concentration.

Larger AuNPs of 35 nm diameter were synthesized by modifying the above-mentioned protocol (see Appendix A.2)¹¹² and functionalized through PIT (see Appendix D.2). The colloidal solution was firstly characterized by UV-Vis spectroscopy revealing a narrow LSPR peak at 528.5 nm for bare AuNPs – as expected for gold nanospheres of 35 nm diameter in water⁹⁷ – and 531.4 nm for functionalized AuNPs (Figure 2.11a). The functionalization gave rise to a dielectric shell surrounding the AuNPs entailing a red-shift of the LSPR of ~ 3 nm (see Figure E.1 for the kinetic study). The DLS measurements provided a hydrodynamic diameter of ~ 36.6 nm for bare AuNPs and ~ 45.3 nm for functionalized AuNPs (Figure 2.11b). Scanning transmission electron microscopy (STEM) images reveal regular spherical monodisperse nanoparticles of approximately 33 nm diameter (Figure 2.11c and d) finding out excellent agreement with the optical characterization.

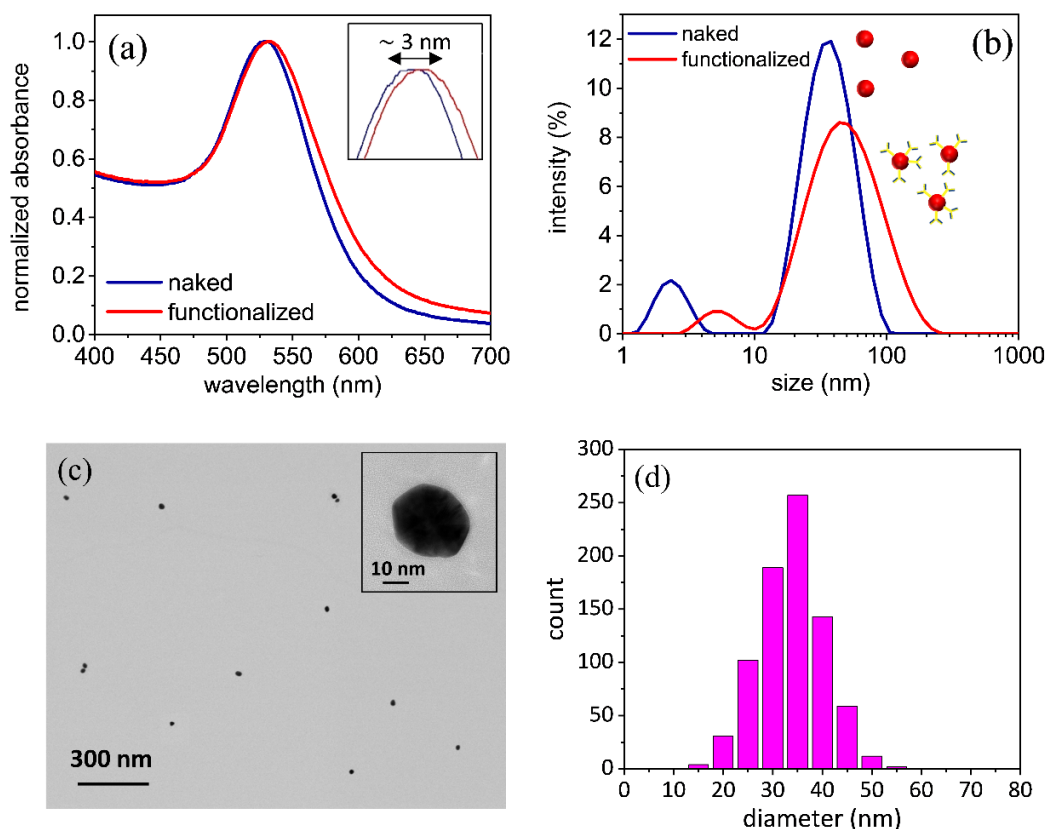


Figure 2.11. (a) Absorbance and (b) intensity-size distribution of bare (blue continuous line) and functionalized (red continuous line) AuNPs. (c) STEM micrograph at low magnification of bare AuNPs, the inset shows a single nanoparticle at high magnification. (d) Bare AuNP diameter distribution resulting from STEM image analysis.

2.3 Detection of 17 β -estradiol in tap water

17 β -estradiol (E2) is an estrogen naturally secreted by the ovaries and involved in several hormonal and carcinogenesis processes in human.^{113,114} Its detection in blood and urine in small concentration is very attractive in medical diagnostics to address menopause symptoms, ovaries and breast cancer, gynecomastia and in pregnancy or infertility treatments. Although many researches in the field of medicine and toxicology deal with estrogens, there is a lack of information about their presence in the environment,^{115,116} a serious issue given their abundant use in dairy livestock industry to enhance cattle growth rates, feed efficiency and to procure lean muscle mass.¹¹⁷ The presence of estrogens in waste waters and agriculture lands can lead to bioaccumulation and biomagnification in the ecosystems;^{118,119} for instance, E2 in low concentration from 0.1 to 1 ng/L may cause estrogen response in male fish.¹¹⁵ It is worth noticing that such a concentration is lower than that usually

detected in the environment,^{120,121} making urgent the need for developing analytical methods and sensors for continuous water monitoring and mapping of the potential contamination points.

In laboratories, estradiol is usually determined by HPLC or LC-MS reaching limits of detection down to 0.03 ng/L.¹²² These methodologies use expensive instrumentation, require trained personnel and spend significant amounts of toxic solvents. A partial alternative is provided by immuno-techniques, like ELISA, currently the main technique for routine E2 detection in real samples (serum or urine). Most of the available ELISA assays provide a large detection range from 10 to 1000 pg/mL,²⁸ but the technique is limited by the assay time (up to 3 hours), the relatively high cost of the kits and a need for a skilled personnel. Thus, reliable, fast, and easy-to-use biosensors are highly desirable as tools for E2 detection at low concentrations in water.

One possible approach relies upon the recognition of estradiol molecules by using electrochemical,^{123–125} optical,^{105,126–129} or chromatographic techniques.¹³⁰ Even though they can reach limits of detection in the fM range (see Table 2.1),¹²³ their current complexity in terms of time consumption, expensive materials and complex realization,¹²³ as well as the occurrence of interference from other analytes commonly present in natural waters, still represent an issue to overcome.¹³¹ In this regard, colorimetric immunosensors based on colloidal solution of functionalized AuNPs (f-AuNPs) are very attractive since they provide a fast and accurate response with a very high sensitivity and easiness-of-use. Moreover, although the non-monotonic LSPR shift measured at E2 concentrations larger than 74 pM makes the proposed biosensor not useful for detection purposes (except for carrying out serial dilutions), the measurable signal up to 100 nM is still suitable if an alert system is to be conceived.

Table 2.1. Comparison among biosensors for the E2 detection

Transducer	Bioreceptor	Method	LOD	Detection range	Ref.
Rhodamine B fluorescence quenched by AuNPs	aptamers	fluorescence	0.48 nM	0.48-200 nM	126
FRET-based turn-on fluorescence	aptamers	fluorescence	0.35 nM	0.35-35000 nM	127
Colloidal solution of AuNPs	aptamers	colorimetry	0.367 nM	0.367-367000 nM	105
TiO ₂ -BiVO ₄ heterostructure	aptamers	photoelectrochemistry	22 fM	0.1-250 pM	123
Electrochemical sensor using split aptamers	aptamers	electrochemistry	0.5 pM	1.5-7000 pM	124

Nanostructured magnetic molecularly imprinted polymers	MIP	electrochemistry	20 nM	50-10 ⁴ nM	125
Indirect probe based immunochromatography assay	antibody	chromatography	0.7 nM	0.7-18 nM	130
Carboxymethylated dextran-coated gold sensor chip	antibody	SPR	7 nM	0.5-20 nM	128
11-MUA/E2-BSA conjugate on gold sensor chip	antibody	SPR	3.6 pM	36-3.6·10 ⁶ pM	129
Colloidal solution of AuNPs	antibody	colorimetry	11 pM	11-74 pM (quantitative) 74-10 ⁵ pM (qualitative)	89

2.3.1 Dose-response curve

The proposed immunosensor – consisting of a colloidal solution of f-AuNPs that aggregate in presence of E2 (the detection scheme is shown in Figure 2.4) – is able to detect E2 at picomolar level in tap water without any sample preconcentration step. Since the tap water contains salts that would induce non-specific AuNP aggregation, it was important to keep as low as possible the volume of the sample to be analysed. A volume of 20 µL tap water diluted in 1 mL of ultrapure water with f-AuNPs, provided a good compromise between a negligible red-shift of the LSPR peak and a large volume that would allow large sensitivity and small error. Figure 2.12b shows the absorption spectra of samples at different E2 concentrations (absorption spectra measured at all the concentrations used throughout the experiments are shown in Figure E.2a). The LSPR peak exhibits a measurable red-shift for concentrations higher than ~3 pg/mL with a marked effect in the range 8-12 pg/mL. Higher concentrations prevented the complexed AuNPs from forming larger clusters, and hence the red-shift was reduced, the so-called hook effect.¹³² This behaviour was visible even by naked eyes (Figure 2.12a): The colour of the solution moved from pink to purple as the E2 concentration reached 10 pg/mL returning to pink as the concentration was further increased. The possibility to get a qualitative *in situ* response, seen even by naked eyes without any specialized instrumentation, makes the proposed immunosensor practical and easy to use.

The aggregation dynamics was quantitatively evaluated by DLS and STEM. Both techniques confirm that the behaviour of the absorption spectra as a function of the E2 concentration is due to the aggregation of complexed AuNPs. In fact, the hydrodynamic diameter increased from 48.5 nm of the control (0 pg/mL) to a maximum of 162.4 nm at 10 pg/mL E2 concentration, to reduce to 66.3 nm for

larger analyte concentrations (Figure 2.12c and Figure E.2b). Similarly, the STEM images of the solution showed (i) only single nanoparticles for the control, (ii) large aggregates for E2 concentrations in the range 8-12 pg/mL, and (iii) dimers and trimers at higher E2 concentrations (>20 pg/mL) (Figure 2.12d and Figure 2.14).

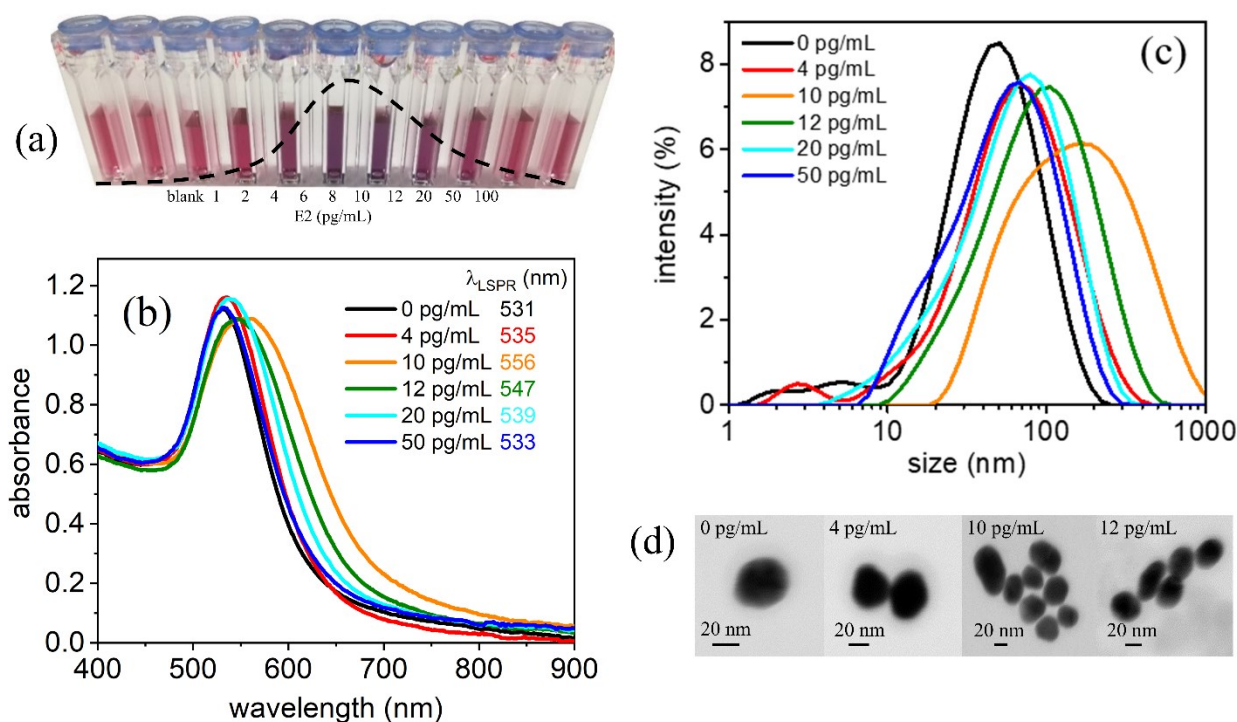


Figure 2.12. (a) Colour change induced by AuNP aggregation. The dashed black line shows qualitatively the behaviour of the colorimetric test in its detection range. The maximum colour change. (b) Absorption spectra, (c) intensity-size distributions, and (d) STEM images measured at different E2 concentration in tap water.

The spectra in Figure 2.12b were fitted by a Gaussian curve around the absorption peak and the LSPR shifts are reported in Figure 2.13 as a function of the E2 concentration in tap water. The concentration that provided the largest red-shift is the so-called hook point, and corresponds to the optimal concentration that ensures the dynamic equilibrium between the largest aggregates of AuNPs and the cluster instability due to electrostatic repulsion and steric hindrance.⁶⁵ For E2 concentrations lower than ~10 pg/mL the analyte was insufficient to yield large AuNP clusters and the LSPR red-shift was only 4-6 nm, thereby suggesting complexed AuNP dimerization⁵⁴ in accordance with DLS and STEM measurements (Figure 2.12c and Figure 2.14, respectively). On the other hand, an excess of E2 molecules leads to the occupation of most of the Ab binding sites thereby hindering the formation of large AuNP aggregates (Figure 2.14).

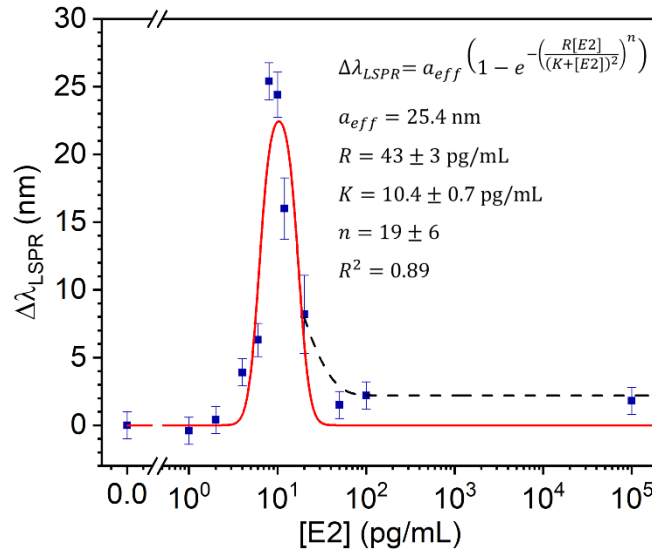


Figure 2.13. Shift of the absorption peak as a function of E2 concentration in tap water (dose-response curve). The dashed black line is included to guide the eye to highlight the presence of a detectable signal even at very high E2 concentration, whereas the red continuous line is the best fit of the experimental data with Equation (2.15), which does not capture the asymptotic behaviour of the dose-response curve.

Even though in our scheme the hook effect arose, it is worth to notice that even at very high E2 concentrations the LSPR shift was still measurable (Figure 2.13). Although the non-monotonic behaviour of the LSPR peak does not allow one to quantify the E2 concentration in this broad range (74-10⁵ pM) without carrying out serial dilutions, this limit is not a real shortcoming if an alert system is considered. Such a nonzero signal beyond the hook point represents an advantageous feature explainable by assuming that the aggregation dynamics consisted of two steps with different temporal dynamics: The first step concerned the interaction between the E2 molecules and f-AuNPs, whereas the second one took place on a longer time scale and was related to the interaction between f-AuNPs whose binding sites were occupied by E2 molecules (E2-f-AuNPs) and f-AuNPs. The initial gentle shaking enhanced the probability that an f-AuNP bound the free E2 molecules within the region where the sample drop was released (~20 μ L), such a region being much smaller than the whole volume (1 mL). In this limited region, the saturation of the Ab binding sites could well be reached, but afterwards the diffusion took place and the aggregation could occur among E2-f-AuNPs and the distanced f-AuNPs (in the whole sample volume) on a much longer time scale.¹³³ Therefore, even if the E2 molecules locally saturated the binding sites, the subsequent diffusion of E2-f-AuNPs ensured the formation of dimers or trimers with f-AuNPs encountered during the diffusion (Figure 2.14).

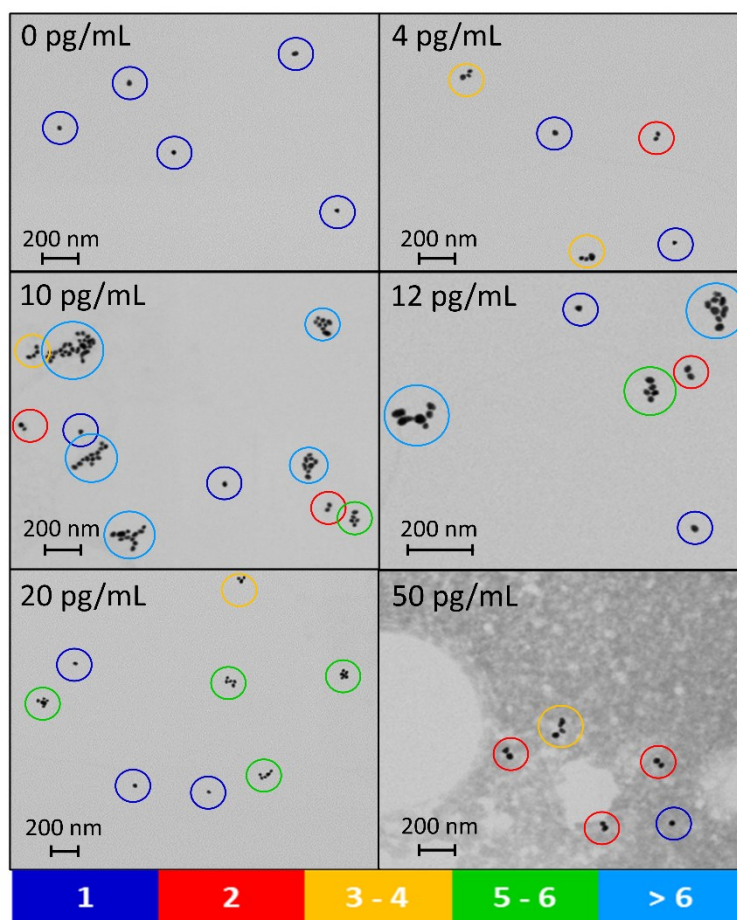


Figure 2.14. STEM images at low magnification acquired at several E2 concentration. The different colours identify the number of AuNPs forming the aggregate contained inside the ring.

2.3.2 Morphological characterization of AuNP aggregates

The average number of AuNPs that form the aggregates was evaluated from STEM images at low magnification (Figure 2.14). The average number was approximately 12 AuNPs for clusters corresponding to 10 pg/mL of E2 concentration. As it concerns the AuNP aggregation, a quantitative analysis of STEM images at high magnification was performed in order to evaluate the interparticle distance due to the presence of both Abs and analyte (Figure 2.15a and b). Such a distance turned out to be approximately 10 nm and is compatible with a dielectric shell thickness of about 5 nm and a negligible size of the analyte. Eventually, aiming at investigating the assumption that the distance among AuNPs was actually due to the Ab functionalization, a quantitative analysis of salt-induced aggregates of non-functionalized AuNPs was performed (Figure 2.15c and d). The vanishingly small interparticle distance in absence of Abs corroborated the assumption that AuNPs shown in Figure 2.15a were surrounded by a 5 nm of protein shell.

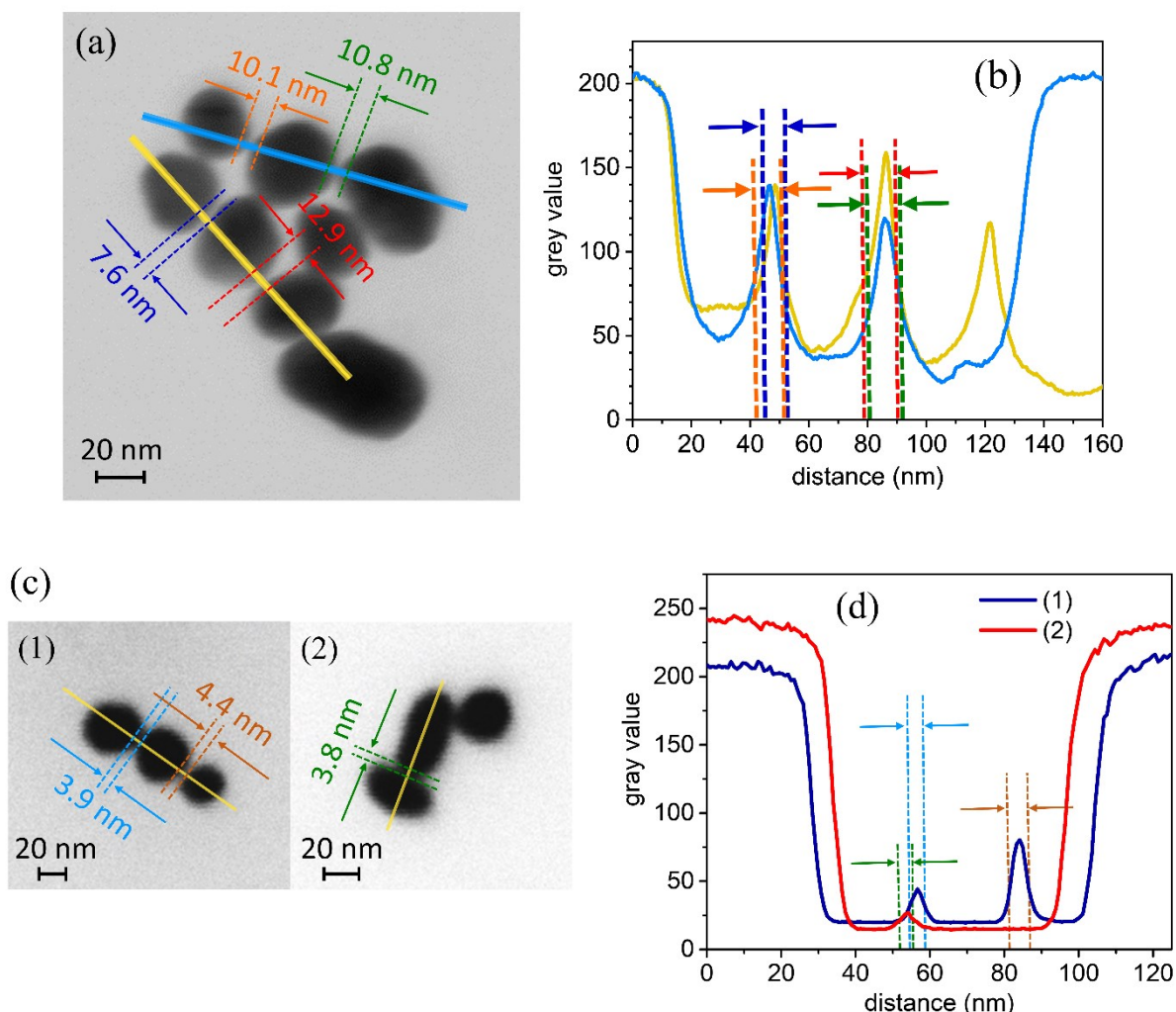


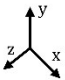
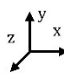
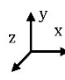
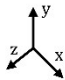






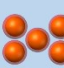
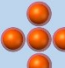


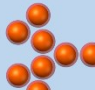
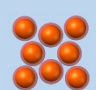


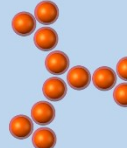
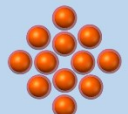

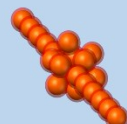
Figure 2.15. Measurement of the interparticle separation from STEM images. Examples of STEM micrographs at high magnification for (a) analyte-induced aggregate of f-AuNPs and (c) salt-induced aggregates of bare AuNPs. In yellow and cyan are highlighted the profiles along which the intensity plots shown in panels (b) and (d) are evaluated, respectively. The interparticle distance was measured by considering the FWHM of the cusps among adjacent intensity wells.

2.3.3 Optical response of AuNP aggregates (FDTD simulations)

A schematic representation of the simulation workspace is shown in Figure 1.22. The light source consisted of a plane wave source with a wavelength range from 400 nm to 700 nm, the embedding medium was water,¹³⁴ AuNPs were modelled as homogeneous gold spheres,⁴⁰ and the Abs anchored to the gold surface were considered as a protein shell around the nanoparticle with a refractive index of 1.42.¹³⁵ The f-AuNPs were arranged in the volume according to the desired geometry. The transmission spectra were acquired by a PD located to the opposite side of the light source with a plot interval of 1 nm. The workspace was discretized over a mesh with 0.5 nm spatial step.

In accordance with the diffusion-limited aggregation (DLA) model, it was reasonable to assume that AuNPs experienced a random walk (Brownian motion) and aggregated exhibiting a quasi-fractal structure.¹³⁶ Although a thoroughly analysis of such complex systems goes beyond the aims of this work, some of them (Table 2.2) were investigated to elucidate the role of the linear dimension against the number of AuNPs.

Table 2.2. Geometry of the AuNP arrays used throughout the numerical simulations. The distinction between asymmetrical and symmetrical 2D configurations refers to any possible symmetry with respect to the system barycentre. The coordinate system reported at the top of each column refers to the below geometries.

number of AuNPs	1D	2D asymmetric	2D symmetric	3D
				
1 (naked)				
1 (functionalized)				
2				
3				
5				
8				
12				
24				

The simulated absorption spectra (Figure 2.16) and the electric field distributions (Table E.1) showed that the optical response was essentially due to the linear branches contained in the structures.¹³⁷ For instance, by considering the electrical field distribution of the 2D asymmetrical geometry for 12 AuNPs (see Table 2.2), the strongest coupling among the nanoparticles is achieved along the polarization direction (x axis) and arises essentially from the two branches made by 6 AuNPs. The

LSPR wavelength for such a configuration (12 AuNPs, 2D asymmetric) is 552 nm (Figure 2.16d) that corresponds to the LSPR of 551 nm for a linear chain of 5 AuNPs aligned with the polarization direction (Figure 2.16b).

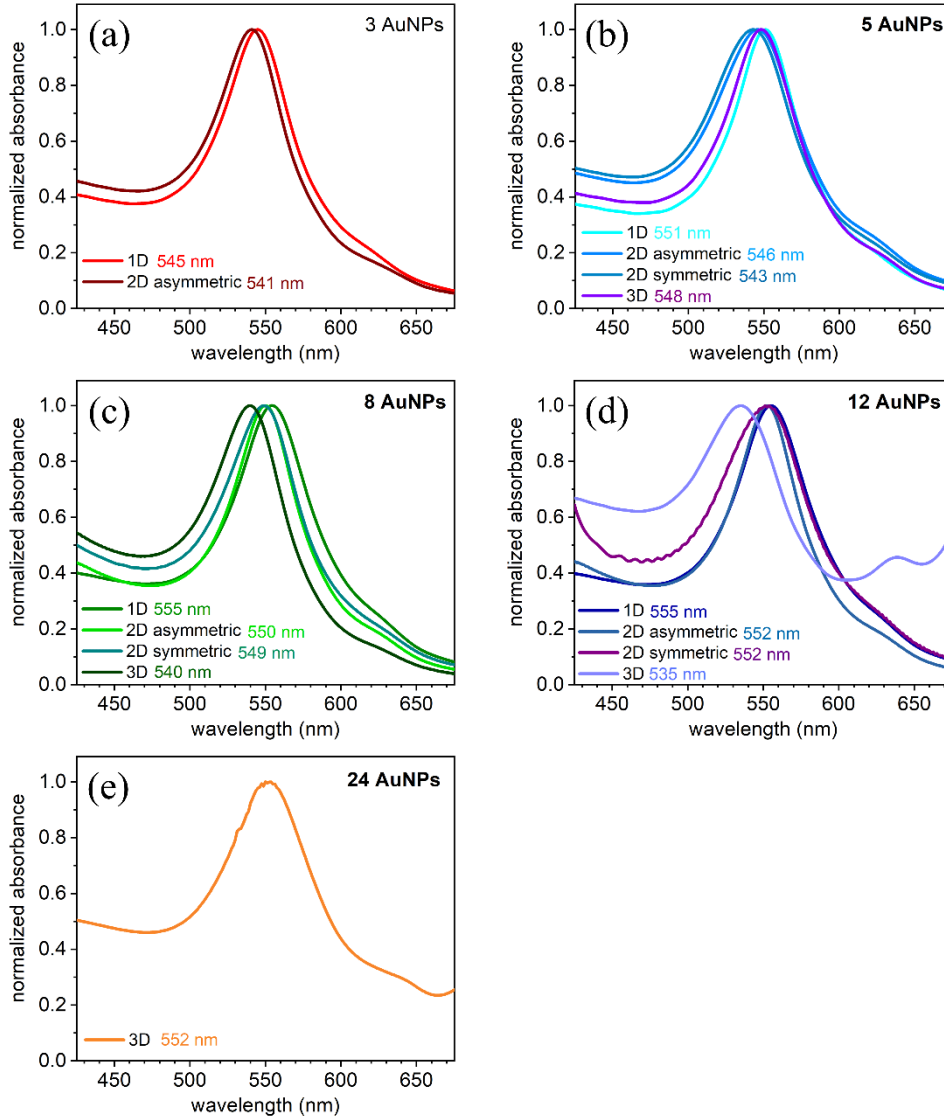


Figure 2.16. Simulated absorption spectra worked out by considering the AuNP array geometries shown in Table 2.2 interacting with x -polarized plane waves.

Since the linear branches dominate the optical response of the clusters,¹³⁸ to capture the essential physics behind the aggregation phenomenon, the plasmonic behaviour of the aggregates was simulated by considering them as linear chains of AuNPs. Thus, the simulated absorption spectra $A(\theta, \lambda, N)$ and the electrical field distribution were worked out by varying the angle θ between the polarization direction of the light and the linear chain from 0° (longitudinal mode) to 90° (transversal mode), and the number N of AuNPs from 1 to 12. An example of such a calculation for a linear chain with 3 AuNPs is shown in Figure 2.17.

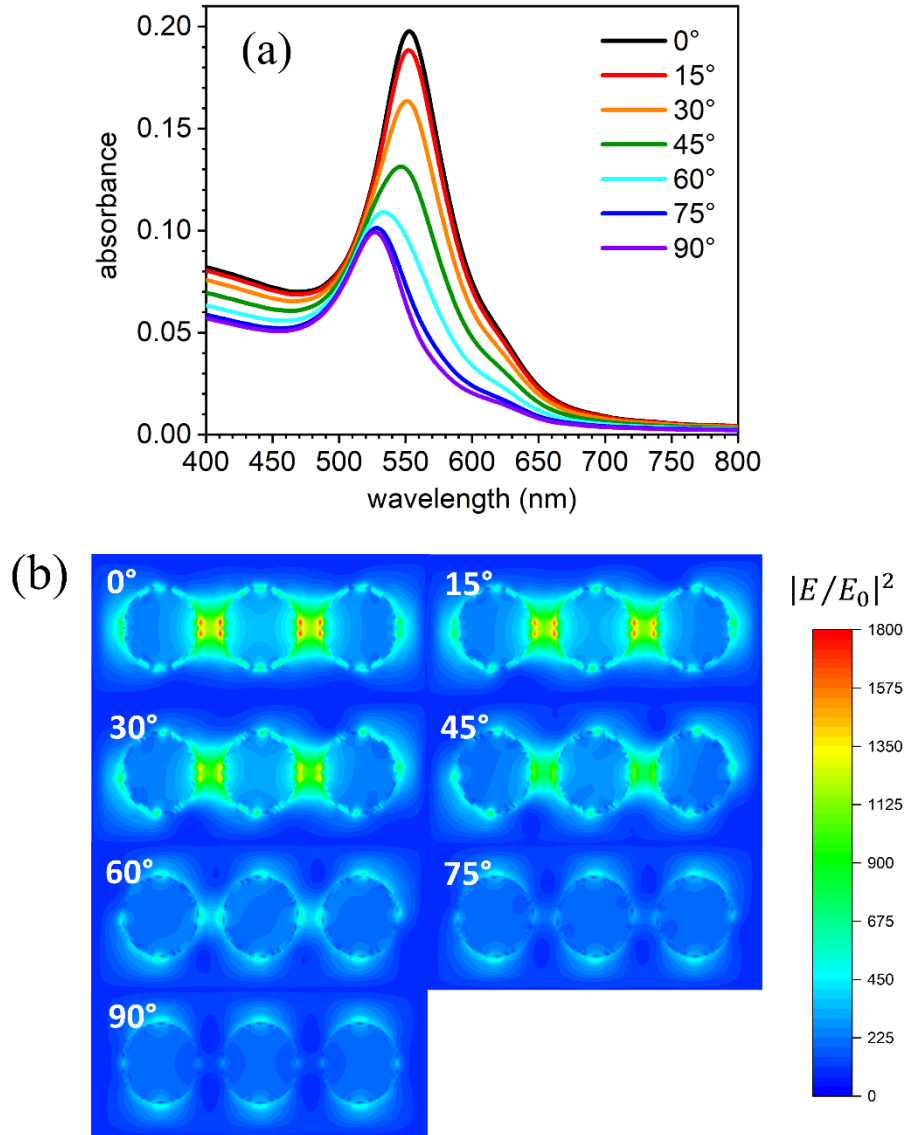


Figure 2.17. (a) Simulated absorption spectra and (b) gain of the E-field intensity worked out by considering a linear chain made of three f-AuNPs interacting with plane waves as a function of the polarization angle.

While the maximum LSPR shift for a single chain took place at $\theta = 0^\circ$ (electric field parallel to chain), the contributions from chains oriented at approximately $\theta = 90^\circ$ (electric field transverse to chain) are vanishingly small (see Figure 2.17a) resulting in a damped effect when the average over the whole distribution is worked out. In fact, when randomly oriented linear chains are considered, the dependence on the solid angle reduces to $\sin(\theta)$ in consideration of the cylindrical symmetry around the direction of the electric field

$$\bar{A}(\lambda, N) = \int_0^{\pi/2} A(\theta, \lambda, N) \sin(\theta) d\theta \quad (2.11)$$

The mean optical response $\bar{A}(\lambda, N)$ was worked out by summing up nine spectra at polarization angles from 0° to 90° with a step of 10° . The LSPR red-shift is clearly visible in Figure 2.18a and b that report the mean simulated spectra and the corresponding Gaussian fit around the LSPR peak, respectively, for linear chains from 1 to 12. The behaviour of LSPR shift $\Delta\lambda_{\text{LSPR}}$ as a function of the number of AuNPs along the linear chain is shown in Figure 2.18c and is well fitted by

$$\Delta\lambda_{\text{LSPR}}(x) = a(1 - e^{-b(x-1)}) \quad (2.12)$$

with $a = (19.3 \pm 0.4) \text{ nm}$ and $b = 0.31 \pm 0.02$. The behaviour of the LSPR shift shown in Figure 2.18c reproduces quite accurately the experimental data for relatively low LSPR shifts corresponding to concentrations in the range $0\text{-}6 \text{ pg/mL}$ and $20\text{-}10^5 \text{ pg/mL}$ that led to clusters whose size did not exceed 5-6 AuNPs (see Figure 2.13 and Figure 2.14).

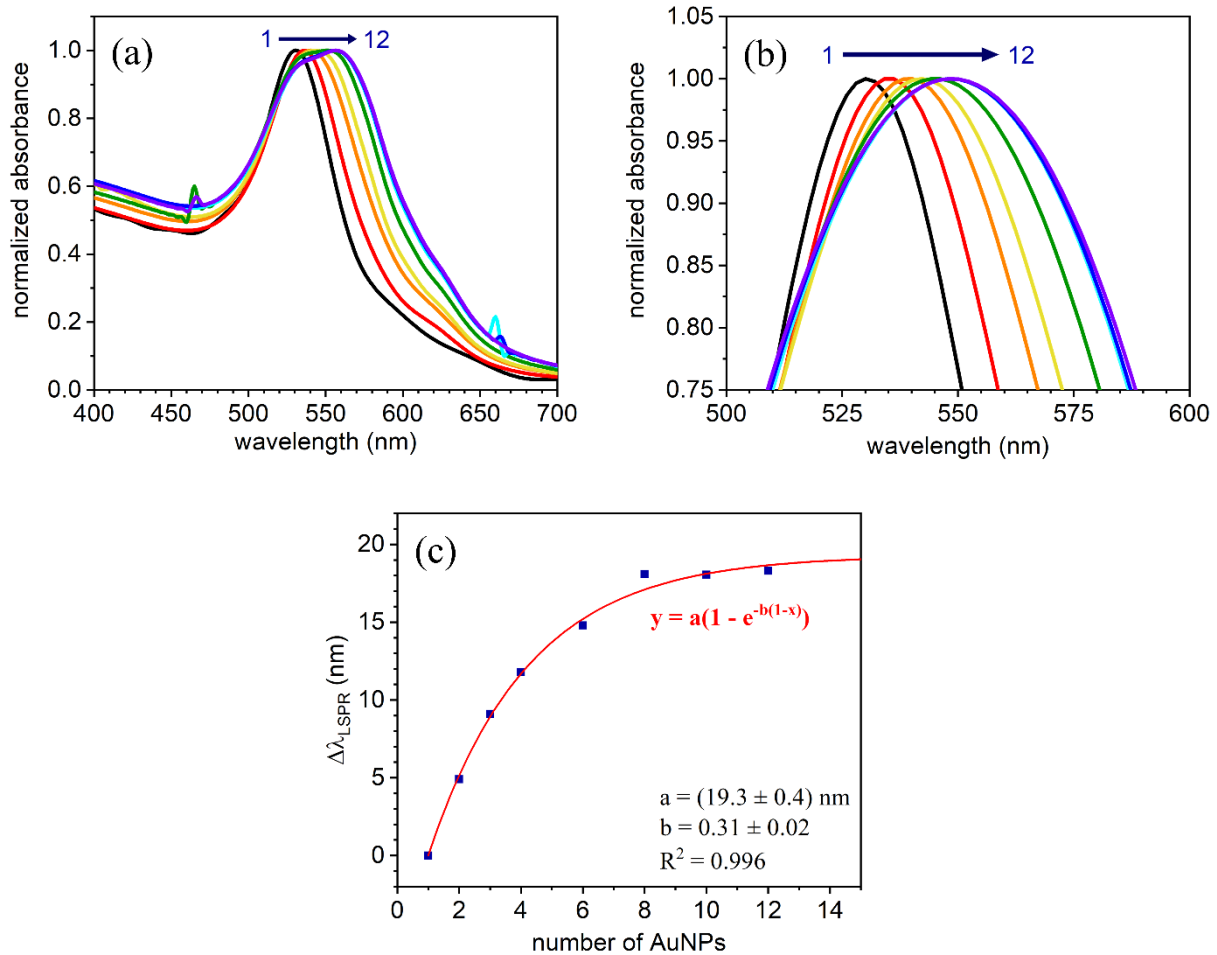


Figure 2.18. (a) Simulated absorption spectra of linear chains made of AuNPs worked out by averaging the absorbance over several polarization angles (from 0° to 90° with a step of 10°). The absorption peak red-shifts as the number of AuNPs increase moving from 1 to 12. (b) Gaussian fits evaluated around the LSPR peaks of the simulated absorption spectra. (c) LSPR shift (from numerical simulations) as a function of the number of AuNPs.

For linear chains with more AuNPs, the LSPR shift from Equation (2.12) tends to saturate at approximately 19 nm, a value that is lower than 25 nm measured at 10 pg/mL (Figure 2.13). This discrepancy may well be explained by considering that the actual morphology of the aggregates was 2- and 3-dimensional. In fact, the damped effect experienced by averaging the linear chains on the solid angle is less significant when the structure to be rotate in the space has a complex 2- or 3-dimensional morphology, since at any angle it forms with the direction of the electric field, there are still significant contributions from linear branches included in the structure. Therefore, the shift behaviour described by Equation (2.12) is an underestimation of the actual experimental shift measured around the hook point.

2.3.4 Dynamics of aggregation

Aiming at explaining the AuNP aggregation dynamics,^{65,139} a simple approach relying on the assumption that the solution contains two species of f-AuNPs was considered: E2-f-AuNPs (species A), i.e. AuNPs whose Abs have bound the analytes, and the free f-AuNPs (species B) that are available to bind the analyte. The concentration of both species is linked by the relation $[A] + [B] = [f \text{ AuNPs}]_0$, in which the right-hand side represents the initial concentration of f-AuNPs. At dynamic equilibrium, it results

$$[A] = \frac{[f \text{ AuNPs}]_0 \cdot [E2]}{K + [E2]} \quad (2.13a)$$

$$[B] = [f \text{ AuNPs}]_0 - [A] = [f \text{ AuNPs}]_0 \frac{K}{K + [E2]} \quad (2.13b)$$

where K is the equilibrium constant of the reaction $B + E2 \leftrightarrow A$. In this simple model, it is easy to realize that an excess of A or B shifts the equilibrium to the right or left of the hook point, respectively. The aggregation dynamics, and hence the cluster size, is a multiple-order complexation between A and B, which can be accounted for the following semi-empirical equation⁹⁰

$$b(x - 1) = \left(\frac{R[E2]}{(K + [E2])^2} \right)^n \quad (2.14)$$

where the factor R includes both the AuNP concentration and instrumental response. The optical response of the colorimetric immunosensor as a function of the analyte concentration can be obtained by inserting Equation (2.14) into Equation (2.12)

$$\Delta\lambda_{\text{LSPR}}([E2]) = a_{\text{eff}} \left(1 - e^{-\left(\frac{R[E2]}{(K+[E2])^2}\right)^n} \right) \quad (2.15)$$

where the term a was replaced by an effective coefficient a_{eff} to account for the actual LSPR shift occurring around the hook point. The data in Figure 2.13 are well fitted by Equation (2.15) with $a_{\text{eff}} = 25.4$ nm, $R = (43 \pm 3)$ pg/mL, $K = (10.4 \pm 0.7)$ pg/mL and $n = 19 \pm 6$, thereby confirming the effectiveness of the proposed approach to describe the complex aggregation dynamics occurring in this experiment. The coefficient a_{eff} was fixed to 25.4 nm that corresponded to the maximum experimental shift.

While this model captures the cluster formation, it fails to reproduce the asymptotic behaviour of the AuNP aggregation occurring at higher E2 concentrations (black dash line in Figure 2.13). This is due to its inherent simplicity which does not include the complex diffusion process that took place in the whole interaction volume. In fact, even if the binding sites of f-AuNPs are locally fully saturated with E2 at high concentration – and hence no aggregation should arise among E2-f-AuNPs – these nanoparticles can form aggregates with f-AuNPs during their diffusion. This was proved by STEM observation since dimer and trimer contributions were clearly visible at 50 pg/mL of E2 (Figure 2.14). Thus, while a detailed description of the aggregation dynamics should include a complex diffusion process, which goes beyond the scope of the present work, it is worth to stress that the present biosensor is able to provide measurable signal even at very high E2 concentration, where usually the hook effect results in the false negative response.

2.3.5 Repeatability, stability, recovery, and specificity assay

The repeatability of the immunosensor response was evaluated by comparing the LSPR shift of several measurements at E2 concentration of 10 pg/mL. Figure 2.19a and b show a great reproducibility of the LSPR shift: Only two measurements out of ten fall outside the 67% confidence interval. The stability was studied by acquiring the absorption spectra of a single sample at E2 concentration of 10 pg/mL after different time intervals from the first measurement. Figure 2.19c confirms the reliability and the long-term stability of the proposed colorimetric biosensor in terms of both functionalization effectiveness and analyte binding. The small blue-shift of the LSPR peak and the slight decrease of the absorption intensity after 24 hours suggest a lack of the contributions of bigger clusters that tend to precipitate in stasis conditions. The recovery was measured for four E2 concentrations (4, 6, 12, 20 pg/mL) and the corresponding values are reported in Table E.2. The

fluctuations from the nominal value of the measured E2 concentration are in the range of 10-25%, a value that is compatible with the experimental error bars (Figure 2.13). The specificity of the immunosensor was proved by detection of the most competitive molecules of E2: progesterone, estrogens (E1 and E3) and testosterone. Figure 2.19d shows the reliability of the immune response at low and high concentration of the interferences: While no detectable signal was observed for progesterone and testosterone, a very small response could be measured for E1 and E3 as a result of the partial lack of specificity of the Abs used for the functionalization. This does not prevent one from using the biosensor since any unlikely false positive due to E1 and E3 detection is anyway important as they are strongly involved in the estrogen metabolism.¹⁴⁰

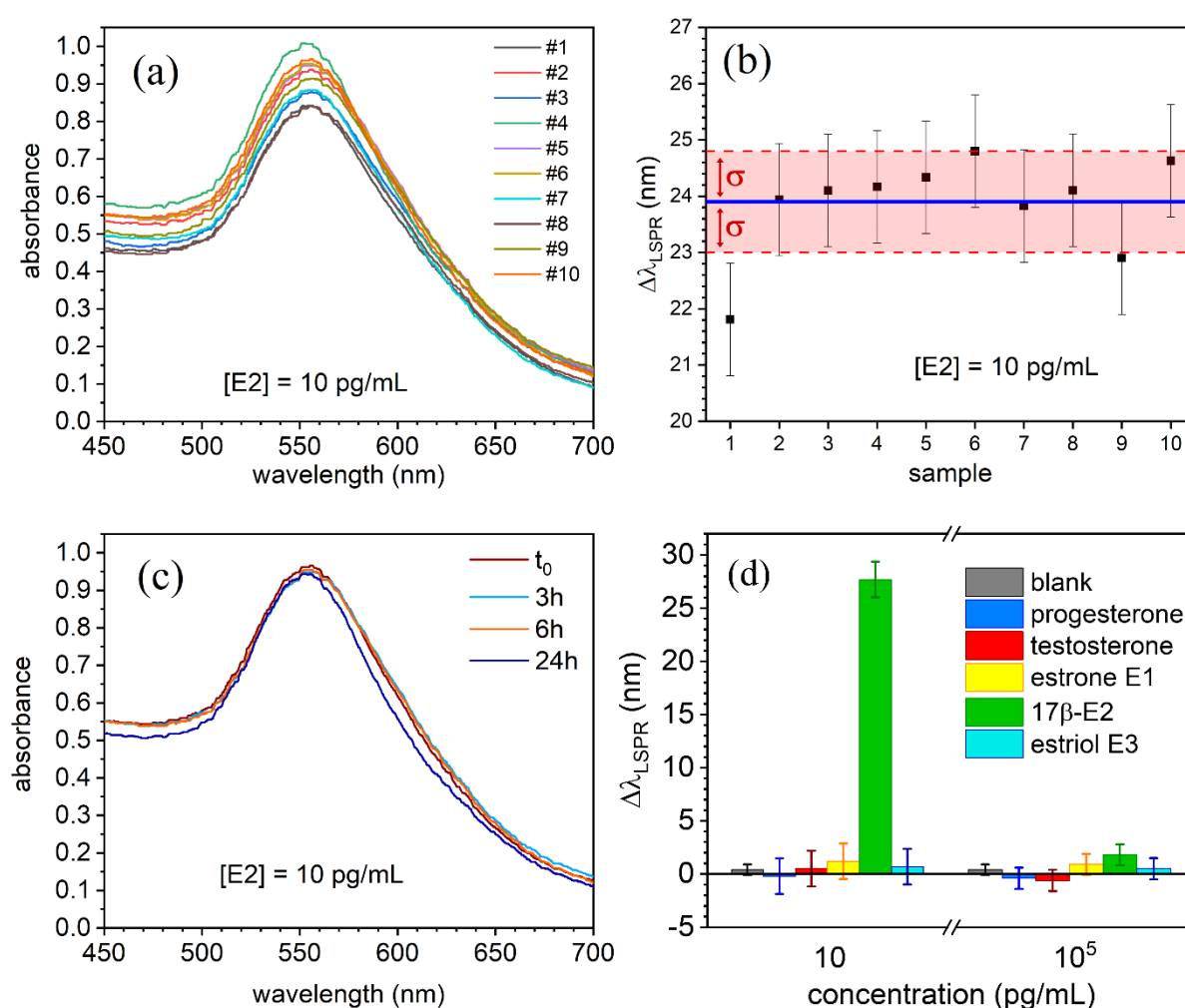


Figure 2.19. (a) Absorbance and (b) LSPR shift of ten samples measured at E2 concentration of 10 pg/mL. In the panel (b), the blue line is the mean value of the measurements, whereas the red band highlights the $\pm\sigma$ interval (c) Absorption spectra of a single sample (10 pg/mL E2 concentration) recorded at different time intervals after the first measurement. (d) LSPR shift measured for different analytes at 10 pg/mL and 10^5 pg/mL concentrations.

2.3.6 Discussion

The colorimetric immunosensor reported here is based on AuNPs functionalized with antibodies for the detection of a small molecule like 17 β -estradiol. The high specificity, very low limit of detection (LOD) (3 pg/mL) and affordable price are the main strengths of the proposed approach.⁸⁹ The specificity is inherently ensured by the Ab functionalization, whereas the plasmonic properties of AuNPs provide an accurate optical transduction of the biological signal. Moreover, the AuNP functionalization through PIT contributes to increase the biosensor sensitivity and long-term stability thanks to the covalent anchorage of the Abs on gold surface in upright orientation. The analyte detection arises from the change of the optical properties of the solution due to the AuNP aggregation. Since the LSPR wavelength of isolated AuNPs as well as that of their aggregates falls in the visible region, the shift of the absorption peak following the analyte concentration entails a colour change visible by naked eyes. This allows a fast and qualitative test to establish the analyte presence in the sample solution viable *in situ*. A quantitative measurement of the analyte concentration only requires an UV-Vis spectrophotometer to carefully assess the wavelength of the absorption peak and, hence, to evaluate the LSPR shift.

This colorimetric immunosensor is able to detect E2 in tap water down to 3 pg/mL within few hours after a 20 μ L sample is added into the cuvette containing 1 mL of f-AuNPs and represents a significant improvement in E2 low levels determination (without any preconcentration step) in terms of LOD, sample preparation, cost and analysis simplicity, thus challenging the usual expensive instrumental laboratory methods.⁸⁹ Although in the current work the mixing was performed by a vortex mixer to warrant high reproducibility, it was observed that simple mechanical pipetting led to a detection time of few minutes, thus showing that the mixing procedure can be further optimized. Moreover, in this procedure the hook effect does not lead to a vanishingly small signal, but to a semi-quantitative response that can be used as an alert signal. Nevertheless, should a quantitative response be required, it is possible to resort to serial dilutions of the sample, a procedure that is customary in immunoassays.¹⁴¹ For instance, four dilutions such as 1:2, 1:5, 1:10 and 1:100 would be suitable to cover the quantification at higher concentration up to 1 ng/mL (see Table E.3).

The reduction of the time required for the mixing process combined with the availability of portable and handheld spectrophotometers will make the proposed biosensor very promising for routinely *in situ* E2 monitoring of river waters. Moreover, the range of the investigated E2 concentration is of interest in several diagnostic and environmental contexts suggesting the possibility to extend this colorimetric biosensors to other matrices (e.g., urine and wastewater) despite some pretreatment step such as desalination, purification or pH modification might be necessary. Eventually, the scheme

described here can be adopted for different analytes (e.g., ochratoxin A and aflatoxin B1) by simply changing the antibody.

2.4 Detection of SARS-CoV-2 in nasal and throat swabs

Since its identification in China in late 2019, the SARS-CoV-2 epidemic has spread rapidly worldwide affecting millions of people, thus pushing the World Health Organization (WHO) to declare a COVID-19 outbreak a global health emergency. Mass testing is fundamental to identify and isolate clusters in order to limit and eventually eradicate SARS-CoV-2.¹⁴² The gold standard for diagnosing COVID-19 infection is a reverse transcription real-time polymerase chain reaction (PCR)¹⁴³ that is able to detect the virus genetic material (RNA) in samples collected via nasopharyngeal swab. Currently, only qualitative real-time PCR assays are available that yield positive/negative results without providing information about the viral load. Due to its complexity, real-time PCR tests are performed in certified laboratories, are time consuming, require experienced personnel, and can hardly lend themselves for mass screening.^{144–147} Huge efforts are put in overcoming such a bottleneck thereby making nucleic acid amplification suitable for POC tests, but the variety of methods¹⁴⁸ and the lack of any commercial solution demonstrates that the gap between research and real applications is still to be filled.¹⁴⁹ The main reason for that has to be found in the detection principle (RNA-extraction, reverse transcription and amplification) whose complexity, though greatly reduced by several approaches (e.g. loop-mediated isothermal amplification and recombinase polymerase amplification) is far from being used for quick POC tests. Lateral flow assays (LFA) are among the actual biosensing platforms for home tests and potentially for mass screening,^{150–153} but the relatively poor sensitivity inherent to this technology¹⁵⁴ makes urgent the quest for a different approach.¹⁵⁵

Biosensors based on metal nanoparticles are often proposed because of their unique optical properties, which makes them potentially suitable to develop easy-to-use and rapid colorimetric diagnostic tests for POC applications or even for home use.¹⁵⁶ An approach relying on nanoparticle aggregation induced by the presence of the antigen was also used to detect the influenza A virus, but no clinical application was reported to demonstrate the effectiveness of the whole procedure in clinical cases.¹⁵⁷ A remarkable result has been obtained by using AuNPs capped with designed thiol-modified antisense oligonucleotides specific for N-gene (nucleocapsid phosphoprotein) of SARS-CoV-2.¹⁵⁸ Although such a visual and rapid test is highly desirable to downregulate the spread of the current

pandemic, no clinical studies have been carried out to validate the diagnostic potential of such an approach. Moreover, the detection of the viral RNA rather than the virion itself may be detrimental since the capability to selectively distinguish active and inactive viral particles is crucial to assess the actual degree of infectiveness of a specimen.

Here, it is reports on the realization of a colorimetric biosensor that can be used for COVID-19 mass testing with sensitivity and specificity higher than 95% as demonstrated by a comparative analysis carried out on a total of 94 samples (45 positive and 49 negative), tested by standard real-time PCR in the Virology Unit of A.O.U. Federico II/Department of Translational Medicine of the University of Naples “Federico II”.¹⁰⁰ The detection scheme is shown in Figure 2.20 and consists of a colloidal solution of PIT-functionalized AuNPs (f-AuNPs) (see Figure 2.9 and Figure 2.10 for the characterization of bare and functionalized AuNPs, respectively) against three surface proteins of SARS-CoV-2: spike, envelope and membrane (S, E, and M, respectively, in Figure 2.21a). In this approach, a volume of 100 μ L of the sample – consisted of 3 mL solution of universal transport medium (UTMTM, Copan Brescia, Italy) in which the naso-oropharyngeal swab specimen was dipped after its collection from hospital patient and without any additional treatment – was mixed with 50 μ L of f-AuNP (Figure 2.20a). Then, optical response of the solution was measured for evaluating the presence of SARS-CoV-2 (Figure 2.20b).

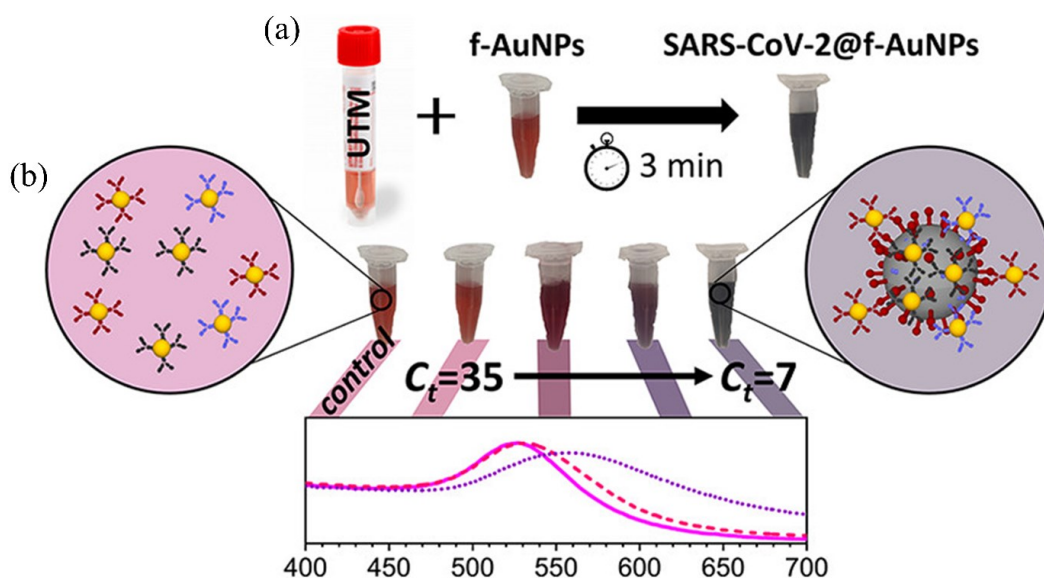


Figure 2.20. Scheme of f-AuNPs-based immunosensor for the detection of SARS-CoV-2 viruses. (a) The release of virus in UTM medium after naso-oropharyngeal swab dipping induces the f-AuNP agglomeration around the virion surface leading to a colour change visible by a naked eye due to the AuNP plasmon coupling. (b) The colour of the solution changes from pink to purple as the SARS-CoV-2 concentration increases. The relative virion concentration can be estimated by evaluating the LSPR shift of the solution after adding the UTM sample.

The samples were independently tested for the presence of SARS-CoV-2 RNA within 24 h of collection by using Abbott Real Time SARS-CoV-2 assay, a dual target assay for RdRp and N-genes. The two SARS-CoV-2-specific probes are labelled with the same fluorophore whereas the internal control (IC)-specific probe is labelled with a different fluorophore, allowing simultaneous detection of both SARS-CoV-2 and IC amplified products in the same reaction well. Swabs were stored at -80° before further assays. A real-time PCR assays detects positives sample by the accumulation of a fluorescent signal indicating the amplification of the target sequence. The cycle threshold (C_t) is defined by the number of cycles required for the fluorescent signal to cross the background level (threshold). C_t levels are inversely proportional to the amount of target nucleic acid in the sample: lower C_t means larger amount of target sequence.

2.4.1 Optical response of SARS-CoV-2@f-AuNPs (measurements and FDTD simulations)

The presence of the viral particles (virions) induced the formation of a nanoparticle layer on its surface (Figure 2.21b) that led to a redshift of the optical density (OD) in the extinction spectrum of the solution (Figure 2.21c). When the viral load was relatively high ($C_t < 15$),¹⁵⁹ the colour change from red to purple was visible even by naked eye (inset of Figure 2.21a and b). The extinction spectrum of f-AuNPs reported in Figure 2.21c (black continuous line) is not distinguishable from the spectrum of a mixed solution with a sample having a very low virion concentration ($C_t = 32$) (dashed light blue curve, C_{t32}). On the contrary, a red-shift is observed for a sample with an intermediate virion concentration ($C_t = 15$) (blue continuous line, C_{t15}), which becomes much more noticeable when very high virion concentration ($C_t = 7$) is explored (red continuous line, C_{t7}). The contribution of the virion (surrounded by AuNPs) to the extinction spectrum can be deduced by subtracting the spectrum of f-AuNPs from C_{t15} . In fact, the curve C_{t15} -(f-AuNPs) (dashed grey line) shows a peak at a wavelength comparable to that exhibited by C_{t7} (approximately 560 nm).

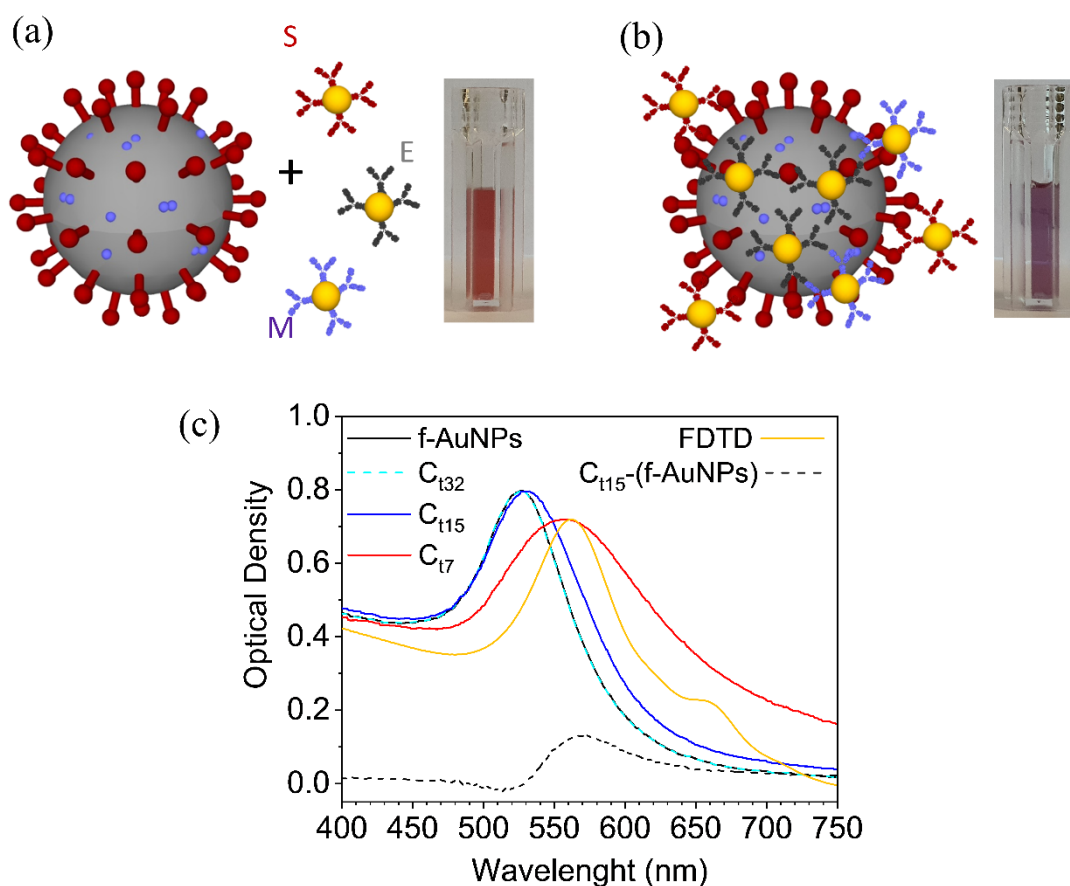


Figure 2.21. (a) Sketch of the SARS-CoV-2 and functionalized AuNPs. SARS-CoV-2 proteins (spike, membrane, and envelope) and their corresponding antibody (S, E, and M) are highlighted in dark red, light violet and grey, respectively. The inset shows the pink colloidal solution containing the anti-SARS-CoV-2 f-AuNPs. (b) The f-AuNPs surround the virion forming a nanoparticle layer on its surface. Their interaction leads to a shift of the resonance peak in the extinction spectrum and, hence, to a colour change visible in the inset. (c) Extinction spectra of f-AuNP colloidal solution mixed with samples from patients with different viral load.

To further confirm that the spectrum C_{t7} arose from f-AuNPs surrounding SARS-CoV-2, the optical response of a virion – as a 100 nm diameter dielectric sphere^{160,161} of 1.45 refractive index¹⁶² – surrounded by a changeable number of AuNPs (20 nm diameter)¹⁶³ randomly positioned on the sphere was simulated. A sketch of the simulation workspace and of the complex virion-AuNPs are depicted in Figure 1.22 and Figure 2.22a, respectively, whereas Figure 2.22b shows the LSPR wavelength as a function of the number of AuNPs on the virion surface.

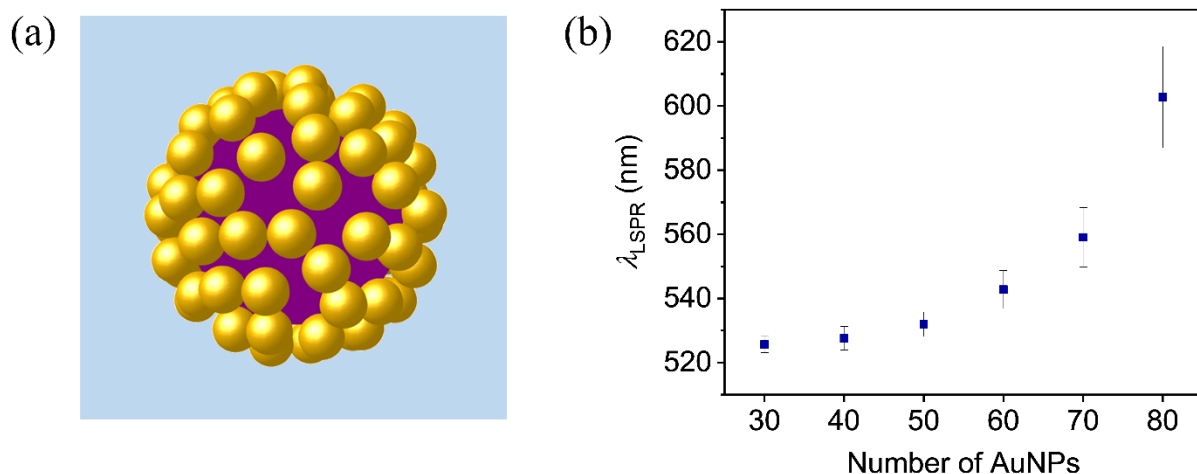


Figure 2.22. (a) Sketch of the virion surrounded by randomly positioned AuNPs used throughout the optical simulations. The surrounding medium is water. (b) LSPR wavelength as a function of the number of AuNPs surrounding the virion. Due to the randomness of the AuNP positioning onto the virion surface, the simulations were conducted by running the code ten times and, hence, the data are shown as mean value \pm SD.

The dependence of the plasmon resonance on the number N of AuNPs onto the virion surface is highly nonlinear (Figure 2.22b). The maximum number of AuNPs that can be placed on a perfectly spherical surface with 100 nm diameter is $N = 80$, but the steric hindrance offered by surface proteins like the spike one surely limits the filling capacity of the virion surface. In fact, Figure 2.22b shows that the experimental value of $\lambda_{\text{LSPR}} = 560$ nm is achieved when $N = 70$, a value only slightly smaller than the maximum achievable. The extinction spectrum corresponding to $N = 70$ AuNPs (scaled to the experimental one) is reported in Figure 2.21c (golden continuous line) and conveys a more than satisfactory agreement with the experimental one (red continuous line), thereby confirming that the simple model proposed here is able to capture the essential physical processes underlying the virion detection.

2.4.2 SARS-CoV-2 testing of hospital patients

In order to test the validity of this colorimetric biosensor, real samples from hospital patients – previously examined by real-time PCR – were analysed. The samples were from 45 positive to SARS-CoV-2 patients for which $C_t \leq 35$ and 49 negative patients ($C_t > 35$). For all of them, the optical density at 560 nm (OD_{560}) was measured by a commercial microplate reader (Figure 2.23a). It is quite evident the correlation between the C_t value (reported on the top scale) of the positives (red circles) and OD_{560} , whereas all the negatives (identified by a progressive number in the bottom scale) are randomly distributed providing a control value of $\text{OD}_{560}^{\text{neg}} = 0.22 \pm 0.02$. The dashed horizontal line at

an OD_{560} value of 0.252 makes clear the ability to discriminate positives from negatives offered by this colorimetric biosensor.¹⁰⁰ In fact, with such a threshold we get 96% and 98% for sensitivity and specificity, respectively. This result is even more remarkable by considering that $C_t > 30$ corresponds to a very low viral load for which the infection aptitude is questioned. To this aim, it is important noticing that in the early phase of the infection, high viral loads are detected by real-time PCR in upper respiratory specimens with low C_t readouts ($C_t < 20$). In the late phase of the infection, a dramatic drop in viral loads is observed with higher C_t readouts ($C_t > 30$). Positive results with high C_t readouts pose a diagnostic challenge since they do not necessarily indicate active infection by a replicating virus. It has been observed using viral culture that patients with high C_t real-time PCR and protracted positivity are not infectious, suggesting that the assay likely detects non active viral particles such as genetic material present in remnants of inactive virus¹⁶⁴ thereby making the proposed approach of high diagnostic value.¹⁰⁰

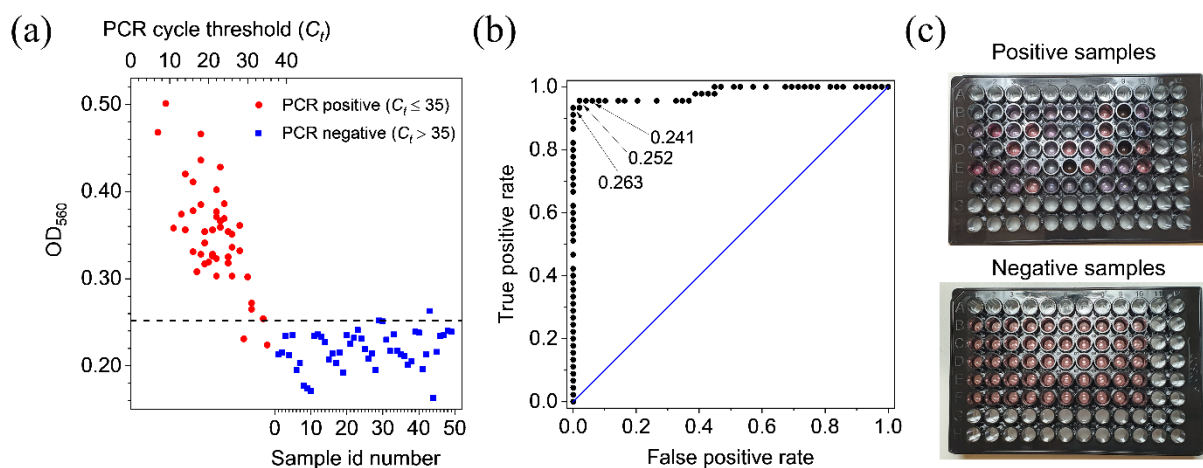


Figure 2.23. (a) Results of the colorimetric test on real thawed samples from 45 positive (red circle points) and 49 negative patients (blue square points) previously tested by real-time PCR. For all of them the extinction coefficient was measured at 560 nm. The positive samples ($C_t \leq 35$) are identified in the plot by their real-time PCR cycle threshold (top scale), whereas the negative sample ($C_t > 35$) are simply numbered (bottom scale). The horizontal line at 0.252 extinction coefficient would lead to a test with 96% sensitivity and 98% specificity. (b) ROC curve retrieved from the data of the panel (a). The area under the curve is 0.98. Also shown three threshold values for the extinction coefficient that would provide the following sensitivity and specificity: 96% and 94% (0.241), 96% and 98% (0.252), and 94% and 100% (0.263), respectively. (c) Picture of the 96 multiwell plate containing 250 μ L of positive (top panel) and negative (bottom panel) samples. The plate reading was carried out by a commercial multiwell reader that took less than 1 min.

The receiver operating characteristic (ROC) curve from the data shown in Figure 2.23a is reported in Figure 2.23b together with the indication of three threshold values, all of them leading to sensitivity and specificity significantly higher than 90%. In particular, the highest threshold value (0.263) leads to 100% specificity while keeping the sensitivity at the remarkable value 94%. Overall, the high performance of the test associated to the colorimetric biosensor is demonstrated by the area under the

ROC curve whose value is 0.98. The qualitative difference in the colour between positives and negatives can be observed in Figure 2.23c that shows a picture of the multiwell containing the samples whose analysis is summarized in Figure 2.23a and b.

2.4.3 Dose-response curve

To measure the dose-response curve of the biosensor, the OD_{560} of samples obtained by serial dilutions (1:10) from an initial volume with very high viral load ($C_t = 7$) was evaluated. The results are shown in Figure 2.24, in which OD_{560} is reported as a function of the relative concentration of SARS-CoV-2. For convenience so to provide a comparison with the cycle threshold of a real-time PCR, the top scale reports the equivalent C_t obtained by considering that 1:10 dilution corresponds to $\log_2 10 \sim 3.32$ change in C_t , whereas the vertical dashed blue line identifies the starting concentration. As it turns out, a detectable signal can be appreciated even after 7 serial dilutions ($1:10^7$) confirming the wide detection range resulting from the validation measurements reported in Figure 2.23.

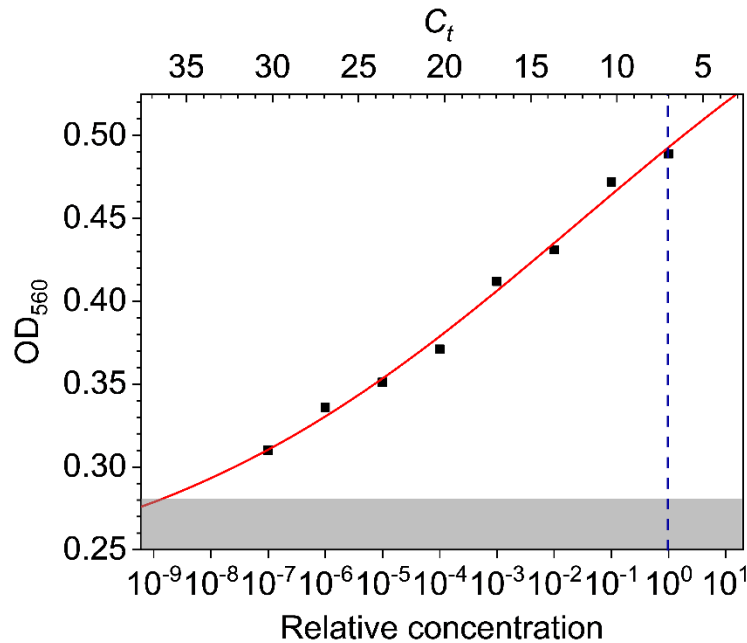


Figure 2.24. Optical density of the solution measured at 560 nm as a function of SARS-CoV-2 concentration (bottom axis). The virion concentration was obtained by serial dilution starting from a threshold cycle value $C_t = 7$ (vertical dashed blue line). Each decrease by a decade in virion concentration (bottom axis) corresponds to an increase of the nominal C_t of approximately 3.32 (top axis). The red continuous line is the best fit of the experimental data by Hill equation (2.16). The uncertainty in the reading is taken as the resolution of the instrument and the error bar is within the data point. The shaded area corresponds to values smaller than $OD_{560} = 0.28$, which is 3 standard deviations from the mean value of the negative controls.

The behaviour of the OD_{560} as a function of the virion concentration C reported in Figure 2.24 can be described by the three parameters Hill equation¹⁶⁵

$$OD_{560}(C) = \Delta(OD_{560}) \frac{C^n}{K^n + C^n} + OD_{560}(0) \quad (2.16)$$

In Equation (2.16), $OD_{560}(0) = OD_{560}^{neg} = 0.22$ is the OD of the control as deduced from the negative samples, $\Delta(OD_{560})$ is the maximum OD_{560} variation, K is the concentration (in this case it is a relative concentration) at which the OD_{560} variation reaches 50% of its maximum and n is the so-called Hill's coefficient.¹⁶⁶ The best fit of the experimental data with Equation (2.16) yielded the red curve in Figure 2.24 and the following values for the parameters: $\Delta(OD_{560}) = 0.45 \pm 0.11$, $K = 0.03 \pm 0.01$ and $n = 0.11 \pm 0.02$. The relative concentration K is essentially undetermined as a consequence of the high detection range of this method, which entails small response to the concentration changes (low sensitivity), and hence, high uncertainty on the concentration measurements. A value for n significantly smaller than 1 indicates the occurrence of a negatively cooperative binding, a behaviour expected by considering that the probability a f-AuNP binds the virion reduces as the surface covering grows. Eventually, $\Delta(OD_{560})$ is the range of the optical densities spanned by the biosensor. The shaded area in Figure 2.24 contains the values of OD_{560} within 3 standard deviation (SD) from the mean value of the control ($OD_{560}^{neg} + 3SD = 0.28$). Thus, according to 3SD criterion, it results $C_t = 36.5$ as the limit of detection of the biosensor in terms of real-time PCR cycle threshold. The uncertainty about such a value is related to that of the initial point at $C_t = 7$ ($OD_{560} = 0.49 \pm \sigma$). An estimation of σ can be deduced from the scattering exhibited by the experimental points in Figure 2.23a. It turns out to be approximately ± 0.05 thereby attaining a more realistic limit of detection at $C_t = 30$ also in view of the error propagation due to the sample serial dilutions. Although real-time PCR sensitivity is hard to surpass, in the context of COVID-19 pandemic in which the detection of SARS-CoV-2 is required in naso-oropharyngeal swabs, this method is an efficient alternative when quick and widespread response cannot be provided by standard laboratory methods.¹⁰⁰

2.4.4 Discussion

The colorimetric immunosensor reported here is based on colloidal solution of AuNPs functionalized with Abs against the three surface proteins of SARS-CoV-2 (spike, envelop and membrane). The ratio among the three kinds of functionalized AuNPs was 1:1:1. Although both the ratio and the size of AuNPs are still susceptible to optimization so to allow one to push even further the LOD, the current performances of the biosensor would already permit its use as a test for mass screening since the detection is based on the interaction among the virions and the f-AuNPs (single step detection) without any pretreatment (e.g. RNA extraction and amplification).¹⁰⁰ The comparison of the readout

of this biosensor at 560 nm with the threshold cycle (C_t) of a real-time PCR proved that viral loads corresponding to $C_t = 36$ are detected by such a colorimetric immunoassay. This threshold is of particular importance because it corresponds to a very low viral load for which the infecting capacity is likely negligible.¹⁶⁴ Such a good performance has to be ascribed to a high filling ratio of the virion surface that results from the presence of multiple Abs (three proteins are targeted) and an effective AuNP surface functionalization procedure. In fact, through PIT not only one Fab is always exposed so to make AuNP highly reactive, but also the Abs are attached to the surface (side-on position) without any linker (e.g. protein A), the latter being detrimental for the plasmonic interactions among AuNPs on which the colorimetric biosensor is based.

Another remarkable feature of the biosensor described here relies on its sensitivity to the virion rather than to its content (RNA). The importance of this is twofold: (i) after the calibration of the optical response, the biosensor lends itself as a powerful tool to quantify the viral load, a non-trivial issue in diagnostic assays in virology; (ii) being sensitive only to the virions, the biosensor detects the presence of active viral particles; thus, this method is apt to assess the actual degree of infectiveness of a specimen. Eventually, it is worth to notice that contrary to the case of small molecules such as 17 β -estradiol, in which the detection arises from link-mediated f-AuNP aggregation and hence the detection range spans few decades around the concentration of immobilized Abs, analytes whose size is much higher than that of f-AuNPs (e.g., viruses) act as multiple anchoring site thereby extending the detection range over several decades; a vanishingly small response due to the hook effect is observable only when the analyte concentration is comparable to the f-AuNP concentration.

Chapter 3. Collective surface plasmon

3.1 Two-dimensional array of AuNPs

3.1.1 Coupled-dipole system

The collective plasmonic modes of metal nanospheres arranged in periodic two-dimensional (2D) arrays can be addressed within a point-dipole description by considering an effective polarizability describing the collective response of a system composed of coupled dipoles.^{21,167} The local EM field at the position of a dipole consists of the superposition of the external incident radiation and the field radiated by all the other dipoles. On the dipole i -th, the local electric field $\mathbf{E}_{\text{local}}$ induces a dipole moment \mathbf{p}_i , which is itself a radiation source to other dipoles. By assuming a harmonic time dependence of the external field $e^{-i\omega t}$ and an isotropic polarizability α equal for every dipole, the coupled-dipole equation for the i -th dipole reads^{21,38,167}

$$\mathbf{p}_i = \alpha \left[\mathbf{E}_{\text{ext},i} + \sum_{j \neq i} \mathbf{G}(\mathbf{R}_i, \mathbf{R}_j) \mathbf{p}_j \right] \quad (3.1a)$$

$$\mathbf{G}(\mathbf{R}_i, \mathbf{R}_j) \mathbf{p}_j = \left[\left(1 - \frac{i\omega r_{ij}}{c} \right) \frac{3(\mathbf{n}_{ij} \cdot \mathbf{p}_j) \mathbf{n}_{ij} - \mathbf{p}_j}{r_{ij}^3} + \frac{\omega^2}{c^2} \frac{\mathbf{p}_j - (\mathbf{n}_{ij} \cdot \mathbf{p}_j) \mathbf{n}_{ij}}{r_{ij}} \right] e^{\left(\frac{i\omega r_{ij}}{c} \right)} \quad (3.1b)$$

where $\mathbf{E}_{\text{ext},i}$ is the incident field at i -th dipole, $\mathbf{G}(\mathbf{R}_i, \mathbf{R}_j) \mathbf{p}_j$ represents the field radiated by j -th dipole at the position \mathbf{R}_i of i -th dipole, $\mathbf{r}_{ij} \equiv \mathbf{R}_i - \mathbf{R}_j$, $\mathbf{n}_{ij} = \mathbf{r}_{ij}/r_{ij}$ is a unit vector parallel to \mathbf{r}_{ij} . Figure 3.1 shows a schematic representation of an infinite honeycomb lattice made of conductive nanoparticles interacting with an external EM wave.

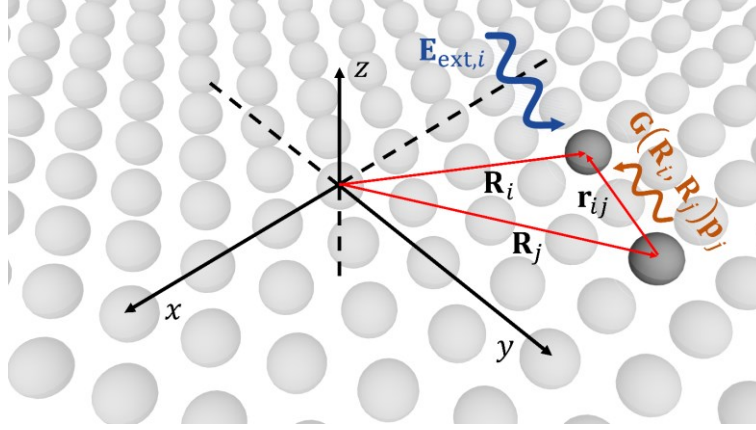


Figure 3.1. Schematic representation of 2D lattice made of metal nanoparticles interacting with an external electric field. Since each nanoparticle acts as an oscillating electric dipole, the local field at the position of a dipole consists of the superposition of the external incident radiation and the field radiated by all the other dipoles.

In Equation (3.1b), the terms proportional to $\sim 1/R$, $\sim 1/R^2$, and $\sim 1/R^3$ represent the short-range, intermediate-range and long-range interactions, respectively, contributing to the dynamic dipolar Green's function. For periodic systems, the dipole moment and the external field fulfil the following boundary conditions^{21,38}

$$\mathbf{p}_i = \mathbf{p} e^{i\mathbf{k}_B \cdot \mathbf{R}_i} \quad (3.2a)$$

$$\mathbf{E}_{\text{ext},i} = \mathbf{E}_{\text{ext}} e^{i\mathbf{k}_B \cdot \mathbf{R}_i} \quad (3.2b)$$

The form of the external field (3.2b) is chosen to excite on particular eigenmode with Bloch wave vector \mathbf{k}_B .^{21,167} By inserting Equations (3.2) into (3.1a), it results

$$\mathbf{M}\mathbf{p} = \mathbf{E}_{\text{ext}} \quad (3.3)$$

where \mathbf{M} is a 3×3 matrix operating on three-dimensional vector \mathbf{p} defined as²¹

$$\mathbf{M} = \frac{1}{\alpha} \mathbf{I} - \boldsymbol{\beta} \quad (3.4a)$$

$$\boldsymbol{\beta} = \sum_{\mathbf{R}' \neq 0} \mathbf{G}(0, \mathbf{r}_{ji}) e^{i\mathbf{k}_B \cdot \mathbf{r}_{ji}} \quad (3.4b)$$

Here, \mathbf{I} is a unit 3×3 matrix while $\boldsymbol{\beta}$ is a dyadic of lattice sum of dipolar Green's function containing the geometrical information. Note that in Equation (3.4b) the equality $\mathbf{G}(\mathbf{R}_i, \mathbf{R}_j) = \mathbf{G}(0, \mathbf{R}_j - \mathbf{R}_i) \equiv \mathbf{G}(0, \mathbf{r}_{ji})$ has been used. In the case of periodic lattice lying in the x - y plane, Equation (3.3) can be separated into in-plane (3.5a) and transverse (3.5b) components

$$\mathbf{M}_{||}\mathbf{p}_{||} = \mathbf{E}_{\text{ext},||} \quad (3.5a)$$

$$M_z p_z = E_{\text{ext},z} \quad (3.5b)$$

where $\mathbf{M}_{||}(\beta_{||})$ is a symmetric 2×2 matrix and $M_z(\beta_z)$ is a scalar.

$$\mathbf{M}_{||} = \frac{1}{\alpha} \mathbf{I} - \beta_{||} \quad (3.6a)$$

$$M_z = \frac{1}{\alpha} - \beta_z \quad (3.6b)$$

Since the in-plane components of the dipole moment p_x and p_y along x and y direction, respectively, are coupled to each other, the matrix $\mathbf{M}_{||}$ can be diagonalized by an orthogonal transformation \mathbf{A} yielding

$$\mathbf{M}'_{||} \mathbf{p}'_{||} = \mathbf{E}'_{\text{ext},||} \quad (3.7a)$$

$$\mathbf{M}'_{||} = \mathbf{A} \mathbf{M}_{||} \mathbf{A}^T = \begin{pmatrix} M'_{||,11} & 0 \\ 0 & M'_{||,22} \end{pmatrix} \quad (3.7b)$$

$$\mathbf{p}'_{||} = \mathbf{A} \mathbf{p}_{||} = \begin{pmatrix} p'_{||,1} \\ p'_{||,2} \end{pmatrix} \quad (3.7c) \quad \mathbf{E}'_{\text{ext},||} = \mathbf{A} \mathbf{E}_{\text{ext},||} = \begin{pmatrix} E'_{\text{ext},1} \\ E'_{\text{ext},2} \end{pmatrix} \quad (3.7d)$$

Such a diagonalization leads to the decoupling of the in-plane components of the dipole moment into transverse in-plane mode (TI mode) – dipole moment perpendicular to Bloch vector – and longitudinal in-plane mode (LI mode) – dipole moment parallel to Bloch vector.²¹

In this framework, the polarizability α_0 (1.60) defined within an electrostatic framework has to be revised by introducing the following radiation correction to account for the field radiated by every dipole¹⁶⁸

$$\frac{1}{\alpha} = \frac{1}{\alpha_0} - i \frac{2\omega^3}{3c^3} = \frac{\varepsilon_1 + 2\varepsilon_2}{\varepsilon_1 - \varepsilon_2} \frac{1}{4\pi a^3} - i \frac{2\omega^3}{3c^3} \quad (3.8)$$

The radiation-corrected polarizability (3.8) enforces the energy conservation condition (3.9) when the contribution of the scattering is not negligible.¹⁶⁸

$$P_{\text{ext}} = P_{\text{sca}} + P_{\text{abs}} \quad (3.9)$$

Here, P_{ext} , P_{sca} and P_{abs} are the extinguished, scattered (radiated) and absorbed power, respectively.

3.1.2 Quasi-static limit

Firstly, the response of a 2D periodic array of lossless metal nanospheres – characterized by a dielectric function (1.18a) – is investigated within a quasi-static framework. In the quasi-static limit, the speed of light is taken to be infinity ($c \rightarrow \infty$). In addition, for lossless metal ($\gamma = 0$) there is no energy loss and the polarizability (3.8) assumes the following form

$$\frac{1}{\alpha} = \frac{1}{a^3} \left(1 - \frac{\omega^2}{\omega_{\text{LSPR}}^2} \right) \quad (3.10)$$

where $\omega_{\text{LSPR}} = \omega_p/\sqrt{3}$ is the plasma resonance frequency for a metal sphere in air ($\epsilon_2 = 1$). In the absence of radiation damping and current dissipation, the quality factor for each eigenmode (transverse or in-plane) is infinity. Thus, the system has no coupling to the external environment and hence the incident radiation can be set to zero ($\mathbf{E}_{\text{ext}} = 0$) for investigating the eigenmodes of the array.²¹ The solutions to dispersion equations (3.5b) and (3.7a) are then $M_z = M'_{||,11} = M'_{||,22} = 0$. Therefore, the dispersion relations for the eigenmodes of 2D periodic array made by lossless metal nanospheres in quasi-static limit result²¹

$$\omega^2 = \omega_{\text{LSPR}}^2 (1 - a^3 \beta_z) \quad (3.11a)$$

$$\omega^2 = \omega_{\text{LSPR}}^2 \left\{ 1 - \frac{a^3}{2} \left[\beta_{||,11} + \beta_{||,22} + \sqrt{(\beta_{||,11} - \beta_{||,22})^2 + 4\beta_{||,21}^2} \right] \right\} \quad (3.11b)$$

$$\omega^2 = \omega_{\text{LSPR}}^2 \left\{ 1 - \frac{a^3}{2} \left[\beta_{||,11} + \beta_{||,22} - \sqrt{(\beta_{||,11} - \beta_{||,22})^2 + 4\beta_{||,21}^2} \right] \right\} \quad (3.11c)$$

for transverse, TI, and LI modes, respectively.

In the quasi-static limit, the $\boldsymbol{\beta}$ is a dyadic of lattice sum of dipolar Green's function in which the retardation is disregarded.²¹

$$\beta_z = - \sum_{\mathbf{R} \neq 0} \frac{e^{i\mathbf{k}_B \cdot \mathbf{R}}}{R^3} \quad (3.12a)$$

$$\beta_{||} = \begin{pmatrix} \beta_{||,11} & \beta_{||,12} \\ \beta_{||,21} & \beta_{||,22} \end{pmatrix} = \sum_{\mathbf{R} \neq 0} \frac{e^{i\mathbf{k}_B \cdot \mathbf{R}}}{R^3} \begin{pmatrix} 3 \frac{R_x^2}{R^2} - 1 & 3 \frac{R_x R_y}{R^2} \\ 3 \frac{R_x R_y}{R^2} & 3 \frac{R_y^2}{R^2} - 1 \end{pmatrix} \quad (3.12b)$$

Since $\boldsymbol{\beta}$ is expressed in $1/d^3$ times a dimensionless number that is independent of d , the dispersion relations (3.11) have bandwidths proportional to a^3/d^3 that corresponds to the coupling strength exhibited by one-dimensional linear chain of metal nanospheres.¹⁶⁹ Because of such coupling coefficient, the coupling effect among dipoles can be enhanced by increasing the radius and decreasing the lattice spacing.²¹ However, in order to guarantee the accuracy of the dipolar

approximation preventing the appearance of Mie resonances at higher-orders, the radius a of nanospheres have to be smaller enough such that the lattice spacing d is not less than $3a$.²¹

3.1.3 Dynamic response

In real cases, the dipole approximation is not still valid due to the retardation effects and the intrinsic loss of the metal, hence an electrodynamic approach is required to investigate the optical response of a 2D infinite array of metal nanospheres.²¹ Such a problem can be addressed by considering the response of plasmonic spheres – characterized by a dielectric function (1.18a) with a finite damping term – to an external driving field oscillating at the resonance frequency. From Equations (3.5b) and (3.7), it results

$$p_z = \alpha_{\text{eff},z} E_{\text{ext},z} \quad (3.13a)$$

$$p'_{||,j} = \alpha_{\text{eff},j} E'_{\text{ext},j} \quad (3.13b)$$

$$\alpha_{\text{eff},z} = \frac{1}{M_z} \quad (3.13c)$$

$$\alpha_{\text{eff},j} = \frac{1}{M'_{||,jj}} \quad (3.13d)$$

with $j = \{1, 2\}$ accounting for the in-plane modes. In Equations (3.13), the effective polarizability α_{eff} represents the effective response of a reference particle to the local field. Thus, both the intrinsic polarizability of the metal and the scattering – arising from the other nanospheres located at the periodic lattice sites – contribute to α_{eff} . By following this approach, both single particle properties and interparticle coupling – in which geometrical information and periodic boundary conditions are included – are inherently considered.²¹ In case of infinite 2D lattice with one sphere per unit cell, each nanoparticle has the same effective polarizability. Therefore, the extinction cross section for each sphere is obtained from the optical theorem.^{38,58}

$$\sigma_{\text{ext}} = \frac{4\pi\omega}{c} \Im\{\alpha_{\text{eff}}(\omega)\} \quad (3.14)$$

As a function of the driving frequency, the imaginary part of α_{eff} exhibits resonance peaks,¹⁷⁰ which are quite well predicted by the dynamic dispersion relations obtained by finite-chain solution.¹⁶⁹

To derive α_{eff} , the lattice sum S of the dynamic dipolar Green's function (3.1b) has to be evaluated.¹⁷¹

$$\alpha_{\text{eff}} = \frac{1}{\frac{1}{\alpha_0} - S} \quad (3.15)$$

While the lattice sums of short-range and intermediate-range terms converge and can be numerically calculated with a satisfactory accuracy – as long as the spatial lattice is large enough –, the lattice sum of the long-range term diverge for real ω .²¹ Several methods have been developed to deal with such kind of lattice sum. If the dipole array is dense, namely, the dipole spacing is far less than the incident wavelength, an integral method can be applied to evaluate that lattice sum.^{172,173} More rigorous and general methods rely upon a straightforward application of the Poisson's equation, in which the summing of the long-range term on an infinite and complete 2D lattice is carried out by splitting the term into two parts, with one fast converging on the spatial lattice and the other on reciprocal lattice.¹⁷⁴ For the case when the wavevector is perpendicular to the plane of the array, the retarded dipole sum reads²²

$$S = \sum_{i \neq j} \left[\frac{(1 - i\mathbf{k} \cdot \mathbf{r}_{ij})(3 \cos^2 \theta_{ij} - 1)}{r_{ij}^3} + \frac{k^2 \sin^2 \theta_{ij}}{r_{ij}} \right] e^{i\mathbf{k} \cdot \mathbf{r}_{ij}} \quad (3.16)$$

where θ_{ij} is the angle between \mathbf{r}_{ij} and the direction of the polarization induced by the incident electric field.

3.1.4 Plasmonic surface lattice resonance

In addition to the near-field coupling – occurring when nanoparticles are arranged in a relatively densely packed way –, a significant improvement in the quality factor of the plasmon resonance is achievable by involving the far-field coupling.^{22,175} When a number of particles are randomly distributed, the scattered fields impinging on a given particle have no particular phase relationship and these effects of the scattered fields are minor.^{22,176} However, when metal nanoparticles are arranged in a periodic array characterized by a lattice spacing comparable with the wavelength of the incident light, the scattered fields impinging on a given particle – producing by the diffraction of the incident light in the plane of the array – can arrive in phase with the impinging waves giving rise to the so-called surface lattice resonance (SLR). Thus, by properly tuning the array design in terms of both nanoparticle size and lattice period, the quality factor of the lattice resonance can be significantly improved since the scattered fields can act to counter the damping of the single particle response (Figure 3.2).^{22,171,177}

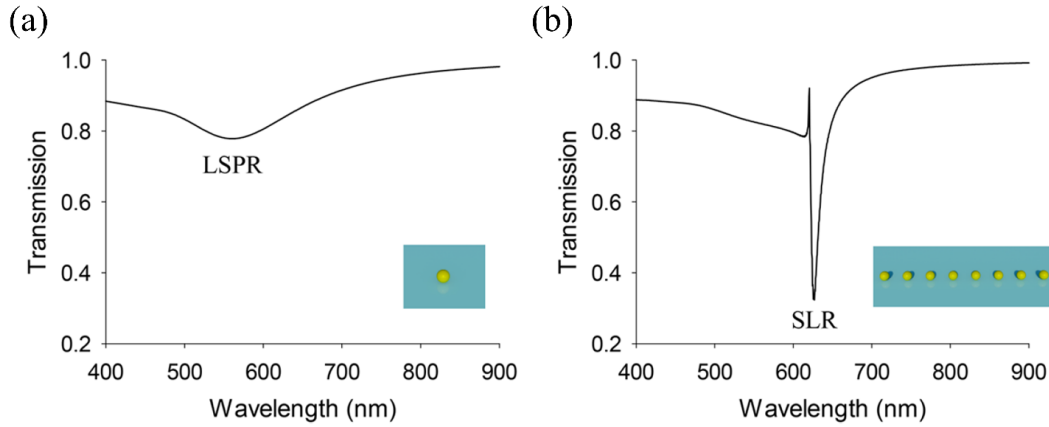


Figure 3.2. Comparison of (a) LSPR and (b) SLR in transmission spectra calculated by considering the retardation effects in DDA method, the so-called Doyle's approximation (AuNPs of 160 nm diameter, lattice period of 620 nm, total number of AuNPs along the chain is 1000). The insets show a schematic representation of the nanoparticle arrangement (from Ref. 22).

3.2 Fabrication of nanostructured substrates

A large variety of techniques to fabricate 2D-arrays of metal nanoparticles is widely emerging in the last few years since their unique properties are of growing interest in many fields of application such as nanoelectronics,¹⁷⁸ optical imaging,¹⁷⁹ biomedicine,¹⁸⁰ sensing,¹⁸¹ photovoltaics.¹⁸² Nevertheless, one of the main challenges in the development of devices relying on such 2D arrays is the particle arrangement and their integration on surfaces. Indeed, some of the most interesting electronic, optical, or biological properties only appear in well-ordered nanoparticle arrays.^{22,171,178,181}

In a first approximation, the optical behaviour of a 2D AuNP array is closely related to the ratio R between the nanoparticle diameter D and the interparticle distance d . In fact, when a nanoparticle is placed in close proximity to its nearest neighbours ($R > 2/3$),⁶⁵ the near-field interaction among the LSPs gives rise to a long-range collective oscillation.^{183,184} Such a collective effect is negligible if $R < 2/3$, in which case the optical response of the array is well-described by a system of decoupled LSPs.⁶⁵

Self-assembly is an intriguing method to efficiently order large numbers of small particles on macroscopic surfaces. In order to obtain arbitrary patterns, nanoparticles can first be self-assembled on a lithography defined template and then be transferred onto the substrate. Such a printing strategy has been proven to be efficient to produce patterns of gold nanoparticles with a single particle

resolution.¹⁸⁵ A promising alternative is represented by colloid lithography where nanoparticles are closely packed to form mono-layer of periodic structure on a substrate which can be then transferred by etching or lift-off.^{186,187} When fabrication affordability and scalability as well as optical tunability are required, chemical self-assembly and block copolymer nanolithography techniques stand out over the rest since their capability to easily produce arrays of randomly positioned and well-ordered nanoparticles, respectively.^{188,189}

3.2.1 Electrostatic self-assembly of gold nanoparticles

Silanization process through (3-Aminopropyl)triethoxysilane (APTES) was used to chemically modify the substrate surface allowing the random immobilization of citrate-stabilized AuNPs by simple adsorption via electrostatic interactions.¹⁸⁸ The procedure included five steps (described in detail in Appendix B.1) schematically shown in Figure 3.3. (a) The substrates were copiously cleaned to remove any impurities. (b) The surface was activated by oxygen plasma treatment leading to its oxidation and formation of silanol bonds, which served as bonding sites for silane molecules. The silanols provided the substrate with hydroxyl surface functionality that gave rise to a high negative surface charge. (c) The activated surface was modified by depositing APTES by controlled low-pressure evaporation inside a vacuum desiccation chamber that provided the surface with a monolayer of positively charged amino-terminated silanes. Silane multilayers could be easily formed during the silanization procedure causing the subsequent AuNP aggregation. In order to avoid the silane polymerization, the abrupt desiccation of APTES onto glass surface had to be avoided by smoothly changing the pressure level into the desiccation chamber. (d) The silanized substrates were incubated with citrate-AuNPs thereby promoting electrostatic interaction between the negatively charged citrate shell of AuNPs and the positively charged amino groups of silane. (e) A low-pressure oxygen plasma treatment etched the free citrate ligands and silane layer leaving the bare AuNPs strongly anchored to the substrate.

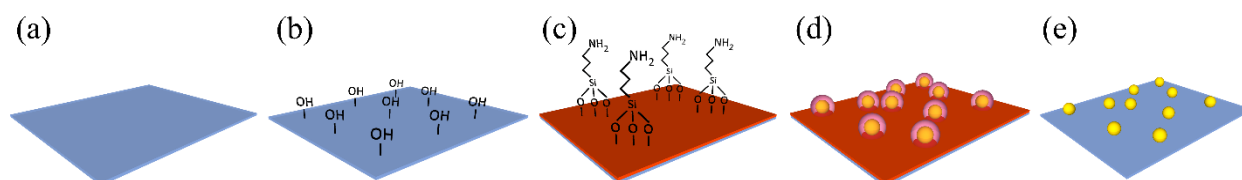


Figure 3.3. Fabrication process of 2D arrays of randomly positioned AuNPs through electrostatic self-assembly. (a) Substrate cleaning. (b) Surface activation by oxygen plasma. (c) Surface silanization. (d) Citrate-AuNP immobilization. (e) Citrate and silane layer etching.

3.2.2 Block copolymer micelle nanolithography

Block copolymer micelle nanolithography (BCMNL) was employed to produce arrays of ordered AuNPs with tunable density, size and interparticle distance (see Appendices B.2 and B.3 for more details about the fabrication).¹⁸⁹ Diblock copolymers with amphiphilic character (Figure 3.4a) were dispersed in a non-polar solvent obtaining reverse micelles with a spherical shape made by a hydrophilic core and an outer hydrophobic shell (Figure 3.4b). The resulting micelle can house the gold precursor inside, allowing the formation of AuNPs covered by a hydrophobic shell (PS-AuNPs) (Figure 3.4c). The substrates were then dipped into the solution containing PS-AuNPs by a dip coater to ensure a careful tuning of the dipping speed. Thus, the PS-AuNPs were transferred on the non-polar surface by hydrophobic interaction giving rise to a self-assembled honeycomb lattice (Figure 3.4d). The close-packing density of PS-AuNPs strongly depends on the dipping speed. In particular, a sufficiently slow dipping speed allows the PS-AuNPs to adhere onto the substrate attaining the highest close-packing density. The reduction of the surface density entailed by an increase of the dipping speed causes the presence of vacancies in the honeycomb lattice thereby promoting the formation of branched arrays of PS-AuNPs (Figure 3.4e). Then, the copolymers were etched by oxygen plasma treatment leaving the AuNPs immobilized onto the substrate at predetermined positions (Figure 3.4f and g).

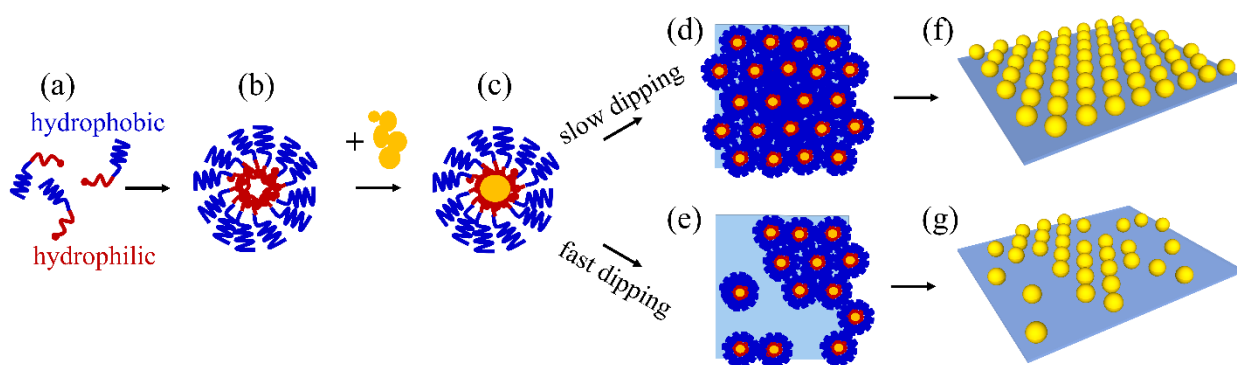


Figure 3.4. Fabrication process of 2D arrays of ordered AuNPs through BCMNL. (a) Dispersion of diblock copolymers with amphiphilic character in non-polar solvent. (b) Formation of reverse micelles with hydrophilic core and outer hydrophobic shell. (c) Loading of the gold precursor inside the micelles. Sticking of the PS-AuNPs onto the substrate through hydrophobic interaction thereby realising honeycomb lattices with (d) high close-packing density (slow dipping speed) and (e) low close-packing density (high dipping speed). (f,g) Copolymer etching by oxygen plasma treatment.

Subsequent incubation in a gold growth solution (see Appendix A.3 for more details) entailed the increase of the AuNP size while holding unchanged the lattice parameter (i.e. the centre-to-centre distances among nearest neighbours) (Figure 3.5).¹⁹⁰ The resulting reduction of the interparticle

distance entailed an increase of the ratio R up to a value large enough to activate collective plasmonic effects of the array.^{65,184}

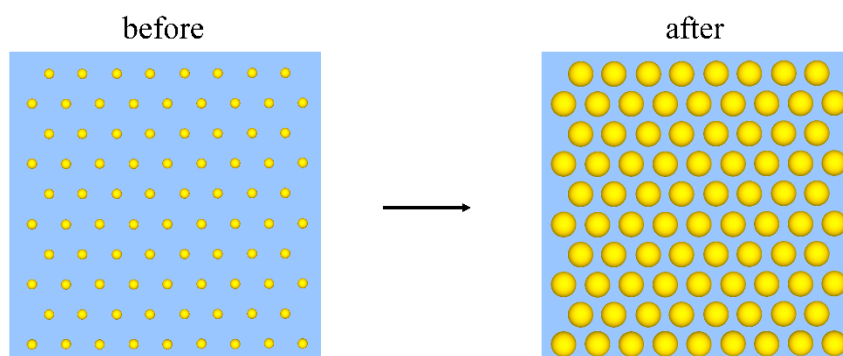


Figure 3.5. Increase of the AuNP size following the substrate incubation with gold growth solution.

3.3 Morphological and optical characterization (measurements and numerical simulations)

3.3.1 Array of randomly positioned AuNPs

The substrates were morphologically characterized by scanning electron microscopy (SEM) (see Appendix C.1 for the details about the analysis of the SEM images). SEM micrographs at low magnification show spherical nanoparticles randomly distributed onto the substrate as both single particles and clusters (Figure 3.6a). The presence of clusters is ascribable to the occurring of nanoparticle aggregation during the incubation of silane-modified substrates with citrate-stabilized AuNPs due to silane multilayer spots that could arise from the silanization process.¹⁸⁸ Particle density can be easily tuned by changing the citrate-stabilized AuNP concentration and the incubation time.¹⁹¹ Aiming at using such nanostructured substrates as biosensing platform (see Figure 4.7), the densest packing of nanoparticles was reached – corresponding to (340 ± 30) AuNPs per μm^2 – to warrant the maximum number of binding sites available for immobilizing the bioreceptors.

Figure 3.6b and c show the distributions concerning the aspect ratio AR and circularity C of the immobilized AuNPs, respectively. The mean values $\overline{AR} = 1.4 \pm 0.4$ and $\bar{C} = 0.90 \pm 0.14$ convey high regularity in nanoparticle roundness. Size distribution is peaked at approximately 31 nm with a standard deviation of 12 nm (Figure 3.6d) pointing out no morphological changes were induced during the substrate fabrication process (see Figure 2.11 for the morphological characterization of colloidal AuNPs). Right tail of the histogram is due to AuNP clusters as a byproduct of silane-induced

aggregation. Figure 3.6e shows the histogram of the centre-to-centre distances whose distribution turns out to be quite broad with 67 nm mean value and 19 nm standard deviation as a result of the randomness of the nanoparticle immobilization onto the substrate.

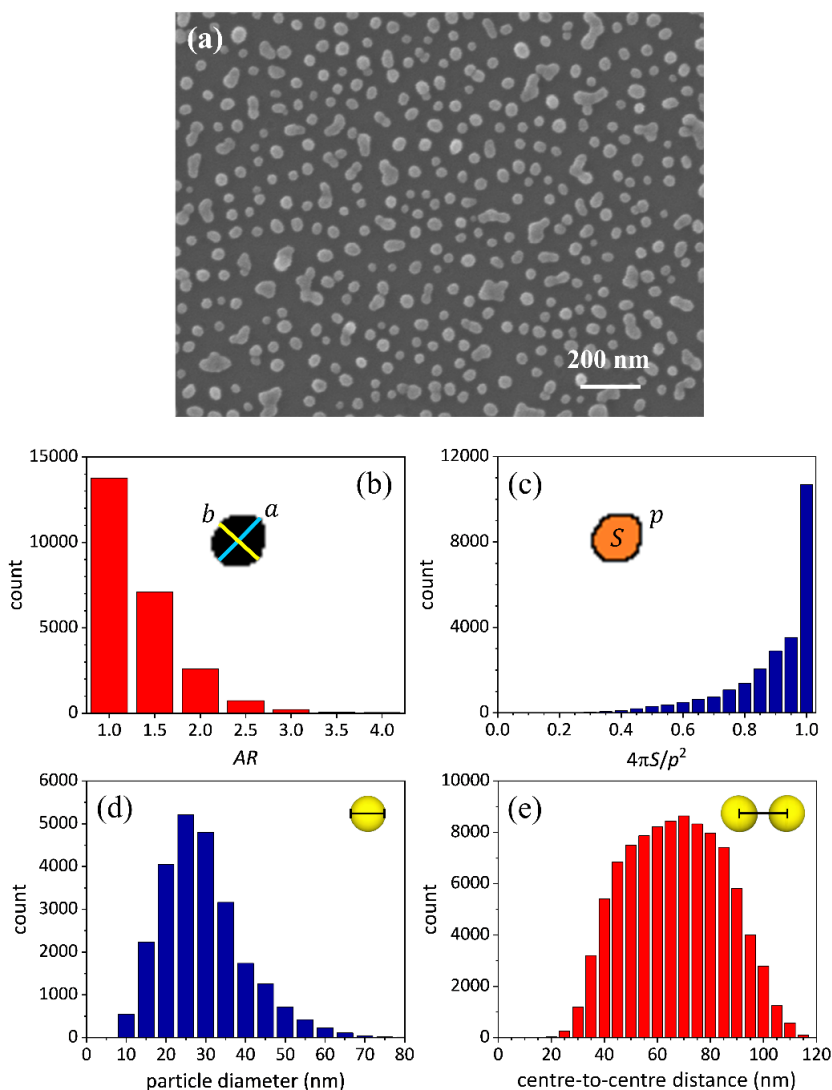


Figure 3.6. Morphological characterization of the substrate. (a) Top view SEM micrograph of the 2D AuNP array. (b) Histogram of AuNP aspect ratio, the highlighted lines in the inset represent the major (light blue) and minor (yellow) axis of the examined object. (c) Histogram of AuNP circularity, the inset shows an example of nanoparticle decomposed in perimeter (black line) and area (orange filling). (d) Nanoparticle diameter distribution. (e) Centre-to-centre distance distribution.

The substrates were also optically characterized through UV-Vis spectroscopy by measuring the extinction spectrum. Figure 3.7 shows the experimental extinction spectrum of the substrate (solid red line), which contains two plasmonic resonances occurring at (i) 524 nm and (ii) 620 nm. (i) Single nanoparticles far enough from their nearest neighbours ($d > 3/2 D$)⁶⁵ contribute to the resonance occurring at smaller wavelength, as expected for 30 nm diameter gold nanospheres in air,^{192,193} whereas (ii) AuNP clusters give rise to a shoulder at higher wavelength.¹⁹² The consistent agreement

between the experimental extinction spectrum (solid red line) and that worked out by numerical simulation (solid blue line) provides assurance about the holding at macroscopic level of the observed micrometric morphology (see Appendix C.2 for the details on the simulation code).

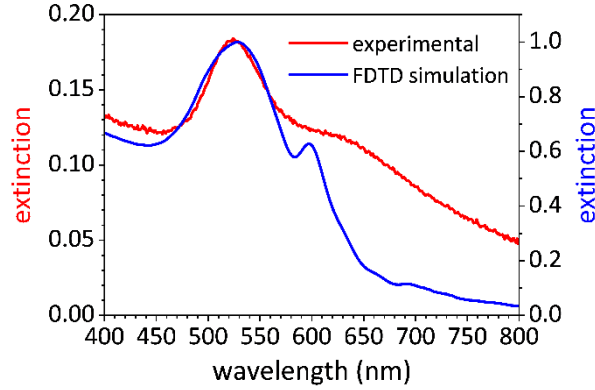


Figure 3.7. Experimental (solid red line) and simulated (solid blue line) extinction spectrum of the substrate.

3.3.2 Array of ordered AuNPs

Aiming at investigating and optimizing the performance of the substrate, a test campaign was conducted through FDTD numerical simulations where the optical response of the system was analysed as a function of both the polarization direction and the characteristics of the 2D lattice. A schematic representation of the simulation workspace and unit cell are shown in Figure 1.22 and Figure 3.8a, respectively. The electric field \mathbf{E} (E-field) intensity exhibits a maximum in the x - y plane along the polarization direction, while it shows a minimum in the transverse direction (Figure 3.8b). By rotating the direction of polarization around z , an azimuthal E-field intensity modulation was observed with an expected period of 60° (Figure 3.8b-e).

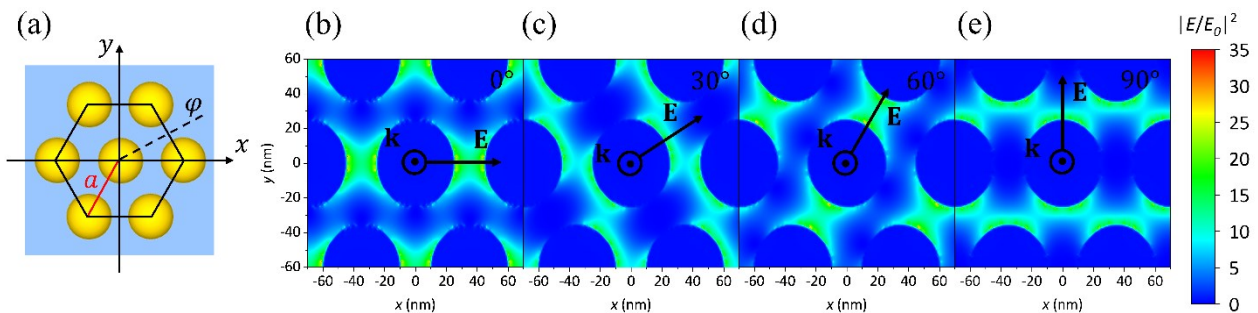


Figure 3.8. (a) Top view sketch of the simulation unit cell; the centres of the spherical AuNPs belong to the plane $z = 0$. The parameter a and φ are the lattice constant and the azimuthal angle, respectively. (b,e) Gain of the E-field intensity delivered by a 2D AuNP honeycomb lattice (50 nm diameter, 20 nm interparticle distance) as a function of the polarization direction worked out in the x - y plane ($z = 0$).

Since all the polarization directions have to be taken into account when non-polarized light is used (e.g., light emitted by a fluorophore), the actual local E-field intensity is the result of the average of all such contributions (Figure 3.9a). It turns out that the gain factor $|E/E_0|^2$ slightly modulates around a value of 4 when φ is changed from 0° - 360° and the distance is 10 nm from the nanoparticle surface (Figure 3.9b), thereby suggesting that the E-field intensity experienced by a molecule placed at approximately 10 nm separation distance has a relatively weak azimuthal dependence. It is worth to highlight that such a separation distance is of interest in many biosensing applications relying on the analyte detection through a sandwich scheme (see Figure 4.7).

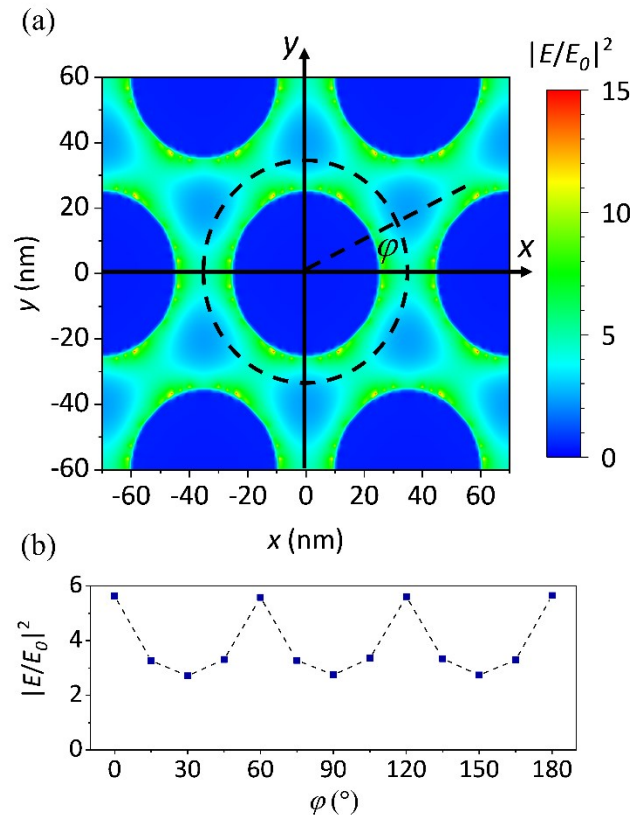


Figure 3.9. (a) Gain of the E-field intensity worked out by averaging the optical response delivered by the AuNP honeycomb lattice (50 nm diameter, 20 nm interparticle distance) at different polarization angle of the interacting E-field from 0° to 165° with a step of 15° . (b) Modulation of the gain factor as a function of the azimuthal angle φ .

The analysis as a function of the polar angle θ is reported in Figure 3.10 that shows the distribution of the E-field intensity in the $y = 0$ plane, resulting from the interaction of an x -polarized plane wave with a 2D honeycomb lattice (Figure 3.8a) made of 50 nm AuNPs distanced 20 nm one from the other. Due to the plasmon coupling, the largest values of the field intensity are recorded along the direction of polarization (x) while the smallest values are measured in the transverse direction to the

plane $z = 0$. In particular, the gain is more effective in the interval $45^\circ \leq \theta \leq 135^\circ$ that contains $\sim 70\%$ of the available surface.

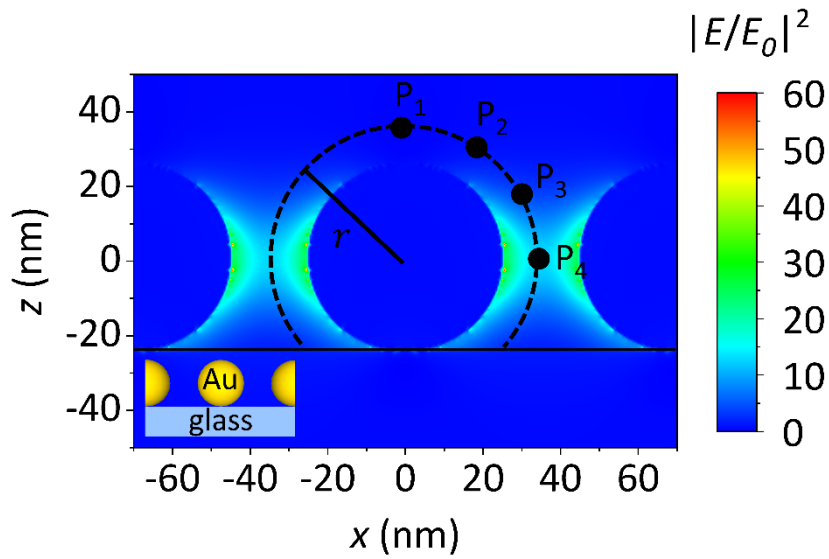


Figure 3.10. Gain of the E-field intensity worked out in the plane $y = 0$ for x -polarized EM plane wave incident on the AuNP honeycomb lattice (50 nm diameter, 20 nm interparticle distance). The points P_1 - P_4 are at a distance of 10 nm from the nanoparticle surface at polar angle $\theta = 0^\circ, 30^\circ, 60^\circ$ and 90° , respectively.

Once the dependence on the light polarization was understood, the optical behaviour of the 2D lattice was investigated by varying the particle size and interparticle distance over large intervals (25 nm/10 nm, 50 nm/20 nm, 75 nm/30 nm, 100 nm/40 nm) while keeping constant their ratio $R = 2.5$, a value that is large enough to warrant a high enhancement factor.^{65,184} Figure 3.11 shows the enhancement of the E-field intensity for several polar angles ($\theta = 0^\circ, 30^\circ, 60^\circ, 90^\circ$) at a distance of 10 nm from AuNP surface (points P_1 - P_4 in Figure 3.10).

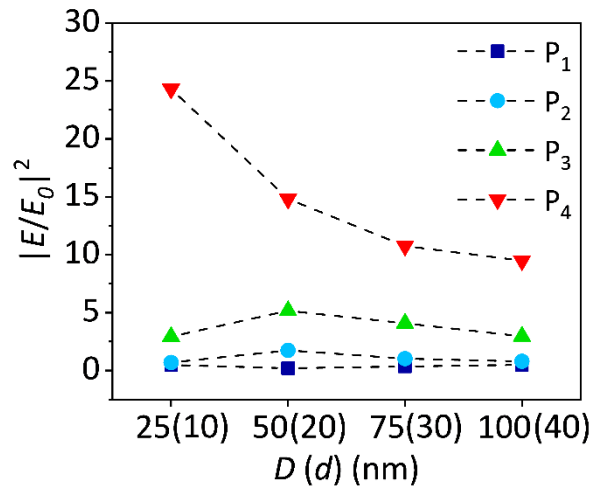


Figure 3.11. Gain of the E-field intensity as a function of AuNP diameter (interparticle distance).

Despite the strongest gain was achieved for the smallest nanoparticles, the need to allow the formation of the sandwiches (capture bioreceptor-analyte-second bioreceptor) in the interparticle gaps suggested one to consider 50 nm/20 nm as the optimal choice to guarantee good enhancement of the E-field intensity while assuring that the process of functionalization and detection occurs correctly.

The characterization of the fabricated substrates was performed by scanning electron microscopy and UV-Vis spectroscopy (see Appendix C.1 for details about the analysis of the SEM micrographs). SEM images of the substrate (Figure 3.12a) show the fabrication process capability to attain maximum control over the geometrical characteristics of the device, including particle size and particle distance. Aiming at realizing a substrate with a unique collective plasmonic behaviour, the nanoparticle growth is carried out to increase the R value (Figure 3.12b). The nanoparticle diameter increased approximately five-fold while the interparticle distance reduced three-fold by holding the lattice period equal to ~ 70 nm. The R value went from 0.17 to 2.5 warranting a collective response of the AuNPs immobilized on the substrate (Figure 3.12c).^{65,184}

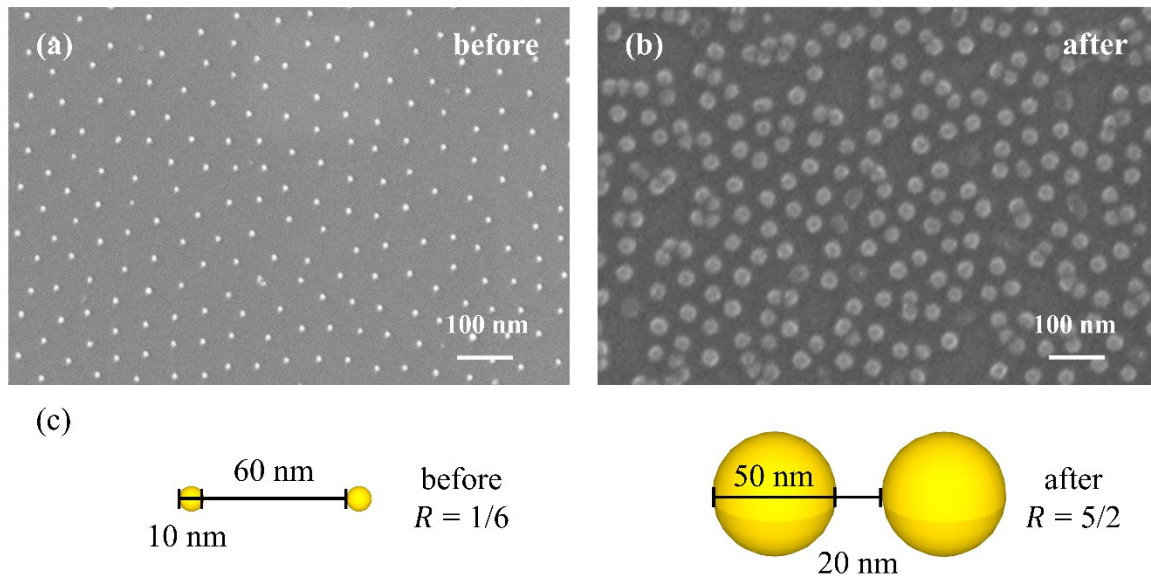


Figure 3.12. Top view SEM micrographs of the substrate (a) before and (b) after the AuNP growth. Defects arising during the growth step such as clusters and vacancies are randomly distributed on the substrate. (c) Sketch of the AuNP growth process.

Figure 3.13a and b show the histograms of the aspect ratio AR and circularity C distributions of the immobilized AuNPs before (blue columns) and after (red columns) gold growth process, respectively. The mean values $\overline{AR} = (1.2 \pm 0.4)$ and (1.3 ± 0.5) measured before and after nanoparticle enlargement, respectively, as well as $\bar{C} = (0.8 \pm 0.2)$ and (0.9 ± 0.2) convey high regularity in nanoparticle

roundness held after nanoparticle growth. The quite long tails on the left side of the circularity distributions are due to the image pixilation that overestimates the perimeter (inset of Figure 3.13b). The size distribution of the AuNPs before the gold growth process (blue columns) is peaked at approximately 10.4 nm with a full width at half maximum (FWHM) of 1.4 nm, while that after nanoparticle growth (red columns) has a mean of ~ 48 nm and a FWHM of 6 nm (Figure 3.13c). The smaller peak at approximately 61 nm (red columns) is due to fewer AuNP clusters as a byproduct of the gold nanoparticle growth process. The centre-to-centre distance d_{C-C} , measured as the distance of each AuNP centroid with its nearest neighbours follows the distributions in Figure 3.13d. The mean values \bar{d}_{C-C} are 69 nm (blue columns) and 68 nm (red columns) with standard deviations of 8 nm and 14 nm, respectively. The high similarity of such distributions confirms the holding of most of AuNP positions also after the growth process, whereas the relatively large values of standard deviation for \bar{d}_{C-C} can be ascribed to defects such as clusters and vacancies. The occurrence of d_{C-C} lower than D after the growing process (red histograms in Figure 3.13c and d) is due to the lack of the AuNP spherical shape arising from nanoparticle clustering (Figure 3.12b).

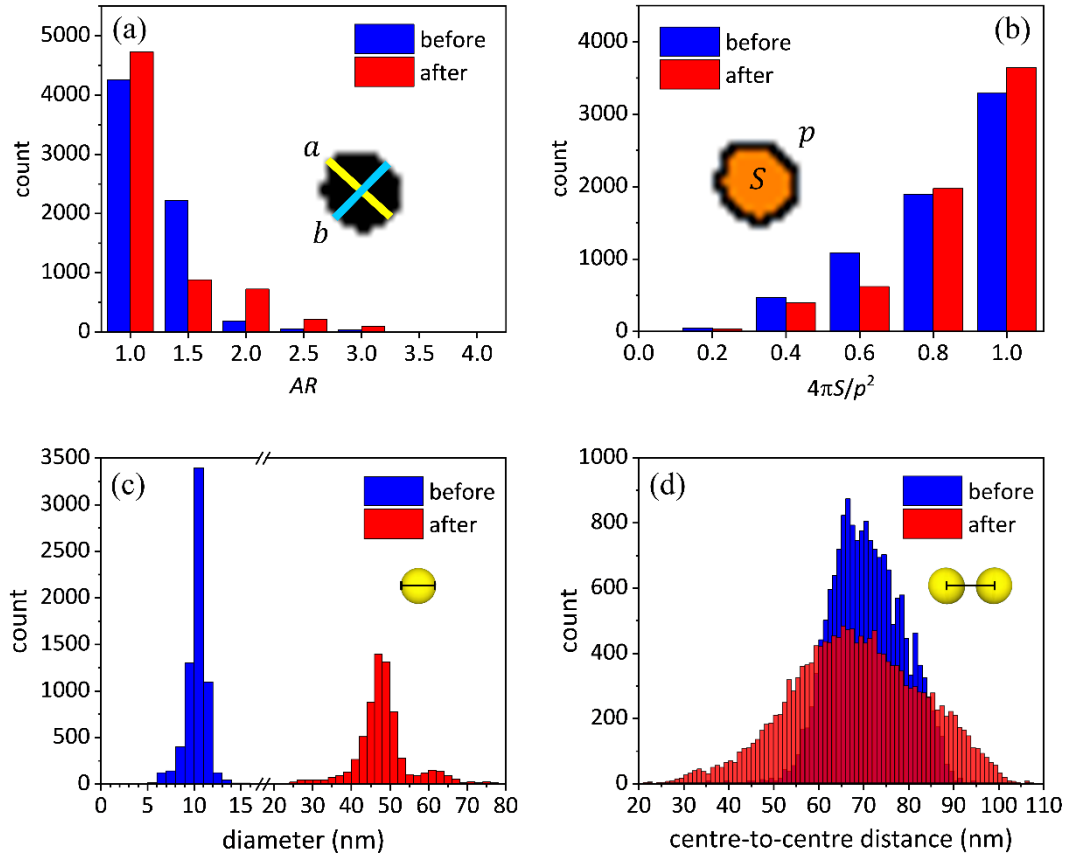


Figure 3.13. Histograms of (a) nanoparticle aspect ratio, (b) nanoparticle circularity, (c) nanoparticle diameter, and (d) centre-to-centre distance before (blue columns) and after (red columns) incubation with gold growth solution. The wider distribution delivered by the substrates after the AuNP growth (red columns) is due to the presence of lattice irregularity and defects arising during the growth process.

The 2D AuNP array was also characterized optically by measuring its extinction spectrum whose resonance wavelength and shape are not only strongly dependent on the ratio R ,^{65,175} but also on the regularity holding at high macroscopic level, a feature warranted by the array fabrication procedure adopted in this work (see Figure E.3 for SEM images at low magnification). The experimental extinction spectrum (solid green line in Figure 3.14) is well reproduced by that one worked out by considering the real morphology of the substrate as provided by SEM (solid gold line) (see Appendix C.2 for details on the simulation code), the latter being obtained by averaging the extinction spectra resulting from fifteen regions of interest sampled from the SEM image shown in Figure E.4a (an example of the rendering provided by Lumerical is shown in Figure E.4b, whereas some of the simulated extinction spectra are reported in Figure E.4c). The consistent agreement between the experimental extinction spectrum and that worked out by FDTD provides assurance that the observed spectral profile is the result of the collective plasmonic behaviour exhibited by a 2D array made of spherical AuNPs, and that the quite large experimental spectral broadening also arises from the partial reduction of the degree of the spatial order due to the growth process.

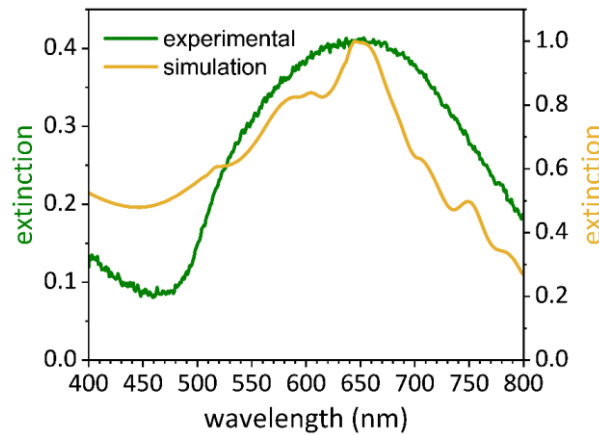


Figure 3.14. Experimental (solid green line) and simulated (solid gold line) extinction spectrum of the substrate.

3.3.3 Branched array of AuNPs

The substrates were morphologically and optically characterized by scanning electron microscopy and UV-Vis spectroscopy, respectively (see Appendix C.1 for details about the analysis of the SEM images). Figure 3.15a shows a SEM micrograph at high magnification of the astonishing branch pattern realized through BCMN by simple increasing the dipping speed of the substrate into the PS-AuNPs solution as depicted in Figure 3.4e (see Figure E.5 for SEM images at low magnification). Aiming to activating the collective response of the AuNPs arranged along the branches, the gold

growth is carried out (Figure 3.15b) to increase five-fold the R value from $3/5$ to 3 (Figure 3.15c).^{65,184} A higher number of isolated AuNPs appears as a byproduct of the growth process. Instead of representing a detriment, such single AuNPs promote the occurrence of localized resonance modes in addition to the collective mode arising along the branches thereby activating two different plasmonic resonances for such a substrate. The nanoparticle size distribution before the gold growth process is peaked at approximately 29 nm with a standard deviation of 7 nm (Figure 3.15d), while that after nanoparticle growth has a mean value at ~ 58 nm and $\sigma = 22$ nm (Figure 3.15e). The relatively broader size distribution as a result of the gold growth is due to the presence of smaller isolated AuNPs and clusters.

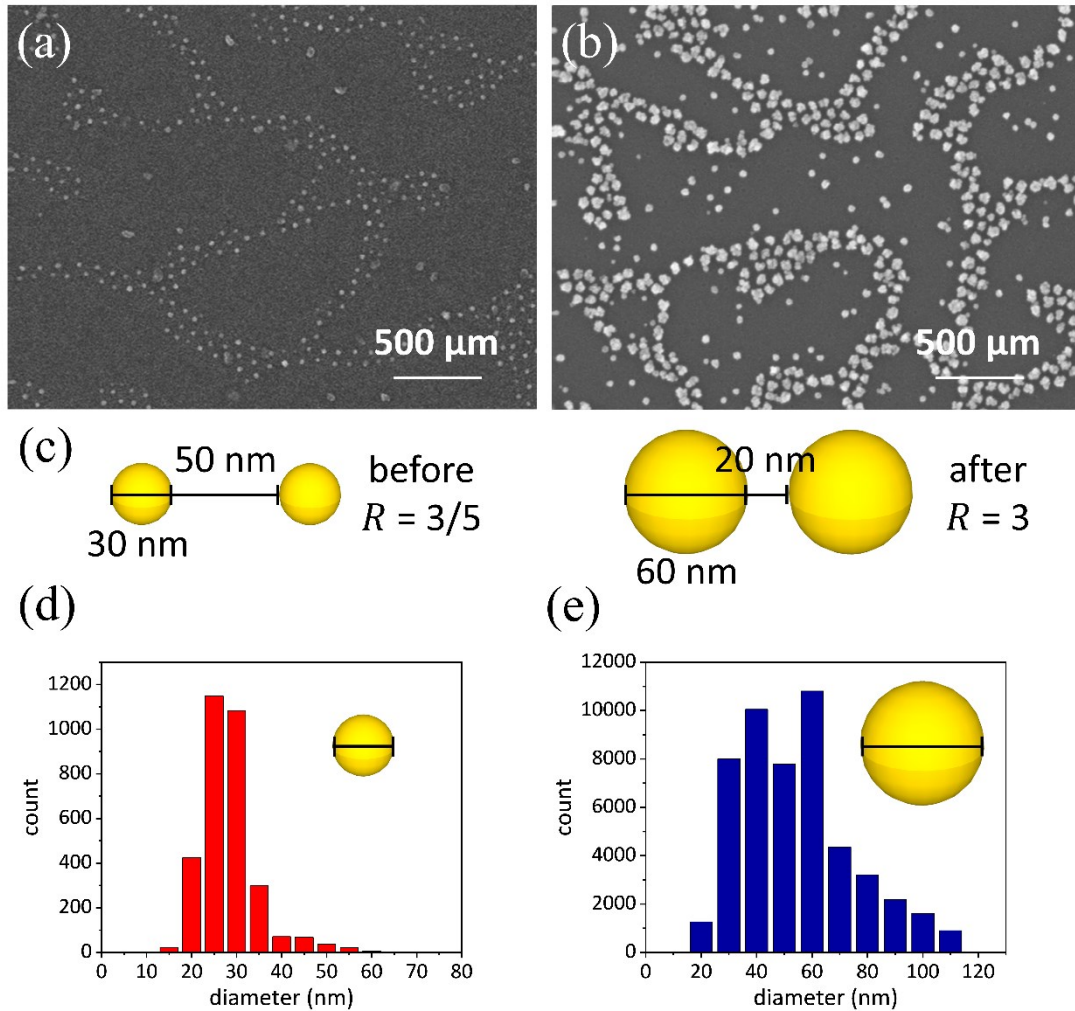


Figure 3.15. Top view SEM micrographs of the substrate at high magnification (a) before and (b) after the AuNP growth. (c) Sketch of the nanoparticle growth process. Histograms of the nanoparticle diameter (d) before and (e) after the gold growth process.

The experimental extinction spectrum (solid blue in Figure 3.16) is well reproduced by that one worked out through FDTD simulations by considering the real morphology of the substrate as

provided by SEM (solid orange line) (see Appendix C.2 for the details on the simulation code). The experimental extinction spectrum of the substrate contains two plasmonic resonances occurring at (i) 524 nm and (ii) 675 nm. (i) Isolated AuNPs contribute to the resonance occurring at smaller wavelength, as expected for 30 nm diameter gold nanospheres in air,^{192,193} whereas (ii) AuNPs arranged along the branches give rise to a collective resonance mode at higher wavelength.¹⁹²

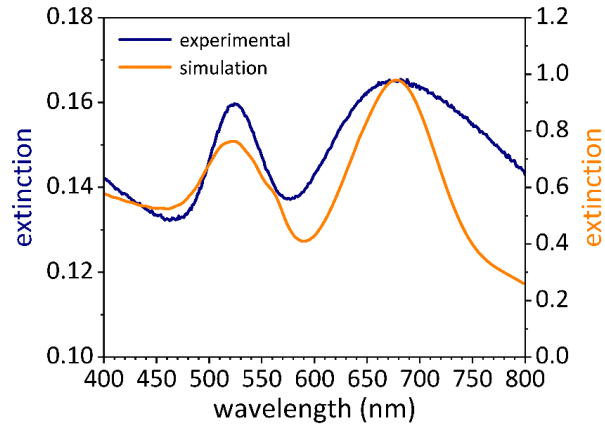


Figure 3.16. Experimental (solid blue line) and simulated (solid orange line) extinction spectrum of the substrate.

Chapter 4. Plasmon-enhanced fluorescence

4.1 Beyond the classical interpretation of the fluorescence

4.1.1 Fluorescence spectral modification

In the last few decades, a considerable literature is rapidly emerging modifying the classical perception of the fluorescence.^{36,194,195} While in free-space conditions the fluorophores typically emit isotropically and are observed in the far field – changes in the refractive index of the bulk sample have only minor effects on the fluorophore free-space spectral properties –, nearby conducting metal particles, colloids, or flat surfaces can alter the fluorophore free-space conditions by increasing (or decreasing) both the electric field experienced by the fluorophores, and hence the excitation rate, and the radiative decay rate. Although the physics underlying the fluorescence enhancement induced by metal nanostructures – the so-called plasmon-enhanced fluorescence (PEF) – is still to be fully understood,¹⁹⁶ these effects can be safely ascribable to the changes in the photonic mode density since a large mode density – as occurs in presence of plasmonic nanostructures – provides more radiative decay pathways and larger radiative decay rates. The radiative decay rate – i.e. the spontaneous rate at which a fluorophore emits photons – is an inherent feature of the fluorophore and it is only slightly affected by the environmental parameters (e.g. solvent polarity and temperature).¹⁹⁷ Thus, the opportunity to enhance the fluorophore emission rate through the coupling with plasmonic nanostructures is of relevance for many biomedical and biochemical applications relying on the fluorescence since it allows one to directly modify the observables such as increasing quantum yield (QY), photostability, and Förster resonance energy transfer (FRET) while reducing lifetime.

In free-space conditions, the absorption of a photon of energy $\hbar\omega_{\text{exc}}$ typically sends the fluorophore to the first excited singlet state S_1 , from which it can relax to the ground state S_0 by emitting a photon of a lower energy $\hbar\omega_{\text{em}}$ or by non-radiative decay processes including heating and quenching mechanisms.¹⁹⁷ The QY and lifetime of a fluorophore in free-space conditions (Q_0 and τ_0 ,

respectively) reflect the competitive behaviours of radiative and non-radiative processes characterized by decay rates $\gamma_0^{(r)}$ and $\gamma_0^{(nr)}$, respectively.¹⁹⁷

$$Q_0 = \frac{\gamma_0^{(r)}}{\gamma_0^{(r)} + \gamma_0^{(nr)}} \quad (4.1a)$$

$$\tau_0 = \frac{1}{\gamma_0^{(r)} + \gamma_0^{(nr)}} \quad (4.1b)$$

Although $\gamma_0^{(r)}$ does not significantly depend on the external conditions, fluorescence QY, lifetime and intensity are strongly affected by the surrounding environment due to the changes in $\gamma_0^{(nr)}$. Thus, the fluorophore spectral properties can be modified by altering $\gamma_0^{(nr)}$. Nevertheless, the enhancement of the fluorescence observables is inherently limited since Q_0 and τ_0 invariably change together. Therefore, a decrease of τ_0 entails not only an increase of $\gamma_0^{(r)}$ – as demanded to enhance the fluorescence intensity – but also a decrease of Q_0 yielding a vanishingly small probability to emit a photon. On the contrary, when a fluorophore is placed at a suitable distance from a metal surface, the enhancement of the radiative decay rate through $\gamma_p^{(r)}$ results in both an increase of the quantum yield Q_p and a reduction of the lifetime τ_p .^{36,194}

$$Q_p = \frac{\gamma_0^{(r)} + \gamma_p^{(r)}}{\gamma_0^{(nr)} + \gamma_p^{(nr)} + \gamma_0^{(nr)} + \gamma_p^{(nr)}} \quad (4.2a)$$

$$\tau_p = \frac{1}{\gamma_0^{(nr)} + \gamma_p^{(nr)} + \gamma_0^{(nr)} + \gamma_p^{(nr)}} \quad (4.2b)$$

where $\gamma_p^{(nr)}$ is rate of the quenching processes entailed by the nearby metal. Figure 4.1 shows the Jablonski diagram for fluorophore in the free-space conditions and the modified form when in close proximity to metal surface.

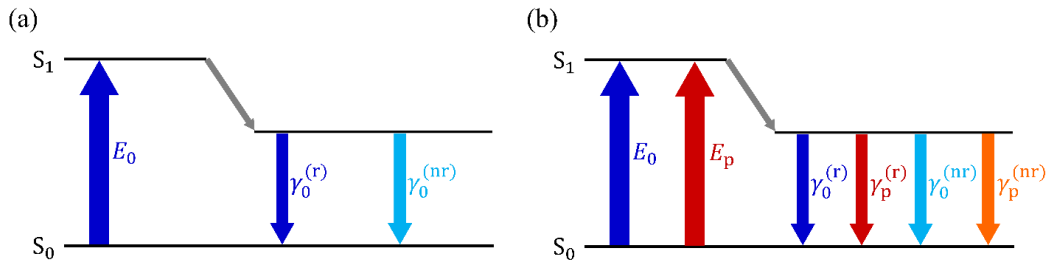


Figure 4.1. (a) Classical Jablonski diagram for the free-space conditions and (b) the modified form in the presence of a conductive nanostructure.

4.1.2 Mechanisms of plasmon-fluorescence interaction

So far three known mechanisms have been ascertained to contribute to the PEF effect: (i) modification of the fluorophore excitation rate, (ii) modification of the fluorophore radiative decay rate, (iii) energy transfer quenching to the nearby metal.^{36,194}

The energy transfer between the plasmon and the fluorophore is dominated by dipole-dipole interactions. If the fluorophore is in close proximity of the nanostructure surface (1-10 nm), the non-radiative local field of one dipole can excite the second one through FRET mechanism (Figure 4.2a and b). The efficiency of energy transfer in FRET strongly depends on the separation distance.¹⁹⁷

$$\eta_{\text{FRET}} = \frac{1}{1 + \left(\frac{R}{R_0}\right)^6} \quad (4.3)$$

where R is the fluorophore-nanostructure distance and R_0 is a factor depending on the spectral overlap between the emission of the donor excited state and the absorption of the acceptor ground state. Since the value of R_0 lies usually in the range of 3-8 nm in plasmon-fluorophore FRET, the process is efficient only for vanishingly small separation distances.¹⁹⁸

Moreover, the plasmon can enhance the radiative rate of the fluorophore through the Purcell effect by varying the local density optical states (LDOS) (Figure 4.2a and b).¹⁹⁹ In fact, if a radiative dipole is placed in a resonant cavity, the emission intensity is amplified on-resonance and quenched off-resonance when compared to free space due to the LDOS modification induced by the cavity.²⁰⁰

$$\gamma_0(\mathbf{r}, \omega) = \frac{\pi\omega}{3\hbar\epsilon_0} |\mathbf{p}|^2 \rho_{\text{LDOS}}(\mathbf{r}, \omega) + \gamma_0^{(\text{nr})} \quad (4.4a)$$

$$\rho_{\text{LDOS}}(\mathbf{r}, \omega) \sim \mathbf{n} \cdot \Im\{G(\mathbf{r}, \mathbf{r})\} \cdot \mathbf{n} \sim |E_{\text{loc}}(\omega)|^2 \quad (4.4b)$$

where γ_0 is the spontaneous emission rate of the dipole, ω is the emission frequency, \mathbf{p} is the transition dipole moment of the emitter, \mathbf{r} is the position, ρ_{LDOS} is the local density of states, \mathbf{n} is the orientation of the transition dipole of the emitter, G is the dyadic Green's function – which is the electric field interacting with the emitter due to its own radiation –, and E_{loc} is the local electric field of the cavity normalized to the incident intensity. While in air the LDOS is nearly constant and the dipole radiates at all emission energies, in the cavity the LDOS is peaked at the resonance wavelength and the dipole can emit into the resonance mode at higher rate as compared to the rate in air. The

cavity can then re-radiate the transferred energy resulting in an overall enhancement of the dipole emission.

Given the intense confinement of the EM field within the near region close to the nanostructure surface, the plasmon acts as a resonant cavity for the fluorophore entailing LDOS increase as compared to free-space conditions.²⁰¹ Thus, if the fluorophore emission spectrally overlaps with the plasmon extinction, the fluorophore emission rate is enhanced due to the change in the LDOS induced by the plasmon (Figure 4.2b). In this case, the plasmon can either absorb the transferred energy or re-radiate it as scatter resulting in a quenching or enhancement of the fluorophore emission intensity, respectively. Since the LDOS goes as $1/R^3$ for a plasmonic dipole,²⁰⁰ the Purcell effect usually takes place at separation distances longer than FRET region (> 10 nm).^{201,202} While FRET can occur equally in both directions – from plasmon to fluorophore or vice versa –, the enhancement of the plasmon radiation or scattering rate entailed by the fluorophore LDOS through Purcell effect is negligible due to the fluorophore E_{loc} comparable to the electric field in free space conditions.

The spectral overlap between the plasmon extinction and the fluorophore excitation and/or emission determines whether FRET or Purcell effect is predominant.^{198,201,203} If the plasmon overlaps with the fluorophore absorption, the fluorophore excitation rate is enhanced through FRET mechanism at separation distances of a few nanometers due to the presence of the intense E_{loc} of the plasmon, whereas a weaker coupling occurring at longer fluorophore-nanostructure distances leads to a vanishingly small enhancement of the fluorophore excitation rate (Figure 4.2a and d).^{198,201,203} On the contrary, the overlap of the plasmon with the fluorophore emission provides a large fluorescence enhancement through the Purcell effect for separation distances beyond FRET region while a progressive decrease of the radiative rate occurring at smaller distances due to the increasing quenching via non-radiative losses into the metal nanostructure (Figure 4.2b and d).^{198,201,203} Although the plasmon could re-radiate the stored energy enhancing the emission intensity, the near field of the dipole also excites higher non-radiative order modes in the plasmon preventing the re-radiation of this energy into the far field, leading to an overall quenching at separation distances of a few nanometers.^{201,202}

It is usually unfeasible to obtain a pure excitation or emission enhancement due to the limited Stoke shift of the fluorophore and the relatively broad extinction line width of the plasmon (Figure 4.2c). Thus, a balance of both mechanisms takes place yielding the so-called dual-mechanism enhancement.²⁰⁴ In such a case, an intense fluorescence enhancement arises at an optimal distances of ~ 10 - 15 nm, a strong quenching being present at shorter separation distances, whereas a return to

the no enhanced fluorescence conditions occurs at longer distances due to the weaker plasmon-fluorophore coupling (Figure 4.2d).^{198,201,202}

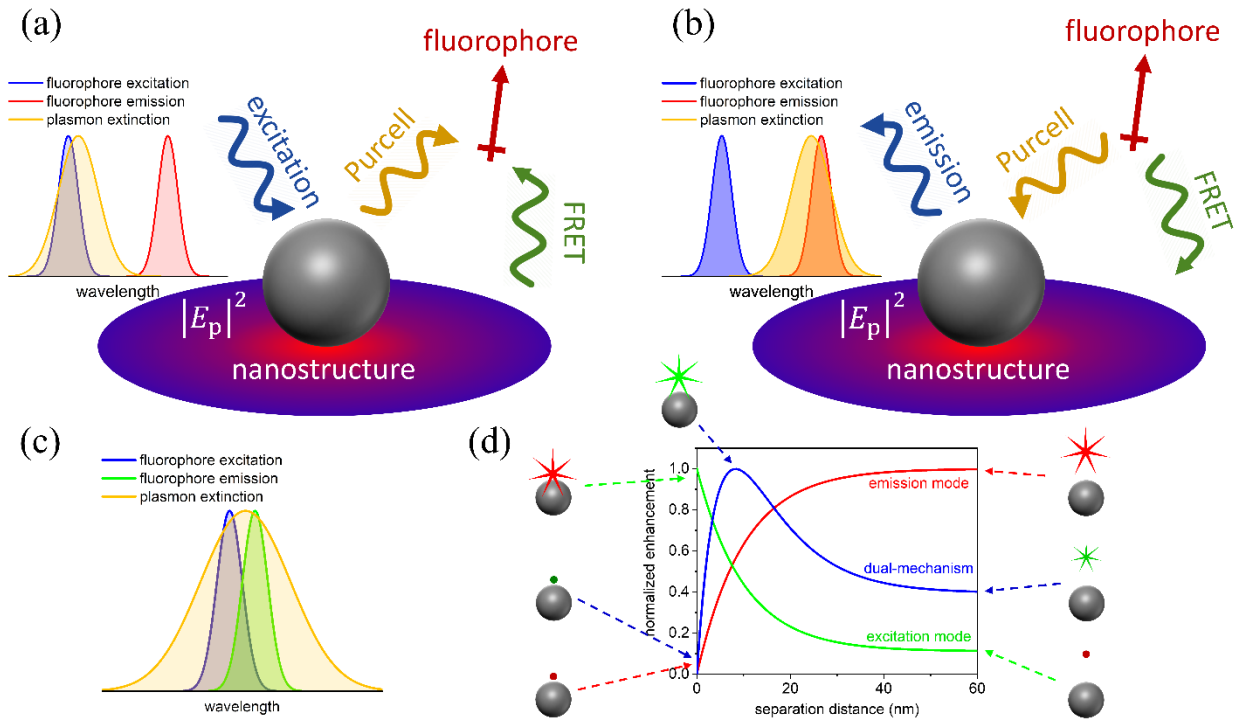


Figure 4.2. (a) Excitation mode enhancement through either FRET and Purcell effect due to the spectral overlap between the plasmon extinction and the fluorophore absorption. (b) Emission mode enhancement through either FRET and Purcell effect due to the spectral overlap between the plasmon extinction and the fluorophore emission. (c) If the plasmon extinction encompasses both the absorption and emission peak of the fluorophore, a dual-mechanism enhancement takes place. (d) Excitation (solid green line), emission (solid red line), and dual mechanism (solid blue line) enhancement as a function of the nanostructure-fluorophore separation distance.

4.2 Calculation of the fluorescence amplification

Aiming at calculating the fluorescence amplification FE delivered by a plasmonic nanostructure, three different contributions have to be considered: (i) enhancement of the fluorophore excitation rate G , (ii) enhancement of the fluorophore radiative decay rate Y , and (iii) gain of the luminescence collection efficiency K .^{200,205,206}

$$FE(\omega, \omega') = G(\omega)Y(\omega')K(\omega') \quad (4.5)$$

where ω and ω' are the excitation and emission frequency, respectively. Quite often the fields are estimated by using an electrostatic approach in which the radiative decay is neglected. Such an

approximation adequately describes the signal amplification only for non-luminescence applications such as SERS, where the strength is proportional to the fourth power of the local electric field. For the cases of photo- and electroluminescence the expression of the luminescence enhancement is more complex due to the highly efficient radiative coupling between the fluorophore and the plasmon. Unfortunately, these nonlinear quantum regimes have not been deeply explored until recently, hence a certain gap in theoretical understanding of the PEF effect has to be still filled.^{196,202}

4.2.1 Enhancement of the fluorophore excitation rate

The calculation of the field enhancement factor G can be analytically addressed within a Mie problem-like framework by considering a spheroidal metal nanoparticle upon illumination by a plane linearly polarized EM wave (see Figure 1.11 for the propagation geometry). The electric field of the incident EM wave can be written in terms of the spherical vectorial functions $\mathbf{m}_{oln}^{(0)}$ and $\mathbf{n}_{eln}^{(0)}$.^{205,207}

$$\mathbf{E}_0(\omega, \mathbf{r}) = -E_0 e^{-i\omega t} \sum_{n=1}^{\infty} i^n \frac{2n+1}{n(n+1)} (\mathbf{m}_{oln}^{(0)} - i\mathbf{n}_{eln}^{(0)}) \quad (4.6a)$$

$$\mathbf{m}_{oln}^{(0)} = \frac{\psi_n(kr)}{kr} \left(\mathbf{e}_\theta \frac{P_n^l(\cos \theta)}{\sin \theta} \cos \varphi - \mathbf{e}_\varphi \frac{\partial P_n^l(\cos \theta)}{\partial \theta} \sin \varphi \right) \quad (4.6b)$$

$$\begin{aligned} \mathbf{n}_{eln}^{(0)} = & \mathbf{e}_r n(n+1) \frac{\psi_n(kr)}{(kr)^2} P_n^l(\cos \theta) \cos \varphi \\ & + \frac{\psi'_n(kr)}{kr} \left(\mathbf{e}_\theta \frac{\partial P_n^l(\cos \theta)}{\partial \theta} \cos \varphi - \mathbf{e}_\varphi \frac{P_n^l(\cos \theta)}{\sin \theta} \sin \varphi \right) \end{aligned} \quad (4.6c)$$

where \mathbf{e}_r , \mathbf{e}_θ and \mathbf{e}_φ are the unit vectors of the spherical coordinate system, $\psi_n(kr) = \sqrt{\pi kr/2} J_{n+1/2}(kr)$ with $J_{n+1/2}(kr)$ being the Bessel function, $\psi'_n(kr)$ is the derivative with respect to the argument, and $P_n^l(\cos \theta)$ is the associated Legendre function.

The electric field induced near a particle in the EM wave field (4.6a) can be written as^{45,48,205,207}

$$\mathbf{E}_p(\omega, \mathbf{r}) = -E_0 e^{-i\omega t} \sum_{n=1}^{\infty} i^n \frac{2n+1}{n(n+1)} (a_n \mathbf{m}_{oln}^{(1)} - i b_n \mathbf{n}_{eln}^{(1)}) \quad (4.7a)$$

$$\mathbf{m}_{oln}^{(1)} = \frac{\zeta_n(kr)}{kr} \left(\mathbf{e}_\theta \frac{P_n^l(\cos \theta)}{\sin \theta} \cos \varphi - \mathbf{e}_\varphi \frac{\partial P_n^l(\cos \theta)}{\partial \theta} \sin \varphi \right) \quad (4.7b)$$

$$\begin{aligned} \mathbf{n}_{eln}^{(0)} = & \mathbf{e}_r n(n+1) \frac{\zeta_n(kr)}{(kr)^2} P_n^l(\cos \theta) \cos \varphi \\ & + \frac{\zeta'_n(kr)}{kr} \left(\mathbf{e}_\theta \frac{\partial P_n^l(\cos \theta)}{\partial \theta} \cos \varphi - \mathbf{e}_\varphi \frac{P_n^l(\cos \theta)}{\sin \theta} \sin \varphi \right) \end{aligned} \quad (4.7c)$$

where $\zeta_n(kr) = \sqrt{\pi kr/2} H_{n+1/2}^{(1)}(kr)$ with $H_{n+1/2}^{(1)}(kr)$ being the Hankel function of the first kind while a_n and b_n are the Mie coefficients (1.51a) and (1.51b), respectively.

Thus, the field enhancement factor G calculated at the position \mathbf{r} near the particle results

$$G(\omega, \mathbf{r}) = \frac{|\mathbf{E}_0(\omega, \mathbf{r}) + \mathbf{E}_p(\omega, \mathbf{r})|^2}{|\mathbf{E}_0(\omega, \mathbf{r})|^2} \quad (4.8)$$

The mean G factor is obtained by averaging Equation (4.8) over all possible directions of \mathbf{r} .

$$\begin{aligned} \langle G(\omega, \mathbf{r}) \rangle = & \frac{1}{2(kr)^2} \left[\frac{1}{(kr)^2} \sum_{n=1}^{\infty} n(n+1)(2n+1) |\psi_n(kr) + b_n \zeta_n(kr)|^2 + \right. \\ & \left. + \sum_{n=1}^{\infty} (2n+1) (|\psi_n(kr) + a_n \zeta_n(kr)|^2 + |\psi'_n(kr) + b_n \zeta'_n(kr)|^2) \right] \end{aligned} \quad (4.9)$$

In the quasistatic limit ($ka \rightarrow 0$), the superposition $\mathbf{E}_0 + \mathbf{E}_p$ reduces to Equation (1.62b). Thus Equation (4.8) for a spherical nanoparticle reads

$$G_{\text{norm}}(\omega, r) = \left| 1 + 2 \left(\frac{\varepsilon(\omega) - 1}{\varepsilon(\omega) + 2} \right) \left(\frac{a}{r} \right)^3 \right|^2 \quad (4.10a)$$

$$G_{\text{tang}}(\omega, r) = \left| 1 - \left(\frac{\varepsilon(\omega) - 1}{\varepsilon(\omega) + 2} \right) \left(\frac{a}{r} \right)^3 \right|^2 \quad (4.10b)$$

where G_{norm} (G_{tang}) corresponds to the radial (tangential) orientation of the \mathbf{E}_0 field with respect to the nanoparticle surface. Equations (4.10) predict the electric field enhancement near a spherical metal nanoparticle whose size is much smaller than the incident light wavelength in satisfactory agreement with numerical simulations.^{205,208} Figure 4.3 shows the G factor calculated in close proximity to a silver nanoparticle (AgNP) through Equation (4.10) at an excitation wavelength of 410 nm.^{40,205}

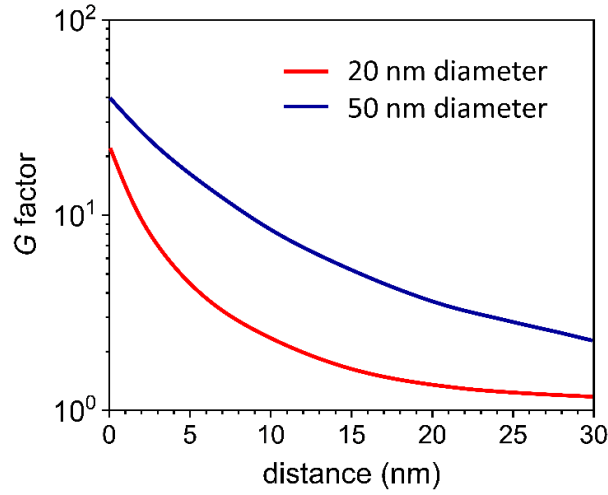


Figure 4.3. G factor calculated for a single AgNP of 20 nm diameter (solid red line) and 50 nm diameter (solid blue line) at an excitation wavelength of 410 nm.

4.2.2 Enhancement of the fluorophore quantum yield

Aiming at analytically determining the enhancement of the quantum yield, the radiative $\gamma_p^{(r)}$ and nonradiative $\gamma_p^{(nr)}$ decay rates of a fluorophore placed near a metal nanosphere have to be calculated in terms of transition probability from the excited to the ground state of the system.²⁰⁹ The radiative decay is determined by the energy radiated in the far-field, whereas the nonradiative decay depends on the energy lost as Joule heating into any dissipative medium present. Since both the decay rates increase in close proximity of a metal nanostructure, the overall intensity will be enhanced or quenched depending on the balance between $\gamma_p^{(r)}$ and $\gamma_p^{(nr)}$.^{36,194,209}

$$Y(\omega', \mathbf{r}) = \frac{Q_p(\omega', \mathbf{r})}{Q_0} = \frac{\frac{\gamma^{(r)}(\omega', \mathbf{r})}{\gamma_0^{(r)}}}{\left[1 + Q_0 \left(\frac{\gamma^{(r)}(\omega', \mathbf{r}) + \gamma_p^{(nr)}(\omega', \mathbf{r})}{\gamma_0^{(r)}} - 1 \right) \right]} \quad (4.11)$$

where $Q_p(\omega', \mathbf{r})$ and Q_0 are the emitter quantum yield in the presence of a metal nanoparticle (4.2a) and in free space (4.1a), respectively, while $\gamma^{(r)} = \gamma_0^{(r)} + \gamma_p^{(r)}$ is the total radiative decay rate. Thus, the problem reduces to compute the ratios $\gamma^{(r)}/\gamma_0^{(r)}$ and $(\gamma^{(r)} + \gamma_p^{(nr)})/\gamma_0^{(r)}$ for normal and tangential dipole orientation with respect to the nanoparticle surface.²⁰⁹

$$\left(\frac{\gamma^{(r)}(\omega', \mathbf{r})}{\gamma_0^{(r)}}\right)_{\text{norm}} = \frac{3}{2(kr)^4} \sum_{n=1}^{\infty} n(n+1)(2n+1) |\psi_n(kr) + b_n \zeta_n(kr)|^2 \quad (4.12a)$$

$$\left(\frac{\gamma^{(r)}(\omega', \mathbf{r})}{\gamma_0^{(r)}}\right)_{\text{tang}} = \frac{3}{4(kr)^2} \sum_{n=1}^{\infty} n(n+1)(2n+1) (|\psi_n(kr) + a_n \zeta_n(kr)|^2 + |\psi'_n(kr) + b_n \zeta'_n(kr)|^2) \quad (4.12b)$$

$$\left(\frac{\gamma^{(\text{tot})}(\omega', \mathbf{r})}{\gamma_0^{(r)}}\right)_{\text{norm}} = 1 + \frac{3}{2(kr)^4} \sum_{n=1}^{\infty} n(n+1)(2n+1) \Re\{b_n \zeta_n^2(kr)\} \quad (4.12c)$$

$$\left(\frac{\gamma^{(\text{tot})}(\omega', \mathbf{r})}{\gamma_0^{(r)}}\right)_{\text{tang}} = 1 + \frac{3}{4(kr)^2} \sum_{n=1}^{\infty} (2n+1) \Re\{a_n \zeta_n^2(kr) + b_n (\zeta'_n(kr))^2\} \quad (4.12d)$$

where $\gamma^{(\text{tot})} = \gamma^{(r)} + \gamma_p^{(\text{nr})}$ is the full decay rate. In the quasistatic limit ($ka \rightarrow 0$), Equations (4.12) reduce to Equations (4.13).²⁰⁵

$$\left(\frac{\gamma^{(r)}(\omega', \mathbf{r})}{\gamma_0^{(r)}}\right)_{\text{norm}} = \left|1 + 2 \left(\frac{\varepsilon(\omega') - 1}{\varepsilon(\omega') + 2}\right) \left(\frac{a}{r}\right)^3\right|^2 \quad (4.13a)$$

$$\left(\frac{\gamma^{(r)}(\omega', \mathbf{r})}{\gamma_0^{(r)}}\right)_{\text{tang}} = \left|1 - \left(\frac{\varepsilon(\omega') - 1}{\varepsilon(\omega') + 2}\right) \left(\frac{a}{r}\right)^3\right|^2 \quad (4.13b)$$

$$\left(\frac{\gamma_p^{(\text{nr})}(\omega', \mathbf{r})}{\gamma_0^{(r)}}\right)_{\text{norm}} = \frac{3}{2(kr)^3} \sum_{n=1}^{\infty} (n+1)^2 \left(\frac{a}{r}\right)^{2n+1} \Im\left\{\frac{\varepsilon(\omega') - 1}{\varepsilon(\omega') + \frac{n+1}{n}}\right\} \quad (4.13c)$$

$$\left(\frac{\gamma_p^{(\text{nr})}(\omega', \mathbf{r})}{\gamma_0^{(r)}}\right)_{\text{tang}} = \frac{3}{4(kr)^3} \sum_{n=1}^{\infty} n(n+1) \left(\frac{a}{r}\right)^{2n+1} \Im\left\{\frac{\varepsilon(\omega') - 1}{\varepsilon(\omega') + \frac{n+1}{n}}\right\} \quad (4.13d)$$

Although Equations (4.13a) and (4.13b) appear formally equal to Equations (4.10), two main differences are worth to highlight: (i) normal or tangential orientation with respect to the nanoparticle surface refers to the incident electric field \mathbf{E}_0 in Equations (4.10), whereas it concerns the dipole moment of the emitter in Equations (4.13); (ii) the enhancement of the excitation rate is evaluated at the excitation frequency ω while the enhancement of the quantum yield at the emission frequency

ω' . From Equations (4.13c) and (4.13d), it results that the ratio $\gamma_p^{(nr)}/\gamma_0^{(r)}$ diverges when the emitter is approaching the nanoparticle surface ($r \rightarrow a$). Therefore, for vanishingly small separation distances, the quenching contribute dominates over the radiative decay thereby entailing Y factor tends to zero. Equations (4.13) predict the quantum yield enhancement undergone by a fluorophore placed near a AgNP in satisfactory agreement with the exact Mie theory and numerical simulations (Figure 4.4).

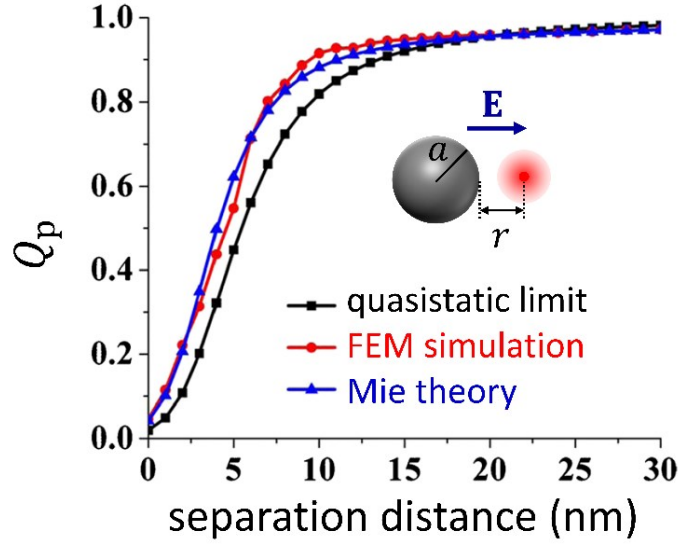


Figure 4.4. QY of a fluorophore emitting at 480 nm as a function of the separation distance from a silver nanosphere of 120 nm diameter calculated by the quasistatic approximation (black curve), numerical simulation (red curve), and exact Mie theory (blue curve). The inset shows a schematic representation of the light polarization and emitter positioning (from Ref. ²⁰⁸).

Unlike the case of single metal nanoparticle in which the quenching contribute becomes predominant by reducing the separation distance between the fluorophore and the nanostructure surface,²¹⁰ it has been recently demonstrated that a fluorescence emitter placed in the gap of a nanoparticle dimer configuration undergoes a quenching effect only when the interparticle gap distance of the dimer is vanishingly small, meaning that the strong plasmonic coupling prevails over the energy engaged in the Joule heating process unless the emitter is extremely close to the metal surface (< 2 nm).^{208,211,212} Figure 4.5 shows the different behaviour of the fluorophore quantum yield in presence of a single AgNP (black curve), dimer configuration (blue curve), and linear chain (red curve).

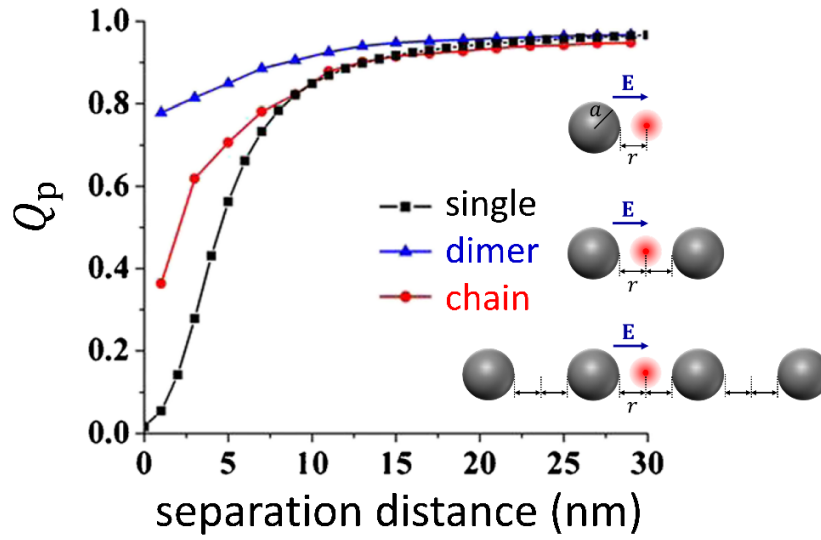


Figure 4.5. Calculated QY of a fluorophore emitting at 480 nm placed near a single AgNP of 90 nm diameter (black curve), in the gap of two AgNPs (blue curve), and in the middle of an AgNP chain (red curve) as a function of the separation distance from the nanoparticle surface. The inset shows a schematic representation of the light polarization and emitter positioning for single, dimer, and chain configuration (from Ref. ²⁰⁸).

4.2.3 Modification of the luminescence collection efficiency

Since the presence of the nanostructure may modify the directivity of the emitted light, the FE factor can be further enlarged by maximizing the collection efficiency gain²⁰⁶

$$K(\omega') = \frac{\kappa_p}{\kappa_0} \quad (4.14)$$

where κ_p and κ_0 are the collection efficiency in presence of the nanostructure and in free-space conditions, respectively. Note that such a contribute is entirely independent on the choice for excitation intensity or fluorophore quantum yield being only dependent on the directivity of the nanoantenna and the light collection setup. A way to maximize the gain K consists of using an objective with low numerical aperture in accordance with the peak angular emission of the nanoantenna radiation pattern.²¹³ Periodic nanostructure, such as arrays of metal nanoparticles and corrugated nanoaperture, can be used to promote the emission of the light in certain directions. Particularly, it has been demonstrated that hexagonal arrays of aluminium nanoparticles combined with a thin layer of luminescent molecules – acting as a waveguide – produce a sideward directional emission into glass for a wavelength band around 620 nm.²¹⁴ On the other hand, Figure 4.6 shows that a single nanoaperture with periodic corrugations produces a straight-forward radiation of $\pm 15^\circ$

cone aperture, thereby leading to a collection efficiency gain up to 10^2 if an objective with a low numerical aperture (NA) is used (< 0.2).^{206,213}

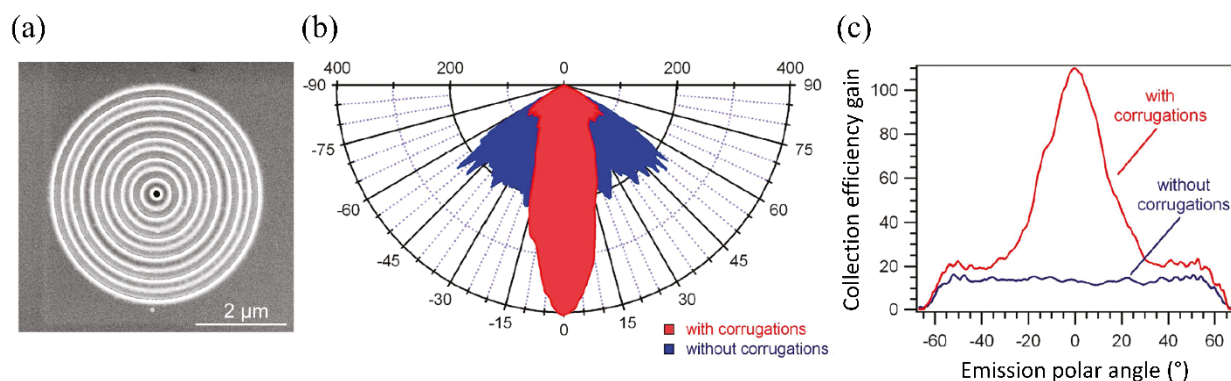


Figure 4.6. (a) Top view SEM micrograph of a single nanoaperture with five periodic concentric corrugations. (b) Angular radiation patterns in the polar angle. (c) Collection efficiency gains per single molecule as function of the emission polar angle (from Ref. ²¹³).

4.3 Applications to biosensing

Fluorescence-based techniques are among the most widespread in the fields of biotechnology, life sciences and biomedical research.^{215–217} Fluorescent probes and fluorescent-labelled bioreceptors are extensively employed in optogenetic studies,²¹⁸ cytogenetic assays – e.g. fluorescent *in situ* hybridization –, ^{219,220} bioimaging analysis for the observation of both the location and motion of cells or subcellular elements,²²¹ molecular dynamic investigation,²²² as well as in fluoroimmunoassays for the detection of molecular biomarkers and in enzyme-linked immunosorbent assay (ELISA).²²³ However, the poor yield of many fluorescent dyes and signal interference can hamper the application of fluorescence to the field of sensing. The detection of analytes in very low abundance ranges is a long-standing goal of the fluorescence. Many efforts have been carried out to enhance the fluorescent signal in order to extend their application to ultra-sensitive fluoroimmunoassays.^{224,225}

Plasmonic nanostructures are realistic candidates to extend the limit of the fluorescence detection to the femtomolar level and beyond by modifying the spectral features of the nearby fluorescent dyes without needing to expensive equipment, specific or toxic reagents, or significant modifications to well-established fluorescence-based assays.^{195,226} In particular, 2D arrays of metal nanostructures are particularly suitable as PEF-based biosensing platforms.¹⁹⁵ Until now, a large variety of fluorescence enhancers, such as gold micro-islands,²²⁷ arrays of metal nano-objects – e.g. nanoparticles,²²⁸

nanorods,²²⁹ nanotriangles,²³⁰ nanocrystals²³¹ –, bow-tie nanoantennas,²³² and resonant nanocavities,^{233,234} have been exploited to push down the detection limit in fluorescence-based assays. Despite significant milestones in terms of LOD (down to fM level),^{235,236} fluorescence enhancement (FE) factor (up to 10⁵-fold),^{234,237} and adaptability to the conventional and well-established fluoroassays,^{238,239} still a number of factors limit the use of those solutions as devices for routine testing, point-of-care analysis and large-scale use of the PEF-based fluoroassays, including, to cite a few, the need for skilled personnel, expensive technologies, time-consuming procedures, poor versatility in tuning of plasmon-fluorophore coupling and not easyscalability.²²⁴

2D-arrays of metal nanoparticles, realized by immobilizing citrate-stabilized AuNPs onto a silane-modified surface (see Figure 3.3)¹⁸⁸ or through BCMN (see Figure 3.4),¹⁸⁹ provide an easy way to overcome most of the aforementioned challenges. The affordable and scalable fabrication and the simple tunability of their plasmonic properties are the main strengths of these devices. Aiming at using such plasmonic substrates as PEF-based biosensing platforms, a key issue to address is the surface biofunctionalization.²⁵ In this regard, PIT offers a fast and simple strategy to covalently tether Abs onto gold surfaces in such a way that one Fab is exposed to the surrounding environment (see Figure 2.3).^{80–82} Thus, Abs offer considerable advantages as a bottom bioreceptor layer in a sandwich configuration not only for their inherently specificity, but also for the densely covering and high capture efficiency warranted by PIT.^{86,87} The top fluorescently labelled bioreceptor layer can be conveniently adapted to the actual case study by simply switching among Abs and Apts. Figure 4.7 shows the operating principle of the proposed PEF-based biosensor for three feasible configurations. It is worth to underline that the combination of Abs and fluorescently labelled Apts (Apts*) provides a powerful approach not only to significantly improve the specificity through a double analyte recognition,²⁴⁰ but also to enable an optimal fluorophore-nanostructure distance (approximately 10-15 nm)^{198,201,202} for PEF-based sensors (Figure 4.7c).

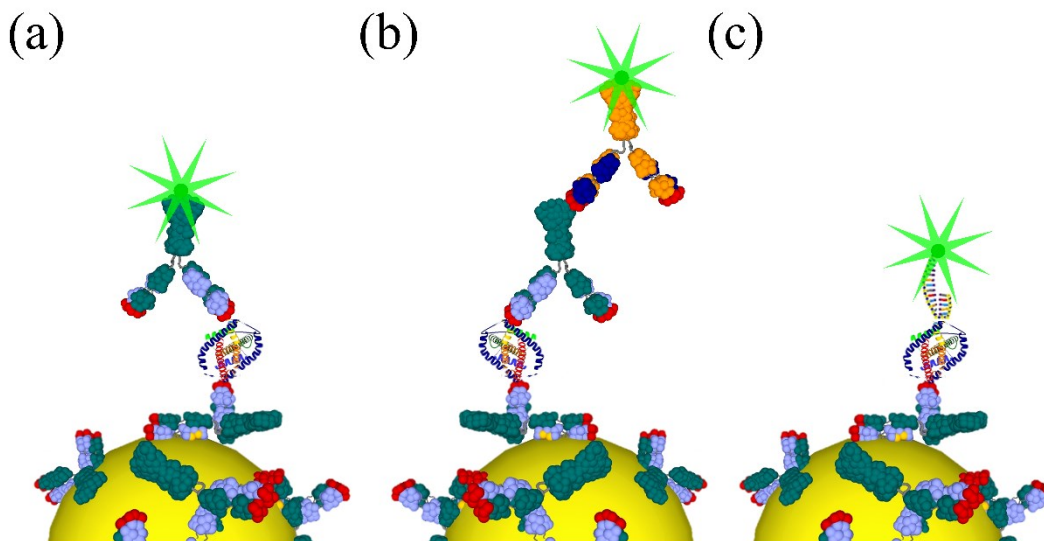


Figure 4.7. Possible detection schemes of a PEF-based biosensor with the capture bioreceptor layer realized by Abs immobilized through PIT. Top bioreceptors can consist of (a) monolayer of fluorescently labelled Abs (Abs*), (b) double layer of Abs-Abs* or (c) monolayer of Apts*.

4.4 A comparative study on device performance

Plasmonic substrates consisting of randomly positioned (Figure 3.6a), honeycomb lattice (Figure 3.12b), and branched arrays (Figure 3.15b) of AuNPs have been employed as fluorescence enhancers in PEF-based sensing for the detection of proteins in human whole blood. Specifically, the performance of the proposed biosensors has been explored for the detection of *Plasmodium falciparum* lactate dehydrogenase (*Pf*LDH), a malaria biomarker present at nanomolar level in red blood cells but only at picomolar levels in serum of infected people.²⁴¹ Malaria is still one of the main causes of disease-related deaths worldwide^{242,243} and it is caused by *Plasmodium* parasites such as *P. vivax* and *P. falciparum*, the latter accounting for 90% of mortality worldwide.²⁴⁴ The conventional serologic antibody-based rapid diagnostic tests rely upon the *Pf*LDH detection in pretreated blood and offer rapid and cost-effective malaria diagnosis. However, the poor LOD as well as the transportation and storage difficulties of pre-functionalized devices in tropical environment make such tests unfit for early diagnosis and screening.^{245–247} PEF-based devices in combination with a unique biofunctionalization procedure, which can be accomplished in a few minutes, have been resulted in immunosensors suitable for detecting *Pf*LDH down to femtomolar level in whole blood without any pretreatment and preconcentration steps.

The fluoroimmunoassays hereafter proposed are inherently specific since the recognition of *Pf*LDH takes place in a sandwich scheme by Abs from the bottom and Apts from the top (Figure 4.7c) (see Appendix D.3.1 for more details on the sandwich scheme realization). Anti-malaria pan-PLDH Abs as capture bioreceptor layer offers simple and fast substrate functionalization and effective detecting of any malaria biomarkers *P. lactate dehydrogenase* (PLDH),²⁴⁸ whereas Apts used as top bioreceptor layer enables a cost-effective and highly specific targeting of *Pf*LDH with discrimination from *Plasmodium vivax* lactate dehydrogenase (*Pv*LDH).²⁴⁹ Moreover, the adopted Ab-*Pf*LDH-Apt* sandwich scheme – used throughout all the experiments – assured a fluorophore-nanoparticle distance of ~10 nm yielding optimal PEF amplification. It turned out to be necessary to dilute the blood in order to reduce the solution turbidity and prevent the clotting. A dilution of 1:100 in 1 mL of 25 mM Tris buffer was used throughout all the measurements as a good tradeoff for retrieving high signal and a treatable solution. The *Pf*LDH was spiked into the diluted uninfected blood solution to obtain the analyte concentration of interest. The Ab-*Pf*LDH-Apt* sandwich configuration used hereafter can be immediately extended to other analytes by simply replacing the bioreceptor layers.

4.4.1 Plasmon-fluorophore spectral overlap

Once the substrates were optically characterized (see Figure 3.7, Figure 3.14, and Figure 3.16), the choice of the fluorescent dye was aimed to achieve the largest FE. In this regard, while narrow LSPR peaks restrict the spectral overlap to only excitation or emission coupling, broad plasmon resonances bands – promoted by collective modes – can encompass both the excitation and emission peak of the fluorophore thereby enabling the occurrence of the dual-mechanism enhancement. Given the wide variety of fluorescent dyes apt to this aim, such a requirement can be easily fulfilled at any resonance wavelength lying in the visible range.

Figure 4.8a shows the superposition of the LSPR peak – obtained in case of a randomly positioned AuNPs – to the only emission peak of 5-carboxyfluorescein (5-FAM) (dashed green line). Although the excitation peak of 5-FAM dye lies outside the plasmon resonance, such a condition enables a large PEF amplification through radiative coupling since the Ab-*Pf*LDH-Apt* sandwich warrants a mean fluorophore-nanoparticle distance of approximately 10-15 nm. On the contrary, the plasmon resonance band delivered by a honeycomb array of AuNPs results large enough to span both the excitation (dotted orange line) and emission (dashed red line) peak of cyanine 5 (Cy5) (Figure 4.8b), thereby promoting a dual-mechanism enhancement of the fluorescence.

If the substrate exhibits two or more plasmon resonances, different fluorescent dyes can be simultaneously employed for enabling multiplexed measurements. Figure 4.8c shows the plasmon-fluorophore spectral overlap for branched arrays of AuNPs with either 5-FAM and Cy5 dyes. While the narrow resonance peak at lower wavelength limits the FE to the only radiative coupling with 5-FAM dye, the broad resonance band at higher wavelength – arising from the collective modes along the branches – leads to a dual-mechanism coupling with Cy5 dye.

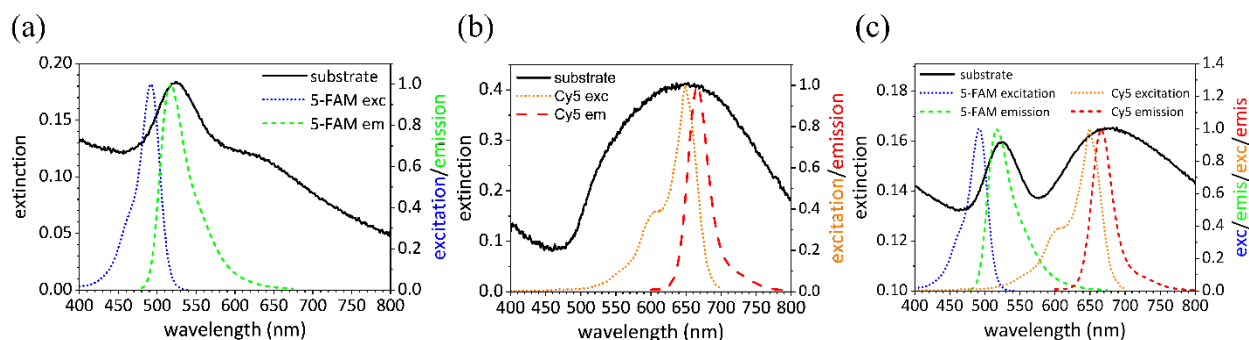


Figure 4.8. Plasmon-fluorophore spectral overlap for (a) randomly positioned AuNPs and 5-FAM dye (emission coupling), (b) honeycomb lattice of AuNPs and Cy5 dye (dual-mechanism coupling), and (c) branched arrays of AuNPs and either 5-FAM (emission coupling) and Cy5 (dual-mechanism coupling) dyes.

4.4.2 Surface biofunctionalization through PIT

The substrates were functionalized with pan malaria Abs (anti-PLDH) by using PIT (see Appendix D.3.1 for details on the surface functionalization). Firstly, the concentration of anti-PLDH was varied over large intervals so to optimize the surface covering (see Figure E.6). The shift of the plasmon resonance wavelength $\Delta\lambda_p$ showed no significant variations for concentrations larger than 50 $\mu\text{g/mL}$, that is a threshold above which no more free gold surface is available for Ab anchoring. Thus, an anti-PLDH concentration of 50 $\mu\text{g/mL}$ was used throughout all the experiments, thereby yielding a plasmon red-shift of approximately 5 nm due to the dielectric protein layer surrounding the AuNPs (Figure 4.9). The close-packed covering is also evident by the lack of any significant optical change in the extinction spectrum after the blocking step (Figure 4.9). By considering a steric hindrance of a single immobilized Ab equal to $\sim 150 \text{ nm}^2$,⁸⁵ the Ab density (number of Abs per AuNP) was estimated as ~ 20 (~ 50) for nanosphere of 30 nm (50 nm) diameter.

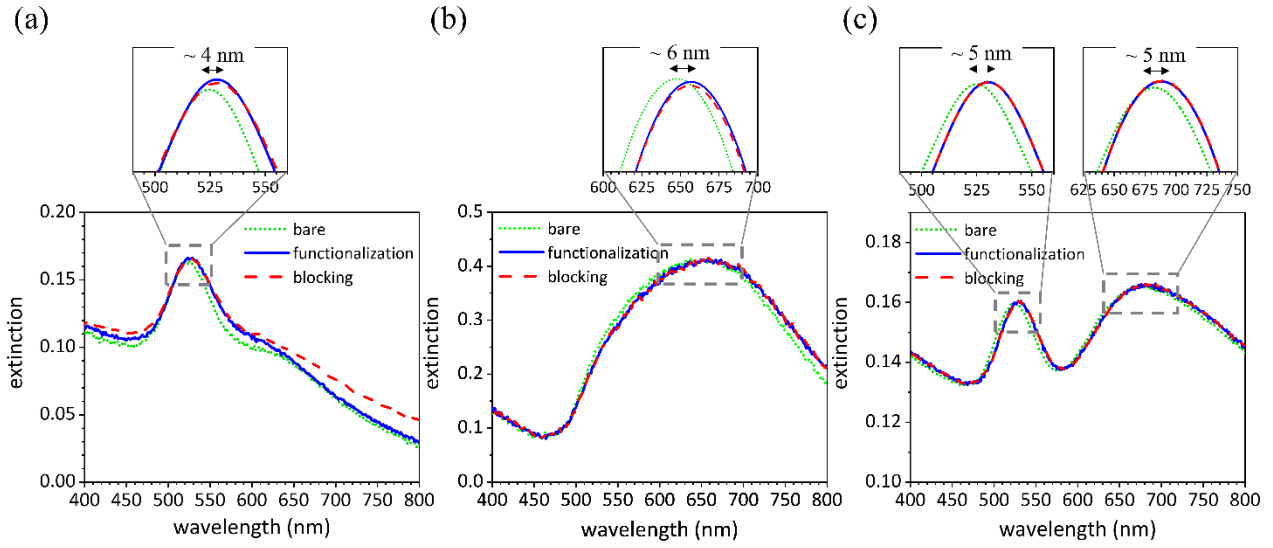


Figure 4.9. Experimental extinction spectrum of the substrates, consisting of (a) randomly positioned AuNPs, (b) honeycomb lattice of AuNPs, and (c) branched arrays of AuNPs, before (dotted green lines) and after functionalization through PIT (solid blue lines) and blocking (dashed red lines). The insets show the Gaussian fits used for evaluating the plasmon resonance wavelength.

4.4.3 Binding kinetic study

Firstly, the fluoroimmunoassay was kinetically characterized by measuring the fluorescence signal at high *Pf*LDH concentration as a function of incubation time for both the binding processes: (1) Ab-analyte and (2) Apt*-analyte. As it concerns the process (1), *Pf*LDH-spiked blood was preliminarily mixed with a solution containing malaria Apts* so that the resulting *Pf*LDH-Apt* complexes were fluorescently visible while the small size of Apts* did not significantly affect the diffusion and binding kinetics. Thus, functionalized substrates were incubated with *Pf*LDH-Apt* solution and fluorescence images were recorded at different incubation time (see Figure E.7). The process (2) was firstly analysed by incubating the functionalized substrates with *Pf*LDH-spiked blood for a time long enough to warrant the reach of the dynamic equilibrium – as a consequence of the empirical study (1) – and then with the solution containing the malaria Apts* (see Figure E.8).

Figure 4.10 shows the fluorescence intensity as a function of the incubation time for both the binding processes obtained in case of (a) 2D array of randomly positioned AuNPs and (b) honeycomb arrays of AuNPs. The data are well fitted by exponential curve

$$F(t) = F_{eq} \left(1 - e^{-\frac{t}{\tau}} \right) \quad (4.15)$$

where F_{eq} is the signal measured approaching the dynamic equilibrium while τ is the time constant of the binding process. Both the processes (1) and (2) exhibit similar kinetics with time constants of 50 ± 10 min (80 ± 30 min) and 30 ± 5 min (45 ± 15 min), respectively, for a substrate consisting of randomly positioned AuNPs (honeycomb array of AuNPs). Thus, if a commercial fluorescence reader is used to record the signal, the whole analysis could be carried out within 2 hours (3 hours), very attractive feature in terms of no time-consuming assay. The slight discrepancy in the asymptotic values $F_{eq}^{(1)} < F_{eq}^{(2)}$ is ascribable to the less effective binding among the *Pf*LDH-Apt* complexes and the immobilized Abs since the Apts* might have targeted all analyte binding sites during their pre-incubation.²⁴⁹

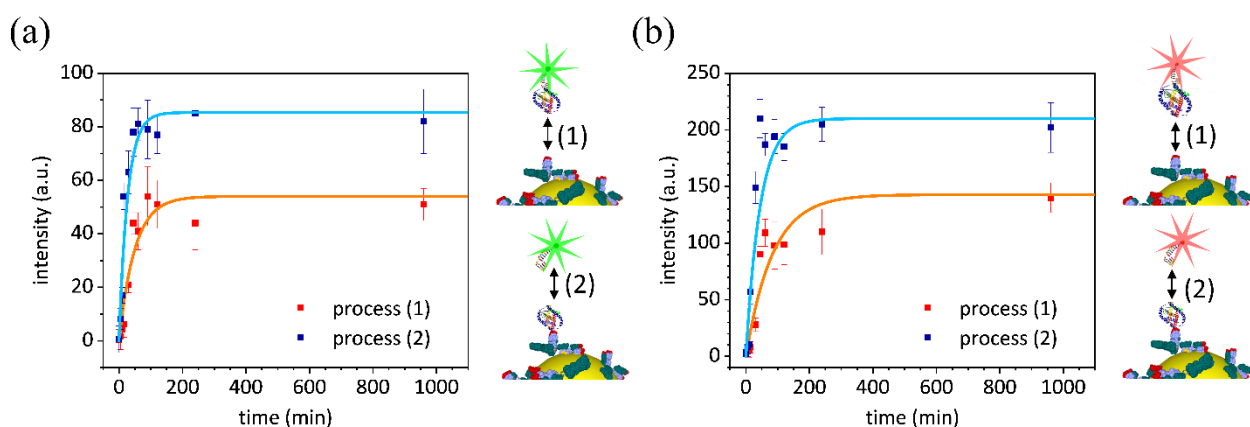


Figure 4.10. Kinetic curves measured for (1) Ab-*Pf*LDH and (2) Apt*-*Pf*LDH binding dynamics in case of (a) 2D array of randomly positioned AuNPs and (b) honeycomb arrays of AuNPs. The data are well fitted by exponential curves (solid orange and blue lines, respectively). The data are presented as mean value \pm standard deviation and are representative of ten technical repeats.

4.4.4 Dose-response curve

Rather than exploiting additive concentrations, each substrate was used for a single concentration measurement so to inherently test the reliability and reproducibility of the detection procedure. A broad range of *Pf*LDH concentrations was explored for each kind of aforementioned substrate – from 1 fM to 1 μ M referring to undiluted whole blood – that is of interest from a medical point of view. Figure 4.11 shows some examples of fluorescence images recorded at different *Pf*LDH concentrations (see Appendix D.3.2 for more details about the processing and analysis of the fluorescence images), in which the number of bright spots is strikingly higher as compared to the control down to 1 pM (33 pg/mL) for both randomly positioned and branched arrays of AuNPs, and 100 fM (3.3 pg/mL) for honeycomb arrays of AuNPs (see Figure E.9 for more images).

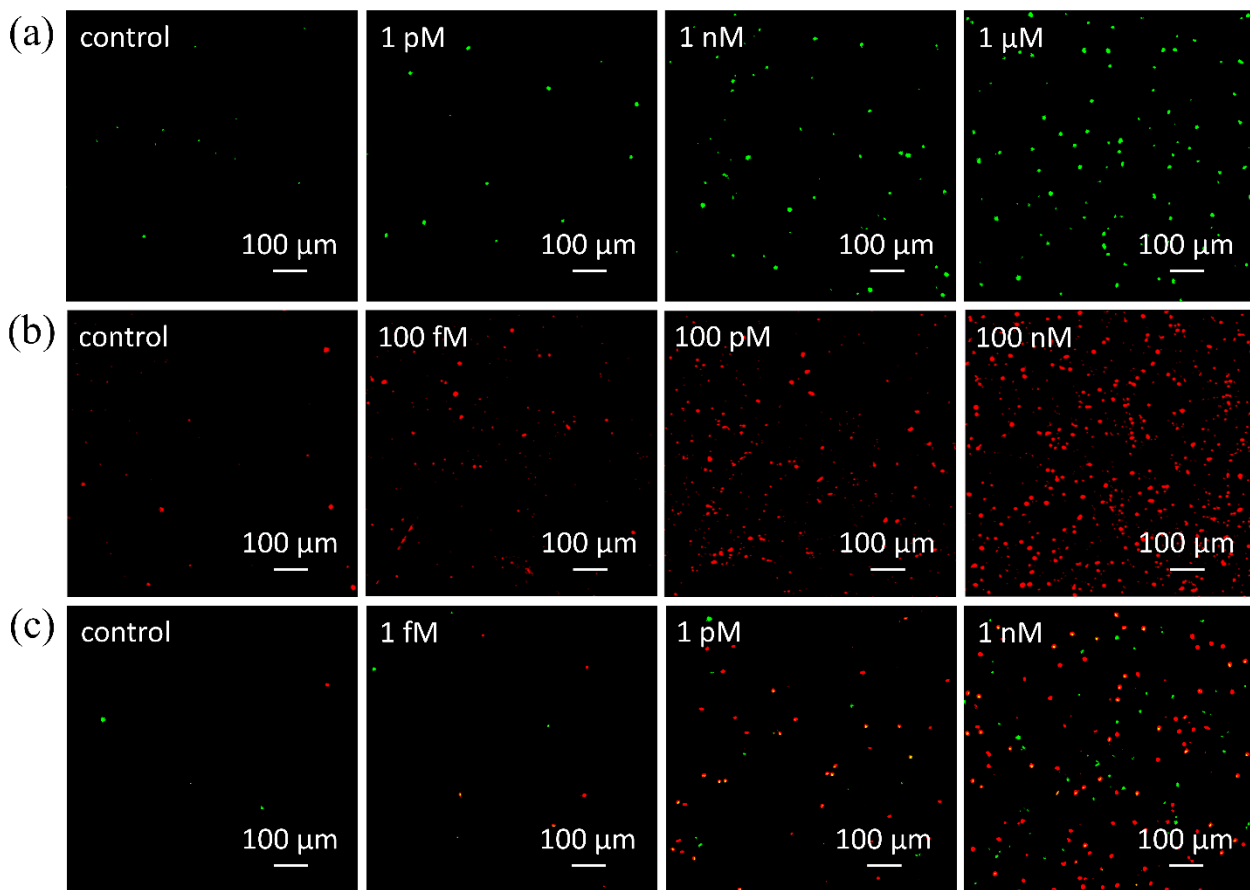


Figure 4.11. Examples of processed fluorescence images recorded at different *P/LDH* concentration in spiked whole blood attained by (a) randomly positioned, (b) honeycomb lattice, and (c) branched arrays of AuNPs.

Fluorescence intensity is strongly related to the number of pixels that collect the signal exhibiting linear correlation with similar behaviours regardless of the analyte concentration (Pearson's $r = 0.95$) (Figure 4.12). The mean spot area turned out to be $34 \mu\text{m}^2$ – corresponding to approximately 80 pixels (pixel area = $650 \times 650 \text{ nm}^2$) – in case of 2D arrays of randomly positioned AuNPs with 5-FAM dye, whereas $\sim 15 \mu\text{m}^2$ – corresponding to 36 pixels – for honeycomb lattice of AuNPs with Cy5 dye. The lower mean area of the bright spots attained by ordered arrays of AuNPs – as a result of the significantly higher number of very small fluorescence spots ($< 5 \mu\text{m}^2$) – corroborates the larger FE factor in case of well-ordered nanostructures and dual-mechanism enhancement since the larger PEF-amplified signal allows the weaker spots to emerge from the background as well.

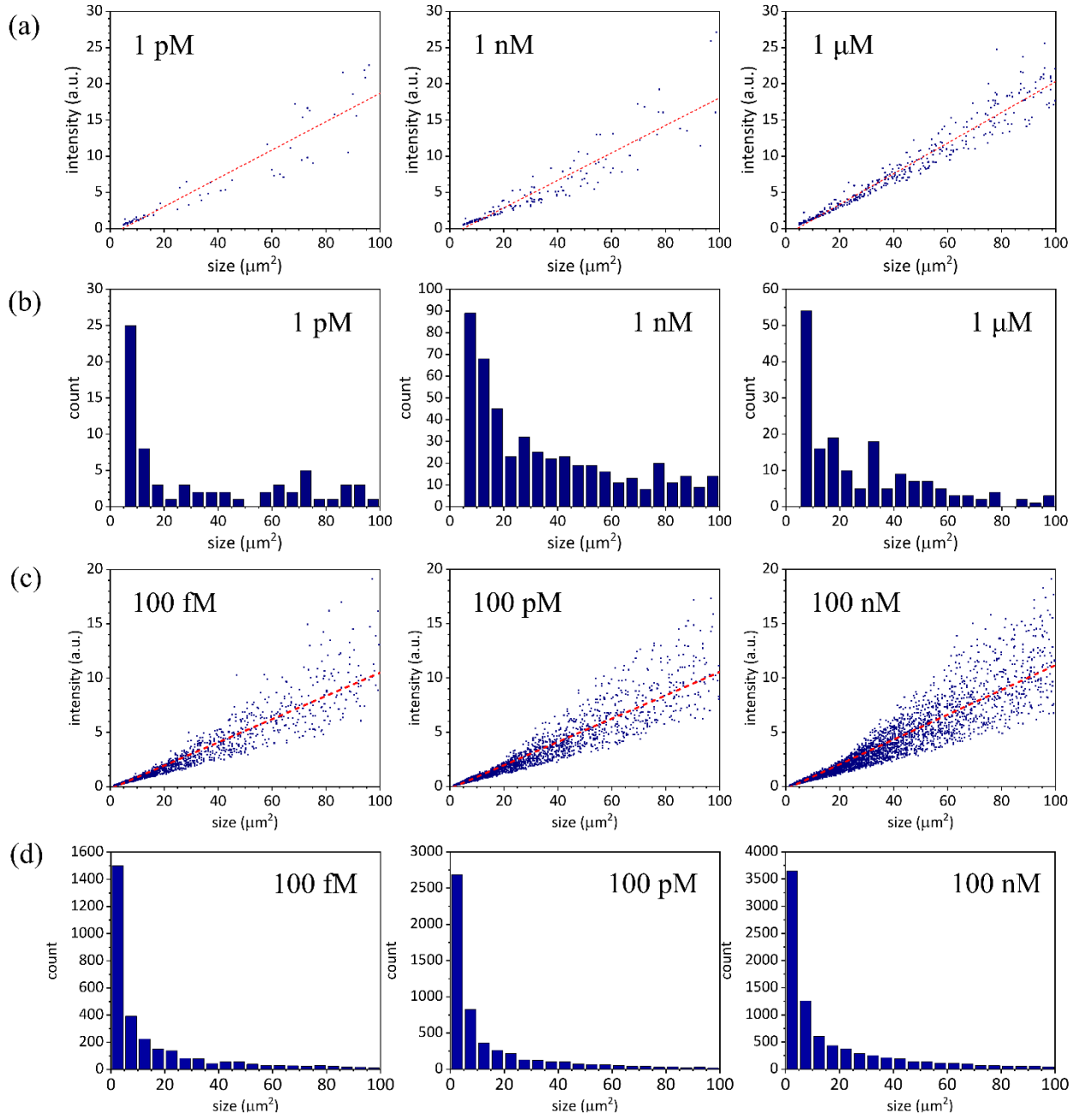


Figure 4.12. (a,c) Correlation curve (intensity vs. area) and (b,d) spot size distribution in case of randomly positioned and honeycomb arrays of AuNPs, respectively.

The fluorescence intensity F as a function of the $PfLDH$ concentration is reported in Figure 4.13. The data are well fitted by the four-parameter Hill equation¹⁶⁵

$$F([PfLDH]) = F_1 + \frac{F_2 - F_1}{1 + \left(\frac{K}{[PfLDH]} \right)^n} \quad (4.16)$$

where F_1 and F_2 are the minimum and maximum value of the fluorescence intensity, respectively, K is the concentration at which the fluorescence intensity reaches its half-maximum value and n is the so-called Hill's coefficient.¹⁶⁶

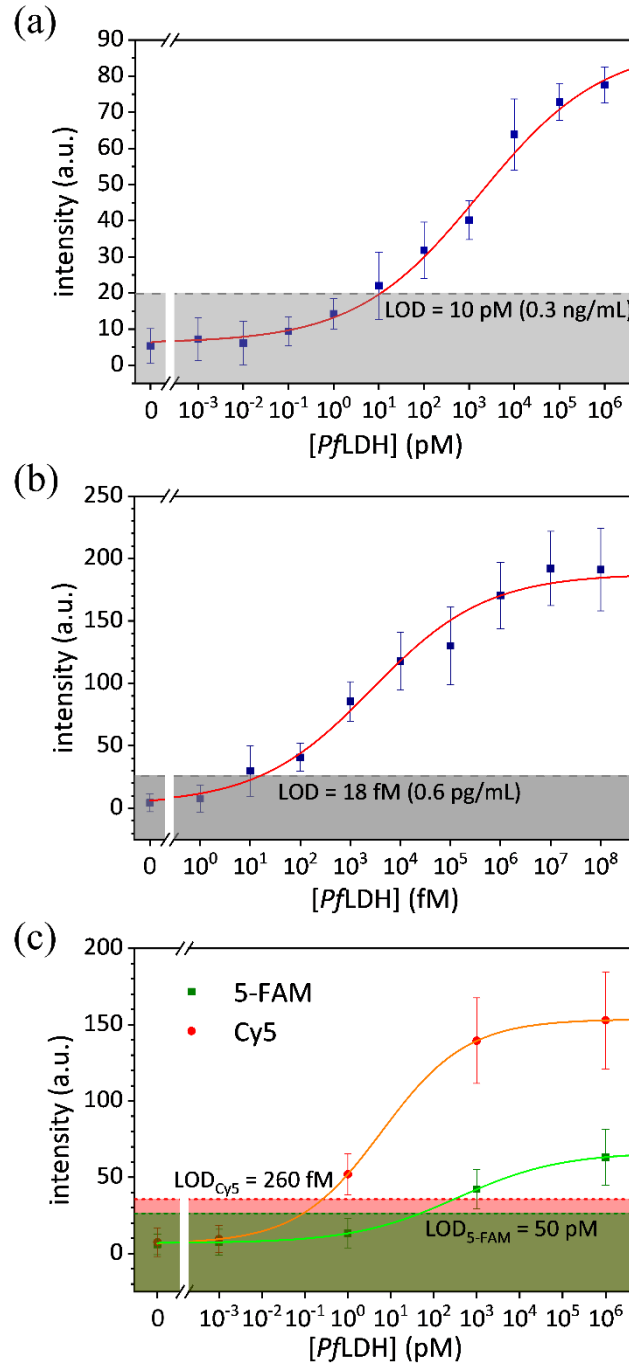


Figure 4.13. Calibration curve (fluorescence intensity vs. *P/LDH* concentration in spiked human blood) of the immunoassays realized by (a) randomly positioned, (b) honeycomb lattice, and (c) branched arrays of AuNPs for *P/LDH* concentration in the range 1 fM to 1 μ M (0.03 pg/mL to 0.03 mg/mL). The data are best fitted by the four-parameter Hill equation (4.16) (solid lines). The shaded regions represent the 3σ noise level measured in uncontaminated blood. The data are presented as mean value \pm standard deviation and are representative of ten technical repeats.

Table 4.1 summarises the best-fit parameter values, the dynamic range, and the limit of detection for each kind of aforementioned substrate.

Table 4.1. Best-fit parameter values, dynamic range (DR), and limit of detection (LOD) obtained by fitting the experimental data of Figure 4.13 with Equation (4.16). The outcomes concerning the branched arrays of AuNPs are highlighted in green and red to distinguish the data referring to 5-FAM and Cy5 dyes, respectively.

Randomly positioned AuNPs	Honeycomb lattice of AuNPs	Branched arrays of AuNPs
$F_1 = 6 \pm 2$ arb. units	$F_1 = 4 \pm 2$ arb. units	$F_1 = 7 \pm 1$ arb. units $F_1 = 6 \pm 2$ arb. units
$F_2 = 88 \pm 6$ arb. units	$F_2 = 190 \pm 10$ arb. units	$F_2 = 66 \pm 3$ arb. units $F_2 = 154 \pm 4$ arb. units
$K = (1.7 \pm 0.9) \times 10^3$ pM	$K = (2.7 \pm 1.4) \times 10^3$ fM	$K = (0.36 \pm 0.15) \times 10^3$ pM $K = 6 \pm 1.7$ pM
$n = 0.32 \pm 0.06$	$n = 0.38 \pm 0.08$	$n = 0.36 \pm 0.05$ $n = 0.44 \pm 0.06$
$\chi^2 = 1.4$	$\chi^2 = 2.0$	$\chi^2 = 1.2$ $\chi^2 = 1.8$
DR = 10 pM – 1 μ M	DR = 10 fM – 1 nM	DR = 10 pM – 1 μ M DR = 100 fM – 1 nM
LOD = 10 pM (0.3 ng/mL)	LOD = 18 fM (0.6 pg/mL)	LOD = 50 pM (1.6 ng/mL) LOD = 260 fM (8.6 pg/mL)

In all the cases, the dynamic range extends over five decades with a LOD – estimated as three standard deviation above the control value (shaded regions in Figure 4.13) – down to femtomolar level for ordered arrays of AuNPs.¹⁸¹

4.4.5 Fluorescence enhancement factor

Aiming at measuring the FE factor delivered by such plasmonic substrates, 100 μ L volume of a solution containing 250 fmol of Apts* was drop-casted onto a bare microscope slide in order to estimate the fluorescence I_0 provided by the single fluorophore in free-space condition. The entire fluorescence intensity F_0 in the case of 5-FAM dye (Cy5 dye) was estimated by considering the dried drop area composed of 12 mm diameter circle surrounded by 0.15 mm (0.10 mm) thick annulus whose

intensity was 10-fold (4-fold) higher than that measured in the inner region (Figure 4.14). Inner region and annulus were separately sampled finding out that the contribution of the annulus to the whole intensity was minor, even though its intensity was locally much higher. Thus, the single fluorophore intensity could be retrieved by assuming $F_0 = k_{\text{ins}} N_0 I_0$, where N_0 is the number of Apts* (approximately 1.5×10^{11}) and k_{ins} an instrumental constant depending on the acquisition parameters.

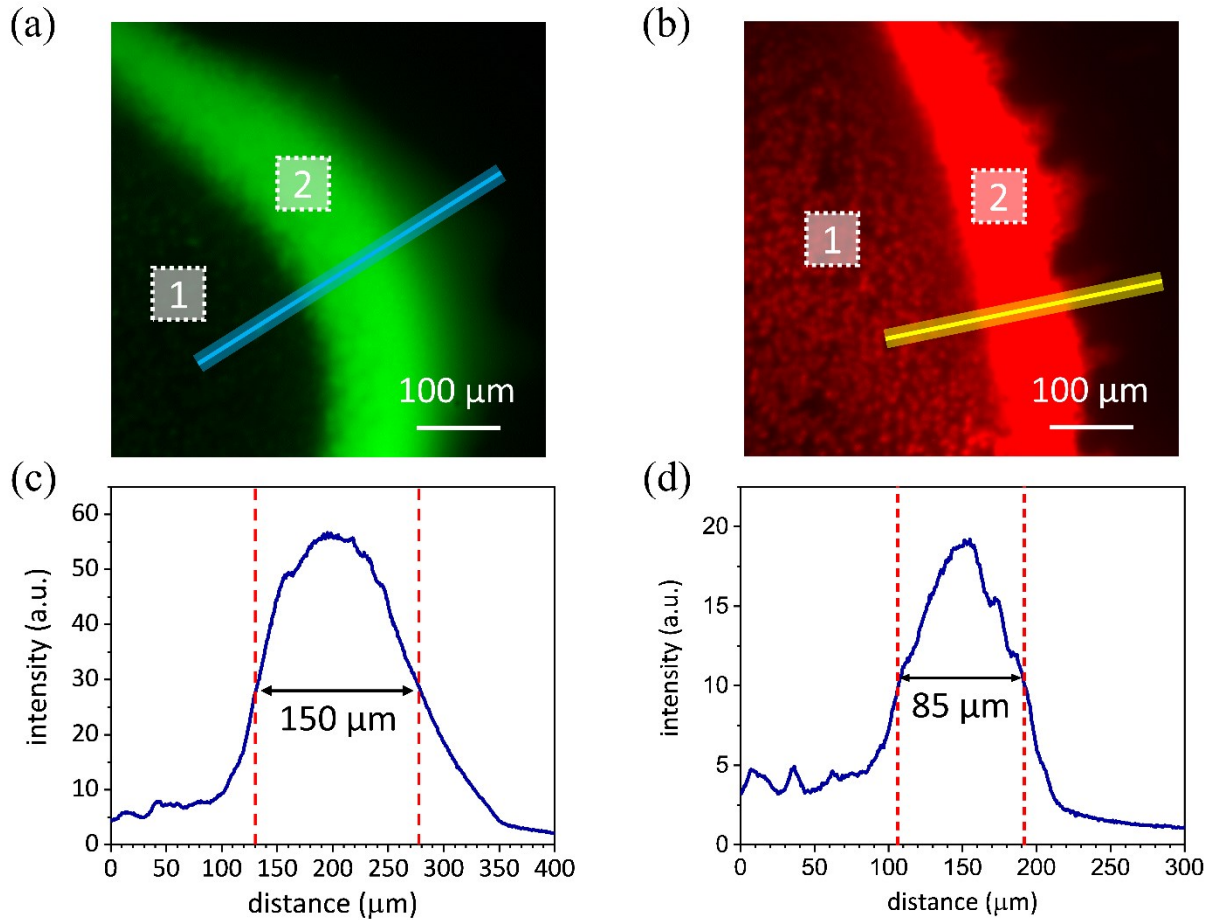


Figure 4.14. Example of fluorescence image recorded over the edge of a dried drop containing 250 fmol of (a) 5-FAM and (b) Cy5 dyes. The whole intensity of the dye drop was measured by sampling the drop area in one hundred regions of interest of size $350 \times 350 \mu\text{m}^2$ in the inner region (shaded white square 1, not in scale) and $70 \times 70 \mu\text{m}^2$ on the annulus (shaded white square 2). (c,d) Thickness of the coffee ring measured as FWHM of the intensity profile evaluated along the light blue and yellow lines highlighted in panels (a) and (b), respectively.

On the other hand, in presence of a plasmonic substrate the fluorescence arose from separated emitters (see Figure 4.11), hence the whole intensity is given by $F_{\text{PEF}} = k_{\text{ins}} N_{\text{PEF}} I_{\text{PEF}}$, where N_{PEF} is the number of fluorescence spots while I_{PEF} their mean intensity. Since the experimental FE factor is defined as $FE = I_{\text{PEF}}/I_0$, the fluorescence amplification delivered by each kind of aforementioned substrate was measured and the obtained values are summarised in Table 4.2.

Table 4.2. Fluorescence enhancement factor measured by coupling randomly positioned AuNPs with 5-FAM dye, honeycomb lattice of AuNPs with Cy5 dye, and branched arrays of AuNPs with either 5-FAM (green) and Cy5 (red) dyes.

Randomly positioned AuNPs	Honeycomb lattice of AuNPs	Branched arrays of AuNPs
$FE = 340$	$FE = 7 \times 10^4$	$FE = 160$ $FE = 5.2 \times 10^3$

Although the physics underlying the FE by plasmonic nanostructures is still to be fully understood,^{196,224} it can be safely asserted that such high values of FE measured in case of Cy5 dye is not only due to the optimal fluorophore-nanostructure separation distance of ~ 10 nm assured by Ab-*Pf*LDH-Apt* sandwich scheme, but also the result of the overlap of the plasmon resonance with both the excitation and emission peak of the fluorophore.^{37,181,203,204} The lower FE factors delivered by branched arrays of AuNPs – as compared with those measured with randomly positioned and honeycomb lattice – can be ascribable to both the partial lack of the spectral coupling efficiency – since some mismatches between the plasmon mode and the right fluorophore might occur due to the randomness of the Ab-*Pf*LDH-Apt* positioning over the substrate – and the presence of vacancies that damp the amplitude of the collective modes.²¹

4.4.6 Specificity

The specificity of a biosensor is very challenging when the analyte has to be detected in a complex matrix such as human blood, but it is also particularly important for malaria diagnostics in areas where both *P. falciparum* and *P. vivax* are endemic as the clinical decision-making for drug treatment is different for infection with each species. In this respect, the response of each aforementioned fluoroimmunoassay was evaluated against *Pv*LDH, which shares high functional and sequence similarity with *Pf*LDH (90% residue identity)²⁵⁰. The *Pv*LDH was spiked into uninfected human blood (1:100 diluted in 1 mL of 25 mM Tris buffer) to reach the highest analyte concentration explored in case of *Pf*LDH (i.e., 1 μ M for randomly positioned and branched arrays of AuNPs and 100 nM for honeycomb lattice of AuNPs, referred to undiluted whole blood). Figure 4.15 shows the fluorescence intensity measured with no analyte (control), competitive analyte (*Pv*LDH), and analyte of interest (*Pf*LDH). Although the bottom bioreceptor layer – consisting of pan malaria anti-*PLDH* – may capture any *PLDH* malaria biomarker, no significant cross-reaction was detected in the case of *Pv*LDH because of the extremely high specificity of the Apts used as top bioreceptor layer. Such a

result is consistent with reports that the Apt used in this assay is highly specific to *Pf*LDH over *Pv*LDH.²⁵¹

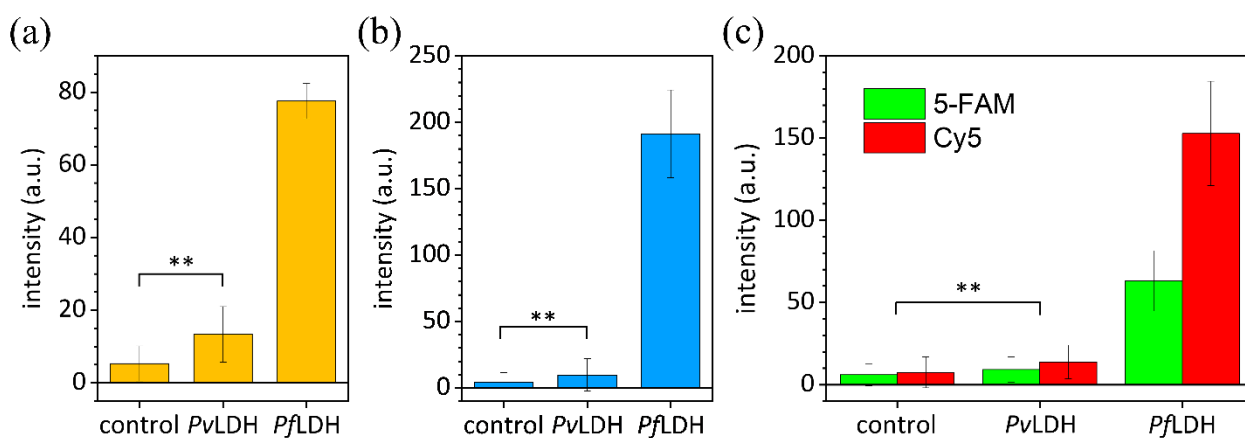


Figure 4.15. Specificity of the Ab-Apt* malaria fluoroassay against *Pv*LDH (** p -value < 0.001) in case of (a) randomly positioned, (b) honeycomb lattice, and (c) branched arrays of AuNPs. The data are presented as mean value \pm standard deviation and are representative of ten technical repeats.

4.4.7 Discussion

The gold standard for diagnosing malaria relies on the microscopic examination of blood films that not only necessitates trained personnel, but is unsuitable for a rapid diagnosis, which is required for a favourable prognosis of the disease.²⁵² Thus, big efforts are put in trying to develop rapid test based on a technology accessible even to the populations more exposed to the risk of infection. The most effective strategy largely adopted entails the detection of some of the enzymes expressed by the *Plasmodium* parasites that cause the disease. Lactate dehydrogenase is expressed in all *Plasmodium* species whilst an alternative biomarker, histidine rich protein II (HRP2), is only expressed in *P. falciparum*. Typically, for *P. falciparum* detection, LDH is preferred to HRP since the former better correlates with the parasite density,²⁴¹ however often species-specific detection requires tests against both LDH and HRP.

The aforementioned apta-immunosensors are able to specifically detect *Pf*LDH in whole blood down to femtomolar level (LOD < 1 pg/mL), which is a limit of detection several orders of magnitude lower than the rapid diagnostic tests²⁵³ or the commercial ELISA kits.^{27,241} Such remarkable outcomes are reached thanks to a unique optimization of two ingredients of a biosensor: the transduction mechanism and the surface biofunctionalization, coupled with the recognition of the biomarker by both Abs and Apts. Furthermore, the functionalization procedure of PIT can be carried out by a simple UV lamp in a few minutes, thereby allowing such an approach to be carried out in low resource

settings which would be critical for many malaria diagnostic applications. Therefore, this approach may provide a solution to the cold transport challenges common to the presently used immunochromatographic lateral flow assays.^{245–247}

Whilst the *Pf*LDH and *Pv*LDH investigated for the data herein were expressed in *E. coli*, previously solved crystal structures of these proteins in complex with aptamers show that these proteins do reflect the native conformation of these proteins.^{249,254} It has been highlighted that sensitivity is a critical issue for malaria rapid diagnostic tests. The limit of detection for *PLDH*-based immunochromatographic rapid diagnostic tests are typically in the range of 25 ng/mL.²⁵³ The approaches herein described are up to 1000-fold more sensitive. This opens up the possibility of point-of-care detection of *PLDH* in saliva which could transform malaria diagnosis as then one could diagnose non-invasively without the need for drawing blood from a patient. Such an approach would also reduce the risk of transmitting blood-borne pathogens. *PLDH* has been demonstrated to be present in saliva,²⁵⁵ but there is no technology yet developed with sufficient sensitivity. Attempts to diagnose in saliva using conventional approaches lead to a high number of false negatives.²⁴⁶ Therefore, aforementioned apta-immunosensors may provide a cost-effective solution providing the first non-invasive approach for a point-of-care diagnosis of malaria. A clinical study will be required to address this possibility.

As it concerns the transduction, the enhancement of the fluorescence intensity occurring by means of plasmonic nanostructures was exploited. Such a process is critically dependent on a number of conditions, the most noticeable being (i) the geometry of the nanostructure, (ii) the amount of spectral overlap between the plasmon resonance with both the fluorophore absorption and emission, and (iii) the separation distance between the fluorophore and the nanostructure. The constraint of realizing a device for practical applications suggested to adopt simple nanolithography techniques relying on electrostatic self-assembly of metal nanoparticles and BCMN, which allows one to rapidly fabricate randomly positioned and ordered arrays of AuNPs over large surfaces,¹⁸⁹ readily usable as a substrate for multiwell plates. Moreover, in the case of BCMN, the final AuNP conformation (i.e., diameter/interparticle distance) is realized through a subsequent chemical growing process. Thus, the resulting honeycomb array has a quite broad interparticle distance distribution, whereas nanoparticle surface shows some degree of roughness. Rather than being a drawback, such features lead to a relatively wide plasmon resonance peak that realizes the so-called dual enhancement mechanism,²⁰⁴ in which the plasmon resonance overlaps with both the excitation and emission peaks of the fluorophore.

Furthermore, the highest fluorescence enhancement only occurs when the fluorophore is placed at approximately 10 nm from the surface. Thus, to achieve precise positioning of the fluorophore, an effective surface biofunctionalization procedure (PIT) was exploited, which binds the Abs so that their Fab region is at approximately 5 nm from the surface,^{82,89} with a sandwich scheme that included a tagged Apt on the top. Since the size of both the *Pf*LDH and the Apt is only a few nanometers, the fluorophore automatically positions itself at the optimal distance from the surface, and this was demonstrated by the measured-experimental enhancement factors delivered by these systems. As a result of the occurrence of optimal conditions for detecting *Pf*LDH, the apta-immunosensors herein described were able to measure a LOD down to 18 fM (0.6 pg/mL) – in case of honeycomb lattice of AuNPs –,¹⁸¹ which is comparable to that recently measured by means of a much more complex Luminex technology.²⁵⁶

By building on such results, two straightforward perspectives can be explored and even combined to make the clinical potential of these approaches of significant impact: multiplexed and ultrasensitive (at attomolar level) detection. The former can be accomplished by functionalizing each section of a large substrate (e.g., multiwell plate) with different Abs so that several analytes can be easily distinguished by their position on the substrate. On the other hand, detection at the attomolar level can be achieved by detecting the analyte in serum or plasma since these matrices would not require the 1:100 dilution carried out in these work to reduce the turbidity of the whole blood.

Conclusions

This work presents a deep investigation into the optical response of a large variety of metal nanostructures when illuminated by visible electromagnetic radiation. Particularly, resonant modes arising from the interaction between surface plasmons and external perturbation represent the aim of this study given their applications in the biosensing field. A plenty of optical biosensors relying upon plasmon-related effects can be conceived to both push down the detection limits and improve the feasibility of testing (e.g., point of care assay, mass screening, high-throughput screening, non-invasive procedure). In this view, AuNPs are the prime candidates for developing optical biosensor – both in colloidal solutions and on solid substrates – given the simplicity and scalability in fabrication, their biocompatibility and inertness, and the thiol-reactive surface chemistry. Antibody-functionalized AuNPs have been used throughout all the experiments described in this thesis since having revealed themselves to be apt to effectively detect a large variety of analytes (e.g., molecules, proteins, viruses) down to femtomolar level even in complex matrices such as human whole blood if implemented in colorimetric sensors or fluoroassays.

The thesis has been organised in four chapters in order to gradually introduce the readers into the world of plasmonics and throughout the conducted experiments. Each chapter opens with a theoretical description of the corresponding subject while ends conveying the obtained experimental and numerical results (except for Chapters 1 that is purely introductory). In particular, two colorimetric immunosensors have been presented in Chapter 2 capable for detecting estrogens in tap water at picomolar level⁸⁹ and SARS-CoV-2 virions in naso-oro-pharyngeal swabs even in case of very low viral loads.¹⁰⁰ The promising outcomes in terms of both sensitivity and reliability open up the possibility to extend such colorimetric immunosensors to routinely tests in clinical trials and environmental contaminant monitoring. Nevertheless, there are still some points that deserve a deeper investigation to further improve the performance of such AuNP-based colorimetric immunosensors. For instance, a test campaign on different nanoparticle sizes and shapes can be conducted to investigate the optical behaviour of the system as a function of the type of analyte to be detected in order to maximize the response from a sensing point of view (i.e., seeking a dynamic equilibrium that

promotes the largest nanoparticle clusters so to extend the detection range over more decades). Moreover, the adoption of core-shell magnetic nanoparticles rather than non-magnetic nanoparticles can pave the way for intriguing new opportunities in biosensing applications relying on a colorimetric approach such as the possibility to preconcentrate the sample by simply magnetically attracting the core-shell nanoparticles after the analyte capture or to improve the sample mixing to gain an advantage from a magnetic stirring at nanometric scale. As future works, the sensing potentialities of such an approach could be explored in viscous, opalescent, and more complex matrices such as saliva to conceive non-invasive POC tests capable to face with the uncontrolled diffusion of endemic diseases.

When metal nanoparticles are immobilized onto solid substrates in such a way as to realise two-dimensional periodic arrays, astonishing collective resonant modes arise from the optical coupling of the surface plasmons if illuminated by a certain electromagnetic radiation. The optical response delivered by three different patterns of AuNPs – fabricated through electrostatic self-assembly and block copolymer micelle nanolithography – has been experimentally and numerically investigated in Chapter 3 finding out that such collective plasmon resonances strongly depend on the ratio between nanoparticle diameter and interparticle distance and only large values promote significant collective effects. Aiming at evaluating the optical performance attainable by taking advantage of these collective plasmon modes, the fabricated two-dimensional patterns of AuNPs have been implemented in fluoroassay techniques as biosensing platforms to effectively enhance the fluorescence emitted by the dye-labelled targets. The experiments described in Chapter 4 have been carried out for detecting a malaria biomarker in human whole blood through an antibody-analyte-aptamer sandwich scheme, in which the fluorescently labelled aptamers resulted to be inherently positioned at approximately 10 nm from the nanoparticle surface. The excellent results in terms of both ultrasensitive detection (down to femtomolar level)¹⁸¹ and fluorescence amplification (up to 7×10^4)¹⁸¹ have been obtained thanks to not only the optimization of the plasmon-fluorophore spectral overlap and fluorescent dye positioning, but also the effective surface functionalization warranted by an innovative photochemical immobilization technique able to covalently tether antibodies onto gold surfaces in a close-packed and upright configuration.⁸²

Although there are still some areas that need further optimization (e.g., a fluidic system that allows one to functionalize several substrates with the same amount of irradiated Abs since only a tiny fraction of them effectively binds the surface), such plasmonic substrates may constitute the bottom of a multiwell plates paving the way to high-throughput analysis, a feature that makes the device promising in several biological applications since the extension to other analytes can be immediately

achieved by properly adapting the sandwich scheme. Moreover, it is expected that the reported LODs lying in the femtomolar-picomolar range may be pushed down to attomolar level if a transparent matrix (e.g., human serum or saliva) rather than whole blood is analysed. As future works, PEF-based devices could be conceived to go “beyond ELISA” assays and as such they will be potential candidates for a change of the gold standards in biochemical analysis. In fact, in the proposed approach, the process underlying the signal amplification relies upon the simpler and more robust PEF phenomenon rather than enzymatic reactions, the latter being inherently less controllable. In addition, the potential multiplexed and high-throughput analysis paves the way for the definition of a panel of several biomarkers whose analysis gives rise to an accurate and personalised diagnosis with a reliable index of risk, extremely useful in several biomedical applications such as for the treatment of the prostate cancer, thereby significantly reducing the number of surgery treatments with remarkable benefits not only for the patients (social impact), but also for the national health system (economic impact).

Appendix A. Nanoparticle synthesis

A.1 Turkevich's method

A volume of 1 mL of $\text{HAuCl}_4 \cdot 3\text{H}_2\text{O}$ (25.4 mM) was spiked in 100 mL of ultrapure water under vigorous stirring and the solution was warmed at 150 °C. During the boiling, 2 mL of sodium citrate (80 mM) was added into the solution by holding the same temperature and vigorous stirring for 20 min. Meanwhile, the colour of the solution changed from yellowish to dark and then to bright red. Thus, the beaker was moved on a cold plate, by holding the stirring for 2 h. Eventually, the colloidal solution exhibits an OD of ~ 0.6 at 450 nm corresponding to a concentration of 6×10^{10} AuNPs/mL for 20 nm diameter AuNPs.^{257,258} Aiming at removing the sodium citrate surrounding the AuNPs thereby allowing them to be functionalized, a volume of 1 mL of citrate-stabilized AuNPs was centrifuged for 30 min at 6500 g. After the centrifugation, the pellet was re-suspended in 1 mL ultrapure water. Afterward, the AuNP colloidal solution was stored in dark conditions at 4°C.

A.2 Pollitt's method

A solution composed of 0.5 mL solvated $\text{HAuCl}_4 \cdot \text{H}_2\text{O}$ (24 mM) and 50 mL of ultrapure water was warmed at 150 °C under vigorous stirring. During the boiling, 6 mL of sodium citrate dihydrate (39 mM) was added into the solution to induce particle nucleation. After 2 minutes, 4.2 mL of $\text{HAuCl}_4 \cdot \text{H}_2\text{O}$ (24 mM) was added to activate particle growth. Within some minutes, the solution colour moved from transparent to black and then to bright red. The solution was cooled down for 2 hours by holding vigorous stirring. Eventually, a volume of 200 μL of synthesized AuNPs diluted into 800 μL of ultrapure water exhibits a narrow LSPR peak at 529 nm and OD approximately of 1.4-1.5. Aiming at removing the sodium citrate surrounding the AuNPs thereby allowing them to be functionalized, a volume of 1 mL made by 200 μL of citrate-stabilized AuNPs and 800 μL of ultrapure water was centrifuged in two steps: i) 15 min at 9000 g, and ii) 10 min at 5000 g. After each

centrifugation, the pellet was re-suspended in 1 mL ultrapure water. This resulted in OD reduction to ~ 1.0 at 529 nm corresponding to approximately 10^{11} AuNPs/mL for 35 nm diameter AuNPs.^{257,258} Afterward, the AuNP colloidal solution was stored in dark conditions at 4°C.

A.3 Gold growth

The gold growth was triggered by using a gold growth solution.²⁵⁹ A volume of 0.384 mL of $\text{HAuCl}_4 \cdot 3\text{H}_2\text{O}$ (40 mM) was added into 6 mL of hexadecyltrimethylammonium bromide (CTAB) (200 mM) under gentle stirring. The solution at this stage appears bright brown-yellow in colour. Then, 0.228 mL of AgNO_3 (10 mM) was spiked into the solution to restrict the gold growth to the spherical shape. Afterwards, 0.960 mL of ascorbic acid (100 mM) was added into the solution that suddenly became colourless. Eventually, the solution was diluted into 11 mL of ultrapure water by holding gentle stirring for 30 min.

Appendix B. Fabrication of 2D AuNP array

B.1 Fabrication of randomly positioned AuNPs

Silanization process by using (3-Aminopropyl)triethoxysilane (APTES) was employed to chemically modify the substrate – consisting of $10 \times 8 \text{ mm}^2$ glass coverslips – allowing the randomly immobilization of citrate-stabilized AuNPs onto the surface by simple adsorption via electrostatic interactions.¹⁸⁸ The procedure included five steps that are schematically shown in Figure 3.3. (a) The coverslips were cleaned by sonication for 5 min in acetone, 2-propanol and pure ethanol sequentially, and extensively rinsed by ultrapure water. (b) The glass surface was activated by oxygen plasma treatment (1.4 mbar pressure, 200 W power, 2 min). (c) The activated substrates were modified with APTES by controlled low-pressure evaporation inside a vacuum desiccation chamber (argon gas, 5 mbar pressure, 1 h). (d) The silanized substrates were incubated with 1 mL of colloidal citrate-AuNPs of 35 nm diameter (OD ~ 1.0) for 4 h at room temperature and dark condition (see Appendix A.2 for more details about AuNP synthesis). (e) A low-pressure oxygen plasma treatment (0.8 mbar pressure, 200 W power, 30 min) was used to etch the free citrate ligands and silane layer.

B.2 Honeycomb lattice of AuNPs

29.2 mg of diblock copolymer P18226-S2VP (made of PS(x)-b-P2VP(y), in which $x = 30000 \text{ g/mol}$ and $y = 8500 \text{ g/mol}$ are the molecular weight of polystyrene (PS) and poly(2-vinylpyridine) (P2VP), respectively) was added into 15 mL of toluene under vigorous stirring and controlled conditions (argon inert gas, $\text{O}_2 < 1 \text{ ppm}$, $\text{H}_2\text{O} < 0.1 \text{ ppm}$) for 72 h achieving homogeneously dispersed reverse micelle. Then, 15.7 mg of $\text{HAuCl}_4 \cdot 3\text{H}_2\text{O}$ was loaded in the solution by holding the vigorous stirring for 72 h allowing the gold precursor to be housed into the hydrophilic core of the reverse micelles. When the gold powder was completely dispersed, the yellowish solution was filtered to remove micelle aggregates and impurities. Before depositing the PS-AuNPs on the glass coverslips (10×8

mm²), the bare substrates were cleaned by sonication for 5 min in acetone, 2-propanol, and pure ethanol sequentially, and dipped in toluene in order to make non-polar the surface so that the hydrophobic shells could stick on that. Then, the glass coverslips were dipped into the PS-AuNPs solution by a dip-coater to carefully tune the dipping speed. A dipping speed of 0.6 mm/s provided an optimal coverage of the glass surface in terms of both PS-AuNPs close-packing and long-range regularity. The copolymers were etched by oxygen plasma treatment (0.8 mbar pressure, 200 W power, 30 min). Afterwards, the substrates were incubated with 2 mL gold growth solution for 2 h in dark condition (see Appendix A.3 for more details about the preparation of the gold growth solution). Then, the substrates were copiously rinsing by ultrapure water and stored in dark condition until use.

B.3 Branched arrays of AuNPs

24.3 mg of diblock copolymer P3807-S2VP (made of PS(*x*)-b-P2VP(*y*), in which *x* = 325000 g/mol and *y* = 92000 g/mol are the molecular weight of polystyrene (PS) and poly(2-vinylpyridine) (P2VP), respectively) was added into 15 mL of toluene under vigorous stirring and controlled conditions (argon inert gas, O₂ < 1 ppm, H₂O < 0.1 ppm) for 72 h achieving homogeneously dispersed reverse micelle. Then, 13.1 mg of HAuCl₄·3H₂O was loaded in the solution by holding the vigorous stirring for 72 h allowing the gold precursor to be housed into the hydrophilic core of the reverse micelles. When the gold powder was completely dispersed, the yellowish solution was filtered to remove micelle aggregates and impurities. Before depositing the PS-AuNPs on the glass coverslips (10 × 8 mm²), the bare substrates were cleaned by sonication for 5 min in acetone, 2-propanol, and pure ethanol sequentially, and dipped in toluene in order to make non-polar the surface so that the hydrophobic shells could stick on that. Then, the glass coverslips were dipped into the PS-AuNPs solution by a dip-coater to carefully tune the dipping speed. A dipping speed of 0.8 mm/s resulted in a reduction of the surface density thereby promoting the formation of branched arrays of PS-AuNPs. The copolymers were etched by oxygen plasma treatment (0.8 mbar pressure, 200 W power, 30 min). Afterwards, the substrates were incubated with 2 mL gold growth solution for 2 h in dark condition (see Appendix A.3 for more details about the preparation of the gold growth solution). Then, the substrates were copiously rinsing by ultrapure water and stored in dark condition until use.

Appendix C. Morphological characterization

C.1 Analysis of SEM images

The substrates were morphologically characterized by Zeiss LEO 1550VP field emission scanning electron microscope (FESEM) with a nominal resolution of 1 nm at 20 kV acceleration voltage. The recorded scanning electron micrographs were processed by ImageJ software to retrieve information concerning the shape and size of nanoparticles and the center-to-center distance. Firstly, raw images (Figure C.1a shows an example of micrograph acquired at high magnification) were thresholded thereby isolating nanoparticles from the background (Figure C.1b). Then, adjacent objects were separated by “Watershed” tool implemented in ImageJ (Figure C.1c). Eventually, perimeter p , area S , centroid coordinates, and shape descriptors (circularity $C = 4\pi S/p^2$ and aspect ratio AR) were measured by decomposing each object in outline and inner region through “Analyze Particles” tool of ImageJ (Figure C.1d). Particle diameter was estimated as $D = 2\sqrt{S/\pi}$ while interparticle distance by computing the distance among each centroid and its nearest neighbours.

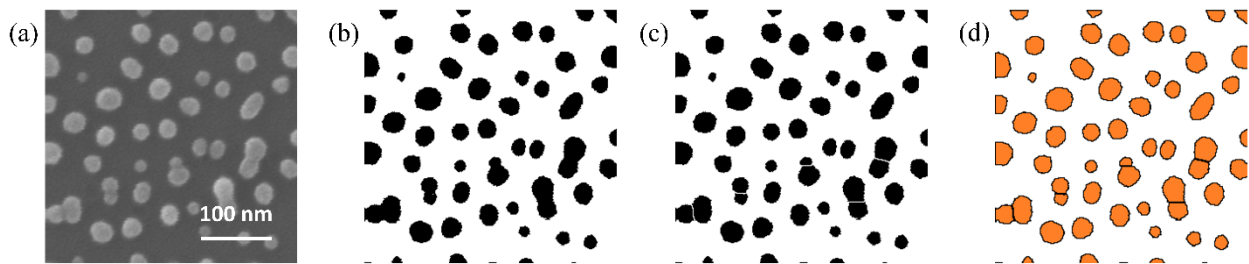


Figure C.1. SEM image analysis. (a) Example of raw top view SEM micrograph at high magnification. Corresponding (b) thresholded and (c) segmented image. (d) Processed image in which the objects are decomposed in outlines (black line) and inner region (orange filling).

C.2 Coding of the simulation model

The optical response of honeycomb lattice of AuNPs and fabricated substrates was worked out by “FDTD solutions” tool implemented in Lumerical software. The workspace was discretized over a mesh with a spatial resolution of 0.5 nm and 1.0 nm for the ideal lattice and the actual substrates, respectively. Such a choice assured high accuracy while keeping the simulation time within few hours. Gold nanoparticles were modelled as homogeneous gold spheres¹⁶³ while the bare substrate as a thick dielectric layer of silicon dioxide (SiO₂).²⁶⁰ Symmetric/anti-symmetric BCs set along x and y direction extend the optical response over an infinite nanoparticle array while reducing the simulation time by a factor 8 without worsening the accuracy of the results. Bloch BCs were used only for polarization study in order to compensate the phase shift arising when an EM wave with a non-zero angle should be re-injected at the opposite workspace site. Perfect matched layer BCs set in z direction assures perfect absorption of the EM waves backscattered through the plane containing the light source and incident upon the opposite side of the workspace.

The extinction spectrum of the actual substrate was carried out by importing the SEM morphology in Lumerical workspace. To this aim, the raw image (Figure C.2a shows an example at high magnification) was thresholded and binarized to create a mask template, in which the object pixel value was set equal to 1 and the background to 0 (Figure C.2b). The centroid coordinates (i_{nc}, j_{nc}) of the n^{th} object were retrieved by running “Analyze Particles” tool implemented in ImageJ software (Figure C.2c). Following to the mask template, the centroid positions were used to shape spherical nanoparticles of 50 nm diameter (Figure C.2d) as

$$z(i_n, j_n) = \pm \sqrt{(D/2)^2 - (i_n - i_{nc})^2 - (j_n - j_{nc})^2} \quad (\text{C.1})$$

Figure E.4b shows an example of the rendering provided by Lumerical framework.

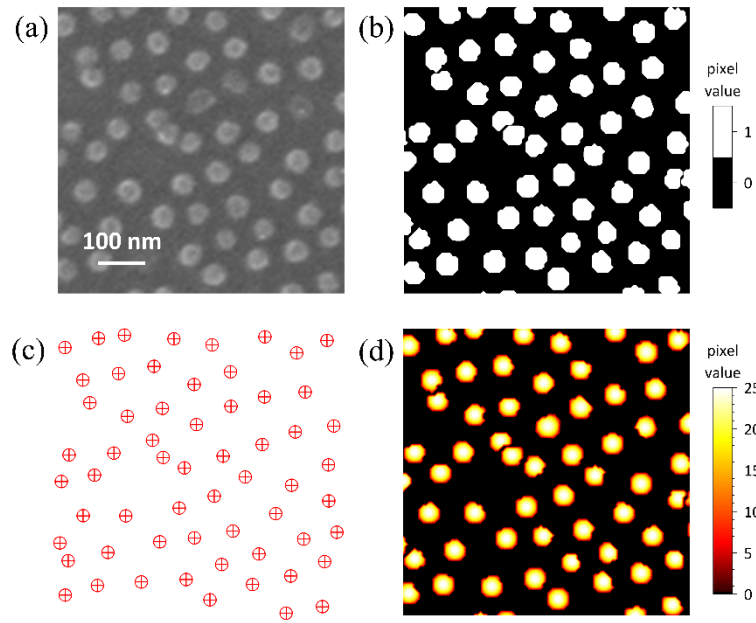


Figure C.2. (a) Example of raw top view SEM image at high magnification. Corresponding (b) mask template and (c) centroid mask. (d) Nanoparticle template created by Equation (C.1).

Appendix D. Biofunctionalization, blocking and detection

D.1 UV-lamp

The UV source (Trylight®, Promete S.r.l.) consisted of two U-shaped low-pressure mercury lamps (6 W at 254 nm) in which a standard 10 mm quartz cuvette could be easily housed (Figure D.1). By considering the wrapping geometry of the lamps and the proximity of the cuvette, the irradiation intensity used for the thiol group production was approximately 0.3 W/cm^2 .



Figure D.1. Low pressure mercury U-shaped UV lamps used to carry out the thiol activation in antibody Fabs. The length of the scale bar in the top-right corner is 1 cm.

D.2 Colloidal solution

Gold nanoparticles in colloidal solution were functionalized through PIT. A certain volume of aqueous solution containing Abs was irradiated by an UV-lamp (Trylight®, Promete S.r.l., Figure

D.1) for 30 s so to activate the thiol groups located in the antibody Fabs. Different volumes and Ab concentrations were used throughout the experiments on colorimetric sensing to effectively tailor the biofunctionalization to the case study of interest.

D.2.1 Colorimetric immunosensor for detecting 17 β -estradiol in tap water

A volume of 25 μ L aqueous solution of irradiated anti-E2 (18 μ g/mL) was added into 1 mL of colloidal solution containing AuNPs of 35 nm diameter (re-suspended in ultrapure water after centrifugations, OD \sim 1.0). The corresponding anti-E2 concentration in the final solution was 450 ng/mL ($\sim 2 \times 10^{12}$ Abs/mL). Such a volume was added in 5 spikes (5 μ L each one) followed by a gentle mixing to avoid non-specific AuNP aggregation. This procedure was a result of an empirical study in which different amounts of anti-E2 were tested to evaluate the LSPR shift (Figure E.1). The resonance peak red-shifted as the anti-E2 concentration increased up to 5 nm corresponding to an Ab concentration of 1 μ g/mL. For larger amounts of anti-E2, no change in LSPR wavelength was observed due to the saturation of the free gold surface. Instead of using such an asymptotic value, the anti-E2 concentration was halved throughout the experiments in order to reduce the amount of free Abs into the solution. Thus, by assuming that most of the irradiated Abs bounded to gold surfaces, the average number of Abs per AuNPs was ~ 20 .⁸⁵ Eventually, 1 mg/mL of bovine serum albumin (BSA) was spiked into the solution for blocking the free AuNP surface so to prevent non-specific adsorption.

The different concentrations of E2 spiked in tap water were achieved by serial dilutions starting from a stock concentration of 20 μ g/mL. A volume of 20 μ L at each E2 concentration was added into 1 mL of f-AuNPs thereby essentially leaving unchanged the total volume. Although mechanical pipetting would speed up the system kinetics reducing the detection time down to few minutes, the solution was gently shaken by vortex mixer (for 10 s) aiming at warranting the reliability and reproducibility of the results without introducing any operator-dependent effects. Such a short mixing time increased the binding effectiveness among E2 molecules and f-AuNPs, while leaving the latter at rest. After mixing, the solution was left to reach the equilibrium via diffusion of complexed AuNPs (E2-f-AuNPs) into the whole reaction volume (1 mL) for 3 hours, a time long enough to warrant the reach of the equilibrium.¹³³ The shift experienced by the LSPR peak after E2 detection was correlated to the E2 concentration.

The repeatability of the optical response was evaluated by performing ten measurements at 10 pg/mL E2 concentration on different f-AuNP samples. The stability was investigated by recording the

absorption spectrum of a single f-AuNP sample at an E2 concentration of 10 pg/mL at different time intervals after the first measurements. The recovery was estimated by the ratio between the theoretical concentration of E2 provided by the dose-response curve and the corresponding nominal value. The specificity was tested on the most competitive molecules of 17 β -E2 like progesterone, estrogens (E1 and E3) and testosterone. Two different concentrations of each analyte were tested: 10 pg/mL (optimal for the E2 detection) and 100 ng/mL (an exceeding concentration) in order to assess the absence of nonspecific detection even in presence of very high interfering analyte concentration.

D.2.2 Colorimetric immunosensor for detecting SARS-CoV-2 in naso-oropharyngeal swabs

Antibodies used throughout the experiments were directed against spike proteins (anti-SARS-CoV-2 Spike S2 C-Term), membrane proteins (anti-SARS-CoV-2 Membrane Protein, SARS-CoV-2 M), and envelope proteins (anti-SARS-CoV-2 Envelope, SARS-CoV-2 E N-Term) of the SARS-CoV-2 virus. A volume of 100 μ L of each polyclonal Ab (pAb) (10 μ g/mL) was irradiated for 30 s and separately spiked (5 spikes, 20 μ L each one) into three 10 mL colloidal solutions of bare AuNPs of 20 nm diameter (OD \sim 1.0). The three solutions containing f-AuNPs were then mixed with 1:1:1 ratio and centrifuged (30 min at 3500 g) to remove free pAbs. The blocking was realized by adding BSA (25 μ g/mL).

Naso-oropharyngeal swab specimens in 3 ml Universal transport medium (UTMTM, Copan Brescia, Italia) were collected in the Infectious Diseases Unit of University Hospital Federico II (Naples, Italy) and tested for the presence of SARS-CoV-2 RNA within 24 h of collection. An Abbott Real Time SARS-CoV-2 assay was used, a dual target assay for RdRp and N-genes. The two SARS-CoV-2-specific probes are labelled with the same fluorophore, whereas the internal control (IC)-specific probe is labelled with a different fluorophore, allowing simultaneous detection of both SARS-CoV-2 and IC amplified products in the same reaction well. The Abbott Real Time SARS-CoV-2 assay were performed on the Abbott m2000 System. Total nucleic acids were extracted from UTM using an input sample volume of 600 μ L. Amplification was performed following manufacturer's instructions. Swabs were stored at -80° before further assays

A volume of 100 μ L drawn from the UTM specimen was mixed with 50 μ L of f-AuNPs and then diluted in 100 μ L of ultrapure water. The absorbance at 560 nm of each sample was measured by a GloMax®-Multi Microplate Reader (Promega Corporation) – capable for reading out the analysis on a 96 multi-well plate in less than 1 minute – for evaluating the presence of SARS-CoV-2.

D.3 Solid substrate

D.3.1 Ab-analyte-Apt* sandwich scheme realization

The Ab-functionalization of AuNPs immobilized onto the substrates was realized through PIT. A volume of 1 mL aqueous solution of Abs (50 $\mu\text{g/mL}$) was irradiated by an UV-lamp (Trylight®, Promete S.r.l., Figure D.1) for 30 s and then flowed onto the substrate (anti-PLDH was used throughout the all the experiments on solid substrates). The latter was integrated in a microfluidic circuit consisting of a cell containing the substrate of $10 \times 8 \text{ mm}^2$ size, a 2 mL syringe and Tygon tubes with a diameter of 1 mm (for both the input and output channel) designed for biological samples (Figure D.2). The volume of the solution in contact with the substrate was $\sim 30 \text{ }\mu\text{L}$, whereas the total volume flowing into the circuit was approximately 200 μL . The syringe was used to repeatedly draw 250 μL of the fresh aqueous solution containing the irradiated Abs (4 draws separated by a time interval of 3 min).

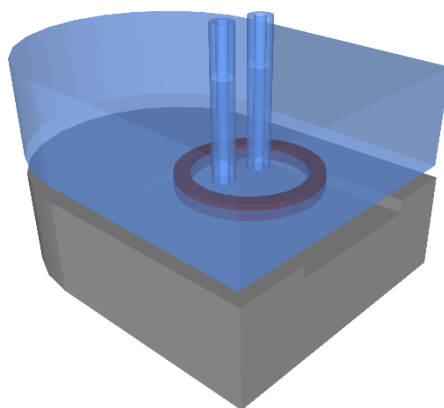


Figure D.2. Sketch of the fluidic cell used to promote an effective interaction of the irradiated Abs contained into the aqueous solution with the nanostructured substrate.

Then, the substrates were rinsed by ultrapure water to remove the unbound Abs. As it concerns the blocking of the free active surface, 1 mL of BSA aqueous solution (50 $\mu\text{g/mL}$) was used to prevent nonspecific adsorption (4 draws of 250 μL separated by a time interval of 1 min). Afterwards, the samples were copiously rinsed by ultrapure water and stored in PBS solution (10 mM) at room temperature until use.

The desired amount of analyte (*Pf*LDH was used throughout all the experiments on solid substrates) was spiked into 1 mL of the matrix of interest (uninfected human whole blood 1:100 diluted in 25 mM Tris buffer). The functionalized substrates were incubated with 1 mL of contaminated matrix solution for 2 h at room temperature; a tilting laboratory shaker was used to improve the analyte

diffusion. Then, the samples were copiously rinsed by Tris buffer (25 mM) and ultrapure water to remove the unbound analytes.

The samples were transferred into 1 mL of PBS solution (10 mM) containing 0.1 μ M of fluorescently-labelled aptamers specific for recognizing the analyte of interest (malaria 2008s labelled with 5-FAM or Cy5 tags was used throughout all the experiments on solid substrates. The aptamer nucleotide sequence is 5'-dye-CTG GGC GGT AGA ACC ATA GTG ACC CAG CCG TCT AC-3'). The solution was gently shaken for 2 h in dark condition by a tilting laboratory shaker so that the sandwich scheme reported in Figure 4.7c is realized. Then, the samples were abundantly rinsed by PBS and ultrapure water to remove the unbound aptamers.

D.3.2 Processing and analysis of the fluorescence images

Fluorescence images were recorded by Zeiss Axio Observer Z1 inverted phase contrast fluorescence microscope equipped by Zeiss Colibri.2 LED light source (modules 470 and 625 nm), Zeiss Plan-Apochromat 10x/0.45 Ph1 M27 (FWD = 2.1 mm) objective, 38 HE filter (excitation 450-490 nm/emission 500-550nm) and cube 50 Cy5 filter (excitation 625-655 nm/emission 665-715 nm), and pco.edge 5.5 sCMOS photodetector (scaling 0.650 μ m \times 0.650 μ m per pixel, image size 2560 \times 2160 pixels, scaled image size 1.66 mm \times 1.40 mm, 16 bit dynamic range, 2 s exposure time was used for each image).

The recorded fluorescence images were processed by ImageJ software. The “rolling ball” algorithm was used to remove the smooth continuous background from the raw images (Figure D.3a).²⁶¹ The background was locally measured for each pixel by averaging over a ball around the pixel. Such a value is then subtracted from the original image flattening the spatial variations of the background (Figure D.3b). The rolling ball radius was set 10 pixels, a length reasonably higher than the size of the largest objects that are not part of the background. A threshold level slightly higher than the flattened background was set to segment the image whose whole intensity was measured by summing the signal contribution of every spots (Figure D.3c). To ease the readability of the fluorescence measurements, the intensities were scaled down by an arbitrary factor. Aiming at carrying out a robust and reliable analysis of the fluorescence signal, ten images were randomly recorded for each sample and the mean of their intensity was found out.

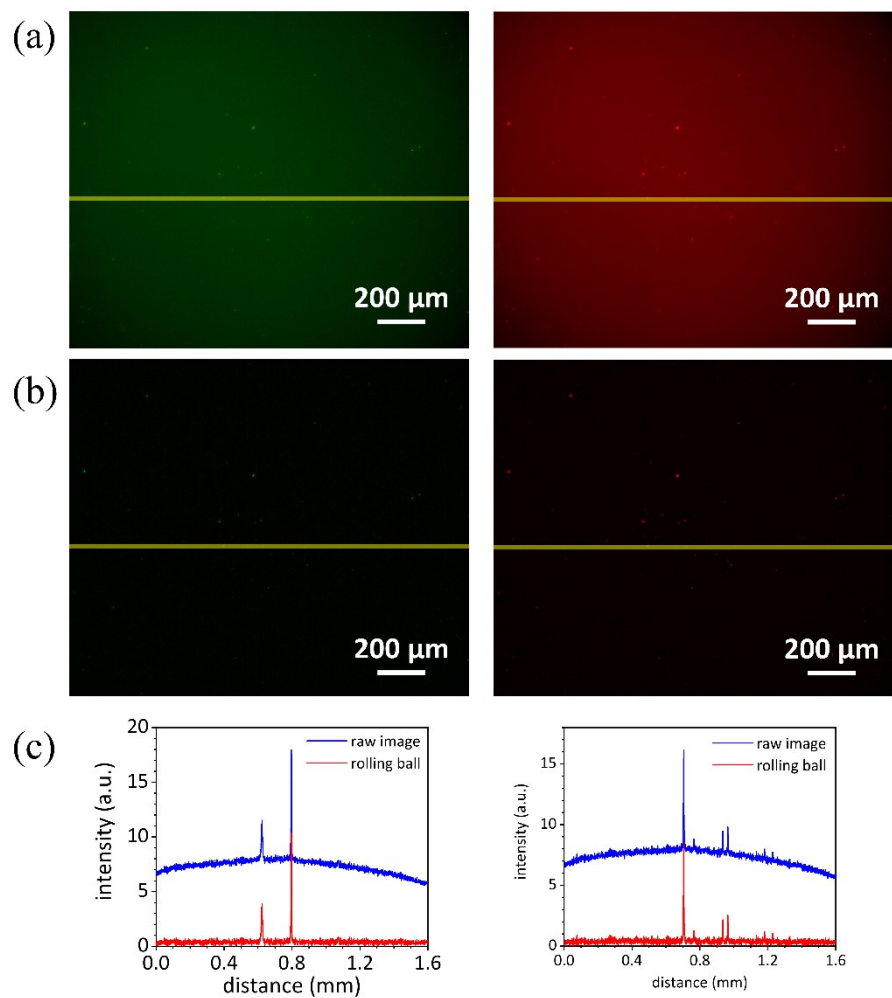


Figure D.3. Fluorescence image processing. (a) Example of raw fluorescence image recorded at low analyte concentration in case of 5-FAM (left panels) and Cy5 (right panels) dyes. The significantly high non-flat background was removed by the “rolling ball” algorithm. (b) Resulting images exhibit a flat background, from which the fluorescence spots are well distinguishable. (c) Intensity profile evaluated along the yellow line highlighted in panels (a) and (b).

Appendix E. Supplementary Data

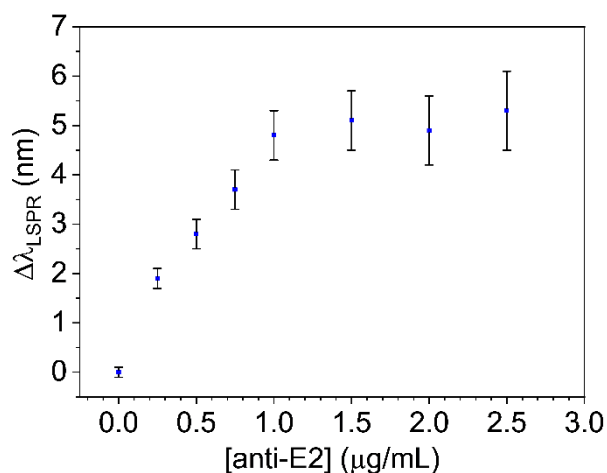


Figure E.1. Functionalization study. LSPR shift as a function of anti-E2 concentration. The functionalization of AuNPs in colloidal solution was realized by spiking 25 μL of irradiated Ab solution (18 $\mu\text{g/mL}$) into 1 mL of bare AuNPs (OD ~ 1.0). Such a volume was added in 5 spikes (5 μL each one) followed by gentle stirring to prevent nanoparticle aggregation.

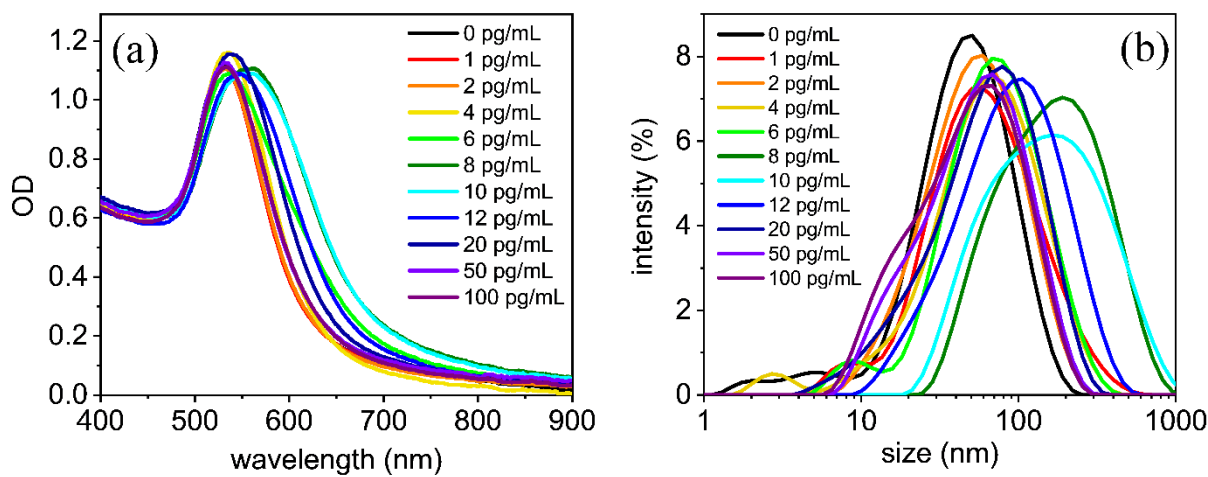


Figure E.2. (a) Absorption spectra and (b) intensity-size distribution measured at all the E2 concentration used throughout the work.

Table E.1. E-field intensity distributions of one- and two-dimensional AuNP geometries shown in Table 2.2 worked out by “FDTD Solutions” tool implemented in Lumerical software. The E-field intensity was evaluated at LSPR wavelength of each configuration.

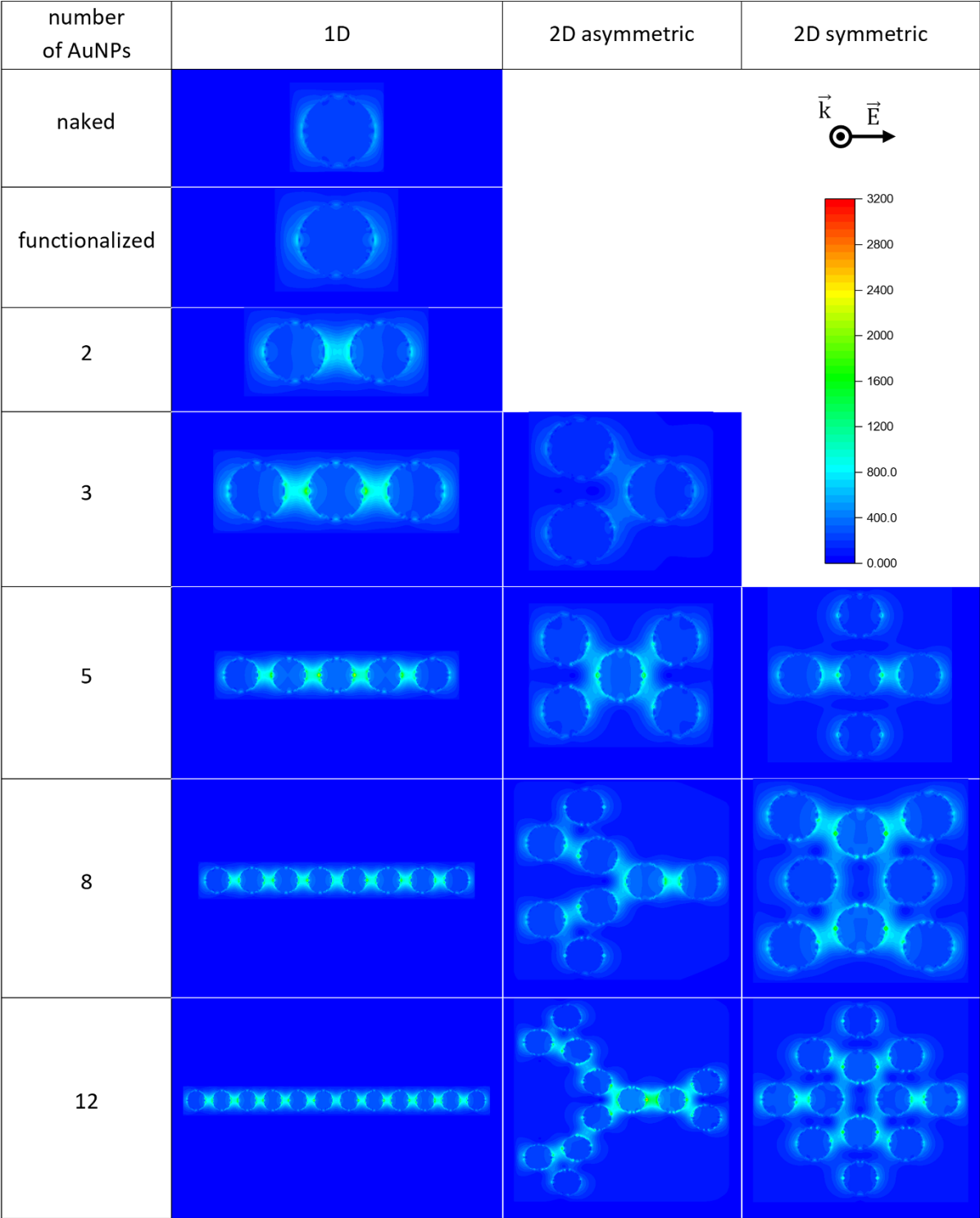


Table E.2. Data for the recovery measurement.

nominal value	$\Delta\lambda_{\text{LSPR}}$	measured value	recovery
pg/mL	nm	pg/mL	%
4	3.6	4.9	122.5
6	7.1	5.4	90.0
12	17.3	15.1	125.8
20	9.1	18.5	92.5

Table E.3. Example of serial dilutions useful to discriminate E2 concentrations up to 1 ng/mL. The numbers in each cell represent only the measurable concentrations of the diluted samples lying in the dynamic range. The concentrations out of the quantification range (3-30 pg/mL) are omitted. An unequivocal response can be attained by matching the LSPR shift of each dilution with the values provided by the dose-response curve. The cells of interest were filled by analogous colours of Figure 2.12a for simplifying the visual reading of the table.

[E2] pg/mL	dilution ratio				
	1:1	1:2	1:5	1:10	1:100
3	3	-	-	-	-
4	4	-	-	-	-
6	6	3	-	-	-
12	12	6	-	-	-
24	24	12	4.8	-	-
50	-	25	10	5	-
100	-	-	20	10	-
300	-	-	-	30	3
1000	-	-	-	-	10

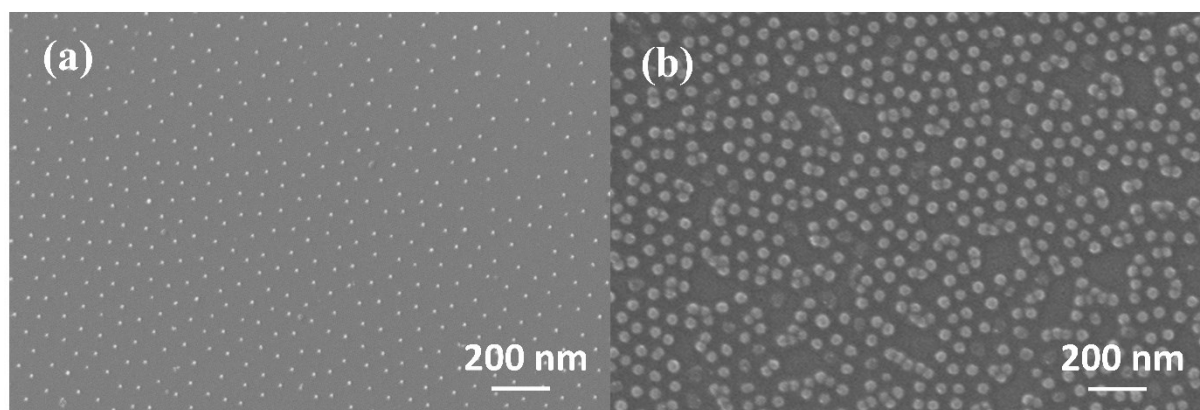


Figure E.3. Top view SEM images of the fabricated honeycomb array (a) before AuNP growth and (b) after 2 h of growth. Lattice defects (e.g., clusters and vacancies), randomly distributed on the substrate, arise during the growth step.

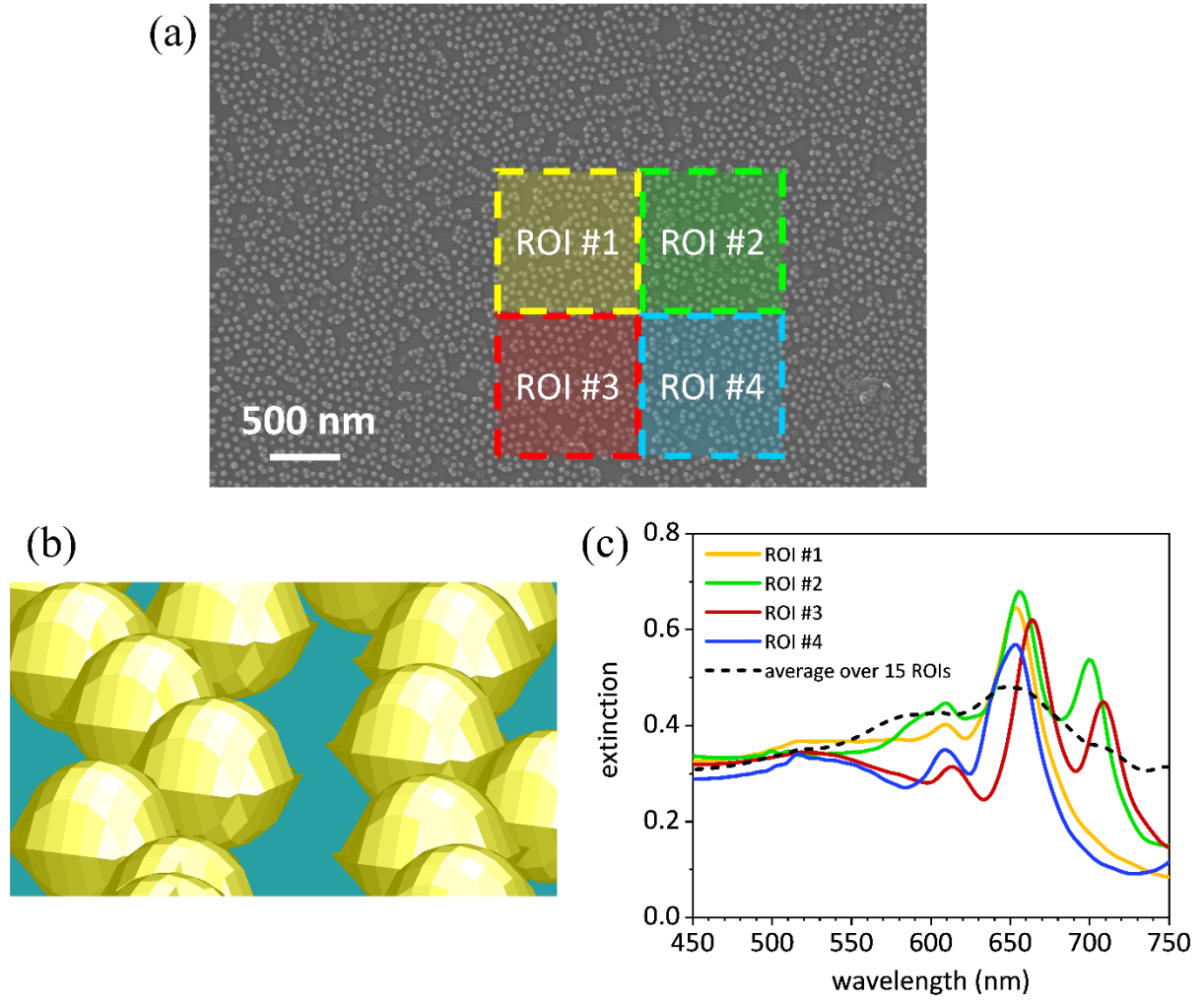


Figure E.4. (a) Top view SEM micrograph at low magnification. The highlighted squares ($1 \times 1 \mu\text{m}^2$) identify four out the fifteen regions of interest (ROIs), in which the optical response was simulated. (b) Detail of the substrate rendering provided by Lumerical software. (c) Example of simulated extinction spectra worked out by considering the actual substrate morphology. Line colours are used to identify the corresponding ROIs in panel (a) for which the optical response was investigated.

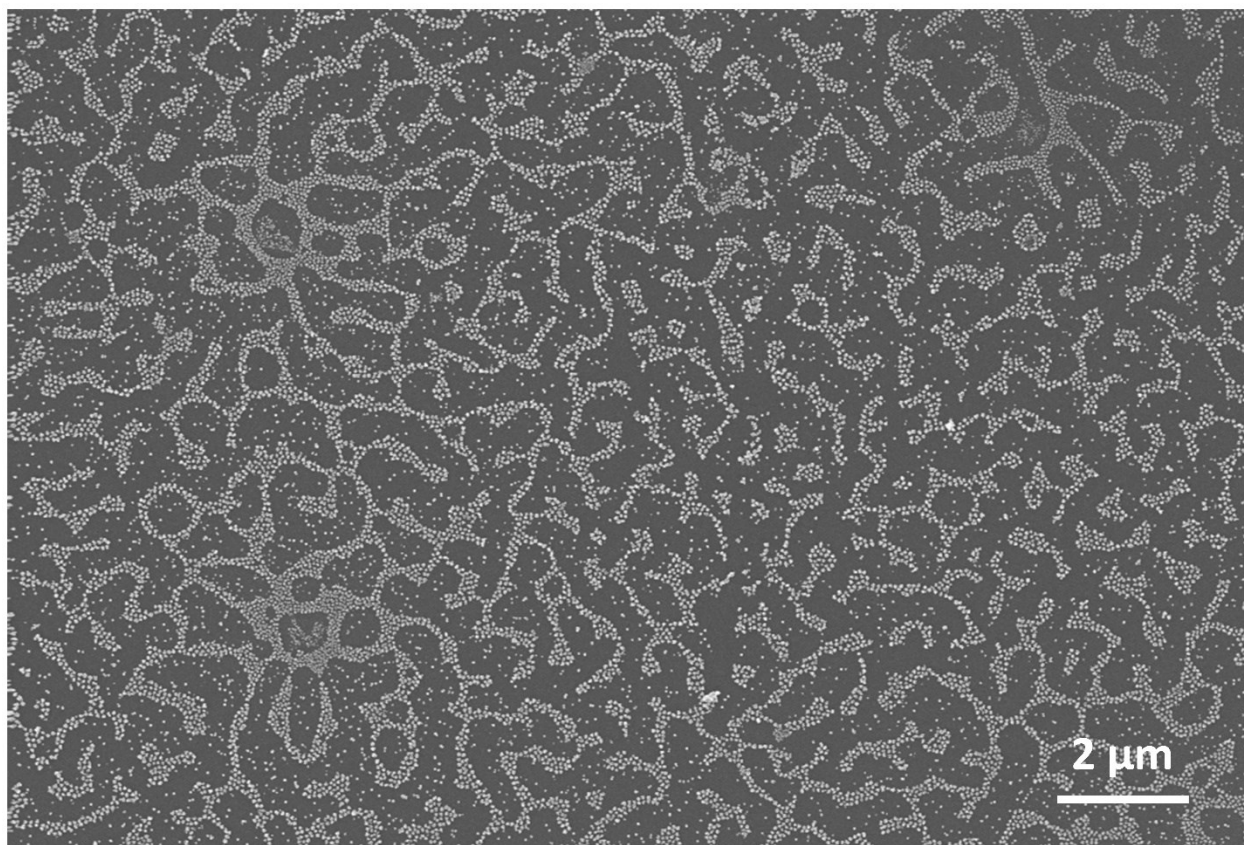


Figure E.5. Top view SEM micrograph at low magnification of the fabricated branched array of AuNPs after 2 h of gold growth.

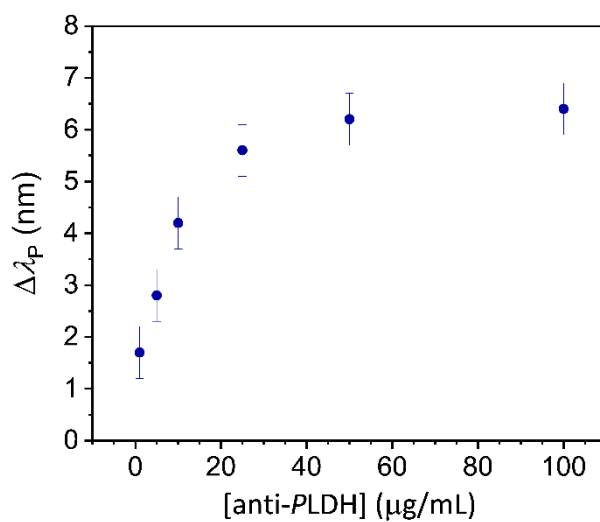


Figure E.6. Functionalization study. Wavelength shift of the resonance peak as a function of anti-PLDH concentration. The functionalization was realized by flowing 1 mL of irradiated Ab aqueous solution onto the bare substrate.

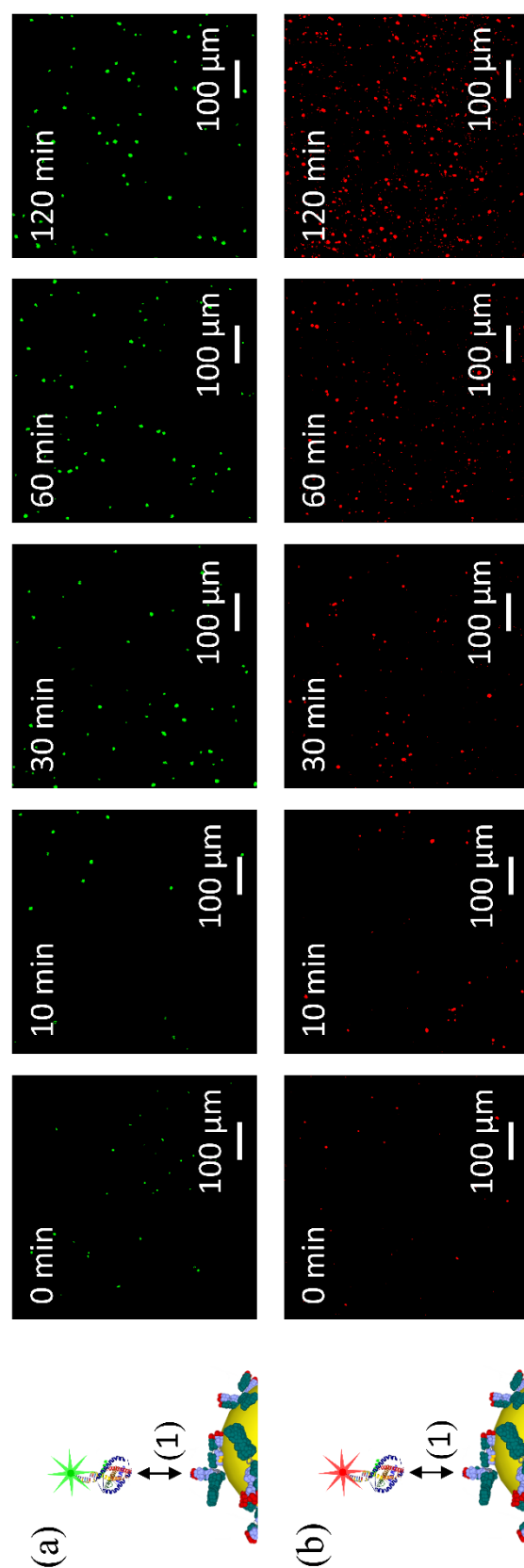


Figure E.7. Fluorescence images recorded at different incubation time of functionalized substrates into a solution containing pre-complexed *Pf*LDH-Apt* in case of (a) randomly positioned AuNPs optically coupled to 5-FAM-labelled Apt* and (b) honeycomb lattice of AuNPs optically coupled to Cy5-labelled Apt*.

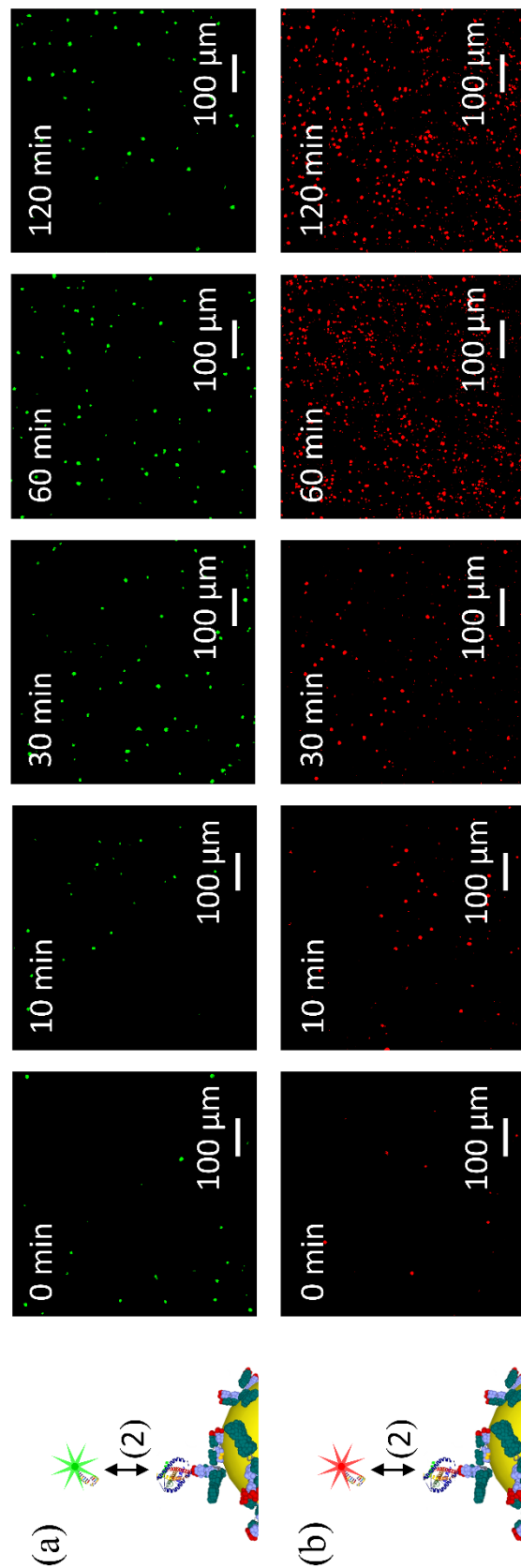


Figure E.8. Fluorescence images recorded at different incubation time of pre-complexed Ab-analyte – immobilized onto the substrate – into a solution containing Apt* in case of (a) randomly positioned AuNPs optically coupled to 5-FAM-labelled Apt* and (b) honeycomb lattice of AuNPs optically coupled to Cy5-labelled Apt*.

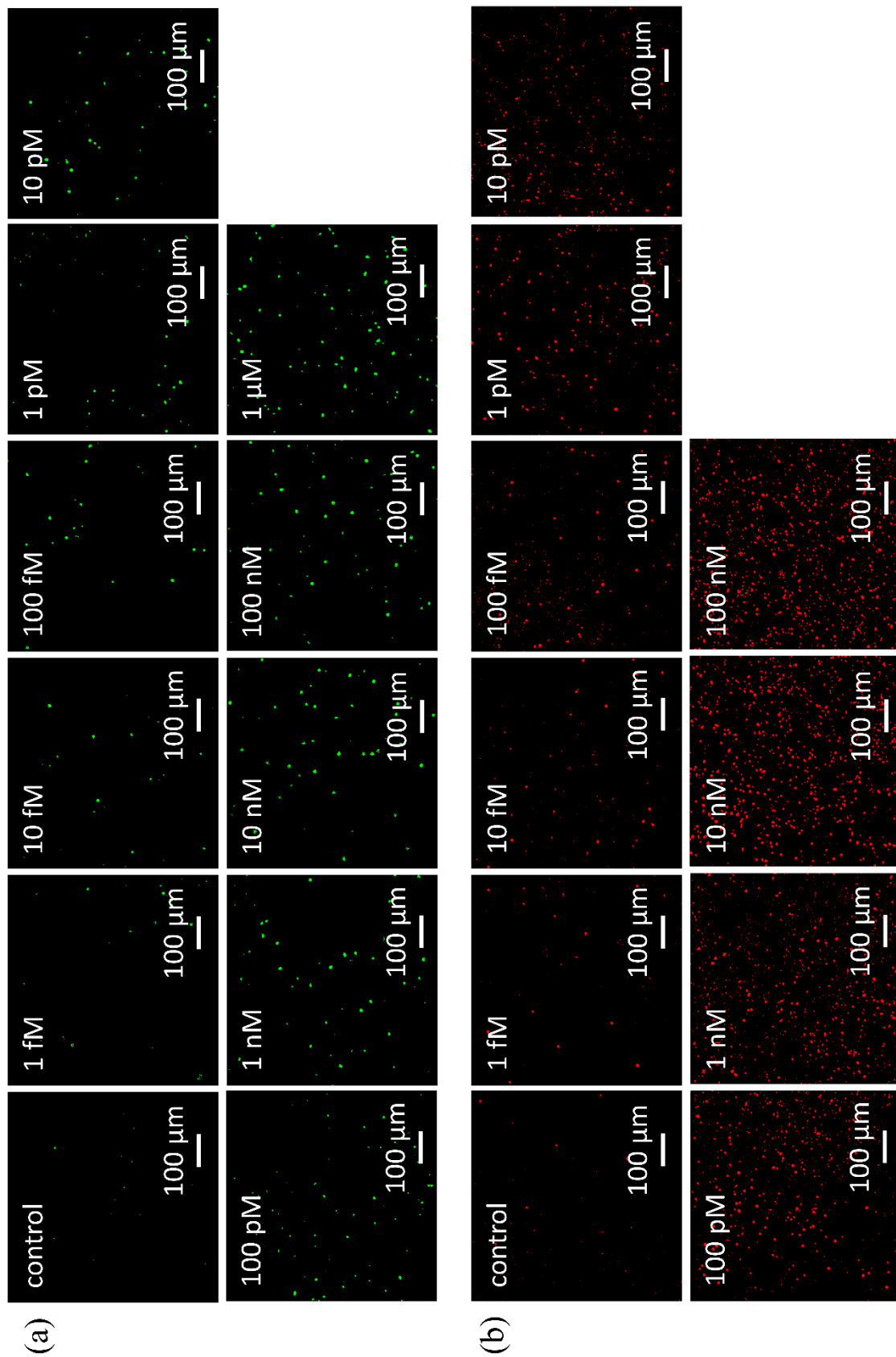


Figure E.9. Example of fluorescence images recorded at different P/LDH concentrations spiked into uninfected whole blood in case of (a) randomly positioned AuNPs optically coupled to 5-FAM-labelled Apt* and (b) honeycomb lattice of AuNPs optically coupled to Cy5-labelled Apt*.

References

1. Sommerfeld, A. Ueber die Fortpflanzung elektrodynamischer Wellen längs eines Drahtes. *Ann. Phys.* **303**, 233–290 (1899).
2. Zenneck, J. Über die Fortpflanzung ebener elektromagnetischer Wellen längs einer ebenen Leiterfläche und ihre Beziehung zur drahtlosen Telegraphie. *Ann. Phys.* **328**, 846–866 (1907).
3. Wood, R. W. On a Remarkable Case of Uneven Distribution of Light in a Diffraction Grating Spectrum. *Proc. Phys. Soc. London* **18**, 269–275 (1902).
4. Rayleigh, Lord. III. Note on the remarkable case of diffraction spectra described by Prof. Wood. *London, Edinburgh, Dublin Philos. Mag. J. Sci.* (1907). doi:10.1080/14786440709463661
5. Fano, U. The Theory of Anomalous Diffraction Gratings and of Quasi-Stationary Waves on Metallic Surfaces (Sommerfeld's Waves). *J. Opt. Soc. Am.* (1941). doi:10.1364/josa.31.000213
6. Ritchie, R. H. Plasma Losses by Fast Electrons in Thin Films. *Phys. Rev.* **106**, 874–881 (1957).
7. Powell, C. J. & Swan, J. B. Origin of the Characteristic Electron Energy Losses in Aluminum. *Phys. Rev.* **115**, 869–875 (1959).
8. Otto, A. Excitation of nonradiative surface plasma waves in silver by the method of frustrated total reflection. *Zeitschrift für Phys.* **216**, 398–410 (1968).
9. Kretschmann, E. & Raether, H. Radiative Decay of Non Radiative Surface Plasmons Excited by Light. *Zeitschrift für Naturforsch. - Sect. A J. Phys. Sci.* **23**, 2135–2136 (1968).
10. Pelton, M., Aizpurua, J. & Bryant, G. Metal-nanoparticle plasmonics. *Laser Photonics Rev.* **2**, 136–159 (2008).
11. Maier, S. A. *Plasmonics: Fundamentals and applications. Plasmonics: Fundamentals and Applications* (Springer US, 2007). doi:10.1007/0-387-37825-1
12. Atwater, H. A. The Promise of Plasmonics. *Sci. Am.* **296**, 56–62 (2007).
13. El-Sayed, I. H., Huang, X. & El-Sayed, M. A. Selective laser photo-thermal therapy of epithelial carcinoma using anti-EGFR antibody conjugated gold nanoparticles. *Cancer Lett.* **239**, 129–135 (2006).
14. Anker, J. N. *et al.* Biosensing with plasmonic nanosensors. *Nat. Mater.* **7**, 442–453 (2008).
15. Fang, Y. & Sun, M. Nanoplasmonic waveguides: Towards applications in integrated nanophotonic circuits. *Light Sci. Appl.* **4**, e294–e294 (2015).
16. Akimov, A. V. *et al.* Generation of single optical plasmons in metallic nanowires coupled to quantum dots. *Nature* **450**, 402–406 (2007).
17. Koller, D. M. *et al.* Organic plasmon-emitting diode. *Nat. Photonics* (2008). doi:10.1038/nphoton.2008.200
18. Ferry, V. E., Sweatlock, L. A., Pacifici, D. & Atwater, H. A. Plasmonic nanostructure design for efficient light coupling into solar cells. *Nano Lett.* (2008). doi:10.1021/nl8022548
19. McLellan, J. M., Li, Z.-Y., Siekkinen, A. R. & Xia, Y. The SERS Activity of a Supported Ag Nanocube Strongly Depends on Its Orientation Relative to Laser Polarization. *Nano Lett.* **7**, 1013–1017 (2007).
20. Jung, J. Y. *et al.* Amplified fluorescence imaging using photonic Ag nanotip array: A comparative study on surface morphology effects. *Appl. Surf. Sci.* **529**, 147139 (2020).
21. Zhen, Y. R., Fung, K. H. & Chan, C. T. Collective plasmonic modes in two-dimensional periodic arrays of metal nanoparticles. *Phys. Rev. B - Condens. Matter Mater. Phys.* **78**, 035419 (2008).
22. Kravets, V. G., Kabashin, A. V., Barnes, W. L. & Grigorenko, A. N. Plasmonic Surface Lattice Resonances: A Review of Properties and Applications. *Chemical Reviews* **118**, 5912–5951 (2018).

23. Justino, C. I. L., Duarte, A. C. & Rocha-Santos, T. A. P. Recent progress in biosensors for environmental monitoring: A review. *Sensors* **17**, 2918 (2017).
24. Metkar, S. K. & Girigoswami, K. Diagnostic biosensors in medicine – A review. *Biocatal. Agric. Biotechnol.* **17**, 271–283 (2019).
25. Oliverio, M., Perotto, S., Messina, G. C., Lovato, L. & De Angelis, F. Chemical Functionalization of Plasmonic Surface Biosensors: A Tutorial Review on Issues, Strategies, and Costs. *ACS Appl. Mater. Interfaces* **9**, 29394–29411 (2017).
26. Bhalla, N., Pan, Y., Yang, Z. & Payam, A. F. Opportunities and Challenges for Biosensors and Nanoscale Analytical Tools for Pandemics: COVID-19. *ACS Nano* **14**, 7783–7807 (2020).
27. Kifude, C. M. *et al.* Enzyme-Linked Immunosorbent Assay for Detection of Plasmodium falciparum Histidine-Rich Protein 2 in Blood, Plasma, and Serum. *Clin. Vaccine Immunol.* **15**, 1012–1018 (2008).
28. Dou, M. *et al.* Reproductive Hormones and Their Receptors May Affect Lung Cancer. *Cell. Physiol. Biochem.* **44**, 1425–1434 (2017).
29. Dirkzwager, R. M., Liang, S. & Tanner, J. A. Development of Aptamer-Based Point-of-Care Diagnostic Devices for Malaria Using Three-Dimensional Printing Rapid Prototyping. *ACS Sensors* **1**, 420–426 (2016).
30. Fraser, L. A. *et al.* A portable microfluidic Aptamer-Tethered Enzyme Capture (APTEC) biosensor for malaria diagnosis. *Biosens. Bioelectron.* **100**, 591–596 (2018).
31. Wang, W.-X. *et al.* Specific and sensitive detection of Plasmodium falciparum lactate dehydrogenase by DNA-scaffolded silver nanoclusters combined with an aptamer. *Analyst* **142**, 800–807 (2017).
32. Kim, C., Hoffmann, G. & Searson, P. C. Integrated Magnetic Bead–Quantum Dot Immunoassay for Malaria Detection. *ACS Sensors* **2**, 766–772 (2017).
33. Aldewachi, H. *et al.* Gold nanoparticle-based colorimetric biosensors. *Nanoscale* **10**, 18–33 (2018).
34. Chang, C. C. *et al.* Gold nanoparticle-based colorimetric strategies for chemical and biological sensing applications. *Nanomaterials* **9**, 861 (2019).
35. Drexhage, K. H. IV Interaction of Light with Monomolecular Dye Layers. *Prog. Opt.* **12**, 163–192 (1974).
36. Geddes, C. D. & Lakowicz, J. R. Metal-Enhanced Fluorescence. *J. Fluoresc.* **12**, 121–129 (2002).
37. Lakowicz, J. R. *et al.* Advances in Surface-Enhanced Fluorescence. *J. Fluoresc.* **14**, 425–441 (2004).
38. Jackson, J. D. *Classical Electrodynamics, 3rd Edition. Classical Electrodynamics* (1998).
39. Kittel, C. *Introduction to Solid State Physics Solution Manual, 8th Edition. John Wiley & Sons, Inc* (2004).
40. Johnson, P. B. & Christy, R. W. Optical Constants of the Noble Metals. *Phys. Rev. B* **6**, 4370–4379 (1972).
41. Klimov, V. *Nanoplasmonics. Nanoplasmonics* (2013). doi:10.4032/9789814267427
42. Gonçalves, P. A. D. & Peres, N. M. R. *An Introduction to Graphene Plasmonics. An Introduction to Graphene Plasmonics* (WORLD SCIENTIFIC, 2016). doi:10.1142/9948
43. Goubau, G. Surface waves and their application to transmission lines. *J. Appl. Phys.* **21**, 1119–1128 (1950).
44. Raether, H., Hohler, G. & Niekisch, E. A. Surface Plasmons on Smooth and Rough Surfaces and on Gratings. *Springer Tracts in Modern Physics* **111**, 136 (1988).
45. van de Hulst, H. C. *Light Scattering by Small Particles.* (Dover Publications, 1981).
46. Fu, Q. & Sun, W. Mie theory for light scattering by a spherical particle in an absorbing medium. *Appl. Opt.* **40**, 1354 (2001).
47. Chen, H., Shao, L., Li, Q. & Wang, J. Gold nanorods and their plasmonic properties. *Chem. Soc. Rev.* **42**, 2679–2724 (2013).

48. Bohren, C. F. & Huffman, D. R. *Absorption and Scattering of Light by Small Particles. Absorption and Scattering of Light by Small Particles* (Wiley, 1998). doi:10.1002/9783527618156
49. Trügler, A. *Optical Properties of Metallic Nanoparticles : Basic Principles and Simulation. Springer Series in Materials Science* (2016).
50. Mayer, K. M. & Hafner, J. H. Localized surface plasmon resonance sensors. *Chem. Rev.* **111**, 3828–3857 (2011).
51. Haes, A. J. & Van Duyne, R. P. Nanoscale optical biosensors based on localized surface plasmon resonance spectroscopy. in *Plasmonics: Metallic Nanostructures and Their Optical Properties* (ed. Halas, N. J.) **5221**, 47 (SPIE, 2003).
52. Hammond, J. L., Bhalla, N., Rafiee, S. D. & Estrela, P. Localized surface plasmon resonance as a biosensing platform for developing countries. *Biosensors* **4**, 172–188 (2014).
53. Jung, L. S., Campbell, C. T., Chinowsky, T. M., Mar, M. N. & Yee, S. S. Quantitative interpretation of the response of surface plasmon resonance sensors to adsorbed films. *Langmuir* **14**, 5636–5648 (1998).
54. Jain, P. K., Huang, W. & El-Sayed, M. A. On the Universal Scaling Behavior of the Distance Decay of Plasmon Coupling in Metal Nanoparticle Pairs: A Plasmon Ruler Equation. *Nano Lett.* **7**, 2080–2088 (2007).
55. Jain, P. K. & El-Sayed, M. A. Plasmonic coupling in noble metal nanostructures. *Chem. Phys. Lett.* **487**, 153–164 (2010).
56. Draine, B. T. & Flatau, P. J. Discrete-Dipole Approximation For Scattering Calculations. *J. Opt. Soc. Am. A* **11**, 1491–1499 (1994).
57. Laczik, Z. Discrete-dipole-approximation-based light-scattering calculations for particles with a real refractive index smaller than unity. *Appl. Opt.* **35**, 3736 (1996).
58. Draine, B. T. The discrete-dipole approximation and its application to interstellar graphite grains. *Astrophys. J.* **333**, 848 (1988).
59. Sutradhar, A., Paulino, G. H. & Gray, L. J. *Symmetric Galerkin Boundary Element Method. Symmetric Galerkin Boundary Element Method* (Springer Berlin Heidelberg, 2008). doi:10.1007/978-3-540-68772-6
60. García de Abajo, F. J. & Howie, A. Retarded field calculation of electron energy loss in inhomogeneous dielectrics. *Phys. Rev. B - Condens. Matter Mater. Phys.* **65**, 1154181–11541817 (2002).
61. Hohenester, U. & Trügler, A. MNPBEM - A Matlab toolbox for the simulation of plasmonic nanoparticles. *Comput. Phys. Commun.* **183**, 370–381 (2012).
62. Archambeault, B., Ramahi, O. M. & Brench, C. *EMI/EMC Computational Modeling Handbook. EMI/EMC Computational Modeling Handbook* (Springer US, 1998). doi:10.1007/978-1-4757-5124-6
63. Taflove, A., Hagness, S. C. & Picket-May, M. Computational Electromagnetics: The Finite-Difference Time-Domain Method. in *The Electrical Engineering Handbook* 629–670 (Elsevier, 2005). doi:10.1016/B978-012170960-0/50046-3
64. Bérenger, J.-P. Perfectly Matched Layer (PML) for Computational Electromagnetics. *Synth. Lect. Comput. Electromagn.* **2**, 1–117 (2007).
65. Ghosh, S. K. & Pal, T. Interparticle Coupling Effect on the Surface Plasmon Resonance of Gold Nanoparticles: From Theory to Applications. *Chem. Rev.* **107**, 4797–4862 (2007).
66. Miller, M. M. & Lazarides, A. A. Sensitivity of metal nanoparticle surface plasmon resonance to the dielectric environment. *J. Phys. Chem. B* **109**, 21556–21565 (2005).
67. Lee, K. S. & El-Sayed, M. A. Gold and silver nanoparticles in sensing and imaging: Sensitivity of plasmon response to size, shape, and metal composition. *J. Phys. Chem. B* **110**, 19220–19225 (2006).
68. Haes, A. J., Zou, S., Schatz, G. C. & Van Duyne, R. P. Nanoscale optical biosensor: Short range distance dependence of the localized surface plasmon resonance of noble metal nanoparticles. *J. Phys. Chem. B* **108**, 6961–

6968 (2004).

69. Haes, A. J., Zou, S., Schatz, G. C. & Van Duyne, R. P. A nanoscale optical biosensor: The long range distance dependence of the localized surface plasmon resonance of noble metal nanoparticles. *J. Phys. Chem. B* **108**, 109–116 (2004).
70. Yonzon, C. R. *et al.* A comparative analysis of localized and propagating surface plasmon resonance sensors: The binding of Concanavalin A to a monosaccharide functionalized self-assembled monolayer. *J. Am. Chem. Soc.* **126**, 12669–12676 (2004).
71. Link, S. & El-Sayed, M. A. Size and temperature dependence of the plasmon absorption of colloidal gold nanoparticles. *J. Phys. Chem. B* **103**, 4212–4217 (1999).
72. Jain, P. K., Lee, K. S., El-Sayed, I. H. & El-Sayed, M. A. Calculated absorption and scattering properties of gold nanoparticles of different size, shape, and composition: Applications in biological imaging and biomedicine. *J. Phys. Chem. B* **110**, 7238–7248 (2006).
73. Chen, H., Kou, X., Yang, Z., Ni, W. & Wang, J. Shape- and size-dependent refractive index sensitivity of gold nanoparticles. *Langmuir* **24**, 5233–5237 (2008).
74. Mock, J. J., Barbic, M., Smith, D. R., Schultz, D. A. & Schultz, S. Shape effects in plasmon resonance of individual colloidal silver nanoparticles. *J. Chem. Phys.* **116**, 6755–6759 (2002).
75. Mock, J. J., Smith, D. R. & Schultz, S. Local refractive index dependence of plasmon resonance spectra from individual nanoparticles. *Nano Lett.* **3**, 485–491 (2003).
76. Sun, Y. & Xia, Y. Increased sensitivity of surface plasmon resonance of gold nanoshells compared to that of gold solid colloids in response to environmental changes. *Anal. Chem.* **74**, 5297–5305 (2002).
77. Sherry, L. J. *et al.* Localized surface plasmon resonance spectroscopy of single silver nanocubes. *Nano Lett.* **5**, 2034–2038 (2005).
78. Chaudhary, A., Khan, S., Gupta, A. & Nandi, C. K. Effect of surface chemistry and morphology of gold nanoparticle on the structure and activity of common blood proteins. *New J. Chem.* **40**, 4879–4883 (2016).
79. Vashist, S. K. & Luong, J. H. T. Antibody Immobilization and Surface Functionalization Chemistries for Immunodiagnosics. in *Handbook of Immunoassay Technologies* 19–46 (Elsevier, 2018). doi:10.1016/B978-0-12-811762-0.00002-5
80. Della Ventura, B., Schiavo, L., Altucci, C., Esposito, R. & Velotta, R. Light assisted antibody immobilization for bio-sensing. *Biomed. Opt. Express* **2**, 3223 (2011).
81. Funari, R. *et al.* Single Molecule Characterization of UV-Activated Antibodies on Gold by Atomic Force Microscopy. *Langmuir* **32**, 8084–8091 (2016).
82. Della Ventura, B. *et al.* Biosensor surface functionalization by a simple photochemical immobilization of antibodies: experimental characterization by mass spectrometry and surface enhanced Raman spectroscopy. *Analyst* **144**, 6871–6880 (2019).
83. Neves-Petersen, M. T. *et al.* High probability of disrupting a disulphide bridge mediated by an endogenous excited tryptophan residue. *Protein Sci.* **11**, 588–600 (2009).
84. Ioerger, T. R., Du, C. & Linthicum, D. S. Conservation of cys–cys trp structural triads and their geometry in the protein domains of immunoglobulin superfamily members. *Mol. Immunol.* **36**, 373–386 (1999).
85. Della Ventura, B. *et al.* Effective antibodies immobilization and functionalized nanoparticles in a quartz-crystal microbalance-based immunosensor for the detection of parathion. *PLoS One* **12**, e0171754 (2017).
86. Fulgione, A. *et al.* QCM-based immunosensor for rapid detection of Salmonella Typhimurium in food. *Sci. Rep.* **8**, 16137 (2018).
87. Cimafonte, M. *et al.* Screen Printed Based Impedimetric Immunosensor for Rapid Detection of Escherichia coli in Drinking Water. *Sensors* **20**, 274 (2020).

88. Campanile, R. *et al.* Core-Shell Magnetic Nanoparticles for Highly Sensitive Magnetoelastic Immunosensor. *Nanomaterials* **10**, 1526 (2020).
89. Minopoli, A. *et al.* LSPR-based colorimetric immunosensor for rapid and sensitive 17 β -estradiol detection in tap water. *Sensors Actuators B Chem.* **308**, 127699 (2020).
90. Iarossi, M. *et al.* Colorimetric Immunosensor by Aggregation of Photochemically Functionalized Gold Nanoparticles. *ACS Omega* **3**, 3805–3812 (2018).
91. Yeh, Y. C., Creran, B. & Rotello, V. M. Gold nanoparticles: Preparation, properties, and applications in bionanotechnology. *Nanoscale* **4**, 1871–1880 (2012).
92. Aslan, K. & Pérez-Luna, V. H. Surface modification of colloidal gold by chemisorption of alkanethiols in the presence of a nonionic surfactant. *Langmuir* **18**, 6059–6065 (2002).
93. Abad, J. M., Mertens, S. F. L., Pita, M., Fernández, V. M. & Schiffrin, D. J. Functionalization of thioctic acid-capped gold nanoparticles for specific immobilization of histidine-tagged proteins. *J. Am. Chem. Soc.* **127**, 5689–5694 (2005).
94. Kudlak, B. & Wieczerek, M. Aptamer based tools for environmental and therapeutic monitoring: A review of developments, applications, future perspectives. *Crit. Rev. Environ. Sci. Technol.* **50**, 816–867 (2020).
95. Zhang, R. *et al.* Ultrasensitive aptamer-based protein assays based on one-dimensional core-shell nanozymes. *Biosens. Bioelectron.* **150**, 111881 (2020).
96. Zhang, Y. *et al.* Electrochemical dual-aptamer biosensors based on nanostructured multielectrode arrays for the detection of neuronal biomarkers. *Nanoscale* **12**, 16501–16513 (2020).
97. Njoki, P. N. *et al.* Size Correlation of Optical and Spectroscopic Properties for Gold Nanoparticles. *J. Phys. Chem. C* **111**, 14664–14669 (2007).
98. Megarajan, S. & Veerappan, A. A selective pink-to-purple colorimetric sensor for aluminium via the aggregation of gold nanoparticles. *Opt. Mater. (Amst.)* **108**, 110177 (2020).
99. Li, H. & Rothberg, L. Colorimetric detection of DNA sequences based on electrostatic interactions with unmodified gold nanoparticles. *Proc. Natl. Acad. Sci. U. S. A.* **101**, 14036–14039 (2004).
100. Ventura, B. Della *et al.* Colorimetric Test for Fast Detection of SARS-CoV-2 in Nasal and Throat Swabs. *ACS Sensors* accsensors.0c01742 (2020). doi:10.1021/acssensors.0c01742
101. Sato, K., Hosokawa, K. & Maeda, M. Rapid aggregation of gold nanoparticles induced by non-cross-linking DNA hybridization. *J. Am. Chem. Soc.* **125**, 8102–8103 (2003).
102. Wang, G., Akiyama, Y., Takarada, T. & Maeda, M. Rapid Non-Crosslinking Aggregation of DNA-Functionalized Gold Nanorods and Nanotriangles for Colorimetric Single-Nucleotide Discrimination. *Chem. - A Eur. J.* **22**, 258–263 (2016).
103. Aldewachi, H. S., Woodroffe, N., Turega, S. & Gardiner, P. H. E. Optimization of gold nanoparticle-based real-time colorimetric assay of dipeptidyl peptidase IV activity. *Talanta* **169**, 13–19 (2017).
104. Ma, X., Kou, X., Xu, Y., Yang, D. & Miao, P. Colorimetric sensing strategy for heparin assay based on PDPA-induced aggregation of gold nanoparticles. *Nanoscale Adv.* **1**, 486–489 (2019).
105. Liu, J. *et al.* Highly sensitive colorimetric detection of 17 β -estradiol using split DNA aptamers immobilized on unmodified gold nanoparticles. *Sci. Rep.* **4**, 7571 (2014).
106. Hussain, I. *et al.* Size-controlled synthesis of near-monodisperse gold nanoparticles in the 1-4 nm range using polymeric stabilizers. *J. Am. Chem. Soc.* **127**, 16398–16399 (2005).
107. Jana, N. R., Gearheart, L. & Murphy, C. J. Seeding growth for size control of 5-40 nm diameter gold nanoparticles. *Langmuir* **17**, 6782–6786 (2001).
108. Grzelczak, M., Pérez-Juste, J., Mulvaney, P. & Liz-Marzán, L. M. Shape control in gold nanoparticle synthesis.

Chem. Soc. Rev. **37**, 1783–1791 (2008).

109. Turkevich, J., Stevenson, P. C. & Hillier, J. A study of the nucleation and growth processes in the synthesis of colloidal gold. *Discuss. Faraday Soc.* **11**, 55–75 (1951).
110. Frens, G. Controlled Nucleation for the Regulation of the Particle Size in Monodisperse Gold Suspensions. *Nat. Phys. Sci.* **241**, 20–22 (1973).
111. Kumar, S., Gandhi, K. S. & Kumar, R. Modeling of formation of gold nanoparticles by citrate method. *Ind. Eng. Chem. Res.* **46**, 3128–3136 (2007).
112. Pollitt, M. J., Buckton, G., Piper, R. & Brocchini, S. Measuring antibody coatings on gold nanoparticles by optical spectroscopy. *RSC Adv.* **5**, 24521–24527 (2015).
113. Tian, J.-M., Ran, B., Zhang, C.-L., Yan, D.-M. & LI, X.-H. Estrogen and progesterone promote breast cancer cell proliferation by inducing cyclin G1 expression. *Brazilian J. Med. Biol. Res.* **51**, 1–7 (2018).
114. Habib, P. *et al.* Estrogen serum concentration affects blood immune cell composition and polarization in human females under controlled ovarian stimulation. *J. Steroid Biochem. Mol. Biol.* **178**, 340–347 (2018).
115. Sumpter, J. P. Endocrine Disrupters in the Aquatic Environment: An Overview. *Acta Hydrochim. Hydrobiol.* **33**, 9–16 (2005).
116. Omar, T. F. T., Ahmad, A., Aris, A. Z. & Yusoff, F. M. Endocrine disrupting compounds (EDCs) in environmental matrices: Review of analytical strategies for pharmaceuticals, estrogenic hormones, and alkylphenol compounds. *TrAC Trends Anal. Chem.* **85**, 241–259 (2016).
117. Kolok, A. S., Ali, J. M., Rogan, E. G. & Bartelt-Hunt, S. L. The Fate of Synthetic and Endogenous Hormones Used in the US Beef and Dairy Industries and the Potential for Human Exposure. *Curr. Environ. Heal. Reports* **5**, 225–232 (2018).
118. Xuan, R., Blassengale, A. A. & Wang, Q. Degradation of Estrogenic Hormones in a Silt Loam Soil. *J. Agric. Food Chem.* **56**, 9152–9158 (2008).
119. Arnon, S. *et al.* Transport of Testosterone and Estrogen from Dairy-Farm Waste Lagoons to Groundwater. *Environ. Sci. Technol.* **42**, 5521–5526 (2008).
120. Brion, F. *et al.* Impacts of 17 β -estradiol, including environmentally relevant concentrations, on reproduction after exposure during embryo-larval-, juvenile- and adult-life stages in zebrafish (*Danio rerio*). *Aquat. Toxicol.* **68**, 193–217 (2004).
121. González, S., López-Roldán, R. & Cortina, J.-L. Presence and biological effects of emerging contaminants in Llobregat River basin: A review. *Environ. Pollut.* **161**, 83–92 (2012).
122. Liscio, C., Magi, E., Di Carro, M., Suter, M. J.-F. & Vermeirssen, E. L. M. Combining passive samplers and biomonitors to evaluate endocrine disrupting compounds in a wastewater treatment plant by LC/MS/MS and bioassay analyses. *Environ. Pollut.* **157**, 2716–2721 (2009).
123. Liu, P. P. *et al.* TiO₂–BiVO₄ Heterostructure to Enhance Photoelectrochemical Efficiency for Sensitive Aptasensing. *ACS Appl. Mater. Interfaces* **9**, 27185–27192 (2017).
124. Nameghi, M. A. *et al.* An ultrasensitive electrochemical sensor for 17 β -estradiol using split aptamers. *Anal. Chim. Acta* **1065**, 107–112 (2019).
125. Lahcen, A. A., Baleg, A. A., Baker, P., Iwuoha, E. & Amine, A. Synthesis and electrochemical characterization of nanostructured magnetic molecularly imprinted polymers for 17- β -Estradiol determination. *Sensors Actuators B Chem.* **241**, 698–705 (2017).
126. Ni, X. *et al.* Fluorescent aptasensor for 17 β -estradiol determination based on gold nanoparticles quenching the fluorescence of Rhodamine B. *Anal. Biochem.* **523**, 17–23 (2017).
127. Zhang, G., Li, T., Zhang, J. & Chen, A. A simple FRET-based turn-on fluorescent aptasensor for 17 β -estradiol determination in environmental water, urine and milk samples. *Sensors Actuators B Chem.* **273**, 1648–1653

(2018).

128. Neo, S. J., Su, X. & Thomsen, J. S. Surface Plasmon Resonance Study of Cooperative Interactions of Estrogen Receptor α and Transcriptional Factor Sp1 with Composite DNA Elements. *Anal. Chem.* **81**, 3344–3349 (2009).
129. Kumbhat, S., Gehlot, R., Sharma, K., Singh, U. & Joshi, V. Surface plasmon resonance based indirect immunoassay for detection of 17 β -estradiol. *J. Pharm. Biomed. Anal.* **163**, 211–216 (2019).
130. Yao, X. *et al.* An innovative immunochromatography assay for highly sensitive detection of 17 β -estradiol based on an indirect probe strategy. *Sensors Actuators B Chem.* **289**, 48–55 (2019).
131. Akki, S. U. & Werth, C. J. Critical Review: DNA Aptasensors, Are They Ready for Monitoring Organic Pollutants in Natural and Treated Water Sources? *Environ. Sci. Technol.* **52**, 8989–9007 (2018).
132. Miller, J. Interference in immunoassays : avoiding erroneous results. *Clin. Lab. Int.* **28**, 14–17 (2004).
133. Kim, T., Lee, C.-H., Joo, S.-W. & Lee, K. Kinetics of gold nanoparticle aggregation: Experiments and modeling. *J. Colloid Interface Sci.* **318**, 238–243 (2008).
134. Palik, E. D. Refractive Index. in *Handbook of Optical Constants of Solids* 5–114 (Elsevier, 1997). doi:10.1016/B978-012544415-6.50149-7
135. Bell, N. C., Minelli, C. & Shard, A. G. Quantitation of IgG protein adsorption to gold nanoparticles using particle size measurement. *Anal. Methods* **5**, 4591 (2013).
136. Witten, T. A. & Sander, L. M. Diffusion-limited aggregation. *Phys. Rev. B* **27**, 5686–5697 (1983).
137. Zámbo, D. & Deák, A. Optical Simulations of Self-assembly Relevant Gold Aggregates: A Comparative Study. *Period. Polytech. Chem. Eng.* **60**, 244–251 (2016).
138. Taylor, R. W. *et al.* Simple Composite Dipole Model for the Optical Modes of Strongly-Coupled Plasmonic Nanoparticle Aggregates. *J. Phys. Chem. C* **116**, 25044–25051 (2012).
139. Kovalchuk, N. M. & Starov, V. M. Aggregation in colloidal suspensions: Effect of colloidal forces and hydrodynamic interactions. *Adv. Colloid Interface Sci.* **179–182**, 99–106 (2012).
140. Kuhl, H. Pharmacology of estrogens and progestogens: influence of different routes of administration. *Climacteric* **8**, 3–63 (2005).
141. Dasgupta, A. & Wahed, A. Laboratory Statistics and Quality Control. in *Clinical Chemistry, Immunology and Laboratory Quality Control* 47–66 (Elsevier, 2014). doi:10.1016/B978-0-12-407821-5.00004-8
142. Guglielmi, G. The explosion of new coronavirus tests that could help to end the pandemic. *Nature* **583**, 506–509 (2020).
143. Bustin, S. A. & Mueller, R. Real-time reverse transcription PCR (qRT-PCR) and its potential use in clinical diagnosis. *Clin. Sci.* **109**, 365–379 (2005).
144. Olofsson, S., Brittain-Long, R., Andersson, L. M., Westin, J. & Lindh, M. PCR for detection of respiratory viruses: Seasonal variations of virus infections. *Expert Rev. Anti. Infect. Ther.* **9**, 615–626 (2011).
145. Appak, Ö., Duman, M., Belet, N. & Sayiner, A. A. Viral respiratory infections diagnosed by multiplex polymerase chain reaction in pediatric patients. *J. Med. Virol.* **91**, 731–737 (2019).
146. Li, Z. *et al.* Development and Clinical Application of A Rapid IgM-IgG Combined Antibody Test for SARS-CoV-2 Infection Diagnosis. *J. Med. Virol.* 0–1 (2020). doi:10.1002/jmv.25727
147. Satyanarayana, M. Shortage of RNA extraction kits hampers efforts to ramp up COVID-19 coronavirus testing. *Chemical & Engineering News* (2020).
148. Esbin, M. N. *et al.* Overcoming the bottleneck to widespread testing: a rapid review of nucleic acid testing approaches for COVID-19 detection. *RNA* **26**, 771–783 (2020).
149. Pokhrel, P., Hu, C. & Mao, H. Detecting the Coronavirus (COVID-19). *ACS Sensors* **05**, accsensors.0c01153

(2020).

150. Wen, T. *et al.* Development of a lateral flow immunoassay strip for rapid detection of IgG antibody against SARS-CoV-2 virus. *Analyst* (2020). doi:10.1039/d0an00629g
151. Baker, A. N. *et al.* The SARS-COV-2 Spike Protein Binds Sialic Acids, and Enables Rapid Detection in a Lateral Flow Point of Care Diagnostic Device. *Chemrxiv* (2020). doi:10.26434/CHEMRXIV.12465680.V1
152. Montesinos, I. *et al.* Evaluation of two automated and three rapid lateral flow immunoassays for the detection of anti-SARS-CoV-2 antibodies. *J. Clin. Virol.* **128**, (2020).
153. Sheridan, C. Fast, portable tests come online to curb coronavirus pandemic. *Nat. Biotechnol.* **38**, 515–518 (2020).
154. Lassaunière, R. *et al.* Evaluation of nine commercial SARS-CoV-2 immunoassays. *medRxiv* 2020.04.09.20056325 (2020). doi:10.1101/2020.04.09.20056325
155. Tromberg, B. J. *et al.* Rapid Scaling Up of Covid-19 Diagnostic Testing in the United States — The NIH RADx Initiative. *N. Engl. J. Med.* 1–7 (2020). doi:10.1056/NEJMs2022263
156. Tang, L. & Li, J. Plasmon-Based Colorimetric Nanosensors for Ultrasensitive Molecular Diagnostics. *ACS Sensors* **2**, 857–875 (2017).
157. Liu, Y. *et al.* Colorimetric detection of influenza A virus using antibody-functionalized gold nanoparticles. *Analyst* **140**, 3989–3995 (2015).
158. Moitra, P. *et al.* Selective Naked-Eye Detection of SARS-CoV-2 Mediated by N Gene Targeted Antisense Oligonucleotide Capped Plasmonic Nanoparticles. *ACS Nano* **14**, 7617–7627 (2020).
159. Tom, M. R. & Mina, M. J. To Interpret the SARS-CoV-2 Test, Consider the Cycle Threshold Value. *Clin. Infect. Dis.* **71**, 2252–2254 (2020).
160. Zhu, N. *et al.* A novel coronavirus from patients with pneumonia in China, 2019. *N. Engl. J. Med.* **382**, 727–733 (2020).
161. Bar-On, Y. M., Flamholz, A., Phillips, R. & Milo, R. SARS-CoV-2 (COVID-19) by the numbers. *Elife* **9**, e57309 (2020).
162. Ma, L. *et al.* Label-Free Analysis of Single Viruses with a Resolution Comparable to That of Electron Microscopy and the Throughput of Flow Cytometry. *Angew. Chemie Int. Ed.* **55**, 10239–10243 (2016).
163. Haynes, W. M. *CRC Handbook of Chemistry and Physics*. *CRC Handbook of Chemistry and Physics* (CRC Press, 2016). doi:10.1201/9781315380476
164. Motley, M. P., Bennett-Guerrero, E., Fries, B. C. & Spitzer, E. D. Review of Viral Testing (Polymerase Chain Reaction) and Antibody/Serology Testing for Severe Acute Respiratory Syndrome-Coronavirus-2 for the Intensivist. *Crit. care Explor.* **2**, e0154–e0154 (2020).
165. Goutelle, S. *et al.* The Hill equation: A review of its capabilities in pharmacological modelling. *Fundam. Clin. Pharmacol.* **22**, 633–648 (2008).
166. Li, Y., Wang, Y., Huang, G. & Gao, J. Cooperativity Principles in Self-Assembled Nanomedicine. *Chem. Rev.* acs.chemrev.8b00195 (2018). doi:10.1021/acs.chemrev.8b00195
167. Markel, V. A. Coupled-dipole approach to scattering of light from a onedimensional periodic dipole structure. *J. Mod. Opt.* **40**, 2281–2291 (1993).
168. Le Ru, E. C., Somerville, W. R. C. & Auguie, B. Radiative correction in approximate treatments of electromagnetic scattering by point and body scatterers. *Phys. Rev. A* **87**, 012504 (2013).
169. Weber, W. H. & Ford, G. W. Propagation of optical excitations by dipolar interactions in metal nanoparticle chains. *Phys. Rev. B - Condens. Matter Mater. Phys.* **70**, 125429 (2004).
170. Fung, K. H. & Chan, C. T. Plasmonic modes in periodic metal nanoparticle chains: a direct dynamic eigenmode analysis. *Opt. Lett.* **32**, 973 (2007).

171. Rajeeva, B. B., Lin, L. & Zheng, Y. Design and applications of lattice plasmon resonances. *Nano Res.* **11**, 4423–4440 (2018).
172. Viitanen, A. J., Hänninen, I. & Tretyakov, S. A. Analytical model for regular dense arrays of planar dipole scatterers. *Prog. Electromagn. Res.* **38**, 97–110 (2003).
173. Belov, P. A., Simovski, C. R. & Kondratiev, M. S. Problem of the local field for plane grids with bianisotropic particles. in *Smart Structures and Materials 1997: Mathematics and Control in Smart Structures* (eds. Varadan, V. V & Chandra, J.) **3039**, 680–691 (SPIE, 1997).
174. Tsang, L., Kong, J. A., Ding, K.-H. & Ao, C. O. *Scattering of Electromagnetic Waves: Numerical Simulations. Scattering of Electromagnetic Waves: Numerical Simulations* (John Wiley & Sons, Inc., 2001). doi:10.1002/0471224308
175. Ross, M. B., Mirkin, C. A. & Schatz, G. C. Optical Properties of One-, Two-, and Three-Dimensional Arrays of Plasmonic Nanostructures. *J. Phys. Chem. C* **120**, 816–830 (2016).
176. Zorić, I., Zäch, M., Kasemo, B. & Langhammer, C. Gold, platinum, and aluminum nanodisk plasmons: Material independence, subradiance, and damping mechanisms. *ACS Nano* **5**, 2535–2546 (2011).
177. Doyle, W. T. Optical properties of a suspension of metal spheres. *Phys. Rev. B* **39**, 9852–9858 (1989).
178. Li, C. & Jin, Y. Shell-Isolated Plasmonic Nanostructures for Biosensing, Catalysis, and Advanced Nanoelectronics. *Adv. Funct. Mater.* 2008031 (2020). doi:10.1002/adfm.202008031
179. Wilson, A. J., Devasia, D. & Jain, P. K. Nanoscale optical imaging in chemistry. *Chem. Soc. Rev.* **49**, 6087–6112 (2020).
180. Gupta, N., Ninawe, A. & Dhawan, A. Design and modeling of SERS based sensor chips for applications in nanomedicine. in *Plasmonics in Biology and Medicine XVII* (eds. Vo-Dinh, T., Ho, H.-P. A. & Ray, K.) **8** (SPIE, 2020). doi:10.1117/12.2546705
181. Minopoli, A. *et al.* Ultrasensitive antibody-aptamer plasmonic biosensor for malaria biomarker detection in whole blood. *Nat. Commun.* **11**, 6134 (2020).
182. Huang, C.-L., Kumar, G., Sharma, G. D. & Chen, F.-C. Plasmonic effects of copper nanoparticles in polymer photovoltaic devices for outdoor and indoor applications. *Appl. Phys. Lett.* **116**, 253302 (2020).
183. Auguie, B. & Barnes, W. L. Collective Resonances in Gold Nanoparticle Arrays. *Phys. Rev. Lett.* **101**, 143902 (2008).
184. Toma, M. *et al.* Collective plasmon modes excited on a silver nanoparticle 2D crystalline sheet. *Phys. Chem. Chem. Phys.* **13**, 7459 (2011).
185. Kraus, T. *et al.* Nanoparticle printing with single-particle resolution. *Nat. Nanotechnol.* **2**, 570–576 (2007).
186. Yin, Y., Lu, Y., Gates, B. & Xia, Y. Template-assisted self-assembly: A practical route to complex aggregates of monodispersed colloids with well-defined sizes, shapes, and structures. *J. Am. Chem. Soc.* **123**, 8718–8729 (2001).
187. Cheung, C. L., Nikolić, R. J., Reinhardt, C. E. & Wang, T. F. Fabrication of nanopillars by nanosphere lithography. *Nanotechnology* **17**, 1339–1343 (2006).
188. Greben, K., Li, P., Mayer, D., Offenhäusser, A. & Wördenweber, R. Immobilization and Surface Functionalization of Gold Nanoparticles Monitored via Streaming Current/Potential Measurements. *J. Phys. Chem. B* **119**, 5988–5994 (2015).
189. Glass, R., Mller, M. & Spatz, J. P. Block copolymer micelle nanolithography. *Nanotechnology* **14**, 1153–1160 (2003).
190. Lee, W., Lee, S. Y., Briber, R. M. & Rabin, O. Self-Assembled SERS Substrates with Tunable Surface Plasmon Resonances. *Adv. Funct. Mater.* **21**, 3424–3429 (2011).

191. Gilles, S. *et al.* Patterned self-assembly of gold nanoparticles on chemical templates fabricated by soft UV nanoimprint lithography. *Nanotechnology* **22**, 295301 (2011).
192. Jiang, C., Markutsya, S. & Tsukruk, V. V. Collective and Individual Plasmon Resonances in Nanoparticle Films Obtained by Spin-Assisted Layer-by-Layer Assembly. *Langmuir* **20**, 882–890 (2004).
193. Jenkins, J. A. *et al.* Blue-Shifted Narrow Localized Surface Plasmon Resonance from Dipole Coupling in Gold Nanoparticle Random Arrays. *J. Phys. Chem. C* **118**, 26276–26283 (2014).
194. Lakowicz, J. R. Radiative decay engineering: Biophysical and biomedical applications. *Anal. Biochem.* **298**, 1–24 (2001).
195. Li, J. F., Li, C. Y. & Aroca, R. F. Plasmon-enhanced fluorescence spectroscopy. *Chem. Soc. Rev.* **46**, 3962–3979 (2017).
196. Lucas, E., Knoblauch, R., Combs-Bosse, M., Broedel, S. E. & Geddes, C. D. Low-concentration trypsin detection from a metal-enhanced fluorescence (MEF) platform: Towards the development of ultra-sensitive and rapid detection of proteolytic enzymes. *Spectrochim. Acta Part A Mol. Biomol. Spectrosc.* **228**, 117739 (2020).
197. Lakowicz, J. R. *Principles of fluorescence spectroscopy. Principles of Fluorescence Spectroscopy* (Springer US, 2006). doi:10.1007/978-0-387-46312-4
198. Bharadwaj, P. & Novotny, L. Spectral dependence of single molecule fluorescence enhancement. *Opt. Express* **15**, 14266 (2007).
199. Frances, G. C. Des *et al.* Plasmonic Purcell factor and coupling efficiency to surface plasmons. Implications for addressing and controlling optical nanosources. *J. Opt.* **18**, 094005 (2016).
200. Akselrod, G. M. *et al.* Probing the mechanisms of large Purcell enhancement in plasmonic nanoantennas. *Nat. Photonics* **8**, 835–840 (2014).
201. Li, M., Cushing, S. K. & Wu, N. Plasmon-enhanced optical sensors: a review. *Analyst* **140**, 386–406 (2015).
202. Khurgin, J. B. & Sun, G. Enhancement of optical properties of nanoscaled objects by metal nanoparticles. *J. Opt. Soc. Am. B* **26**, B83 (2009).
203. Chen, Y., Munechika, K. & Ginger, D. S. Dependence of Fluorescence Intensity on the Spectral Overlap between Fluorophores and Plasmon Resonant Single Silver Nanoparticles. *Nano Lett.* **7**, 690–696 (2007).
204. Knoblauch, R. & Geddes, C. D. Review of Advances in Metal-Enhanced Fluorescence. in *Reviews in Plasmonics* (ed. Geddes, C. D.) **2017**, 253–283 (Springer International Publishing, 2019).
205. Guzatov, D. V. *et al.* Plasmonic Enhancement of Molecular Fluorescence near Silver Nanoparticles: Theory, Modeling, and Experiment. *J. Phys. Chem. C* **116**, 10723–10733 (2012).
206. Wenger, J. Fluorescence enhancement factors on optical antennas: Enlarging the experimental values without changing the antenna design. *Int. J. Opt.* **2012**, 1–7 (2012).
207. Stratton, J. A. *Electromagnetic Theory. Electromagnetic Theory* (John Wiley & Sons, Inc., 2015). doi:10.1002/9781119134640
208. Le, K. Q. Nanoplasmonic Enhancement of Molecular Fluorescence: Theory and Numerical Modeling. *Plasmonics* **10**, 475–482 (2015).
209. Guzatov, D. V., Gaponenko, S. V. & Demir, H. V. Plasmonic enhancement of electroluminescence. *AIP Adv.* **8**, 015324 (2018).
210. Reineck, P. *et al.* Distance and wavelength dependent quenching of molecular fluorescence by Au@SiO₂ core-shell nanoparticles. *ACS Nano* **7**, 6636–6648 (2013).
211. Polemi, A. & Shuford, K. L. Distance dependent quenching effect in nanoparticle dimers. *J. Chem. Phys.* **136**, 184703 (2012).
212. Klimov, V. V & Guzatov, D. V. Optical properties of an atom in the presence of a two-nanosphere cluster.

Quantum Electron. **37**, 209–230 (2007).

213. Aouani, H. *et al.* Bright unidirectional fluorescence emission of molecules in a nanoaperture with plasmonic corrugations. *Nano Lett.* **11**, 637–644 (2011).
214. de Boer, D. K. G. *et al.* Directional sideward emission from luminescent plasmonic nanostructures. *Opt. Express* **24**, A388 (2016).
215. Tran, N. H. T., Trinh, K. T. L., Lee, J.-H., Yoon, W. J. & Ju, H. Reproducible Enhancement of Fluorescence by Bimetal Mediated Surface Plasmon Coupled Emission for Highly Sensitive Quantitative Diagnosis of Double-Stranded DNA. *Small* **14**, 1801385 (2018).
216. Yousefi, H., Ali, M. M., Su, H.-M., Filipe, C. D. M. & Didar, T. F. Sentinel Wraps: Real-Time Monitoring of Food Contamination by Printing DNAzyme Probes on Food Packaging. *ACS Nano* **12**, 3287–3294 (2018).
217. Liu, P. *et al.* Fluorescence-enhanced bio-detection platforms obtained through controlled ‘step-by-step’ clustering of silver nanoparticles. *Nanoscale* **10**, 848–855 (2018).
218. Markov, A. *et al.* Engineering of Neuron Growth and Enhancing Cell-Chip Communication via Mixed SAMs. *ACS Appl. Mater. Interfaces* **10**, 18507–18514 (2018).
219. Fehrenbacher, L. *et al.* NSABP B-47/NRG Oncology Phase III Randomized Trial Comparing Adjuvant Chemotherapy With or Without Trastuzumab in High-Risk Invasive Breast Cancer Negative for HER2 by FISH and With IHC 1+ or 2+. *J. Clin. Oncol.* **38**, 444–453 (2020).
220. Cirrone, G. A. P. *et al.* First experimental proof of Proton Boron Capture Therapy (PBCT) to enhance protontherapy effectiveness. *Sci. Rep.* **8**, 1141 (2018).
221. Michalet, X. *et al.* Quantum dots for live cells, in vivo imaging, and diagnostics. *Science* **307**, 538–544 (2005).
222. Shima, T. & Uemura, S. Molecular Dynamics Revealed by Single-Molecule FRET Measurement. *Make Life Visible* 105–113 (2020). doi:10.1007/978-981-13-7908-6_10
223. Liang, Y., Huang, X., Yu, R., Zhou, Y. & Xiong, Y. Fluorescence ELISA for sensitive detection of ochratoxin A based on glucose oxidase-mediated fluorescence quenching of CdTe QDs. *Anal. Chim. Acta* **936**, 195–201 (2016).
224. Jeong, Y., Kook, Y.-M., Lee, K. & Koh, W.-G. Metal enhanced fluorescence (MEF) for biosensors: General approaches and a review of recent developments. *Biosens. Bioelectron.* **111**, 102–116 (2018).
225. Fothergill, S. M., Joyce, C. & Xie, F. Metal enhanced fluorescence biosensing: from ultra-violet towards second near-infrared window. *Nanoscale* **10**, 20914–20929 (2018).
226. Lakowicz, J. R. *et al.* Plasmon-controlled fluorescence: a new paradigm in fluorescence spectroscopy. *Analyst* **133**, 1308 (2008).
227. Della Ventura, B. *et al.* Biosensor for Point-of-Care Analysis of Immunoglobulins in Urine by Metal Enhanced Fluorescence from Gold Nanoparticles. *ACS Appl. Mater. Interfaces* **11**, 3753–3762 (2019).
228. Usukura, E. *et al.* Highly confined, enhanced surface fluorescence imaging with two-dimensional silver nanoparticle sheets. *Appl. Phys. Lett.* **104**, 121906 (2014).
229. Du, B. *et al.* Diameter-optimized high-order waveguide nanorods for fluorescence enhancement applied in ultrasensitive bioassays. *Nanoscale* **11**, 14322–14329 (2019).
230. Xie, F., Centeno, A., Ryan, M. R., Riley, D. J. & Alford, N. M. Au nanostructures by colloidal lithography: from quenching to extensive fluorescence enhancement. *J. Mater. Chem. B* **1**, 536–543 (2013).
231. Pompa, P. P. *et al.* Metal-enhanced fluorescence of colloidal nanocrystals with nanoscale control. *Nat. Nanotechnol.* **1**, 126–130 (2006).
232. Kinkhabwala, A. *et al.* Large single-molecule fluorescence enhancements produced by a bowtie nanoantenna. *Nat. Photonics* **3**, 654–657 (2009).
233. Zhou, L. *et al.* Enhancement of Immunoassay’s Fluorescence and Detection Sensitivity Using Three-Dimensional

- Plasmonic Nano-Antenna-Dots Array. *Anal. Chem.* **84**, 4489–4495 (2012).
234. Flauraud, V. *et al.* In-Plane Plasmonic Antenna Arrays with Surface Nanogaps for Giant Fluorescence Enhancement. *Nano Lett.* **17**, 1703–1710 (2017).
 235. Tabakman, S. M. *et al.* Plasmonic substrates for multiplexed protein microarrays with femtomolar sensitivity and broad dynamic range. *Nat. Commun.* **2**, 466 (2011).
 236. Zang, F. *et al.* Ultrasensitive Ebola Virus Antigen Sensing via 3D Nanoantenna Arrays. *Adv. Mater.* **31**, 1902331 (2019).
 237. Puchkova, A. *et al.* DNA Origami Nanoantennas with over 5000-fold Fluorescence Enhancement and Single-Molecule Detection at 25 μ M. *Nano Lett.* **15**, 8354–8359 (2015).
 238. Zhang, B., Kumar, R. B., Dai, H. & Feldman, B. J. A plasmonic chip for biomarker discovery and diagnosis of type 1 diabetes. *Nat. Med.* **20**, 948–953 (2014).
 239. Luan, J. *et al.* Add-on plasmonic patch as a universal fluorescence enhancer. *Light Sci. Appl.* **7**, 29 (2018).
 240. Zhou, Y. *et al.* Fabrication of an antibody-aptamer sandwich assay for electrochemical evaluation of levels of β -amyloid oligomers. *Sci. Rep.* **6**, 35186 (2016).
 241. Waitumbi, J., Awinda, G., Rajasekariah, G.-H., Kifude, C. & Martin, S. K. Unified Parasite Lactate Dehydrogenase and Histidine-Rich Protein ELISA for Quantification of *Plasmodium falciparum*. *Am. J. Trop. Med. Hyg.* **80**, 516–522 (2009).
 242. Phillips, M. A. *et al.* Malaria. *Nat. Rev. Dis. Prim.* **3**, 17050 (2017).
 243. World Health Organization. *World Malaria Report 2019*. Geneva. (2019).
 244. Snow, R. W. Global malaria eradication and the importance of *Plasmodium falciparum* epidemiology in Africa. *BMC Med.* **13**, 23 (2015).
 245. Bell, D., Jorgensen, P., Tsuyuoka, R., Chanthap, L. & Rebuena, A. Malaria rapid diagnostic tests in tropical climates: the need for a cool chain. *Am. J. Trop. Med. Hyg.* **74**, 750–754 (2006).
 246. Nambati, E. A. *et al.* Unclear association between levels of *Plasmodium falciparum* lactate dehydrogenase (pLDH) in saliva of malaria patients and blood parasitaemia: diagnostic implications? *Malar. J.* **17**, 9 (2018).
 247. Lee, W. S. *et al.* Simple, rapid, and accurate malaria diagnostic platform using microfluidic-based immunoassay of *Plasmodium falciparum* lactate dehydrogenase. *Nano Converg.* **7**, 13 (2020).
 248. Low, Y. K. *et al.* Development of an Ultrasensitive Impedimetric Immunosensor Platform for Detection of *Plasmodium* Lactate Dehydrogenase. *Sensors* **19**, 2446 (2019).
 249. Cheung, Y.-W. *et al.* Structural basis for discriminatory recognition of *Plasmodium* lactate dehydrogenase by a DNA aptamer. *Proc. Natl. Acad. Sci.* **110**, 15967–15972 (2013).
 250. Turgut-Balik, D. *et al.* Cloning, sequence and expression of the lactate dehydrogenase gene from the human malaria parasite, *Plasmodium vivax*. *Biotechnol. Lett.* **26**, 1051–1055 (2004).
 251. Cheung, Y.-W. *et al.* Aptamer-mediated *Plasmodium*-specific diagnosis of malaria. *Biochimie* **145**, 131–136 (2018).
 252. Mathison, B. A. & Pritt, B. S. Update on Malaria Diagnostics and Test Utilization. *J. Clin. Microbiol.* **55**, 2009–2017 (2017).
 253. Jimenez, A. *et al.* Analytical sensitivity of current best-in-class malaria rapid diagnostic tests. *Malar. J.* **16**, 128 (2017).
 254. Cheung, Y. W. *et al.* Evolution of abiotic cubane chemistries in a nucleic acid aptamer allows selective recognition of a malaria biomarker. *Proc. Natl. Acad. Sci. U. S. A.* **117**, 16790–16798 (2020).
 255. Gbotosho, G. O. *et al.* Rapid detection of lactate dehydrogenase and genotyping of *Plasmodium falciparum* in

saliva of children with acute uncomplicated malaria. *Am. J. Trop. Med. Hyg.* **83**, 496–501 (2010).

256. Marti  n  z-Vendrell, X. *et al.* Quantification of malaria antigens PfHRP2 and pLDH by quantitative suspension array technology in whole blood, dried blood spot and plasma. *Malar. J.* **19**, 12 (2020).
257. Amendola, V. & Meneghetti, M. Size evaluation of gold nanoparticles by UV-vis spectroscopy. *J. Phys. Chem. C* (2009). doi:10.1021/jp8082425
258. Haiss, W., Thanh, N. T. K., Aveyard, J. & Fernig, D. G. Determination of Size and Concentration of Gold Nanoparticles from UV-Vis Spectra. *Anal. Chem.* **79**, 4215–4221 (2007).
259. Sau, T. K. & Murphy, C. J. Seeded high yield synthesis of short Au nanorods in aqueous solution. *Langmuir* **20**, 6414–6420 (2004).
260. Palik, E. D. *Handbook of Optical Constants of Solids. Handbook of Optical Constants of Solids* (Elsevier, 1985). doi:10.1016/C2009-0-20920-2
261. Sternberg, S. R. Biomedical Image Processing. *Computer (Long Beach, Calif.)*. **16**, 22–34 (1983).